Mid-Infrared Integrated Photonic Sensors of Water and Ice Films for Harsh Environments

Javier Martínez García

UNIVERSITAT ROVIRA i VIRGILI

Mid-Infrared Integrated Photonic Sensors of Water and Ice Films for Harsh Environments

JAVIER MARTÍNEZ GARCÍA

DOCTORAL THESIS
2017

UNIVERSITAT ROVIRA I VIRGILI
Mid-Infrared Integrated Photonic Sensors of Water and Ice Films for Harsh Environments
Javier Martínez García

UNIVERSITAT ROVIRA I VIRGILI
Mid-Infrared Integrated Photonic Sensors of Water and Ice Films for Harsh Environments
Javier Martínez García

Cover picture: 3D render of a photonic icing sensor.

Credit: Alberto Trujillo. https://atrujo.artstation.com/

UNIVERSITAT ROVIRA I VIRGILI
Mid-Infrared Integrated Photonic Sensors of Water and Ice Films for Harsh Environments
Javier Martínez García

Javier Martínez García

MID-INFRARED INTEGRATED PHOTONIC SENSORS OF WATER AND ICE FILMS FOR HARSH ENVIRONMENTS

DOCTORAL THESIS

Supervised by Dr. Airán Ródenas Seguí and
Prof. Dr. Francesc Díaz González

Department of Physical and Inorganic Chemistry

Physics and Crystallography of Materials (FiCMA)

UNIVERSITAT ROVIRA i VIRGILI

Tarragona

2017

UNIVERSITAT ROVIRA I VIRGILI
Mid-Infrared Integrated Photonic Sensors of Water and Ice Films for Harsh Environments
Javier Martínez García

UNIVERSITAT ROVIRA I VIRGILI

DEPARTAMENT DE QUÍMICA FÍSICA I INORGÀNICA

Campus Sescelades
Marcel·lí Domingo, s/n
43007 Tarragona
Tel. +34 977 55 81 37
Fax +34 977 55 95 63
www.quimica.urv.es

We STATE that the present study, entitled “Mid-Infrared Integrated Photonic Sensors of Water and Ice Films for Harsh Environments”, presented by Javier Martínez García for the award of the degree of Doctor, has been carried out under our supervision at the Department of Physical and Inorganic Chemistry of this university.

Tarragona, 27th February 2017

Doctoral Thesis Supervisors

Dr. Airán Ródenas Seguí

Prof. Dr. Francesc Díaz González

UNIVERSITAT ROVIRA I VIRGILI
Mid-Infrared Integrated Photonic Sensors of Water and Ice Films for Harsh Environments
Javier Martínez García

Acknowledgments

The work included in this Thesis has received financial support from the Spanish Government (Projects No. MAT2013-47395-C4-4-R, TEC2014-52642-C2-1-R, TEC2014-55948-R), the Catalan Government (Project No. 2009SGR235, and Scholarship No. 2014FI_B00274) and the European Commission (Project No. ACP2-GA-2013-314335-JEDI ACE).

I am very grateful to my supervisors Airán and Quico for, firstly, giving me the opportunity to take an active part in the JEDI ACE project starting back in 2013 and, secondly, assisting me throughout the past four years in the development of all my research.

I acknowledge Prof. Ajoy K. Kar (Heriot Watt University, Edinburgh, UK), Javier Vázquez de Aldana (Universidad de Salamanca), Javier Solís and Toney Fernández (Instituto de Óptica CSIC, Madrid), and Nadine Rehfeld (Fraunhofer IFAM, Bremen, Germany) to kindly allow me to use their research facilities and equipment.

Also, I would like to thank the rest of the FiCMA group, professors, technicians (Nicole, Agustí, Gemma and Laura) and students (Dat, Sasha, Ali, Olek, Josep Maria, Eric, Josué, Irina, Marc, Arnau and Esrom) for making this hard -but finally rewarding- experience more pleasant.

Lastly and most important, thanks to my friends and family for their constant emotional support, especially to my mother Mari Luz, father Alonso, brother Sergio and girlfriend Anna because although I had to stop seeing them every day for a while, they have been always there for me.

List of related publications and conferences

Paper I

J. Martínez, A. Ródenas, T. Fernandez, J. Vázquez de Aldana, R. Thomson, M. Aguiló, A. Kar, J. Solis, and F. Díaz, "3D laser-written silica glass step-index high-contrast waveguides for the 3.5 μm mid-infrared range," Optics Letters **40**, 5818-5821 (2015).

Paper II

J. Martínez, A. Ródenas, M. Aguiló, T. Fernandez, J. Solis, and F. Díaz, "Mid-infrared surface plasmon polariton chemical sensing on fiber-coupled ITO coated glass," Optics Letters **41**, 2493-2496 (2016).

Paper III

J. Martínez, A. Ródenas, A. Stake, M. Traveria, M. Aguiló, J. Solis, R. Osellame, T. Tanaka, B. Berton, S. Kimura, N. Rehfeld, and F. Díaz, "Harsh-environment resistant OH-vibrations sensitive mid-infrared water-ice photonic sensor". *Submitted to Advanced Functional Materials*.

Patent

F. Díaz, A. Ródenas, M. Traveria, J. Martínez. "OPTICAL SENSOR, SYSTEM AND METHOD FOR DETECTING THE PRESENCE OF ICE ON SURFACES". Application number: PCT/ES2014/070226. Publication date: November 2014.

Conference

J. Martínez, A. Ródenas, T. Fernandez, M. Aguiló, J. R. Vázquez de Aldana, J. Solis, and F. Díaz, "3D Direct-Laser-Written Mid-Infrared Waveguide Circuits in Fused Silica and Crystalline Quartz". Oral communication in ECIO-MOC 2014. Date: 24th-27th June 2014. Place: Nice (France).

Other publications

Paper IV

H.-D. Nguyen, A. Ródenas, J. R. Vázquez de Aldana, J. Martínez, F. Chen, M. Aguiló, M. C. Pujol, and F. Díaz, "Heuristic modelling of laser written mid-infrared LiNbO3 stressed-cladding waveguides," Optics Express **24**, 7777-7791 (2016).

Paper V

H.-D. Nguyen, A. Ródenas, J. Vázquez de Aldana, G. Martín, J. Martínez, M. Aguiló, M. Pujol, and F. Díaz, "Low-loss 3D-laser-written mid-infrared LiNbO3 depressed-index cladding waveguides for both TE and TM polarizations," Optics Express **25**, 3722-3736 (2017).

Table of contents

Abstract

When aircrafts fly through mid-level clouds which are mainly composed of countless supercooled water droplets, they are facing a high risk of icing on their most exposed parts. Even the accretion of thin sub-mm ice films on key elements such as wings, engine inlets or pitot tubes can seriously reduce the aircraft lift and performance, thus making it less fuel-efficient and deteriorating its maneuverability up to the dangerous point of causing loss of control and subsequent accident. Anti-icing technologies deployed on modern aircrafts seek to overcome this issue by means of protection systems capable of not only melting the accreted ice but also of detecting their presence before icing is too severe. In this Thesis, a novel, ultrasensitive icing sensor and yet robust against harsh in-flight conditions which is based on fiber-coupled mid-IR integrated photonics and can be flush-mounted on virtually any aircraft surface without aerodynamic penalty is proposed. By detecting changes in the mid-IR features of water which are intrinsically associated to variations in its molecular structure across its different phases, high-sensitivity and fast response of ice sensing for early-alert operation are demonstrated. Throughout this Thesis, the full development of the device from the theoretical concept to the experimental demonstration of its sensing performance and reliability in a wind tunnel is addressed from both fundamental and applied perspectives. Lastly, a second sensor, with improved sensitivity at the expense of a reduced robustness, for the detection of small volumes of chemical contaminants in water is presented. It takes advantage of the excitation of a mid-IR surface plasmon that enhances the light-analyte interaction around molecular resonances. This further emphasizes the major benefits that operating in the mid-IR can bring to future integrated photonic sensors.

CHAPTER 1

Introduction

In this first chapter, all the elements that one needs to be aware of before going into the development of a mid-infrared integrated photonic surface sensor of water and ice films are introduced. To begin with, water is presented as an indispensable substance for everyday life which, in spite of its harmless appearance, hides countless and intriguing physical and chemical properties. Among them, the ability to remain in a metastable supercooled state (i.e. below freezing temperatures) within clouds is analyzed. Next, it is shown that supercooled water droplets will freeze upon contact with any part of aircrafts flying through those clouds containing them which pose a serious risk for in-flight safety and makes the aircraft significantly less energy-efficient. For this reason, after reviewing the anti-icing technologies implemented on aircrafts as well as those that are still subject of research, a novel icing sensor is introduced. The adequacy mid-IR integrated photonics as a platform for the sensor development, which is still relatively unseen in commercial devices, is discussed considering the aviation industry demands of robust, non-intrusive and early-alert icing sensors. Finally, the main goals to fulfill throughout this Thesis are identified.

1.1. Water is not just water

Water (H_2O) is the most common inorganic liquid on Earth and essential for the existence of life on the planet [1]. It can be naturally found in many places, such as oceans, seas, rivers, lakes and even clouds as countless tiny droplets. The gaseous phase of water, known as water vapor, is one of the compounds of the air we breathe and is also the responsible, for example, of the high attenuation that electromagnetic waves of certain frequencies undergo when transmitted through the atmosphere in radar or satellite applications. Frozen water, namely ice, is present (commonly in its hexagonal phase I_h), among others, in snowflakes, freezing clouds as micro-crystals and glaciers packed in huge and compact amounts. Water in all its three phases (liquid, gaseous and solid) is continuously circulating through different parts of the Earth's biosphere in what is known as the hydrological cycle [1].

Nowadays, water is not only used by humans for basic survival purposes (i.e. drinking) but also for hygiene, agricultural, industrial activities and energy generation. Thus, availability and supply of freshwater together with the control of its quality and conservation are crucial for the future existence of the human species and, in turn, for the rest of living things on Earth.

Paradoxically, the most common and indispensable liquid in the world, has puzzled many researchers who have investigated its exceptional and anomalous properties [2, 3] over decades. For instance, water has a maximum of density at 4 ºC [3, 4] which decreases for lower temperatures and, when frozen, ice can float on liquid water given its lower density. Many other special characteristics have attracted the scientific interest, such as decreased viscosity under pressure or high surface tension [2]. All in all, water is an extremely complex substance and reviewing all its physical and chemical properties of water is out of the scope of this Thesis. A small sample of the water complexity is obvious just from its phase diagram as shown in Figure 1.1.

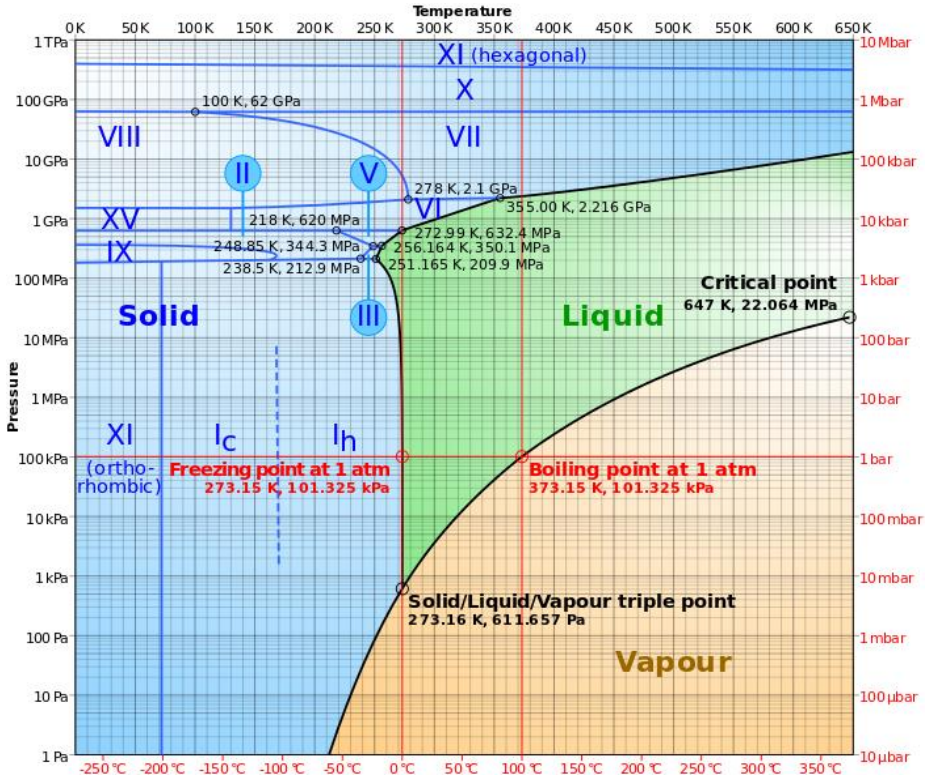

Figure 1.1. Phase diagram of water. Adapted from [5] under CC license.

1.2. From supercooled water to the icing problem

The aforementioned water anomalies are more evident in liquid water at very low (negative) temperatures which has not been frozen [2-4, 6]. Water like that is said to be in a metastable state called supercooled water (SW) [7]. Fundamental research on the structure and dynamics of water have been carried out in this supercooled region of water [8, 9] at temperatures as low as -46 ºC [6] to gain insight in the unique properties of water.

Although water normally freezes at temperatures below 0 ºC at normal pressure, if it is very pure, it is cooled with no vibrations or perturbations and/or there are not nucleation centers on which starting the crystallization process, the liquid phase can be maintained. This is what happens, for instance, in clouds below certain altitude from the sea level which are composed of a special type of µm-

sized sub-zero ºC droplets that will freeze and accrete as ice to any object, at sub-zero temperature as well, hitting them, such as the rotors of wind turbines or the wings of aircrafts [10] (see Figure 1.2 below).

Figure 1.2. (a) Ice accreted on the blade of a wind turbine rotor and (b) on the wing of an aircraft. Adapted from [11] and [12], respectively, under CC license.

The troposphere, which extends up to about 12 km above the sea level (see Figure 1.3), is the region of the atmosphere where the majority of clouds, water vapor, dust and other particles are found. Clouds form due to the condensation of water vapor which is one of the processes involved in the hydrological cycle. Convection of cold and warm air masses are responsible of the cooling of water vapor and the subsequent condensation into the water droplets that clouds are made of. Depending on the clouds composition the likelihood of ice accretion on any structure crossing them will vary [10].

Clouds above 8 km (cirrus, cirrocumulus and cirrostratus) are made of ice crystals due to the low temperatures (see Figure 1.3) which will not adhere after impact; between 3 km and 8 km clouds (altocumulus and altostratus) contain both liquid water droplets and ice crystals; finally, clouds that are below 3 km (nimbostratus, stratocumulus and stratus) are most probably composed of liquid water droplets. Regardless the exact type of cloud, micrometric water droplets may be encountered inside clouds at temperatures below 0 ºC without freezing, down to -40 ºC approximately, which are known as supercooled water droplets (SWD) [7, 10, 13]. These SWD are not stable and will instantly freeze as soon as they contact any substrate at sub-zero temperature as they are provided with a

nucleation center on which crystallization can take place [14]. The substrate asperities promote heterogeneous nucleation through a reduction of the required activation energy for phase change with the respect to that associated to homogenous nucleation [8]. As it is observed in Figure 1.3, the temperature of the cloud is directly related to its height, so that the probability of having high content SWD in a cloud increases in the region from 3 to 8 km.

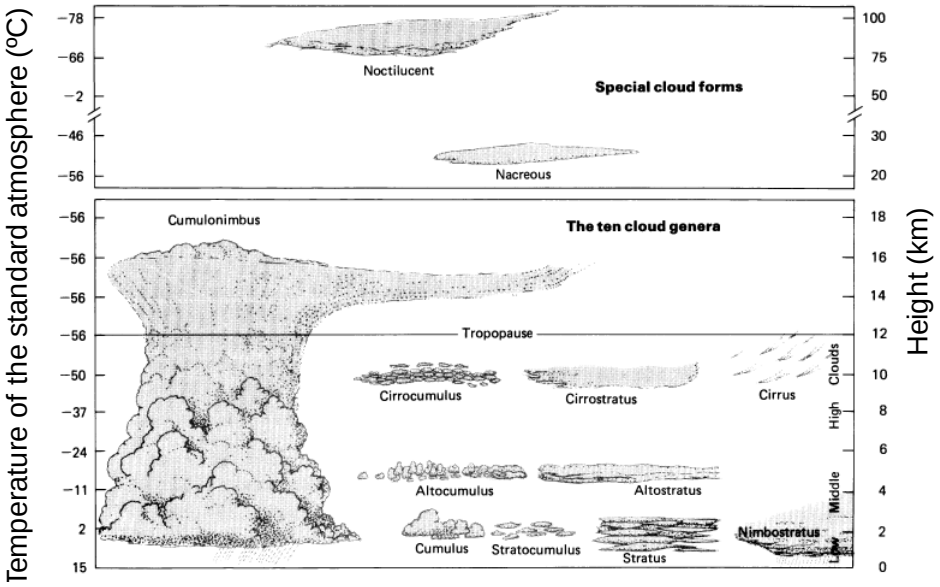

Figure 1.3. Types of clouds of the atmosphere. Adapted from [10].

The presence in clouds of SWD are a recognized issue by aerospace agencies [14, 15] because they increase the risk of in-flight icing leading to aircraft fatalities. Even worse, supercooled large water droplets (SLWD), i.e. those exceeding 50 μm in median volume diameter (MVD), make the icing conditions more severe [13]. SLWD are known to be, for example, the cause of the accident in Roselawn (Indiana, US) in 1994 [13, 16]. The US Federal Aviation Administration (FAA) revealed that from 2003 to 2007 aircraft icing caused up to an 6.7 % of the weather-related accidents [17], as it can be seen in Figure 1.4.

Since the typical altitude at which commercial aircrafts fly is between 9 and 12 km approximately, they need to cross cold regions of low and mid cloud development,

which are more likely composed of SWD, as aforementioned. If, due to sub-zero temperatures (i.e. below the water freezing point) of the airframe and the presence SWD or any form of water in the ambient, ice manages to form on aerodynamic key structures, such as the leading edges of wings or winglets, turbulences may appear on the airflow (even for thin sub-mm ice films) as a result of the modification of the airfoil surface which impedes the smooth flow of air over it. Consequently, aircraft drag is increased and the lift reduced [10] which is a tremendously risky situation for the flight safety. Icing on other important parts of aircrafts like engines inlets or turbines (see Section 1.3) can be also dangerous. Apart from safety issues related to icing, the increased drag makes the flight less energy-efficient (more power and fuel needed) which hampers the current trends of making aviation a greener transport. Therefore, given that aircrafts need to frequently deal with icing conditions for obvious safety reasons, dedicated protection anti-icing systems are required (see Section 1.3) to minimize the risk of accident and reduce fuel consumption.

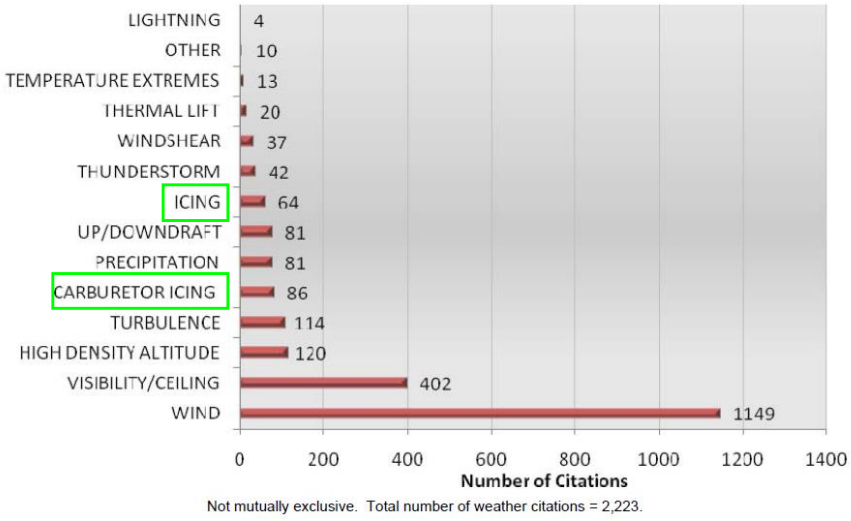

Figure 1.4. Statistics of the weather-related accidents produced in US from 2003 to 2007 according to the FAA. Adapted from [17].

Apart from the accretion on surfaces of SWD contained in clouds, precipitation is the other main cause of icing [10, 14, 18]. Unlike in-cloud SWD icing which, as its

names indicates, happens inside a cold cloud [18], precipitation icing results from relatively large water drops (0.4 to 4 mm) that fall due to gravity. If the falling drops are supercooled (freezing rain or drizzle) they may freeze upon contact on surfaces below 0 ºC at a rate that can be greater than that occurring inside a cloud due to a higher rate of catch of the larger water drops [10]. The falling water drops can also be already frozen in the form of ice crystals and snow which are typically less dangerous than freezing rain drops [10] because they do not adhere instantly when hitting fast moving objects. Lastly, ice can form on surfaces directly by desublimation of water vapor into frost on very cold (sub-zero) surfaces that are in humid environments [14].

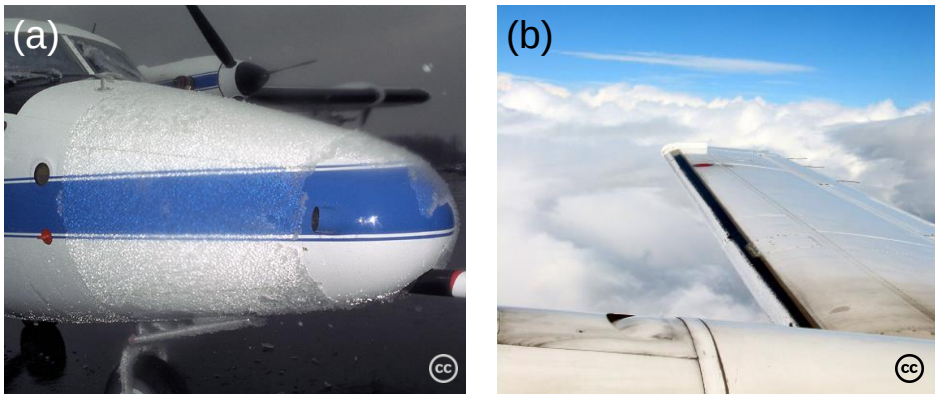

Figure 1.5. Examples of (a) clear ice and (b) rime ice accretion on aircraft external surfaces. Images adapted from [19] and [20], respectively, under CC license.

According to the morphology of the accreted ice, it can be classified into three main categories:

1. Rime ice. This type of ice has a white milky appearance which is induced by its micro-porous nature. It contains μm-sized air bubbles which are responsible for the increased light scattering that makes rime ice look white and shiny. Normally, it appears for in-cloud conditions involving low air speed, relatively low temperature (< -15 ºC) and low liquid water content (LWC[1]) derived from small (< 50 μm) SWD [10]. Rime ice occurs

[1] LWC is the amount of liquid water contained in a given volume of cloud. It is normally expressed in g/m^3. Typical values range approximately from 0.1 to 2 g/m^3 for light to severe icing, respectively.

when SWD instantly freeze upon contact with a surface. An example of rime ice accreted on the leading edge of an aircraft wing can be seen in Figure 1.5(b).

2. Clear or glaze ice. This is a transparent type of ice which can be difficult to see with naked eyes. Freezing rain and high LWC in-cloud conditions containing SLWD promote the accretion of clear ice. Moreover, high speed air and higher temperatures (< 0 ºC and > 15 ºC) are required for the in-cloud formation of this type of ice. Not all the water droplets giving rise to clear ice instantly freeze upon impact as in the rime ice case, but many of them run back along the surface and freeze later, which is known as runback ice. An example of clear ice on the fuselage of an aircraft is shown in Figure 1.5(a).
3. Mixed ice. Sometimes the accreted ice is not purely rime nor clear but a combination of both since the environmental conditions are changing over the flight course and/or are somewhere in the middle relative to the two opposite cases.

Between the two opposite forms of ice, clear ice is considered as the most problematic because it adheres stronger to the aircraft structures and changes more significantly their original shape, which implies a higher aerodynamic penalty than that arising from rime accretion [10, 14]. Regardless the exact type of icing, aviation agencies and industry have been completely aware of the risks since the beginning of commercial flights [21], so that protocols and technologies to prevent, detect and remove ice have been developed over the years [14], as explained in the next section. For a deeper insight into the physics of icing specifically on aircrafts the reader is referred to the broad available literature on the topic, such as [10, 14].

1.3. Fighting against aircraft icing

Before briefly reviewing the state-of-the-art of anti-icing technologies, a more detailed analysis of the places of the aircraft on which ice accumulates with increased probability is given below.

Admittedly, the most commonly studied part exposed to icing are the leading edges of wings. This is due to their direct exposure to the airflow as well as their fundamental role in providing the aircraft with the required lift to fly. This lift can be seriously diminished (while drag increases) even for sub-mm layers of rime or clear ice perturbing the airflow. On the other hand, other aerodynamic, mechanical and electronic parts can suffer from icing with consequences as dangerous as those happening when ice forms on the wings [14]. Figure 1.6 shows an aircraft schematic indicating the parts with higher icing risk.

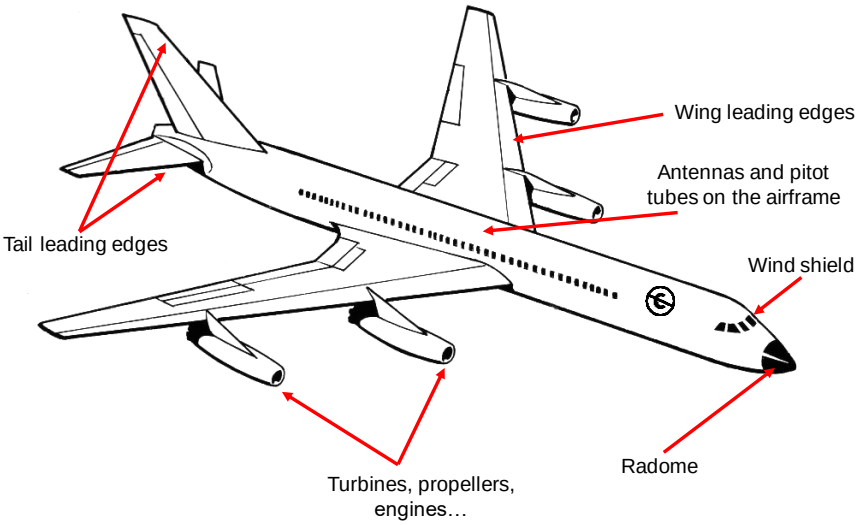

Figure 1.6. Aircraft parts with high risk of icing.

For instance, antennas can be affected by the presence of ice since it detunes their emitting/receiving frequency, thus altering or even disabling normal communication between aircraft and ground stations and satellites. Meteorological radars can also loss functionality due to ice on the radome which “blinds” the aircraft pilot so he/she cannot anticipate the forthcoming weather conditions. Engine air intakes can be blocked by ice which reduces the available air for the combustion process and the power generated is therefore limited. Finally, ice can accumulate inside pitot tubes making unreliable such important sensors of airspeed, pressure and altitude.

To fight against the icing on aircrafts and therefore minimize the risk of accidents as well as making the air transport greener, aviation agencies (e.g. FAA in USA and EASA in Europe), government institutions and industry have made substantial efforts over the last decades to promote the research and development of new anti-ice technologies. Consequently, most aircrafts are already equipped with some sort of anti-icing device to protect their most critical parts whereas many other devices are proposed every year. In general, anti-icing technologies are divided into three main groups.

1. Anti-icing coatings. They basically consist of permanent or temporary coatings applied on surfaces with high risk of icing. These coatings have controlled physical and chemical characteristics with the aim of preventing and reducing the ice accretion (either rime or glaze) to the surface. In commercial aviation is common the use of glycol-based fluid which as a freezing point depressants [14] that are dispersed on the surface to protect either by pumping it through porous materials or spraying it (note that this method could be also encompassed in the next category). Recent research has taken multiple approaches including particle-polymer superhydrophobic micro- and nanostructured surfaces [22], liquid-infused nanostructured icephobic coatings on aluminum [23] or stimulated-antifreeze-secreting anti-icing coatings [24]. The main concern about these coatings is their erosion resistance [25] against high-speed water, ice and dust impingements.
2. Active anti/de-icing devices. The goal of these devices is to prevent the ice formation (anti-icing) and/or remove the already accreted ice (de-icing) by means of some sort of physical effect [26] (mechanical, thermal, etc.) that requires an energy supply. Historically, pneumatic boot surface de-icing systems [14] for in-flight operation have been used to cover large areas needing protection. These boots can inflate to destabilize and destroy the structure of the ice once it has accreted to the surface. Another conventional method is direct the hot air [14] coming from e.g. the engine to either prevent icing or melt and remove after it is formed. A more modern way which typically is less invasive than the previous ones

is to implement electro-thermal devices [14, 27, 28] that are integrated into the aircraft structure, normally into the wings. They are fundamentally resistive materials that heat when an electrical current is applied (e.g. heating mats). Moreover, they can be activated periodically without the pilot intervention during the flight, after an icing sensor triggers an alarm or manually at the pilot's discretion. Lastly, examples of current research trends of anti/de-icing devices are, among others, integrated electro-thermal devices on polymer composite wings [28] and advanced coatings with passive and active anti-icing and de-icing capabilities [29].

3. Icing sensors. Their objective is to assist the anti-icing and de-icing systems (or the pilot who is in charge of activating them when required) by detecting icing conditions in an early stage so that the icing harmful effect can be efficiently and promptly reversed. The dominant ice sensor in the aviation industry is the Goodrich [30] magnetostrictive sensor, which detects changes on a probe vibration frequency when ice forms on it and is typically mounted on the lower area of the aircraft fuselage. Although it gives an *in situ* direct measurement of the ice accretion, it does not provide actual information of the icing on other parts of the aircraft, but only extrapolates the icing severity from one point to the rest by calculations. Other less trustable methods are the so-called indirect methods [18] which consist of measuring certain weather-related magnitudes, such as temperature or humidity to guess ice formation conditions. Apart from the Goodrich sensor, many other direct icing sensors have been developed and proposed which are based on different sensing mechanisms, for instance, ultrasonic pulse-echo sensors that measure the reflection of ultrasonic waves caused by the ice presence [31]; optical fiber sensors detecting changes in the light reflection and scattering as a result of glaze or rime accreting on the surface [32]; thermographic remote icing monitoring [33], and microwave sensor resonators which detect changes on the complex permittivity of the material on the surface so that different types of ice can be distinguished [34].

Only those solutions integrating the three technological categories described above and offering the best trade-off between anti/de-ice performance, energy efficiency and reliability to work in harsh and hostile in-flight environments will be successfully implemented by the industry. Furthermore, they should be specifically adapted to each part of the aircraft needing protection (see Figure 1.6). However, given the amount processes that aviation authorities require for certification and approval of new devices specially those related to safety, it is still soon to see any of these novel technological concepts applied to commercial flights.

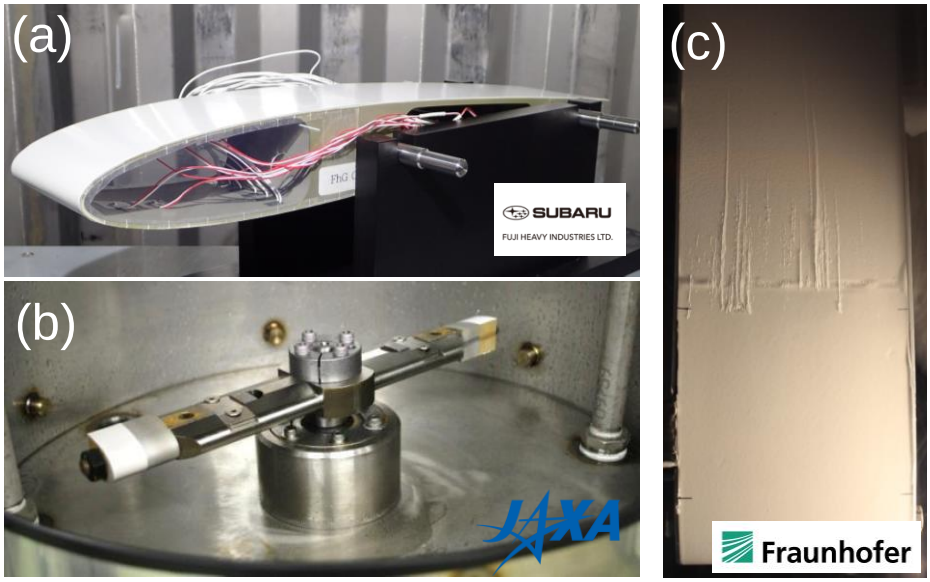

Figure 1.7. Some of the prototypes and tasks carried out during the JEDI ACE project. (a) Wing mock-up with an icing integrated protection system consisting of an electro-thermal system coupled with an icephobic coating developed by Fuji Heavy Industries (FHI). (b) Equipment for rain erosion tests conducted by the Japan Aerospace Exploration Agency (JAXA). (c) Anti-icing coating in action developed by the Fraunhofer Institut.

The author of this Thesis has been actively involved between the years 2013 and 2016 in an EU 7th Framework Programme (FP7) project called Japanese-European De-Icing Aircraft Collaborative Exploration [35] (JEDI ACE) as a part of

the URV team which has been one of the beneficiary institutions. The JEDI ACE project have provided innovative concepts of integrated ice protection systems (specifically for aircraft wings), combining passive anti-icing coatings, active de-icing devices and icing sensors, which are intended to be implemented in future composite wings. A sample of the work done by the different teams, apart from the URV, can be seen in Figure 1.7. The URV team has been responsible for the design and development of a novel ultra-sensitive ice sensor prototype based on integrated photonics technology. Because of this, a substantial part of the contents and outcomes of the present Thesis are result of the tasks carried out during the JEDI ACE project.

1.4. Mid-infrared integrated photonics technology for ultra-sensitive early-alert ice sensing

Ice sensors are nowadays regarded as a key element to rapidly identify icing conditions in real-time. Given the current needs of modern aircrafts in terms of in-flight safety and fuel economy, they should be lightweight and small, aerodynamically non-intrusive, erosion-resistant and, most importantly, sensitive and fast enough to detect ice formation before affecting the normal course of a flight (i.e. in its early micrometer stage) and, therefore, easily removable. Could all these be accomplished by a mid-infrared (mid-IR) integrated photonic sensor as proposed in the present Thesis?

1.4.1. Integrated photonics for sensing

As it will be demonstrated along the following chapters, a properly and specifically designed icing sensor based on integrated photonics (IPh, also known as integrated optics) technology can cope with all the previously listed requirements. IPh is a branch of optics [36] which stems from the combination of waveguide optics with other disciplines such as electro-optics or acousto-optics [36]. Initially by the end of the 1960s, IPh emerged as the technology capable of exceeding the limitation bandwidth imposed by electronics (below ≈ 100 GHz) which was a bottleneck for the rapidly evolving optical communications industry. IPh chips

include various elements with particular functions, such as generating, modulating, splitting or detecting light, which are interconnected by optical waveguides.

Optical waveguides are IPh basic building blocks that are capable of confining and guiding light by means of either 1D/2D total internal reflection (TIR) or 3D photonic crystal effect [36]. Typical building materials of optical waveguides are dielectrics that are transparent at the operation wavelength of the used light source. TIR waveguides in its simple form are either a 1D (planar) or 2D (channel, ridge, etc.) structure that encompasses a volume of material with a certain refractive index (*core*) surrounded by another with a lower one (*cladding*). When the core is small enough for a certain index difference (normally hundreds of nm to tens of μm), light can only travel through it in a finite number of ways called *guided modes*. For the fundamentals on integrated photonics and waveguide theory the reader is referred to the extensive available literature, such as [36, 37]

Even though the development and improvement of waveguides and, in general, of IPh chips significantly benefited the telecommunications field, others like the sensing field [38], and particularly the biochemical sensing [39, 40] field have also taken advantage of them. The most appealing features for this type of sensors are higher miniaturization and enhanced sensitivity [40] relative to those achieved with conventional benchtop devices. Certainly, a waveguide working as an optical transducer enables maximum interaction of photons and analytes while at the same time keeping the device small (mm and cm range). Many of the employed sensing mechanisms rely on detecting changes in the refractive index or the absorption of the analyte which is in close contact to the waveguide using various engineered schemes [40] (gratings, bimodal waveguides, Mach-Zehnder interferometers, ring resonators, etc).

Apart from the waveguide transducer, integrated photonic sensors, as any other IPh device, may include other active or passive elements into a single substrate as well, such as sources, detectors or input/output optical fiber ports for interconnection with other sub-systems. What is more, over the last years, integrated photonic sensors have been combined with microfluidics, giving raise

to the opto-fluidics field which aims to incorporate IPh technology and all the required hardware into lab-on-a-chip devices [40, 41] that, for example, healthcare personnel could use for fast and reliable diagnosis.

1.4.2. Opportunities in the mid-IR

The mid-IR is the electromagnetic spectral region encompassing wavelengths from 2.5 μm to 20 μm [42] (note some discrepancies on the exact range found among different authors). It contains numerous, strong and well-defined molecular fingerprints [42, 43] associated to the corresponding vibrational and rotational motions of atoms within different molecules (see Figure 1.8).

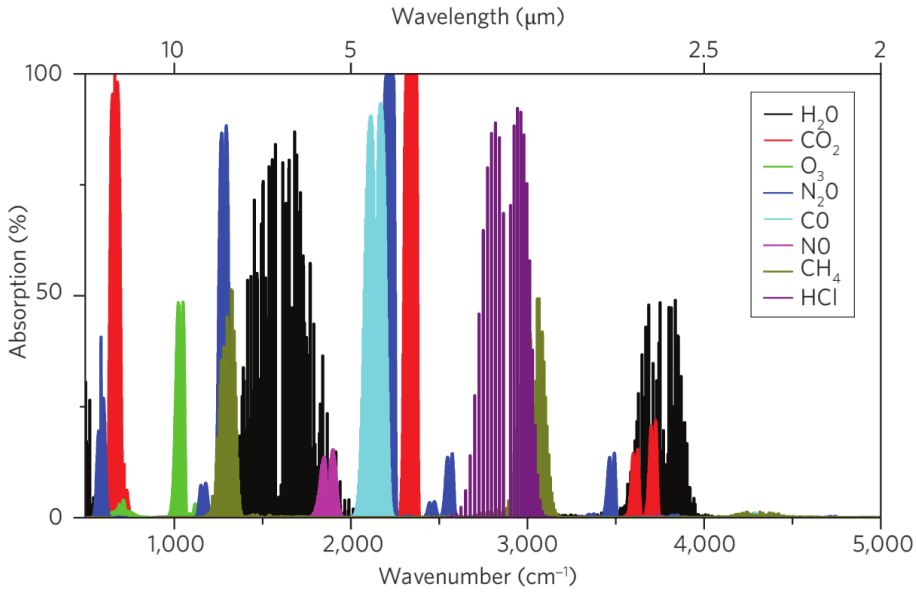

Figure 1.8. Examples of mid-IR absorptions of various molecules (first isotope) demonstrating the potential of this range. Adapted from [44].

If compared to the visible and near-IR ranges, the mid-IR seems to be more convenient to directly and unequivocally target and discriminate different compounds due to the narrower and sharper molecular features there [42]. For these reasons, the use of mid-infrared light has already been shown to enhance the performance of optical devices belonging to multiple fields, such as laser

imaging [45], environmental monitoring [46], biomedicine [43], astronomy [47] or bio/chemical sensing [42].

Below 2.5 μm and above the UV (i.e. in the visible and near-IR ranges), it is where the vast majority of optical devices, including IPh ones, work. The reason for that is, until recently, most of the commercially available optical fibers and coherent sources (i.e. lasers) operated in the visible and near-IR ranges. On the other hand, the corresponding mid-IR counterparts have not reached yet their extensive deployment and relatively low-cost, although considerable progress is being made given the increasing demand of mid-IR-based products.

Before the first quantum cascade laser (QCL) invention emitting at 4.2 μm [48], access to long wavelengths was achieved by either inefficient and incoherent blackbody light sources or by a variety of cumbersome laser sources. These included semiconductors lead salt lasers, gas lasers, doped insulator solid-state lasers or sources based on nonlinear frequency generation of other seed lasers. All of them had important drawbacks (e.g. operation at cryogenic temperatures, highly stable environment needed, low powered, small efficiencies, large size or few number of operating wavelengths available) which impeded their successful integration into other complex devices.

Today's QCLs, and their cousins interband cascade lasers (ICLs), have matured enough in terms of miniaturization and efficiency so that industry has started to adopt them. A well-known demonstration of the covenience of these lasers and their reliability is the recent utilization of a mid-IR tunable laser spectrometer and an ICL emitting at 3.27 μm by the NASA's rover Curiosity to look for methane in Mars [49]. They have also been incorporated into lab-on-a-chip devices as integrated waveguide lasers [50] which shows the high level of compactness they can achieve. Other excellent mid-IR spatially coherent sources but emitting in a broad range of frequencies have been developed, namely mid-IR supercontinuum [51] and frequency combs [44] sources.

The previously mentioned spatial coherence is a fundamental requisite to efficiently couple the light into (single-mode) mid-IR waveguides. Obviously, the building material of such waveguides needs to be transparent into the specific

mid-IR range of operation. Popular mid-IR materials for IPh are zinc selenide [52], silicon [53], germanium [54] and chalcogenide glasses [55]. Fabrication techniques are dependent on the specific material and, in general, are the same as those used for visible and near-IR IPh (i.e. diffusion and deposition techniques [36]). Since a broad range like the mid-IR cannot rely on only one material, newer techniques like three-dimensional direct laser writing (3DLW) [56] have emerged as a flexible alternative because it allows rapid prototyping 3D circuits in virtually almost any material. All in all, the huge advances in mid-IR technology and the constant reduction of their cost are enabling the development of more and more industrial devices exploiting the competitive advantages of this spectral range.

1.4.3. The challenge: a waveguide mid-IR icing sensor working in harsh in-flight conditions

As an icing sensor, the device presented in this Thesis needs to deal with water (i.e. the substance to detect) in its various forms, namely liquid water, supercooled water and ice. Water optical properties are significantly complex and variable across the different light frequencies. As an example of this complexity, Figure 1.9 shows the absorption spectrum of liquid water at room temperature from the UV to the Far-IR.

The absorption features are result of the vibrational and rotational motions of the of the two hydrogens (H) and the oxygen (O) atoms, being the H atoms movements those having the dominant impact on the spectrum as they are lighter [57]. In the mid-IR, strong and distinct absorption bands are found at 2.87 μm, 3.05 μm, 4.65 μm, 6.08 μm and 15 μm which arise, respectively from the molecule (ν_3) asymmetric stretch, (ν_1) symmetric stretch, ($\nu_2 + L_2$) bending librations, (ν_2) bending and (L_2) librations [57]. All these bands are notably altered (spectral position and amplitude) when the substance changes structurally, for example when it freezes to form ice. Moreover, not only the optical absorption but also the refractive index of the water respond to its structural changes since both are linked through the Kramers-Kronig relations. Therefore, a sensor probing directly those changes in real-time at the micrometer scale would have a clear

advantage over other optical sensors detecting macroscopic variations in properties such as scattering, transmission or birefringence (e.g. [32]). This added to the inherent sensitivity of IPh sensors would certainly meet the requirements of the industry regarding early-alert icing sensors.

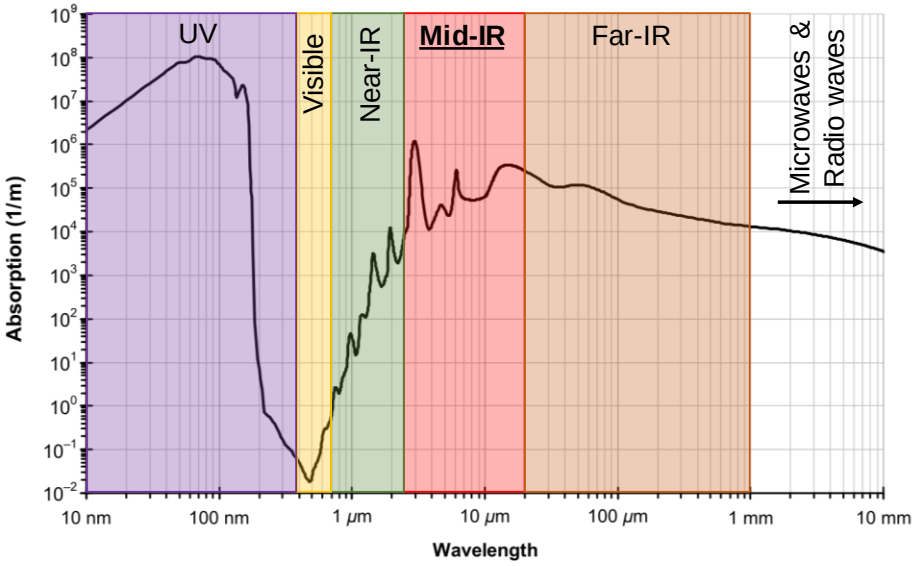

Figure 1.9. Light absorption spectrum of liquid water for wavelengths from 10 nm to 10 mm. Adapted from [58] under CC license.

Naturally, highly sensitive integrated nanophotonic and microphotonic sensors rely on the direct exposure to the external environment of their guiding structures [40, 42, 53]. This would definitely be problematic for the physical integrity of the waveguide transducer and, hence, for the correct performance of a sensor operating in harsh in-flight conditions (i.e. undergoing chemical corrosion, mechanical vibrations, large temperature variations and water/dust erosion). Consequently, the optical sensor presented in this Thesis must somehow overcome this issue together with others such as its integration on aircraft structures minimizing the aerodynamic penalty or the coupling of light into μm-sized waveguides in a not very optical-friendly environment.

1.5. Goals of this Thesis

To close this first introductory Chapter, the global objectives of the Thesis are summarized below.

a) To theoretically design and demonstrate a mid-IR icing integrated photonic sensor capable of being flush-mounted on aircraft surfaces to accurately assess the presence of water and ice films in the μm scale so that an early-alert can be sent. Numerical simulations proving the waveguiding sensing mechanism and testing its high sensitivity for different types of ice, varying thicknesses and its selectivity between liquid water and ice are needed.

b) To find the proper technique to fabricate the sensing structure (i.e. the waveguide) on the selected solid substrate. To demonstrate why the 3DLW technique is the best alternative for this particular job given its unique features. Finally, to the describe the followed fabrication process and the parameters required for the selected substrate material.

c) To fully characterize the fabricated waveguides used for the sensor from an engineering (mode profiles, losses, refractive index change) and fundamental (origin of the refractive index change) point of view.

d) To fabricate the required prototypes and evaluate experimentally the water-ice sensing mechanism in a static environment. To implement, in a robust and non-intrusive way through optical fiber connection, the sensor into a wing mock-up to carry out icing wind tunnel experiments in realistic in-flight conditions. Then, to test the temporal and spectral sensor response against different types of ices accreted at different speeds and temperatures. To check the reliability of the sensor along all these tests and thus confirm its convenience to be safely incorporated into aircrafts.

e) Finally, to upgrade the sensitivity of the previous photonic sensor in order to explore the possibility of detecting ppm volumes of contaminants in water in controlled laboratory conditions via the excitation of a mid-IR plasmonic mode. Given its different characteristics, this new sensor will

require the development of a supercontinuum source together with slightly different experimental methods. Thus, mid-IR IPh will be further proved as a powerful platform for integrated photonics sensing.

References

1. F. R. Spellman, *The Science of Water* (CRC Press, 2008).
2. L. G. M. Pettersson, R. H. Henchman, and A. Nilsson, "Water—The Most Anomalous Liquid," Chemical Reviews **116**, 7459-7462 (2016).
3. F. Mallamace, C. Corsaro, and H. E. Stanley, "Possible relation of water structural relaxation to water anomalies," Proceedings of the National Academy of Sciences **110**, 4899-4904 (2013).
4. O. Mishima, and H. E. Stanley, "The relationship between liquid, supercooled and glassy water," Nature **396**, 329-335 (1998).
5. http://commons.wikimedia.org/wiki/File:Phase_diagram_of_water.svg
6. A. Nilsson, S. Schreck, F. Perakis, and L. G. M. Pettersson, "Probing water with X-ray lasers," Advances in Physics: X **1**, 226-245 (2016).
7. F. C. Frank, "Molecular Structure of Deeply Super-cooled Water," Nature **157**, 267 (1946).
8. S. Jung, M. K. Tiwari, N. V. Doan, and D. Poulikakos, "Mechanism of supercooled droplet freezing on surfaces," Nature Communications **3**, 615 (2012).
9. S. Jung, M. K. Tiwari, and D. Poulikakos, "Frost halos from supercooled water droplets," Proceedings of the National Academy of Sciences **109**, 16073-16078 (2012).
10. I. Paraschivoiu, and F. Saeed, *Aircraft and Wind Turbine Icing* (Polytechnique International Press, Québec, Canada, 2015).
11. http://commons.wikimedia.org/wiki/File:Ice-at-rotor-blade-of-wind-turbine.jpg
12. http://commons.wikimedia.org/wiki/File:Ice_on_an_aircraft_wing.jpg
13. M. Brahimi, P. Tran, D. Chocron, F. Tezok, and I. Paraschivoiu, "Effect of supercooled large droplets on ice accretion characteristics," (American Institute of Aeronautics and Astronautics, 1997).
14. A. Heinrich, R. Ross, G. Zumwalt, J. Provorse, V. Padmanabhan, J. Thompson, and J. Riley, *Aircraft icing handbook* (1991).
15. http://www.regulations.gov/document?D=FAA_FRDOC_0001-11426
16. "Proceedings of the FAA International Conference on Aircraft Inflight Icing," (US Department of Transportation, Springfield, Virginia, 1996).
17. http://www.asias.faa.gov/i/2003-2007weatherrelatedaviationaccidentstudy.pdf
18. M. C. Homola, P. J. Nicklasson, and P. A. Sundsbø, "Ice sensors for wind turbines," Cold Regions Science and Technology **46**, 125-131 (2006).
19. http://commons.wikimedia.org/wiki/File:Icing_on_a_plane.jpg
20. http://commons.wikimedia.org/wiki/File:A_little_rime_for_ya%3F_(228877806).jpg
21. http://archive.org/details/gov.archives.arc.75096
22. L. Cao, A. K. Jones, V. K. Sikka, J. Wu, and D. Gao, "Anti-Icing Superhydrophobic Coatings," Langmuir **25**, 12444-12448 (2009).
23. P. Kim, T.-S. Wong, J. Alvarenga, M. J. Kreder, W. E. Adorno-Martinez, and J. Aizenberg, "Liquid-Infused Nanostructured Surfaces with Extreme Anti-Ice and Anti-Frost Performance," ACS Nano **6**, 6569-6577 (2012).

24. X. Sun, V. G. Damle, S. Liu, and K. Rykaczewski, "Bioinspired Stimuli-Responsive and Antifreeze-Secreting Anti-Icing Coatings," Advanced Materials Interfaces **2**, 1400479-n/a (2015).
25. K. Golovin, S. P. R. Kobaku, D. H. Lee, E. T. DiLoreto, J. M. Mabry, and A. Tuteja, "Designing durable icephobic surfaces," Science Advances **2** (2016).
26. S. K. Thomas, R. P. Cassoni, and C. D. MacArthur, "Aircraft anti-icing and de-icing techniques and modeling," Journal of Aircraft **33**, 841-854 (1996).
27. "Electro-thermal ice protection system for the B-787," Aircraft Engineering and Aerospace Technology **79** (2007).
28. M. Mohseni, and A. Amirfazli, "A novel electro-thermal anti-icing system for fiber-reinforced polymer composite airfoils," Cold Regions Science and Technology **87**, 47-58 (2013).
29. T. Wang, Y. Zheng, A.-R. O. Raji, Y. Li, W. K. A. Sikkema, and J. M. Tour, "Passive Anti-Icing and Active Deicing Films," ACS Applied Materials & Interfaces **8**, 14169-14173 (2016).
30. http://utcaerospacesystems.com/cap/systems/sisdocuments/Ice%20Detection%20and%20Protection%20Systems/Ice%20Detector%20Model%200871NA.pdf
31. R. J. Hansman, and M. S. Kirby, "Measurement of ice growth during simulated and natural icing conditions using ultrasonic pulse-echo techniques," Journal of Aircraft **23**, 492-498 (1986).
32. J. Ge, L. Ye, and J. Zou, "A novel fiber-optic ice sensor capable of identifying ice type accurately," Sensors and Actuators A: Physical **175**, 35-42 (2012).
33. M. Mohseni, M. Frioult, and A. Amirfazli, "Simultaneous monitoring of ice accretion and thermography of an airfoil: an IR imaging methodology," Measurement Science and Technology **23**, 105405 (2012).
34. N. O. Rennó, "Aircraft icing detector ", US9302777 B2 (2016)
35. http://www.jediace.net
36. G. Lifante, *Integrated Photonics: Fundamentals* (Wiley & Sons, 2003).
37. A. W. Snyder, and J. Love, *Optical Waveguide Theory* (Springer, 1983).
38. M. V. Passaro, D. C. Tullio, B. Troia, L. M. Notte, G. Giannoccaro, and D. F. Leonardis, "Recent Advances in Integrated Photonic Sensors," Sensors **12** (2012).
39. M. V. Passaro, F. Dell'Olio, B. Casamassima, and F. De Leonardis, "Guided-Wave Optical Biosensors," Sensors **7** (2007).
40. M. C. Estevez, M. Alvarez, and L. M. Lechuga, "Integrated optical devices for lab-on-a-chip biosensing applications," Laser & Photonics Reviews **6**, 463-487 (2012).
41. A. L. Washburn, and R. C. Bailey, "Photonics-on-a-chip: recent advances in integrated waveguides as enabling detection elements for real-world, lab-on-a-chip biosensing applications," Analyst **136**, 227-236 (2011).
42. B. Mizaikoff, "Waveguide-enhanced mid-infrared chem/bio sensors," Chemical Society Reviews **42**, 8683-8699 (2013).
43. R. W. Waynant, I. K. Ilev, and I. Gannot, "Mid–infrared laser applications in medicine and biology," Philosophical Transactions of the Royal Society of London. Series A: Mathematical, Physical and Engineering Sciences **359**, 635 (2001).

44. A. Schliesser, N. Picque, and T. W. Hansch, "Mid-infrared frequency combs," Nature Photonics **6**, 440-449 (2012).
45. Y. Wang, Y. Wang, and H. Q. Le, "Multi-spectral mid-infrared laser stand-off imaging," Optics Express **13**, 6572-6586 (2005).
46. R. Muda, E. Lewis, S. O. Keeffe, G. Dooly, and J. Clifford, "Detection of high level carbon dioxide emissions using a compact optical fibre based mid-infrared sensor system for applications in environmental pollution monitoring," Journal of Physics: Conference Series **178**, 012008 (2009).
47. L. Labadie, and O. Wallner, "Mid-infrared guided optics: a perspective for astronomical instruments," Optics Express **17**, 1947-1962 (2009).
48. J. Faist, F. Capasso, D. L. Sivco, C. Sirtori, A. L. Hutchinson, and A. Y. Cho, "Quantum Cascade Laser," Science **264**, 553 (1994).
49. C. R. Webster, P. R. Mahaffy, S. K. Atreya, G. J. Flesch, M. A. Mischna, P.-Y. Meslin, K. A. Farley, P. G. Conrad, L. E. Christensen, A. A. Pavlov, J. Martín-Torres, M.-P. Zorzano, T. H. McConnochie, T. Owen, J. L. Eigenbrode, D. P. Glavin, A. Steele, C. A. Malespin, P. D. Archer, B. Sutter, P. Coll, C. Freissinet, C. P. McKay, J. E. Moores, S. P. Schwenzer, J. C. Bridges, R. Navarro-Gonzalez, R. Gellert, and M. T. Lemmon, "Mars methane detection and variability at Gale crater," Science **347**, 415 (2015).
50. B. Schwarz, P. Reininger, D. Ristanić, H. Detz, A. M. Andrews, W. Schrenk, and G. Strasser, "Monolithically integrated mid-infrared lab-on-a-chip using plasmonics and quantum cascade structures," Nature Communications **5**, 4085 (2014).
51. C. Xia, M. Kumar, O. P. Kulkarni, M. N. Islam, J. F. L. Terry, M. J. Freeman, M. Poulain, and G. Mazé, "Mid-infrared supercontinuum generation to 4.5 μm in ZBLAN fluoride fibers by nanosecond diode pumping," Optics Letters **31**, 2553-2555 (2006).
52. J. R. Macdonald, S. J. Beecher, P. A. Berry, K. L. Schepler, and A. K. Kar, "Compact mid-infrared Cr:ZnSe channel waveguide laser," Applied Physics Letters **102**, 161110 (2013).
53. P. T. Lin, V. Singh, J. Hu, K. Richardson, J. D. Musgraves, I. Luzinov, J. Hensley, L. C. Kimerling, and A. Agarwal, "Chip-scale Mid-Infrared chemical sensors using air-clad pedestal silicon waveguides," Lab on a Chip **13**, 2161-2166 (2013).
54. U. Younis, S. K. Vanga, A. E.-J. Lim, P. G.-Q. Lo, A. A. Bettiol, and K.-W. Ang, "Germanium-on-SOI waveguides for mid-infrared wavelengths," Optics Express **24**, 11987-11993 (2016).
55. A. Ródenas, G. Martin, B. Arezki, N. Psaila, G. Jose, A. Jha, L. Labadie, P. Kern, A. Kar, and R. Thomson, "Three-dimensional mid-infrared photonic circuits in chalcogenide glass," Optics Letters **37**, 392-394 (2012).
56. R. Osellame, G. Cerullo, and R. Ramponi, *Femtosecond Laser Micromachining: Photonic and Microfluidic Devices in Transparent Materials* (Springer, 2012).
57. http://www1.lsbu.ac.uk/water/water_vibrational_spectrum.html
58. http://commons.wikimedia.org/wiki/File:Absorption_spectrum_of_liquid_water.png

CHAPTER 2

Concept development of a harsh environment-resistant OH-vibration-sensitive optical surface sensor for precise monitoring of water-ice phase changes and ice microstructures

In this chapter, an OH-vibration mode sensitive infrared surface sensor which can be flush-mounted and fiber-coupled on almost any surface to detect from sub-micrometric (~100 nm) to macroscopic water and ice films is theoretically investigated. One of the main competitive advantages of the sensor is its robustness making it capable of working in rough industrial environments. Specifically, the sensor is designed for the aircraft industry which currently needs effective means to overcome the dangerous in-flight icing issue. For this reason, the main requirements to meet are based on the aviation particular demands, although other industries may also find the sensor suitable for their needs. Based on these requirements a sensor model conveniently parametrized is presented. The fundamentals of the interaction mechanism that allows the sensor to instantly detect thin ice layers as well as water-ice phase changes are described along with electromagnetic simulations that can predict the sensor performance. Lastly, general design guidelines that will be useful in the fabrication and testing stages are provided.

2.1. Requirements for an industrial water-ice sensor

The technical requirements for the surface water-ice (term used to denote H_2O phase sensitivity) integrated photonics sensor presented in this Thesis depend strongly on the final application. Since the development of the sensor has been carried out within the frame of the JEDI ACE project, special emphasis has been placed on the aircraft industry demands.

2.1.1. Aviation industry

As mentioned in the introduction, the aerospace agencies together with the aviation industry are continuously seeking for improved anti-icing systems, including anti-icing coatings to prevent ice accretion, de-icing devices to remove the already accreted ice and icing sensors to detect the ice formation.

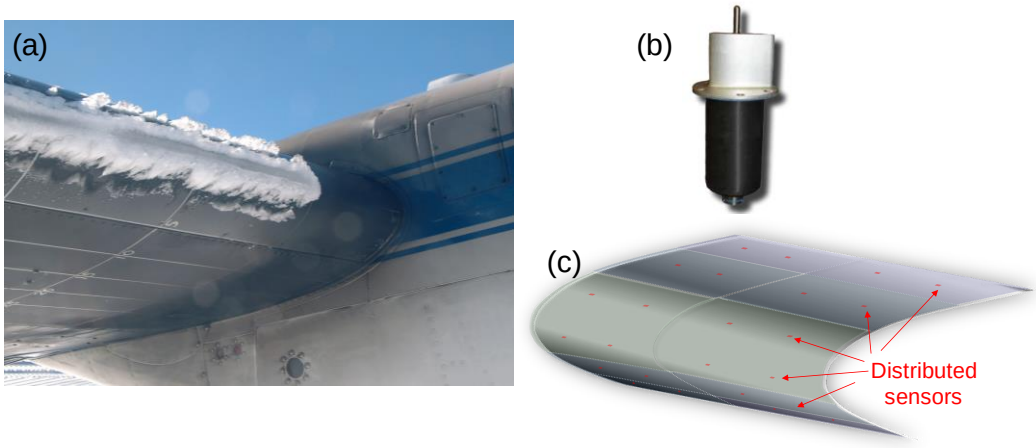

Figure 2.1. (a) Ice accretion on an aircraft wing (credit: NASA). (b) Magnetostrictive Goodrich ice sensor used in aircrafts and wind turbines [1]. (c) Distributed flush-mounted sensor concept.

The most deployed ice sensor in all types of aircrafts, and approved by the corresponding regulating agencies, is the Goodrich magnetostrictive sensor [1, 2] which consists of a protruding metallic probe (see Figure 2.1(b)), mounted on selected areas of the fuselage, resonating normally at a specific kHz frequency

which varies slightly when ice starts to form on it. According to the specifications sheet [1], the minimum detectable ice thickness is 0.001" and the threshold for ice alert activation is 0.020". Obviously, a high ice thickness sensitivity is necessarily one of the requirements for the optical sensor developed in Thesis since it means that, immediately after ice starts to nucleate, a rapid alert can be sent to the pilot or de-icing systems, which would take the corresponding actions.

The type of ice sensor was chosen to be a sub-mm sized flush-mounted early-alert optical sensor. In Table 2.1, the ice sensor qualitative requirements suggested in this Thesis with a brief general description can be found.

Requirement	Description
Distributed sensor	For a complete monitoring of the ice accretion on all the problematic surfaces the sensor needs to be distributed across them. This concept (e.g. Figure 2.1(c)) is not developed in this Thesis.
Anti/de-icing technology compatible	The sensor implementation should not interfere with the anti-icing and de-icing devices. Hence, a reduced footprint is required.
EMI immunity	No radiofrequency signal interference should affect the sensing mechanism. Optical technology guarantees this.
Physically and chemically resistant	Given the erosion and other external agents affecting the body of an aircraft, the sensor should be designed taking into account those materials providing enough in-flight robustness, i.e. hardness and chemical inertness.
High ice detection sensitivity	The sensor needs to detect the early stages of ice nucleation (first few μm) on the critical surface to minimize dangerous ice accumulation and save energy in the de-icing process. To do so, the sensor must be sensitive to the phase changes of the H_2O molecules.
Fast response	This is directly linked to the previous one but also includes the processing and decision time of the electronics that work on the transducer raw signal. Ideally it should be in the order of 1 second or less.
Flush-mounted	The sensor should not protrude from the surface and the interface should be as smooth as possible. This has two purposes, 1) not disturbing the aerodynamic airflow and 2) avoiding new ice nucleation centers.
Ice thickness and type identification capability	This is an optional requirement since it is not essential to know the type of ice in the early accretion stages.

Table 2.1. Development requirements of the ice sensor.

2.1.2. Other industries

Even though the ice sensor was specifically designed for the aviation industry, other industries may also demand ice sensors with similar requirements and features. For example, food and pharmaceutical industries might also be interested in such kind of early-alert ice sensor for monitoring freeze-drying processes [3] (also known as lyophilization), which consists of the dehydration of a material by freezing it and decreasing the surrounding pressure in order to make the frozen water to sublimate to the gas state directly. Implementing highly sensitive early-alert ice sensors inside freeze-drying chambers could allow to immediately detect water phase transitions (liquid-solid) which would provide information about the state of the process and whether it is evolving properly. As it will be seen later, due to the morphology of the proposed ice sensor would be easily adaptable and installable inside lyophilization systems.

The development of real-time sensors capable of discriminating the phase of water molecules within micro to nanometric layers would also have immediate application in other industries and research fields, such as biogenic ice nucleation studies [4], wind turbines [5], nuclear reactors [6], or fundamental atmospheric science [7].

2.2. Theoretical development of an integrated photonics mid-IR surface water-ice sensor

In this section, the fundamentals of the optical ice sensor developed in this Thesis are introduced from a theoretical point of view. Firstly, the sensor structure is presented and the sensing mechanism is explained. Later, with the help of electromagnetic numerical simulations, the most important aspects affecting the sensor performance are thoroughly discussed. As it will be noticed, the proposed design is intended to satisfy the maximum number of requirements of Table 2.1.

2.2.1. Sensor concept

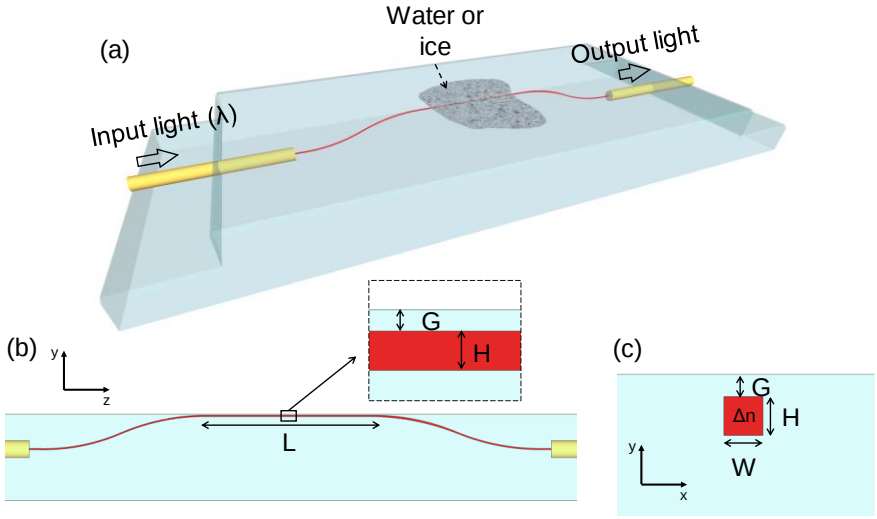

Figure 2.2. Sketch of the proposed water-ice sensor. (a) 3D representation showing the input and output optical fibers (yellow), the sensing optical waveguide (red) and water/ice deposited onto the sensor surface. (b) Side and (c) cross-section views.

The water-ice sensor uses optical waveguide and integrated optics technology (see Section 1.4) to fast detect on its surface either direct ice accretion/nucleation or general phase changes of the H_2O molecule (liquid to solid phase and vice versa). A general 3D sketch of one of the possible implementations of the sensor is shown in Figure 2.2(a). As it can be observed, a step-index [8], weakly guiding [9] optical channel waveguide (waveguide core in red) embedded in a solid material passes slightly underneath (few μm's) the interface with the external medium. All the design has been carried out considering single-mode waveguides, although few-mode waveguides should also work. This sensing waveguide carries mid-IR light spectrally centered around the OH-vibration mode of the water molecule, so that any change in the intermolecular distances between water molecules will modify the specific index matching conditions and spatial overlap of the waveguide evanescent tail and the outside water layer. The proposed sensor will be used as an intensity modulated sensor, where the intensity output (and output spectral shape when spectrally resolved) will give the

type of water layer on the sensor, since the output waveguide intensity is a function of the waveguide coupling to the substance on the interface (water, ice or air). The use of microphotonics technology ensures the sensor will naturally detect layer thickness changes in the sub-μm level and, hence, ultrafast and sensitive early-alert detection will be feasible, as it will be later demonstrated with simulations in Section 2.2.6.

The light in and out the waveguide is injected and collected, respectively, by means of suitable optical fibers (in yellow) which coupled to the waveguide that is brought to the surface through the appropriate S-bends. This surface is flat and the fibers are buried within the bulk material so that the whole structure can be flush-mounted on numerous parts of the aircraft body (wings, tail engine inlets, fuselage…). Given the low refractive index of the building materials that will be proposed (around 1.5) and the low refractive index contrast of the sensing waveguides, coupling losses (i.e. Fresnel plus mode mismatch losses) to commercially available mid-IR fluoride fibers are very small. In Chapter 5, the fiber-waveguide connection issue will be fully addressed from the manufacturing and experimental perspective.

Parameter	Influence on device performance	Range
λ	It is definitely the most critical parameter to tune. As it will be shown in the next Section, the optical properties of water and ice are wavelength dependent over the mid-IR range due to molecular absorptions. This enables stronger refractive index differentiation which is the base of the sensing mechanism.	3 to 4 μm (astronomical L band)
L	The longer the interaction of the waveguide with the external medium, the higher the light intensity attenuation.	1 to 10 mm
W & *H*	The waveguide dimensions affect the effective refractive index of the waveguide's supported modes as well as their field profiles [8]. Therefore, a change of these two parameters will modify the matching conditions for water-ice detection.	10 to 50 μm
Δn	The higher index change (Δn > 0), the more sensitive and selective the sensor (see Section 2.2.5). Greater Δn allow higher device miniaturization (shorter *L* needed and tighter bending radius possible).	0.001 to 0.01 (weak guidance)

G	As it will be demonstrated in Section 2.2.5, this gap heavily determines the sensitivity of the sensor, i.e. the smaller gap, the more sensitive. Conversely, increasing the gap makes the sensor more resistant against erosion.	1 to 10 µm

Table 2.2. Influence of the design parameters on the sensor performance and the range of considered values.

Side and cross-section schematic views of the waveguide sensor are depicted in Figures 2.2(b) and (c), respectively. There, relevant design parameters are indicated, i.e. the light wavelength (λ), the interaction length (*L*), the waveguide width (*W*) and height (*H*), the gap (*G*) from the top of the waveguide to the surface and the refractive index change (Δn) of the waveguide core relative to the surrounding cladding. In Table 2.2, a brief qualitative description of the effect of the individual variation of each parameter on the sensor performance is provided which will be supported by simulations in the following sections. Moreover, a range of possible values is specified so as to give an overall idea of the device dimensions.

Apart from these design parameters, the material of the substrate in which the waveguide is embedded needs to be carefully chosen to meet the Table 2.1 requirements. This issue will be addressed from the manufacturing and engineering point of view in Chapter 3, Sections 3.6 and 3.7, and from the optical perspective (since the material needs to meet certain dispersion requirements to accomplish the aforementioned mode matching conditions) in the next Section.

2.2.2. Sensing the water structural phase by monitoring the variation of its mid-IR OH-stretching vibrations

In the visible and near-IR spectral range, the refractive index of water and ice have normal dispersion (i.e. refractive index decreases with wavelength) due to the absence of strong light absorption bands, just like in typical glasses and crystals. However, across the mid-IR molecular resonances, the dispersion

undergoes a sudden variation which is dictated by molecular resonances, which, therefore, might be exploited for molecular sensing purposes.

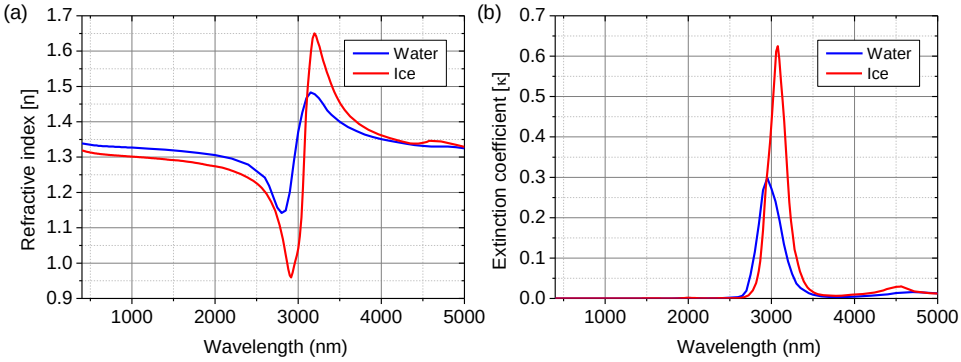

Figure 2.3. Refractive index dispersion of water [10] at 25 ºC and ice [11] at -7 ºC: (a) real and (b) imaginary parts.

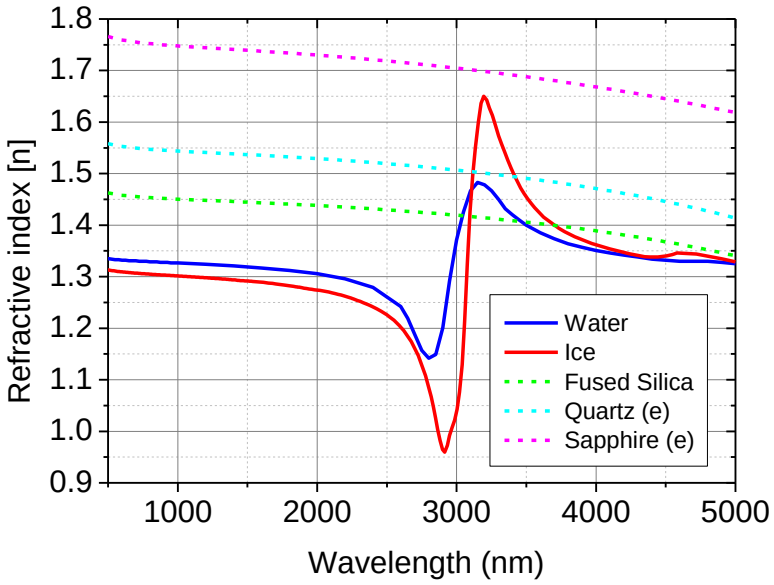

Figure 2.4. Refractive index dispersion of water [10] at 25 ºC, ice [11] at - 7 ºC, fused silica [12], quartz crystal [13] (extraordinary axis) and sapphire [14] (extraordinary axis).

Figure 2.3 shows the dispersion of the complex refractive index (i.e. real [n] and imaginary [κ] part) of water in liquid [10] and solid state [11]. For $\lambda <\approx 2.5$ µm,

water can be considered roughly transparent, so *n* normally decreases for longer wavelengths. Around 3 μm (Figure 2.3(b)), a well-known strong absorption band emerges which is associated to the vibrational stretching atomic motion of the OH bonds [15] within the H_2O molecule. Indeed, this is the band that will be useful for the water-ice sensing mechanism. As mentioned in Chapter 1, water has other mid-IR weaker absorption bands [15] at longer wavelengths originating from the bending of the OH bonds, and other less intense in the visible and near-IR region due to a combination or overtones of the main bands.

Accompanying the strong water absorption at about λ = 3 μm, an abrupt change of the refractive index dispersion (Figure 2.3(a)) can be observed as it is typically found close to molecular resonances and can be understood in terms of Kramers-Kronig relations [16]. A minimum of refractive index followed promptly by a maximum reveals a region of anomalous dispersion which leads to an increased value of refractive index (≈ 1.45) compared to that at shorter wavelengths (≈ 1.30). This fact makes the refractive index of water to be close to that of some relevant harsh environment resistant mid-IR transparent materials that might contain the sensor (see Figure 2.4), like high purity fused silica, quartz crystal or sapphire.

Since the OH-stretching vibrational mode of water molecules is a highly sensitive probe of intermolecular distances and water structure, sensing the index of refraction of water across this resonance would be a very powerful method to detect water phase changes such as liquid-solid transitions or others. As shown in Figure 2.3, for the case of solid water (hexagonal ice crystalline structure) at -7 ºC the absorption peak is even stronger and redshifted than for liquid water (so does the refractive index swinging) and, hence, it makes not only feasible to discriminate ice from liquid water but also to do it with high precision, as it will be shown later.

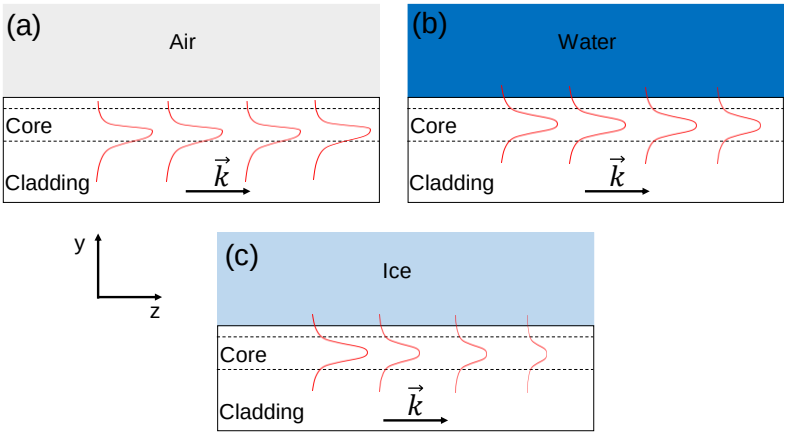

Figure 2.5. Qualitative schematic of the light propagation through the sensing waveguide from left to right (2D intensity profile depicted in red) when (a) air, (b) liquid water or (c) ice are covering the sensor.

Fundamentally, the sensing mechanism is based on the matching of the effective index of the waveguide mode (n_{mode}) to that of the external medium to be detected (i.e. ice) which acts as an infinite power sink [17] as light propagates just underneath, through the waveguide (Figure 2.5). A necessary condition is spatial overlap between the evanescent field of the waveguide mode and the external medium. As a result, when the sensor parameters are properly tuned, there is a strong power reduction of the guided light which is transferred outside and lost when ice is formed on the surface (Figure 2.5(c)). Conversely, when the sensor is covered by liquid water or air, little or no light is lost (Figures 2.5(a) and (b)). Thus, the device can be adjusted to be sensitive to water phase changes. The detection principle is similar to that used in side-polished fiber devices [18], except here the operating wavelengths are shifted to longer mid-IR wavelengths so as to take advantage of the OH resonances that abnormally increase the water refractive index effectively triggering the index matching effect (Figure 2.4). Moreover, water and ice have high absorption in this particular range which also plays a significant role in the coupling performance to different water phases.

In general, and considering for the moment that the sensor is working at one single wavelength, the refractive index of liquid water n_{water}, ice n_{ice} and the sensor material n_{mat} (see Figure 2.4) must meet the following condition:

$$n_{water} < n_{mat} < n_{ice} \qquad \textit{Eq. 2.1}$$

This condition is particularly true in the 3 – 4 μm range for some of the materials shown in Figure 2.4. Now, assuming weakly guiding waveguides, so that $n_{mat} \lesssim n_{mode}$, and taking the optimum wavelength (λ_{match}) for perfect phase matching and ice sensing, the condition can be further restricted to:

$$n_{water} < n_{mat} \lesssim n_{mode} \approx n_{ice} \qquad \textit{Eq. 2.2}$$

This ensures that the guided light will be mainly lost only when ice is on the surface, since air or water have lower refractive index at this wavelength which make them act as a cladding. Nevertheless, in practice, the presence of water on the surface also induces attenuation of the guided light due to absorption at mid-IR wavelengths of the guided mode evanescent field.

By inspecting Figure 2.4, one can find the intersection points of the refractive index of three different materials with those of liquid water and ice. The sapphire curve does not intersect with the others, whereas the quartz crystal curve does it with ice (two points), and the fused silica one intersects with both water (two points) and ice (two points). Consequently, sapphire does not meet the refractive index matching conditions needed for sensing. In contrast, quartz and fused silica can, in principle, be used as a host material for the water/ice sensor. Table 2.3 shows specifically the approximate index matching points.

From all the displayed values, only λ = 3.42 μm for quartz crystal and λ = 3.70 μm (green color) for fused silica meet the condition of Equation 2.2 for ice sensing (λ_{match}). Those from the first column (in blue) are discarded because do not meet Equation 2.2, although they could be still interesting for some type of water sensors (i.e. fused silica matching liquid water at 3.46 μm). Similarly, points in red do not meet the equation and, furthermore, at this wavelength so close to 3 μm,

water and ice have very high absorption which completely inhibits the index matching of the guided mode with ice or water from occurring, similarly to what happens in the "Slightly absorbing fibers" example analyzed in the book [19].

Material	λ for water matching		λ for ice matching	
	1st point	2nd point	1st point	2nd point
Sapphire	-	-	-	-
Quartz	-	-	~~3.11 µm~~	**3.42 µm**
Silica	~~3.04 µm~~	3.46 µm	~~3.09 µm~~	**3.70 µm**

Table 2.3. Approximate index matching points which are candidates for water/ice detection extracted from Figure 2.4.

Note that so far only two individual phase states of the H_2O substance (liquid water and ice) at specific temperatures have been considered, even though it is known that water properties vary with temperature and other variables. When water is cooling down, its dielectric constant tends to spectrally approach towards that of ice [20, 21], and therefore to that giving index matching for ice since the OH's features are redshifted accordingly. Nevertheless, even in the limit case, which could be supercooled water at -35 ºC vs. ice, there is a noticeable difference in refractive indices [21] which makes Equation 2.2 be still valid. Furthermore, temperature variations of water and ice could be a problem for unequivocal ice detection as they can move away the matching point λ_{match} from the chosen operating wavelength. However, the non-zero absorption of water/ice helps the sensing mechanism to be robust against such fluctuations, as it will be explained in Section 2.2.4.

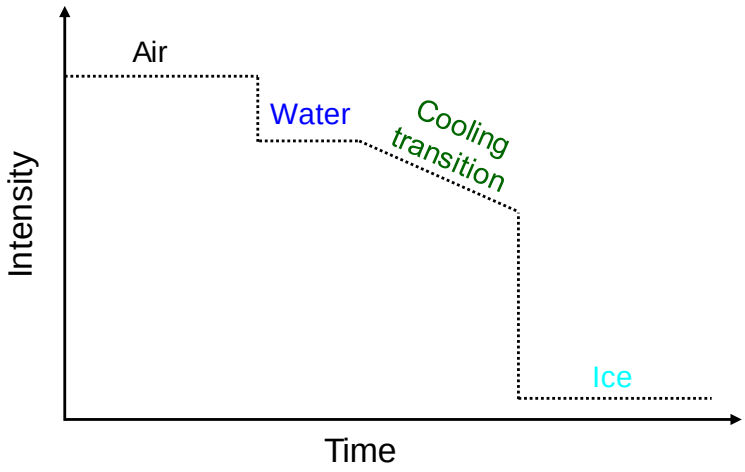

Figure 2.6. Qualitative sensing waveguide output intensity evolution when a drop of water is placed on the sensor surface and cooled down.

Finally, a qualitative graph is shown in Figure 2.6 plotting the hypothetical temporal evolution of the output intensity of a sensing waveguide made of fused silica and driven by monochromatic light at 3.70 µm. As it is observed, when the sensor surface is covered by water, the signal is slightly attenuated not due to index matching, but to the non-zero absorption of liquid water at this wavelength and the higher penetration depth of the evanescent field into water compared to air. As water cools down, its optical properties approach to those of ice and hence the signal decreases accordingly because the absorption increases. At some point, the phase transition occurs, the water freezes and the signal suddenly drops meaning that the matching conditions are met and ice is formed on the sensor surface. This is a simplified explanation that overlooks many aspects of the real ice formation process such as the ice microstructure, the rate of accretion, layer thickness, etc. In Chapter 5, the results of temporal experiments in both static laboratory and simulated in-flight conditions will be provided so that the impact of such aspects on the effectiveness of the sensor can be evaluated.

2.2.3. Beam propagation method simulations: initial considerations

In this and the forthcoming sections, computational electromagnetic simulations demonstrating the sensor performance are described. The chosen numerical method is the beam propagation method (BPM) [22] on which is based the software package used throughout this Thesis, i.e. Rsoft BeamPROP. The finite difference BPM is used to solve the parabolic or paraxial approximation of the Helmholtz equation in order to compute the propagation of light in arbitrary (2D and 3D) waveguiding geometries. Since the contrast of the waveguide is relatively small and the light propagation is always in the forward direction, the BPM is the perfect technique for simulating accurately and efficiently cm's long structures within few seconds, which would be totally unfeasible with other methods such as the finite-difference time-domain method (FDTD). Furthermore, only scalar simulations, which require less computational time, are carried out because each pair of orthogonally polarized waveguide modes have very similar effective index (again since they are weakly guiding circuits) and, therefore, the light attenuation undergone when sensing is identical for both cases.

The 3D model used is shown in Figure 2.7 (already presented in Figure 2.2), with exception of the optical fibers connections which are not included for the sake of simplicity. The values of the parameters defining the structure (*L*, *W*, *H*, Δn and *G*), which were described in Table 2.2, together with the sensor material are varied in each simulation so as to obtain a global perspective on their impact on the sensing performance. The main simulation output to look at, for a given input power (P_{in}), is the waveguide output power (P_o), which BeamPROP calculates as the surface integral of the field intensity at the output port of the sensing waveguide. Finally, for each set of parameters, three different simulations are run having air, water or ice as a covering material, respectively. All the necessary refractive index information is taken from the literature (see Figures 2.3 and 2.4). In the first group of simulations the covering material is considered to extend infinitely above the sensor surface.

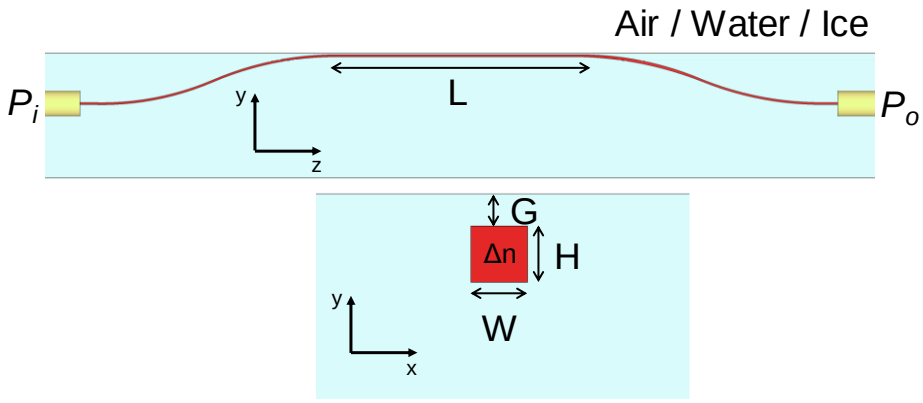

Figure 2.7. Basic parameterized sensor model for BPM simulations.

On the other hand, a convenient figure or merit (FOM) to measure the ability of the sensor to detect ice and/or water (i.e. its sensitivity) is the attenuation produced on the light intensity due to their presence on the surface. Particularly, it is interesting to define the attenuation at a given wavelength (λ) as the ratio of the waveguide output power when ice/water is on the surface to the output power when there is just air. A further normalization factor is included, namely the interaction length *L* (see Table 2.2), which accounts for the discrepancies in the covered length of different simulations thus making them comparable. The resulting expression is presented below.

$$A_{i/w}(\lambda) = \frac{-10\log\left(\frac{P_{o,i/w}(\lambda)}{P_{o,a}(\lambda)}\right)}{L} \qquad \textit{Eq. 2.3}$$

where $A_{i/w}$ is the attenuation corresponding to presence of ice/water in dB/mm, $P_{o,i/w}$ the output power for ice/water, $P_{o,a}$ the output power for air and *L* the interaction length expressed in mm. The use of logarithmic units is appropriate to easily get an idea of the sensing performance so, for example, a 3 dB/mm attenuation means that for every millimeter of interaction, half of the guided power will be lost. Another FOM derived directly from the attenuation is the sensing selectivity of ice in front of water (S_{i-w}), which is useful to indicate the sensor's capability of detecting water-ice phase changes. The selectivity is calculated as,

$$S_{i-w}(\lambda) = A_i(\lambda) - A_w(\lambda) \qquad \textit{Eq. 2.4}$$

In the following sections both selectivity and attenuation will be used interchangeably since they are directly related to each other. Spectral variations in both FOM's will prove to be excellent indicators of changes of the water structural state, temperature, and microstructure.

It should also be mentioned that, in general, a higher attenuation value is associated to better sensitivity and in simulations this value can be as high as one needs. However, in reality this is only true up to an extent since the detected output power should be always above a certain level, here called "noise floor" of the corresponding light detector to avoid signal clipping. In other words, the maximum attenuation of the sensor system should be lower than the dynamic range (*DNR*) of the system. Mathematically,

$$A_{max} \cdot L \; < DNR = 10 \log\left(\frac{V_{o,max}}{V_{\mu_{NF}}}\right) \qquad \textit{Eq. 2.5}$$

where A_{max} is the maximum attenuation to be measured in dB/mm, *L* is the sensing interaction length in mm, $V_{o,max}$ is the maximum voltage that can be generated by the light detector (resulting from the maximum allowed light intensity reaching the detector at any moment) in V, and $V_{\mu_{NF}}$ is the detector's noise floor average in V. Having this limitation into account, if, for instance, the *DNR* is 50 dB, the maximum attenuation for a sensing waveguide of 5 mm should be lower than 10 dB/mm. At the simulation stage this is not a relevant issue, although it should be kept in mind for the experimental stage and for the design of application-specific sensors (see Chapter 5).

2.2.4. Broadband simulations for searching the optimum index matching condition

Previously, a first order approximation of the wavelength for perfect index matching was provided (see Table 2.3). However, in order to computationally find λ_{match} in a more accurate way, a broadband simulation is required, i.e. an array of simulations, each one accounting for a different individual wavelength.

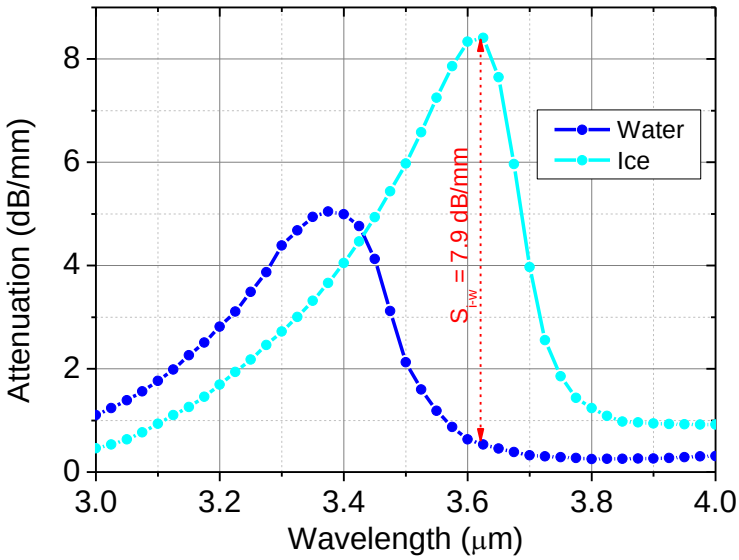

Figure 2.8. BPM simulated attenuation spectrum for homogenous water and ice of a fused silica sensor. Parameters: L = 2 mm, W = H = 14 μm, Δn = 0.008, G = 2 μm.

Figure 2.8 shows the attenuation spectrums (λ = 3 – 4 μm) for water and ice, in which each spectral point was calculated using Equation 2.3, assuming in this case that the sensor is built in fused silica with parameters: L = 2 mm, W = H = 14 μm, Δn = 0.008 and G = 2 μm. As expected, the graph allows to find the wavelength for optimum index matching (i.e. maximum attenuation) which are $\lambda_{match,w}$ = 3.38 μm and $\lambda_{match,i}$ = 3.62 μm, and result in $A_w(\lambda_{match,w})$ = 5.0 dB/mm and $A_i(\lambda_{match,i})$ = 8.4 dB/mm for liquid water and ice, respectively. In addition, the selectively as defined in Equation 2.4 is

$S_{i-w}(\lambda_{match,i})$ = 7.9 dB/mm. The matching wavelengths found in the simulation are about 80 nm below those expected from Table 2.3. The reason behind this shift is the relatively high value of Δn which makes the index matching to occur at shorter wavelengths since n_{mode} is slightly increased.

In addition, Figure 2.8 also reveals the profile of the attenuation spectrums, which can help in the sensor design process by means of defining "fingerprints" for each water phase. Due to the complex dispersion of the different materials involved in each simulation, the obtained curves resemble those of a damped resonant harmonic oscillator (except for the asymmetry arising from the strong background absorption at shorter wavelengths). Narrower "resonances", such as that of the ice curve in Figure 2.8, stem from a reduced absorption and imply a better selectivity. At the same time, the non-negligible width of the resonances makes the sensor robust against the possible temperature (and thus index) fluctuations that water or ice may undergo. Furthermore, in the case of ice sensing, shifting the operating wavelength ± 50 nm around the optimum does not significantly deteriorate the sensor performance. This clearly provides increased flexibility in the light source selection and makes the sensor outstandingly robust for industrial applications.

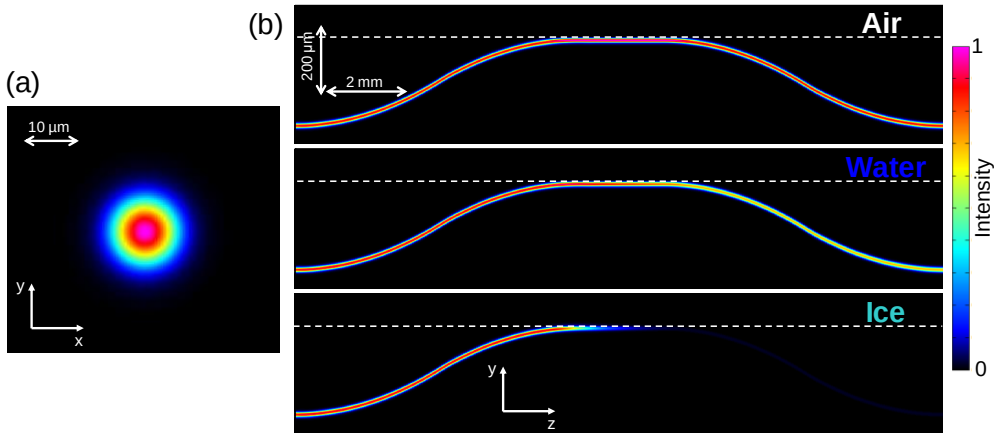

Figure 2.9. BPM calculated field intensity profiles at $\lambda = \lambda_{match,i}$ = 3.62 µm. (a) Transversal intensity profile of the launched mode. (b) Longitudinal profile of the light propagation through the sensing waveguide when the sensor is covered by air, liquid water or ice. Parameters: L = 2 mm, W = H = 14 µm, Δn = 0.008, G = 2 µm.

BeamPROP also generates 2D electric field profiles representing the light propagation through the sensing waveguide. Figure 2.9(b) shows the ZY cut of the field intensity (i.e. $|E|^2$) normalized to the unity when the own fundamental waveguide mode (XY mode profile in Figure 2.9(a)) is launched from the input port. The operating wavelength is set at the one previously found ($\lambda_{match,i}$ = 3.62 µm) for optimum ice detection. Notice again the strong power loss along the interaction region in the ice simulation and the opposite in the other two cases. Moreover, the relative high refractive index change allows for moderately low bending radius (50 mm) with negligible power loss, as it can be seen around the waveguide bending zones of Figure 2.9(b).

2.2.5. Sensor engineering: core size, gap and index change

In order to assess the impact of the design parameters on the sensor performance several parametrized BPM simulations independent from each other were run. Firstly, Figure 2.10 shows the computed selectivity (S_{i-w}) relative to the width (W) and height (H) of the waveguide core, both being swept from 20 to 50 µm using 13 steps for each parameter. Note that the resulting values of 169 simulations were interpolated to depict a smooth 2D graph (Figure 2.10). The building material is quartz crystal and the operating wavelength is λ = 3.39 µm which is close to the ice matching wavelength for this material and coincides with the emitting wavelength of the mid-IR He-Ne laser used for the waveguides experimental characterization. The rest of the parameters are given in the figure caption.

The maximum value of S_{i-w} is only about 0.6 dB/mm which is lower than that of the previous simulation (see Figure 2.8). This is due to the higher absorption of liquid water and ice at this shorter wavelength, the higher gap and the lower refractive index change. Leaving aside this fact, the relevant trend to look at is the increase of selectivity, and hence attenuation as well, when the waveguide is made wider and shorter (bottom right corner of Figure 2.10). This effect is generally observed in waveguide sensors and is due to a higher portion of

evanescent field penetrating into the external medium when H is reduced. This needs to be accompanied as well by a W increase in order to avoid the waveguide mode cut-off [8] and enlarging the sensing surface at the same time. On the contrary, if the waveguide becomes taller and thinner (i.e. higher H and lower W), the sensing capability of the waveguides tends to be cancelled (upper left corner of Figure 2.10).

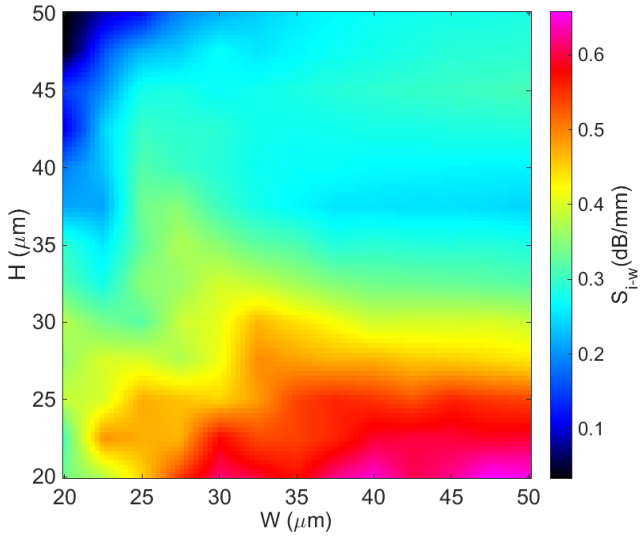

Figure 2.10. Ice-water selectivity vs. core width (W) and height (H) for a sensor built in quartz crystal and operating at 3.39 μm. Parameters: L = 5 mm, Δn = 0.001, G = 5 μm. W and H swept independently from 20 to 50 μm.

Secondly, for the same parameters and still quartz crystal as a building material, the influence of the gap (*G*) from the top of the core of the waveguide to the surface was evaluated. *G* was swept from 0 to 10 μm (11 steps), λ from 3 to 3.5 μm (11 steps) and again the interpolated results were depicted in the 2D graph shown in Figure 2.11.

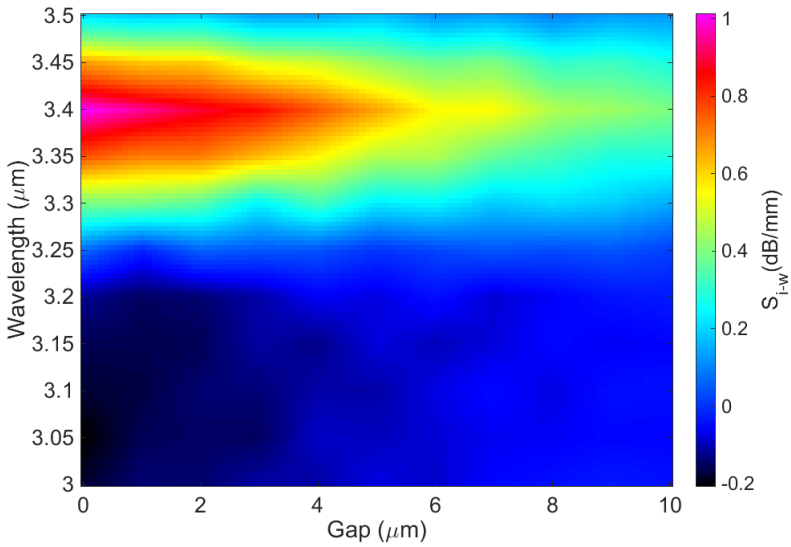

Figure 2.11. Dependence of the ice-water selectivity on the gap (G) and the wavelength (λ) for a sensor built in quartz crystal. Parameters: L = 5 mm, W = 50 µm, H = 20 µm, Δn = 0.001.

As expected, the smallest *G*, the higher the selectivity around the optimum wavelength for ice sensing in quartz (i.e. $\lambda_{match,i}$ = 3.40 µm). Obviously, the gap giving maximum sensitivity is *G* = 0 µm which, however, would reduce to the minimum extent the erosion resistance of the whole sensor since the waveguide core is no longer buried and protected from scratches. Whether that could be acceptable or not depends on the final application and the external environment. Moreover, unlike with the core size, the variation of the gap does not determine the position of the matching wavelength as it can be deduced from Figure 2.11. This result is of extreme importance for the applicability of the sensor in harsh environments, since it implies that sensor can indeed sustain surface material erosion while it continues performing with invariable spectral "fingerprints" for each water phase. This feature of the sensor is unique within state-of-the-art photonic surface sensors, since other designs such as evanescent-field sensing waveguides, photonic crystals, whispering gallery mode or ring resonators, cannot sustain any material erosion without malfunctioning since they rely on the

precisely design nanostructures. It is due to this radical difference in design approach that this sensor is novel, and very effective for industrial applications.

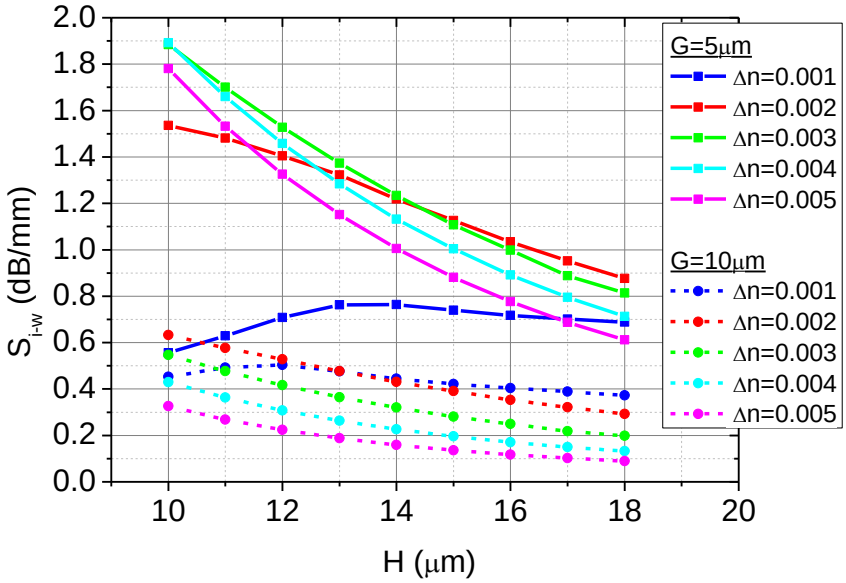

Figure 2.12. Dependence of the ice-water selectivity on Δn, H and G for a sensor built in quartz crystal operating at 3.39 μm. Parameters: L = 5 mm, W = 50 μm.

In third place, various simulations showing the effect of the core refractive index change (Δn) in conjunction with its height (*H*) and gap (*G*) were performed. The results in terms of selectivity (S_{i-w}) are depicted in Figure 2.12 and the selected constant parameters are included below in the caption. Focusing on the *G* = 10 μm case, one observes that in general the selectivity diminishes for higher refractive index change which seems to conflict with the statement of Table 2.2. What is actually happening is that for a given gap and height (*H* > 13 μm), a more contrasted waveguide makes the mode more confined within the core so that the interaction of the electric field with the external medium lessens. Consequently, to fully take advantage of the benefits of using high-contrast waveguides, one needs to reduce *G* accordingly to approach the evanescence field to the surface and increase the coupling efficiency. This is evident for all the simulations corresponding to reduced *G* = 5 μm which have a notably higher selectivity.

Additionally, the decrease of the core height *H* further raises the sensor selectivity due to the reasons mentioned previously in the analysis of Figure 2.10.

For instance, for *H* = 18 μm and Δn = 0.001, if the gap is reduced from 10 μm to 5 μm, the selectivity increases from 0.37 dB/mm to 0.69 dB/mm (0.32 dB/mm difference), whereas if Δn = 0.002, if the gap is reduced from 10 μm to 5 μm, the selectivity increases more, from 0.29 dB/mm to 0.88 dB/mm (0.59 dB/mm difference). Hence, shortening the gap and increasing Δn add up, thereby obtaining higher attenuation/selectivity gains than those obtained only varying one of the two variables individually.

The last fact to highlight from Figure 2.12 is that *H* cannot be reduced unlimitedly without losing performance at a given point. This is clearly observed for Δn = 0.001 when *H* is below 13 μm and 12 μm for *G* = 5 μm and 10 μm, respectively. In these cases, the waveguide mode is at cut-off which means that it is not a proper guided mode but a leaky mode and the selective coupling mechanism is cancelled.

2.2.6. Simulating ice microstructure: thickness and homogeneity

So far, the layer covering the sensor has been assumed to be infinite above the surface as well as homogenous in terms of refractive index. However, in real scenarios, the sensor will deal with μm-sized ice films which must be detected early enough to be removed by the de-icing systems before they become too thick (early-alert requirement of Table 2.1). To check whether the sensor would be sensitive to the accretion of thin films of ice, a set of multiple simulations with varying ice thickness from 0.2 to 40 μm in steps of 0.2 μm were performed. Figure 2.13 shows the computed attenuation (left axis) together with the calculated effective index dispersion (right axis) corresponding to the first five modes of a slab waveguide laying above the sensing waveguide which consisted of an ice core, a silica substrate and air superstrate. For the modal simulations, ice was considered lossless. The building material of the sensor was fused silica and the

operating wavelength was 3.60 µm, which is close to the matching one. The rest of the parameters are provided in the Figure 2.13 caption.

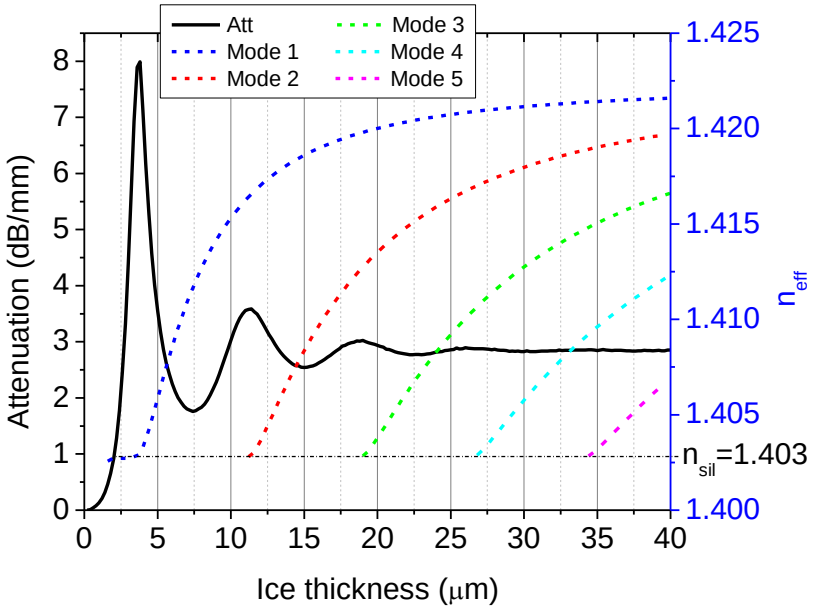

Figure 2.13. Attenuation of a fused silica sensor operating at 3.60 µm for increasing ice layer thickness (solid black line). The dashed colored lines represent the dispersion relative to the thickness of a hypothetical lossless planar silica-ice-air waveguide for its different supported modes. Parameters: L = 3 mm, W = 40 µm, H = 15 µm, Δn = 0.002, G = 5 µm.

As it is observed, the attenuation curve (black line) illustrates the evanescent coupling effect of the channel waveguide mode to the slab modes of the ice layer. Theoretical investigations using coupled-mode theory of the coupling of channel and slab waveguides can be found in [23] and [17].

In the particular case of the studied ice sensor, when the ice thickness is 3.7 µm the strongest coupling (i.e. maximum attenuation of 8 dB/mm) is produced. For this thickness, perfect matching of the effective indices of the waveguide and slab modes is produced as it is evident from the intersection of the “Mode 1” dispersion curve with the constant line corresponding to the refractive index of fused silica

at the operating wavelength. After the power transfer to the ice layer, the light does not return like in conventional directional couplers due to ice absorption.

For a thicker ice layer, the coupling of such modes weakens and so the attenuation does. However, as soon as the slab can support a new second mode to couple light into, the sensor attenuation has a new relative maximum (thickness about 11.3 µm) which is not as strong as the previous one. This is probably due to the different field profile of this second slab mode and its reduced symmetry with respect to the confined waveguide mode below as well as the fact that the fundamental ice mode is out of perfect phase matching. Likewise, as the slab supports more modes, the attenuation curve has new associated relative maximums but they tend to dampen so that the attenuation stabilizes around 2.8 dB/mm for thick ice layers and these particular design parameters. Certainly, when the thickness is larger than about 30 µm, the ice slab can be already understood as an infinite slab supporting a continuum of modes, which is the case assumed in all the previous simulations. Most of the modes are not bound to the channel waveguide region but spread to into the infinite volume of the slab [17]. This together with the non-zero absorption of the ice layer contribute to further improving the final sensing loss mechanism and, at the same time, inhibit the power beating of normal evanescent couplers. Far from being a problem, the latter is an advantage for the sensor design because it removes the issue of varying the transference of light back to the waveguide when modifying the device length (*L*). In any case, Figure 2.13 clearly demonstrates that the proposed sensor is sensitive to sub-µm layers of ice, outperforming in almost one order of magnitude the minimum detectable thickness of the Goodrich ice sensor (i.e. 0.001” = 25.4 µm).

Specifically, if the ice layer was, for example, 300 nm thick the induced attenuation according to the simulation of Figure 2.13 would be of 0.006 dB/mm which makes $P_{o,i}$ = 0.998619 a.u. when $P_{o,a}$ = 1 a.u. and *L* = 1 mm. This is a reduction of 0.14 % of the power when such a thin layer of ice is formed on the glass surface. A realistic value of the noise of the detection system relative to the signal of interest is found to be 0.06 % which here is expressed as the standard deviation of the signal (calculated from the raw data of Figure 5.5 in Chapter 5)

divided by its average (i.e. σ/μ). This value would correspond to a SNR of 32 dB considering that the noise is additive with average zero. Since the relative power reduction (0.14 %) is larger than the noise (0.06 %), a 300 nm layer of ice could be detected provided that the real sensitivity of the sensor matched the simulated one. Thinner ice layers could be detected by making the device more sensitive (tuning its parameters as described in Section 2.2.5) or by employing a lower noise detection system. This further points out that the sensor can be used for fundamental ice nucleation studies or surface science of water which, however, are out of the scope of the present work.

Besides the homogenous morphology, ice can also exist forming microstructures combined with air pores or liquid water micro-domains. Indeed, as it is described in Chapter 1, mainly two types of ice can form on aircraft surfaces [24]: 1) clear or glaze ice and 2) rime ice. Clear ice is a type of transparent, smooth and homogenous ice, while rime ice has an opaque and milky appearance and is less dense due to the air microbubbles that are trapped inside its structure. Clearly, all previous simulations correspond to the clear ice case, so one may wonder how a complex ice microstructure can affect the sensor performance.

BPM simulations were carried out with slight modifications in the covering layer of the sensor. The infinite homogenous layer of liquid water/ice was substituted by a 50 µm thick layer consisting of alternative blocks of ice and air, having a random length averaging 80 µm and 20 µm, respectively, which simulated the rime ice microstructure. As in the simulation corresponding to Figure 2.13, the building material was fused silica and the operating wavelength was swept from 3.3 µm to 3.8 µm in order to compute the attenuation spectrum, which is shown in Figure 2.14. The green line represents the attenuation due to the presence of the presumed rime ice. The homogenous water and ice curves, corresponding to a 50 µm thick film as well, are also depicted for comparison purposes.

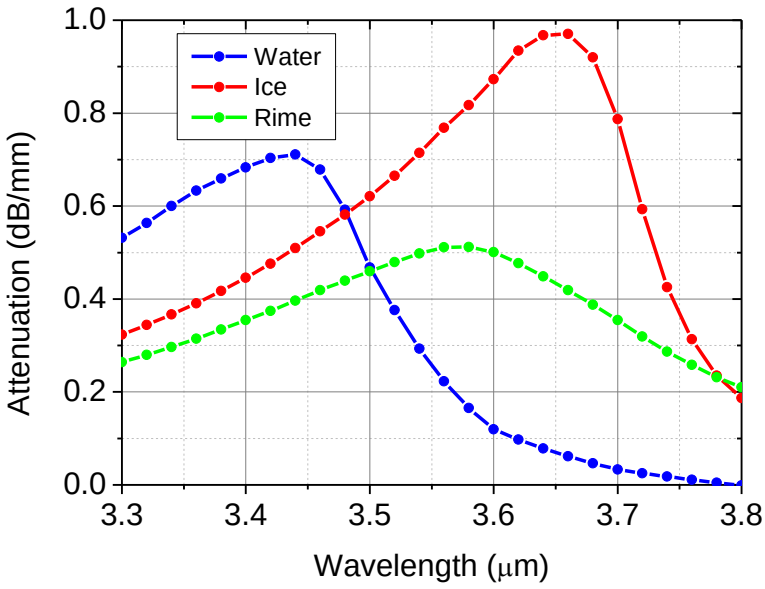

Figure 2.14. Computed attenuation spectrum of a fused silica sensor when covered with a 50 μm layer thick of water (blue), clear ice (red) and rime ice (green). Parameters: L = 1 mm, W = 40 μm, H = 20 μm, Δn = 0.0015, G = 5 μm.

As it could be expected, the attenuation caused by rime ice is decreased for most wavelengths with respect to that of ice. Moreover, the wavelength for maximum attenuation is blueshifted by about 70 nm. Arguably, the introduction of relatively larger air blocks would further reduce the magnitude and blueshift the spectrum of the computed attenuation. Consequently, the specific ice microstructure in each case can modify the attenuation pattern which might obstruct the correct detection of ice. This could lead, for instance, to false alarms when subzero water is present since it could cause a similar attenuation level at the corresponding operating wavelength. For this reason, adding another degree of complexity to the system in the form of a new detection parameter could help to diminish this new source of uncertainty. A possible solution is the use of broad or tunable light sources (see experimental implementation in Chapter 5) that may facilitate spectral distinction of different types of ices when needed. In this case, rather than analyzing discrete values of attenuation at a given fixed wavelength, the

whole spectral shape of the output spectrum would be used to identify previously known “fingerprints” for clear/rime ice, or warm/supercooled water.

2.3. Sensor design guidelines summary

After going through the previous series of simulations of the water-ice sensor and carefully analyzing the results, general design guidelines are provided below.

a) The chosen building material directly influences the ideal operational mid-IR wavelength of the sensor since it determines the matching conditions. For ice sensing, if the building material is quartz crystal, the operational wavelength should be around 3.40 μm, whereas if it is fused silica, the operational wavelength is redshifted to 3.65 μm approximately. The exact wavelength for optimum detection also depends on the refractive index change of the waveguide core.
b) The sensor is required to work in harsh, thermally changeable environments which involve the alteration of the optical constants of water in its liquid and solid phases to the nominal ones and, hence, the matching conditions can be spectrally shifted. For this reason and because of the specific spectral attenuation profiles, the operating wavelength does not need to be chosen with extreme accuracy. It has been calculated that a range of about ±50nm around the optimum wavelength is valid for distinguishing liquid water from ice.
c) The increase interaction length can make the device more sensitive. In practice this comes at the expense of larger device footprint.
d) By properly tuning the waveguide core dimensions, the detection capability of the sensor can be improved. In general, a wider and shorter core gives better performance.
e) The gap to the surface and the index change of the waveguide core play a relevant role in the sensing performance. Smaller gaps (1 – 5 μm) will always result in improved attenuation/selectivity, as well as higher index contrast (0.005 – 0.01). Both parameters can exponentially amplify their respective effects when combined. Nevertheless, if the gap is reduced

too much, the erosion resistance is deteriorated because less bulk material protects the sensing waveguide.

f) Apart from making the device more sensitive, higher index changes also help to miniaturize the sensor by shortening the required interaction (down to ≈ 1 mm in length) and by allowing waveguide bends with smaller radius.

g) The sensing mechanism can respond to ice layers thinner than 1 µm with no special variations of the design, which satisfies the early-alert requirement.

h) The sensor can detect ice with a non-homogenous microstructure and distinguish it from homogenous water or ice but it might need increased spectral working points provided either by a broad source or by a tunable laser.

References

1. http://utcaerospacesystems.com/cap/systems/sisdocuments/Ice%20Detection%20and%20Protection%20Systems/Ice%20Detector%20Model%200871NA.pdf
2. http://utcaerospacesystems.com/cap/products/Pages/ice-detection-protection-systems.aspx
3. S. L. Nail, S. Jiang, S. Chongprasert, and S. A. Knopp, "Development and Manufacture of Protein Pharmaceuticals," (Springer, New York, 2002), pp. 281-360.
4. R. Pandey, K. Usui, R. A. Livingstone, S. A. Fischer, J. Pfaendtner, E. H. G. Backus, Y. Nagata, J. Fröhlich-Nowoisky, L. Schmüser, S. Mauri, J. F. Scheel, D. A. Knopf, U. Pöschl, M. Bonn, and T. Weidner, "Ice-nucleating bacteria control the order and dynamics of interfacial water," Science Advances **2** (2016).
5. M. C. Homola, P. J. Nicklasson, and P. A. Sundsbø, "Ice sensors for wind turbines," Cold Regions Science and Technology **46**, 125-131 (2006).
6. T. S. Kim, H. Park, K. Ko, G. Lim, Y. H. Cha, J. Han, and D. Y. Jeong, "Laser-based sensor for a coolant leak detection in a nuclear reactor," Applied Physics B **100**, 437-442 (2010).
7. S. Sastry, "Water: Ins and outs of ice nucleation," Nature **438**, 746-747 (2005).
8. G. Lifante, *Integrated Photonics: Fundamentals* (Wiley & Sons, 2003).
9. D. Gloge, "Weakly Guiding Fibers," Applied Optics **10**, 2252-2258 (1971).
10. G. M. Hale, and M. R. Querry, "Optical Constants of Water in the 200-nm to 200-μm Wavelength Region," Applied Optics **12**, 555-563 (1973).
11. S. G. Warren, "Optical constants of ice from the ultraviolet to the microwave," Applied Optics **23**, 1206-1225 (1984).
12. I. H. Malitson, "Interspecimen Comparison of the Refractive Index of Fused Silica," Journal of the Optical Society of America **55**, 1205-1209 (1965).
13. G. Ghosh, "Dispersion-equation coefficients for the refractive index and birefringence of calcite and quartz crystals," Optics Communications **163**, 95-102 (1999).
14. M. J. Weber, *Handbook of Laser Science and Technology* (CRC Press, 1986).
15. D. Eisenberg, and W. Kauzmann, *The structure and properties of water* (Oxford University Press, 1969).
16. R. de L. Kronig, "On the Theory of Dispersion of X-Rays," Journal of the Optical Society of America **12**, 547-557 (1926).
17. D. Marcuse, "Investigation of coupling between a fiber and an infinite slab," Journal of Lightwave Technology **7**, 122-130 (1989).
18. S.-M. Tseng, and C.-L. Chen, "Side-polished fibers," Applied Optics **31**, 3438-3447 (1992).
19. A. W. Snyder, and J. Love, *Optical Waveguide Theory* (Springer, 1983).
20. Y. Raichlin, A. Millo, and A. Katzir, "Investigations of the Structure of Water Using Mid-IR Fiberoptic Evanescent Wave Spectroscopy," Physical Review Letters **93**, 185703 (2004).

21. R. Wagner, S. Benz, O. Möhler, H. Saathoff, M. Schnaiter, and U. Schurath, "Mid-infrared Extinction Spectra and Optical Constants of Supercooled Water Droplets," The Journal of Physical Chemistry A **109**, 7099-7112 (2005).
22. J. Van Roey, J. van der Donk, and P. E. Lagasse, "Beam-propagation method: analysis and assessment," Journal of the Optical Society of America **71**, 803-810 (1981).
23. Z. Shu, L. N. Binh, and G. P. Simon, "Light coupling and propagation in composite optical fiber-slab waveguides," Journal of Lightwave Technology **13**, 244-251 (1995).
24. I. Paraschivoiu, and F. Saeed, *Aircraft and Wind Turbine Icing* (Polytechnique International Press, Québec, Canada, 2015).

CHAPTER 3

Three-dimensional direct laser writing of waveguides

In this chapter, the three-dimensional direct laser writing (3DLW) technique is first presented as the technique employed for waveguide fabrication. A brief description of the fundamental physical processes involved in the interaction of tightly focused sub-picosecond laser pulses with solid materials is given, together with a discussion on how these processes can be tailored to promote different types of permanent material micromodifications which will form the building blocks of complex integrated photonic chips. A brief overview on various technological considerations that allow to control the properties of the written structures is provided as well as a summary on the main applications of 3DLW fabricated optical circuits in some important scientific and industrial fields. Later, the selection of the 3DLW technique is justified for the purpose of fabricating the surface sensors addressed in this Thesis. Lastly, details on the waveguides writing parameters used in three distinct SiO_2 based materials are shown. One of them will be finally chosen as the material containing the sensor.

3.1. Introduction to 3D direct laser writing

The three-dimensional direct laser writing (3DLW) technique essentially consists on tightly focusing sub-picosecond (ranging from few to hundreds of femtoseconds) laser pulses inside the appropriate transparent material in order to induce a localized permanent refractive index modification with a volume typically smaller than the point spread function of the focusing lens, thus allowing for the writing of three-dimensional (3D) arbitrary shape structures [1]. The photomodification process first involves the nonlinear optical absorption of the focused pulse energy, the generation of a localized plasma, and the subsequent electronic and phononic energy transfer to the surroundings of the ionized volume (see next section for a more detailed description). Interestingly, by appropriately controlling the induced refractive index variation (in both volume size and magnitude), one can rapidly create 3D embedded microstructures, that can perform predesigned optical functions such as confining, reflecting or diffracting light beams.

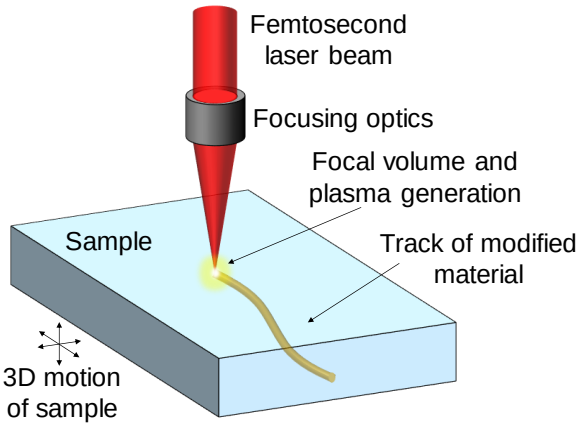

Figure 3.1. Sketch of the femtosecond pulse 3D direct laser writing process inside transparent media.

As shown in Figure 3.1, the desired circuit shape and path is controlled through the use 3D motion stages for translating the sample through the focal spot. Even though it is not addressed in this Thesis, the 3DLW technique can also be used

to locally enhance the material chemical reactivity (by means of modifying or even breaking chemical bonds) which allows 3D wet-etching processes to be performed where the written structures feature an etching rate typically a few orders of magnitude greater than the non-irradiated material [2]. This has enabled new research on 3D microfluidics [3] and micro-optic devices [4, 5] specially in fused silica and photosensitive glass, as well as on their integration in one single complex platform [6, 7].

Since the first demonstration of waveguide writing inside bulk materials using femtosecond laser pulses in 1996 [8], a growing number of researchers have been studying the underlying physical processes involved in irradiating a bulk material with such pulses. Gaining physical insight into the technique has definitely contributed to the optimization of the process and subsequently to the development of a refined new generation of 3D integrated optical devices, like waveguide couplers [9], gratings [10], multiplexers [11], modulators [12], sensors [13] or lasers [14]. One of the most recognized strengths of the 3DLW technique is its capability to produce integrated photonic devices in an ultra-wide range of materials, encompassing glasses [15], crystals [16], ceramics [17] and even polymers [18]. Furthermore, the 3DLW technique is not limited by the external geometry of the substrate or working piece, allowing for example, to embed written structures inside optical fibers [19] or any other transparent piece.

Throughout the last two decades since the first demonstration of waveguide writing in 1996, 3DLW devices have been matching, and sometimes even surpassing [20, 21] the performance of those typically fabricated via lithography-based techniques, such as ion implantation, chemical vapor deposition, pulsed laser deposition, ion/proton exchange, sputtering, etc. Many of those fabrication methods, which are partially inherited from the mature microelectronics industry, require expensive equipment, clean room facilities and multistep procedures (i.e. masking, deposition, etching, irradiation). On the contrary, while the 3DLW technique might not provide yet the high quality standards that can be obtained in clean rooms and may not compete in final photonic circuit compactness (refractive change up to 0.01), it is certainly simpler, it requires normally one or two fabrication steps, the initial financial investment is considerably lower and the

obtained optical circuits can benefit from the increased versatility of a 3D design against 2D planar schemes. Because of these unique features nowadays 3DLW is a tool used in many research and industrial fields including telecommunications, astrophotonics, laser generation, sensors, quantum mechanics simulations and microfluidics.

3.2. The physics of the 3D direct laser writing

A laser pulse with an energy of just 10 nJ, but tightly focused with a lens of numerical aperture 0.75, and having a temporal duration of 400 fs, will develop an intensity at the focus above the TeraWatt per cm^2 level (1.2 TW/cm^2). These enormous intensities (TW/cm^2) are typically reached when visible or near-IR femtosecond laser pulses are tightly focused inside a dielectric transparent material to fabricate 3DLW waveguides, and induce a large nonlinear optical absorption [1]. The electrons excited in this process form a free electron plasma, and the energy transfer to the lattice and surrounding material occurs in the picosecond scale, resulting in nano/micro-sized localized modifications in a great absence of detrimental thermal effects, which are unavoidable when using picosecond or nanosecond pulsed lasers [1]. The nonlinear absorption process is typically described by three different mechanisms, namely multiphoton ionization, tunneling photoionization, and avalanche photoionization, the latter encompassing free carrier absorption followed by impact ionization [1]. Depending on the wavelength, intensity and temporal duration of the laser pulse, one of the three non-linear processes will dominate over the others [1, 22]. A sketch summarizing the different nonlinear ionization mechanisms and how electrons move between valence and conduction bands during each process is shown in Figure 3.2.

After the formation of the free electron plasma there is a local energy transference to the lattice of the material, as pointed out previously. This energy transference is done via electron-phonon coupling in a time scale much longer that the one during which the nonlinear light absorption occurs [22]. As a result, after each femtosecond pulse there are many “hot” electrons in a still “cold” ionic lattice

which involves a non-equilibrium state [22]. The final types of induced morphological changes which will remain in this micro-volume will be determined by the evolution of this state towards a relaxed equilibrium state [22], and will strongly depend on the properties of the material as well as on the specific laser writing conditions.

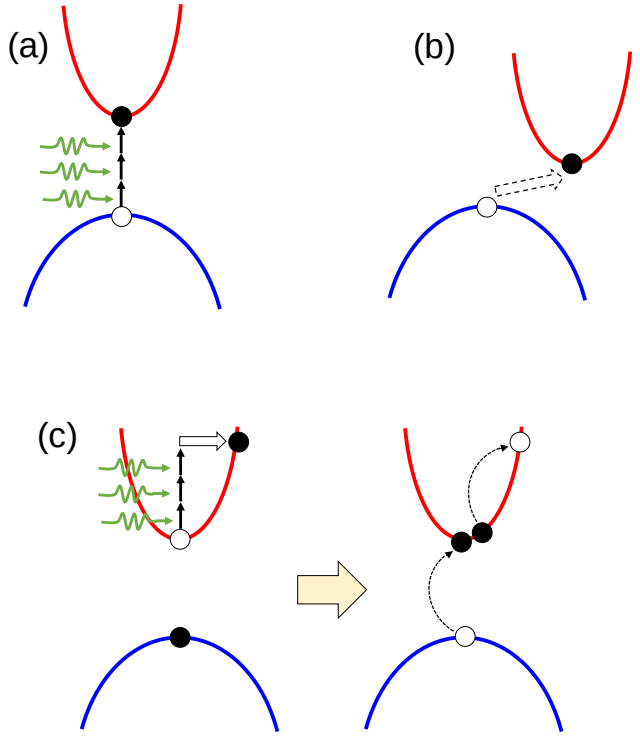

Figure 3.2. Nonlinear ionization processes involved in the direct laser writing. (a) Multiphoton ionization. (b) Tunneling ionization. (c) Avalanche ionization, including free carrier absorption and impact ionization.

Leaving aside the fundamentals on light-matter interaction and from an applied point of view, it has been extensively observed that depending on the material (its bandgap and thermal conductivity), as well as on the exposure laser parameters (pulse temporal width, energy, repetition rate, writing speed, wavelength, polarization, focusing numerical aperture, etc.) the type of morphological modification varies.

In crystals (e.g. Quartz, YAG, $LiNbO_3$, YVO_4, KTP, …), damage tracks with reduced refractive index are normally produced which are associated to a local amorphization of the crystalline material [23]. Such tracks can be arranged forming reduced index cladding structures inside which the light is confined. Less commonly, a smooth refractive index increase linked to point defects has been demonstrated in a few crystals like $LiNbO_3$ [24] and YCOB [25]. It is worth mentioning that the modifications in crystalline materials are in general anisotropic which usually results in a strongly birefringent optical behavior of the structures [23, 26].

In glasses, with the adequate laser writing parameters, positive refractive index changes (normally attributed to densification) are more easily produced than in crystals [1]. They are employed to form waveguides frequently with higher index contrast than those in crystals which consequently allow for increased device miniaturization. This is the case of silica based glasses [27], phosphate glasses [28] and chalcogenide glasses [15]. On the other hand, in some other glasses like ZBLAN only negative index modification have been achieved [29].

Since the 3DLW technique involves complex light-matter interactions that rely on many variables, a complete study on the different fabrication regimes leading to multiple morphological changes is needed for each material in order to gain control on what is being fabricated. Regarding this fact, fused silica is probably the most representative example because by varying the laser parameters one can obtain various kinds of morphologies [22]: refractive index increase, (birefringent) nanogratings, and voids. As silica is the base material of the sensors reported in this work, the 3DLW waveguides produced in this particular material will be analyzed more carefully in Chapter 4.

3.3. Types of optical waveguides produced by 3DLW

A well accepted classification of 3DLW waveguides is [23]: a) directly written waveguides (Type I), b) stress-induced waveguides (Type II) and c) depressed cladding waveguides (Type III). This is essentially based on the kind of modification induced in the material and on how the 2D light confinement is

achieved by using either positive index change regions, negative index change regions, or both, in different arrangements (see Figure 3.3).

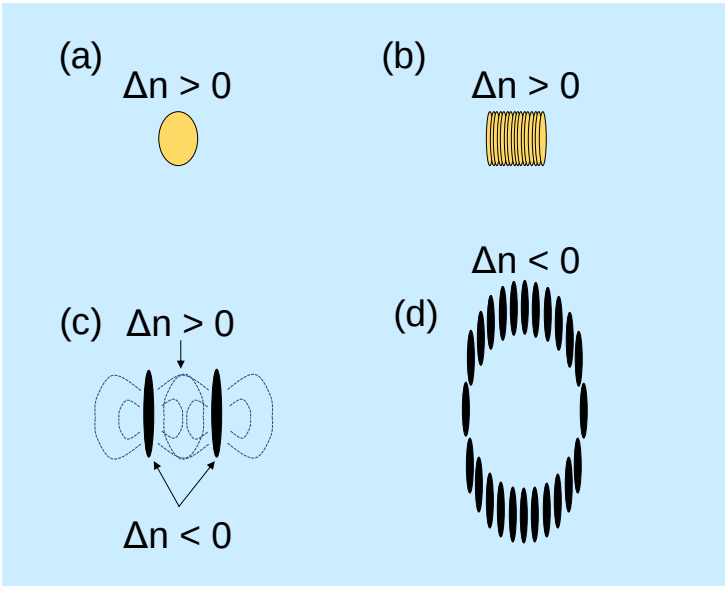

Figure 3.3. Cross-section of different types of waveguides written according to the morphological change (sign of the refractive index indicated) and geometry. (a) Type I single scan and (b) multiscan. (c) Type II double track design with stress fields in between. (d) Depressed cladding Type III in a tubular cladding design.

Type I waveguides [8] are equivalent to step-index or graded-index optical fiber waveguides where light is confined in a high index core, as shown in Figures 3.3 (a) and (b). They consist of a laser-induced core surrounded by the unmodified volume which acts as a cladding, with positive refractive index contrasts ranging from 10^{-4} to 10^{-2} [30]. As stated previously, these waveguides are normally fabricated in amorphous glassy materials and preferentially used for passive integrated components (like splitters, evanescent couplers, gratings, etc.), although they have also been written in ion doped glasses for lasing operation. Typically, only one single laser scan is needed to obtain the proper core size and index contrast for monomode operation (Figure 3.3(a)). However, due to the usual large elongation of Gaussian focal volumes, a different strategy must be followed

to obtain symmetric or quasi-symmetric core shapes, which might be needed in some specific cases. These kind of cores are obtained by either beam shaping techniques [30], which can produce more circular core shapes, or the simple yet powerful multiscan technique (firstly demonstrated in 2005 [31]), which allows to design rectangular or square step-index cores. The multiscan technique relies on writing thin adjacent tracks so as to “paint” a rectangular waveguide core (Figure 3.3(b)), whose height depends only on the type of focusing lens used and laser parameters, and its width depends only on the number of scans as well as on the scan separation. Multiscan waveguides can be used for complex integrated photonics structures such as (de)multiplexers and photonic lanterns (see Section 3.5), or any other application requiring different core sizes or extended index change regions, such as the waveguide sensor here reported (see Section 3.7.3).

Type II waveguides [24] in crystalline media are created using 3DLW tracks which have negative refractive index change due to damage at the track volume [23]. Surrounding those tracks, stress-induced anisotropic positive index regions are produced, so that light can be confined there if properly engineered. A common Type II configuration consists of two parallel tracks that confine the stressed positive index area between two low-index tracks, so that the index profile is a graded-index type in the vertical cross-section, and a W-type in the horizontal (Figure 3.3(c)). This configuration has been extensively studied for waveguide writing in crystals, where damage lines are straightforward to write and guiding is therefore easy to achieve for visible and near-IR light [23].

Type III waveguides [32] are fabricated in a similar way than Type II, but the design does not rely on stress to guide light, but on a negative index 2D cladding produced by damage tracks which acts as continuous low-index barrier [23] supporting only optical leaky modes inside (Figure 3.3(d). The index profile of Type III waveguides is also of W-type. Sometimes, Type III waveguides also have some degree of stress inside the cladding which is unavoidable due to the closed packaged arrangement of damage tracks, and which can allow for further tuning of the guiding properties [26]. Cladding waveguides have been proved to be a very efficient way to confine and control mid-IR light inside crystals, which has been shown not practicable with the simpler Type II approach [26].

In general, laser written waveguides always present a high degree of birefringence, regardless of the type of waveguide configuration. Depending on the material and the kind of laser induced modification, one of the polarizations may be guided more efficiently than the other, and even in some cases guiding can occur for only one linear polarization.

3.4. Practical considerations

There is a large number of parameters and material properties that need to be taken into account when writing structures using sub-picosecond laser pulses. Variations in them determine the type and the extent of the morphological change induced in the solid.

Regarding the laser parameters, the laser wavelength, and therefore the specific material bandgap, directly influence the physical dynamics of nonlinear process underlying the 3DLW [1]. Pulse energy and pulse duration control the threshold for plasma formation that triggers the material modification. Furthermore, specifically in glasses (and some crystals), the energy adjustment is important in order to find the regime in which positive index increase is obtained. Likewise, for a given energy, the pulse duration (few to hundreds of fs, i.e. typically sub-ps) affects the contribution of each nonlinear ionization process and consequently the morphology changes on certain materials [33]. Beam polarization has been also shown to affect the characteristics of the 3DLW waveguides [34].

In parallel to the pulse energy and duration, the spatial shape of the focused beam (or point spread function) that is given by the laser beam profile and the focusing optics used, has an impact on the final energy density generated on the focal volume and the shape of the written tracks. Focusing optics also determine the focal length and hence the distortion of the focused spot due to the change of medium that the light experience when entering the dielectric sample [23]. Distortions can be easily compensated previously, by means of slits or spatial light modulators, although this has not been studied in this work. Instead of adding complexity to a basic laser writing setup, the previously mentioned multiscan technique is then a practical way to control the final core shape.

Cumulative effects (i.e. various successive pulses irradiating the same volume) are controlled by the repetition rate of the laser system and the scan speed of the stage holding the sample. Both parameters determine the irradiation dose that the samples receive. For high repetition rates (>100 kHz), also known as the thermal regime, there is not enough time for heat to diffuse out of the focal volume before the next pulse arrives, so heat accumulation occurs [35], and the scan speed can be increased up to mm/s. In contrast, in the athermal regime (few kHz repetition rate), the heat generated by each pulse is completely diffused out of the focal volume before the next pulse arrives and, consequently, no heat accumulation exists. Furthermore, when using kHz systems the scan speed needs to be reduced down to μm/s so as to ensure sufficient overlap for homogenous structures in the propagation direction [30]. As it happens with the other parameters, for each material, selecting the proper repetition rate is crucial to get the desired type of morphological change.

3.5. Short overview of some 3DLW applications

In this section, it is briefly shown how 3DLW technology has been applied successfully to relevant research fields.

3.5.1. Telecommunications

Arguably the telecom field, which is continuously looking for more bandwidth, has been the one pushing more intensively the development of new and more efficient 3DLW integrated optical devices [10, 11, 36-39]. Mainly taking advantage of the 3D capability of the technique, novel and competitive spatial division multiplexing (SDM) designs such as mode-division multiplexers for few-mode fibers [37] or fan-out chips for multicore fibers [38] are being already deployed in the industry [40, 41]. SDM is a technology that seeks to overcome the nonlinear Shannon limit [42] of optical fibers by adding more spatial light paths inside them [43].

Generally, telecom 3DLW optical circuits consists of step-index-like (Type I) waveguides embedded in low index silica-based glass making them directly

compatible with optical fibers. Butt-coupling fibers and 3DLW waveguides results in low-loss interconnection as the waveguide mode field diameters are tailored to match those of the fibers. Although the propagation losses are not as low as those obtained with deposition-based techniques (~0.1 vs. ~0.01 dB/cm) [1], and the bending radius is not as tight (20 vs. 2 mm) [1], the 3DLW technique provides a third spatial dimension to exploit which breaks the limits imposed by a 2D planar geometry yielding telecom interconnection devices that offer more capacity to already existing optical networks. An example of a 3DLW SDM device [20] taking advantage of a 3D architecture is shown in Figure 3.4.

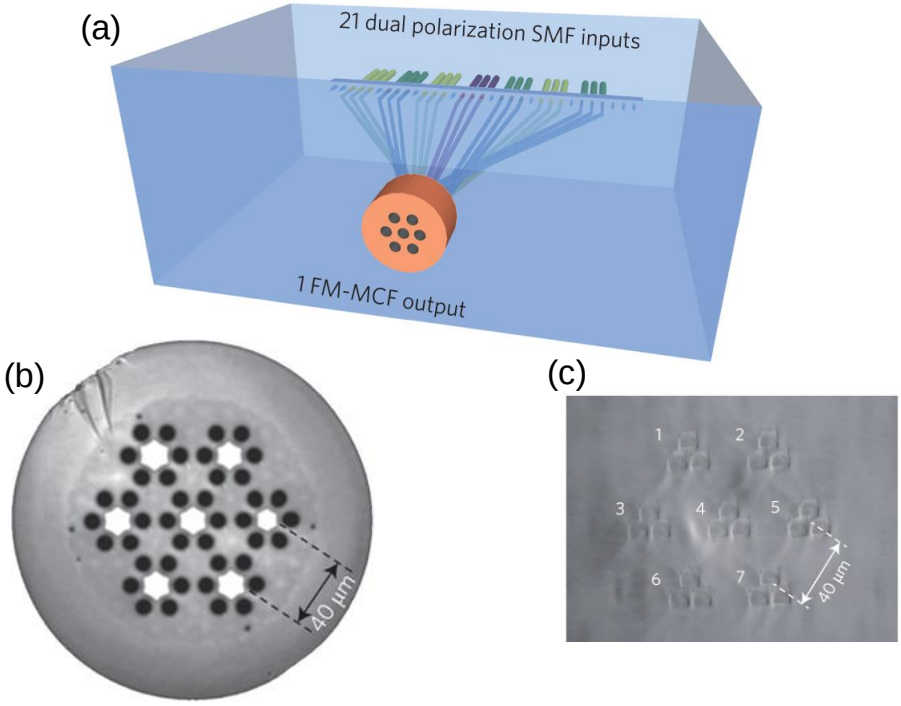

Figure 3.4. Telecom SDM fan-out device fabricated with the 3DLW technique. (a) Sketch of the device: a few-mode multicore fiber is 3D demultiplexed. (b) Microscope view of the optical fiber. (c) Microscope view of the matched 3DLW chip input. Adapted from [20].

3.5.2. Astrophotonics

Astrophotonics is another research area that can hugely benefit from the 3DLW technique for improved photonic 3D circuits. The research subject of astrophotonics is the incorporation of integrated photonics technology into astronomical observatories, by either substituting enormously complex and delicate bulk optical systems, or creating completely new photonic components that can offer new science to astronomers which was previously impossible by using bulk optics [44]. As in the telecom field, the most useful characteristic of laser written circuits is that they allow to design 3D waveguide architectures hitherto impossible with planar fabrication techniques. Moreover, the inherent robustness and stability of monolithic waveguide chips as compared to bulk instruments, which must be periodically maintained and realigned, is essential in experimental environments where measurements have to be done in a limited period of time and therefore the use of photonic instruments that are alignment-free and easy to install involves a boost in the amount of data that astrophysicists can collect in a given mission, which in turn imply further benefits for astronomical observatories.

3DLW also offers researchers the opportunity to choose virtually any transparent material up to mid-IR wavelengths [15] making the technique even more appealing to astrophysicists who need to perform measurements across different astronomical bands from the near-IR to mid-IR range. Recently, the possibility of fabricating 3D waveguide combiners working in the whole range from the J to N band (≈ 1 to 15 μm) on a single chip was demonstrated for the first time and applied to stellar interferometry. These first prototypes were written by means of the multiscan technique in IR transparent chalcogenide glass [15, 21].

A revealing illustration of 3DLW applied to astrophotonics is the on-chip 3DLW photonic lantern [45] (see Figure 3.5), which is a device that adiabatically transforms a multimode input coming from a telescope into a series of single-mode outputs that are normally coupled to a spectrograph to retrieve certain information such as chemical composition of the celestial signal analyzed [46].

Other noteworthy 3DLW devices are fan-outs for the bidirectional 2D - 3D reformatting of a waveguide array [21].

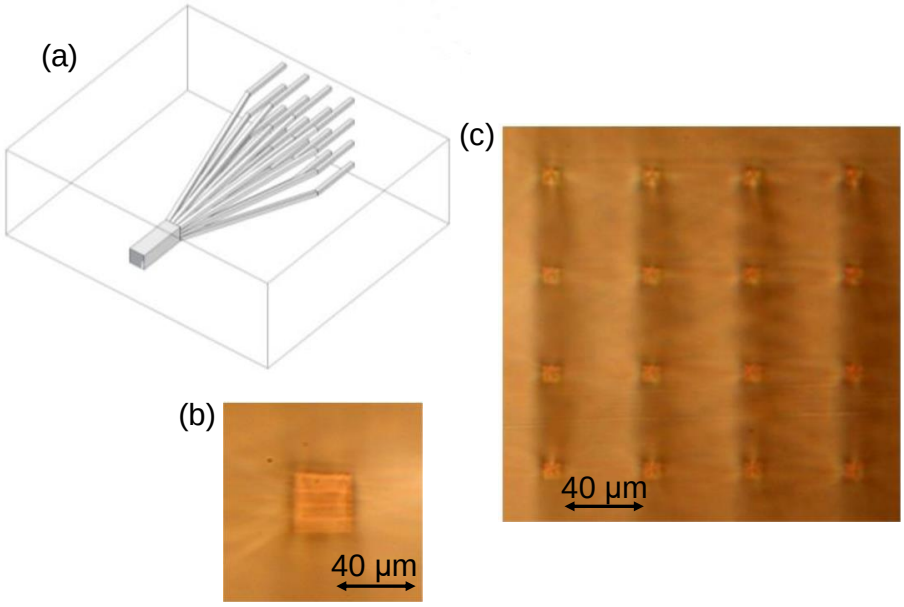

Figure 3.5. The 3DLW photonic lantern demonstrated in [45]. (a) Sketch of the three-dimensional device coupling light from a multimode input to a 2D array of single-mode outputs. (b, c) Microscope images of the inputs and outputs, respectively. The multiscan technique is employed to write the whole device.

3.5.3. Sensors and microfluidics

Either fibered or on-chip, optical waveguide technology has strongly contributed to the enhancement of the sensitivity, selectivity and miniaturization of all types of physical and biochemical sensors [47-49]. In the specific case of 3DLW technology, a 3D high temperature and strain sensor embedded in fused silica has been demonstrated in [13]. Moreover, by combining 3DLW with wet chemical etching, complex micron-sized opto-mechanical displacement sensors with nanometer resolution that are suitable for harsh environments have been presented in [50].

The lab-on-a-chip field [51] has also been benefited from the 3DLW as 3D microfluidic channels have been produced alongside photonic circuits inside bulk glass [52, 53]. Again, a wet etching treatment after the femtosecond laser irradiation is needed to selectively etch the desired area. Although the 3DLW optofluidic research is still in its infancy, it is already providing several advantages over other fabrication methods, like its relatively low cost, natural integration of microfluidic channels and optical waveguides, 3D designs and circular cross-section of the structures.

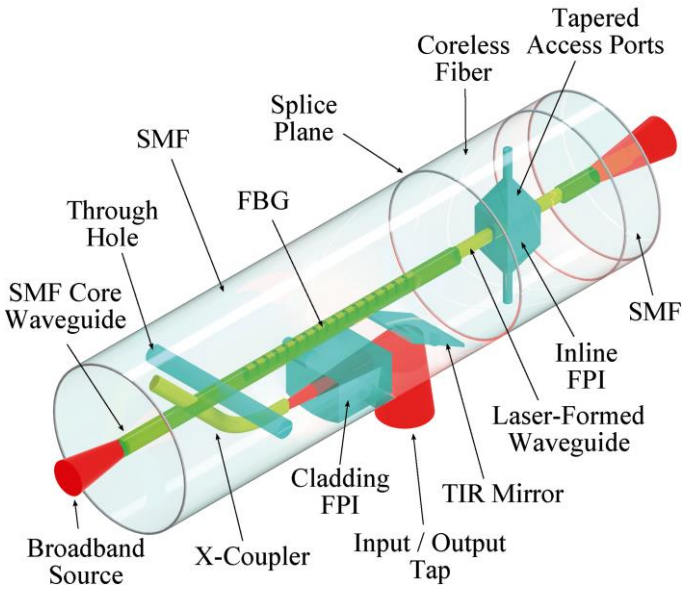

Figure 3.6. Concept of lab-in-fiber fabricated by 3DLW and subsequent chemical etching [54]. Multiple optofluidic elements are embedded in the cladding of a fiber that allow for simultaneous refractive index, temperature and bending sensing.

Thanks to adding a third dimension to the fabrication process, it has been possible, for example, to easily implement 3D hydrodynamic focusing [53] for more efficient single cell counting. Furthermore, due to the versatility of the 3DLW technique, optical circuits have been added to commercial microfluidic chips [52] for localized refractive index sensing. Last but not least, 3DLW optofluidic devices have been fabricated inside optical fibers, also called “lab-in-fiber” devices, as it

is shown in the example of Figure 3.6. Using the same procedure as in a planar substrate one can combine different building blocks (waveguides, mirrors, reservoirs, microchannels, etc) into the cladding volume of a fiber, in order to build a multiplexed sensing platform which can be easily distributed as it is typically done in fiber sensors [54].

3.6. Why using 3DLW for a water-ice sensor?

The most important element of the sensor presented in this Thesis is the optical waveguide embedded in the dielectric substrate. Therefore, the selection of the fabrication process of the waveguide is crucial for its successful performance. Among all the techniques for waveguide fabrication, the 3DLW technique has been chosen because, in the context of the sensor, it possesses at least five distinguishing advantages:

a) The fabricated waveguide circuits can be designed to have low coupling loss to commercial optical fibers, and a strong and robust fiber-chip bond, which is crucial for demanding applications and harsh environments.
b) For a given laser system with enough tunable parameters (pulse energy and duration, repetition rate, polarization, writing speed, focusing lens), a large range of materials can be considered for embedding the waveguides in it. Consequently, one can employ the material offering a better trade-off in the requirements for working in rough external environments (as in the sensor case), such as hardness or chemical stability, together with optical transparency at the chosen wavelength range, with only a few adjustments of the laser writing parameters.
c) Unlike other lithographic techniques, it does not require masking since the process relies on scanning the sample relative to the focused laser light. This eases quick prototyping at the expense of slower mass deployment, that during the Thesis work was not needed. Likewise, in one single chip one is able to write tens of waveguides with different geometries and properties so that the sensing performance optimization becomes faster.

d) The fabrication of the waveguides normally requires only one step without the need of multiple deposition of different types of materials which may diminish robustness of the whole sensor. Since the whole sensor is made of the same material, thermal expansion issues are minimized. However, this problem needs to be unavoidably addressed when connecting the chip to the optical fibers made of a different material.
e) The written waveguides are intrinsically three-dimensional which makes the 3DLW technique unique and remarkably different from the rest of fabrication processes which are capable only of providing in-plane optical elements. This characteristic allows the fiber-to-waveguide interconnection to be done far below the sensor external sensing face, enabling the design of a flush-mounted and non-intrusive sensing surface which can be seamlessly connected to other fibered sub-systems.

3.7. First fabricated waveguides and materials considered for the water-ice waveguide sensor

At the beginning of the project, three different silica-based materials were chosen as candidates to be the sensor building material. They were Gorilla Glass (popular in smartphone screens), α-quartz crystal, and low-OH fused silica glass. The fundamental requirements (review Table 2.1 from Chapter 2) that the material had to meet were: 1) enough hardness to face environmental erosion, 2) chemical inertness, 3) an appropriate index of refraction for enabling the differentiation between liquid water and ice and, obviously, 4) good IR transparency in the 3 – 4 μm operating range. Regarding the transparency, the IR transmission of the different bulk materials considered was measured by means of a FTIR spectrometer (see Figure 3.7). It needs to be taken into account, however, that the actual transparency of the 3DLW waveguide cores might vary with respect to the bulk non-irradiated material.

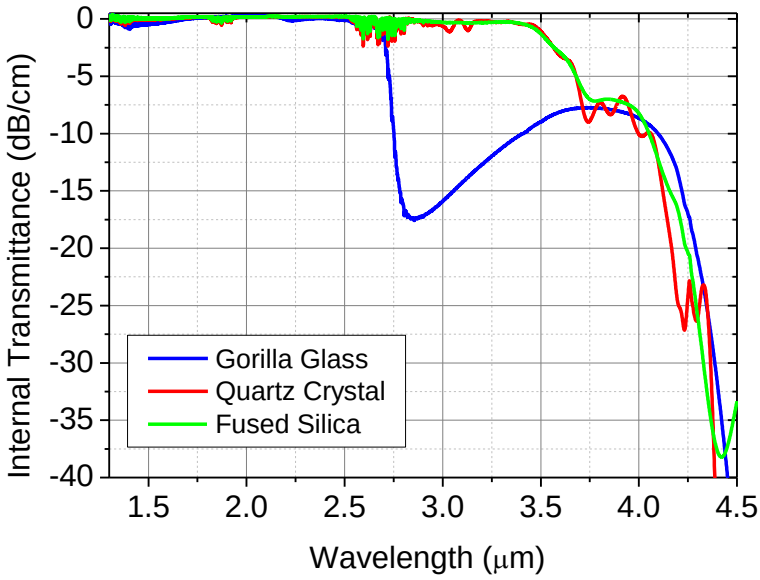

Figure 3.7. Measured internal IR transmittance of the candidates for the sensor material.

Next, a general overview of the 3DLW waveguides fabricated during the Thesis experimental work is given. A description of the characterization techniques corresponding to the images shown (microscope or output near-field images) together with a more detailed analysis of the final sensing waveguides fabricated in fused silica can be found separately in Chapter 4.

3.7.1. Gorilla Glass

Corning Gorilla Glass is nowadays extensively used in the smartphone industry as a cover glass with improved mechanical properties, such as higher scratch and crack resistance [55]. It is basically an alkali-aluminosilicate glass having a surface toughening treatment by ion exchange in which sodium ions are replaced by larger potassium ions [56]. This produces a layer with high compressive stress which is more resistant to damage [56]. Because Gorilla Glass has excellent mechanical properties, chemical stability, and adequate low refractive index (1.49

at λ = 590 nm), which makes it low-loss for butt-coupling to fluoride IR fibers, some preliminary waveguides were written inside it.

Laser system	IMRA fiber laser
Polarization	Circular
Wavelength (λ)	1033 nm
Pulse width (Δt)	≈ 400 fs
Repetition rate (RR)	500 kHz
Lens Numerical Aperture (NA)	0.25
Number of scans/waveguide (NS)	76
Scan separation (SS)	0.4 μm
Expected width (W)	≈ 30 μm
Pulse energy (E)	0.15 to 0.52 μJ (16 energies)
Scan speed (SSp)	8, 4, 2, 1 mm/s (4 speeds)

Table 3.1. Fabrication parameters for the 3DLW Gorilla Glass waveguides.

The initial fabrication was done at Heriot Watt University (Edinburgh, Scotland, United Kingdom) in the Nonlinear Optics research group of Professor Ajoy K. Kar. The multiscan technique to produce 64 Type I channel waveguides with an approximate core width of 30 μm was used, which a priori should be large enough to support guided modes at the mid-IR operating wavelengths. In Table 3.1, the fabrication parameters that were employed are listed.

As can be seen in the table, within the same substrate different writing powers and speeds were tried in order to get a significant number of waveguides with varying properties. In this manner, the optimum parameters for high index contrast and low loss can be retrieved quickly. The inscription process was performed at 500 kHz, hence in the thermal regime, which allowed the use of faster scan speeds. The energy levels that were selected are close to the ones used in similar materials (borosilicate) to obtain Type I waveguides as well [11].

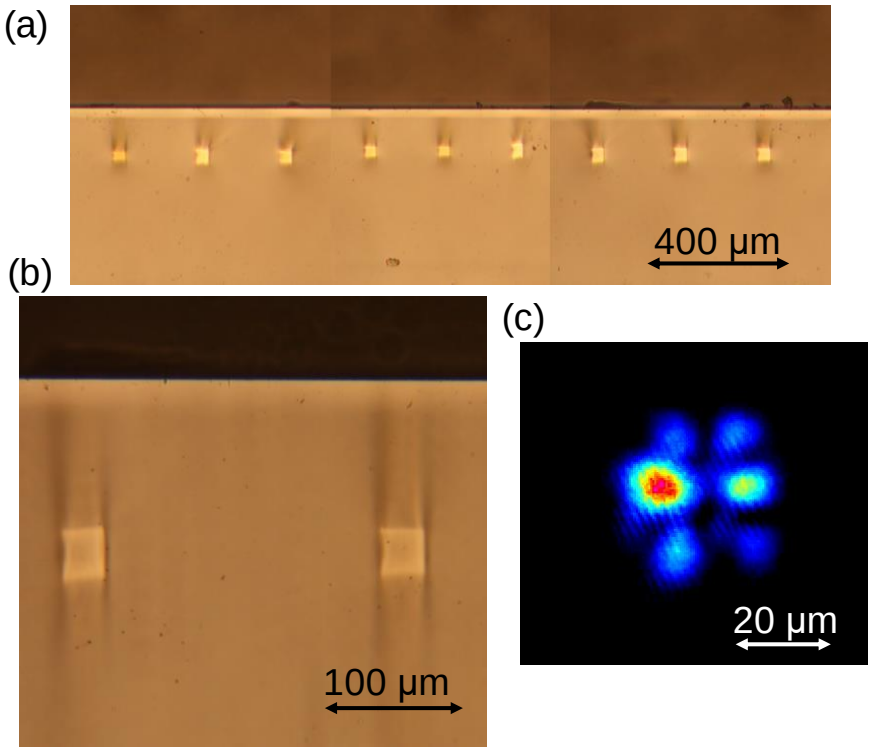

Figure 3.8. 3DLW multiscan Type I waveguides on Gorilla Glass. (a, b) Transmission microscope view of some the waveguides cross-section. (c) Near-field output of one of the waveguides at λ = 1.52 µm.

Transmission microscope images of the waveguides cross-section, and a waveguide output near-field at λ = 1.52 µm, are shown in Figures 3.8(a) and (b). The microscope images revealed a smooth refractive index increase since the higher core brightness indicated confinement of, at least, visible light. This higher brightness can also be observed within the surface compression layer, which is consistent with a higher refractive index (1.51 at λ = 590 nm).

This index increase of the 3DLW waveguides was further indeed confirmed when 1.52 µm laser light was launched into the different waveguides and guiding was verified (see Figure 3.8(c)). On the contrary, at 3.39 µm, no waveguiding was experimentally observed. This might be due to high absorption of the modified waveguide core which adds up to the absorption (≈ 10 dB/cm) of the Gorilla Glass

bulk at this wavelength. Due to the lack of light guiding in the 3–4 μm, Gorilla Glass was discarded as a material for embedding the sensor.

3.7.2. Quartz crystal

The crystalline phase of SiO_2, specifically the alpha phase, was also investigated as a base material for the sensor. Having a very high hardness (7 in Mohs scale), mid-IR transparency, and still moderately low refractive index, α-quartz was initially regarded as the most promising material for building the sensor.

Laser system	IMRA fiber laser
Polarization	Circular
Wavelength (λ)	1033 nm
Pulse width (Δt)	≈ 400 fs
Repetition rate (RR)	100 kHz
Lens Numerical Aperture (NA)	0.25
Number of scans/waveguide (NS)	52
Scan separation (SS)	0.4 μm
Pulse energy (E)	0.59 to 2.60 μJ (30 energies)
Scan speed (SSp)	16, 8, 4, 2, 1 mm/s (5 speeds)

Table 3.2. Fabrication parameters of the attempt of fabrication of Type I waveguides on quartz crystal.

First of all, it was attempted to obtain Type I waveguides like in Gorilla Glass by using the parameters shown in Table 3.2. The repetition rate was reduced to 100 kHz and it was swept the irradiated power and scan speed as before.

As it can be seen in Figure 3.9(a), the microscope view of the written waveguides does not resemble a step-index with increased index core. Moreover, cracks were present due to the effect of high intensity laser pulses on the crystalline lattice. This result was not surprising because of the crystalline nature of the material and only in very few reported cases it has been possible to induce Type I modifications in crystals, as pointed out in Sections 3.2 and 3.3.

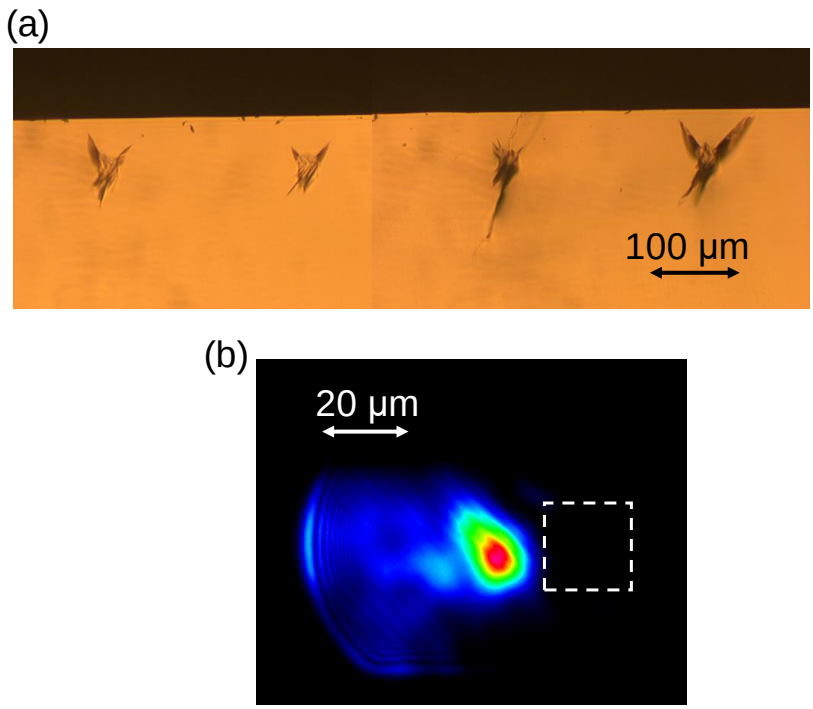

Figure 3.9. Attempt of 3DLW multiscan waveguides on α-quartz. a) Transmission microscope view of the waveguides cross-section. b) Near-field output of one of the waveguides at λ = 3.39 µm. No waveguiding observed inside the laser written cores (dashed square) but only besides it (i.e. due to stress-optic induced refractive index increase).

On the other hand, waveguiding at 3.39 µm was still found in the regions adjacent to the laser written core (Figure 3.9(b)), most probably due to induced stress fields surrounding the 3DLW tracks area and the index increment from the piezo-optic effect, as it has been previously studied and reported in [57]. Note that the guiding is quite leaky because the index increase arising from laser induced stress fields is typically weak (~5E-4) and vanish in a few micrometers distance from the written structures.

Given the unfeasibility of fabricating Type I waveguides, a different approach was taken which consisted of producing a Type III depressed-cladding structures which should offer good light confinement in the mid-IR since the tracks had a

reduced refractive index. This new set of waveguides were fabricated in a low repetition rate laser writing facility, in the Laser Microprocessing Group at Universidad de Salamanca (Spain) led by Dr. Javier Vázquez de Aldana. The parameters used in this different setup are shown in Table 3.3.

Laser system	Spitfire Ti:Sapphire
Polarization	Linear
Wavelength (λ)	795 nm
Pulse width (Δt)	≈120 fs
Repetition rate (RR)	1 kHz
Lens Numerical Aperture (NA)	0.4
Pulse energy on sample (E)	0.8 μJ
Scan speed (SSp)	0.35 mm/s

Table 3.3. Fabrication parameters for the 3DLW quartz crystal Type III waveguides.

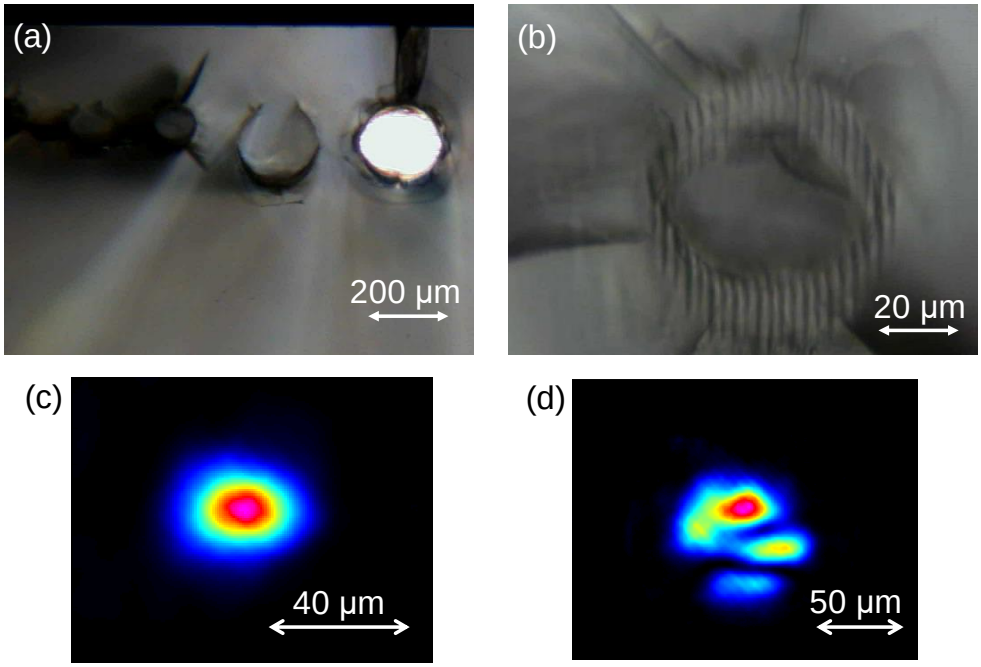

Figure 3.10. 3DLW Type III waveguides on α-quartz. a b) Transmission microscope view of the waveguides cross-section. c) Near-field output of a single-mode waveguide at λ = 3.39 μm and d) of a multimode one.

The laser system and the writing parameters utilized were significantly different than those in Gorilla Glass. The pulse width was shorter and, more importantly, the repetition rate was 500 times lower, so that the sample was irradiated in the non-thermal regime. As a consequence of the lower repetition rate, the writing speed had to be reduced with respect to the glass sample as well. Figure 3.10 shows microscope and near-field output images of the tubular designed Type III waveguides in α-quartz made in different sizes. Note the presence of open-cladding waveguides that were inscribed in order to eventually test their surface sensing performance. Considering the provided good confinement at mid-IR wavelengths (Figure 3.10(c) and (d)), Type III waveguides on α-quartz were a good option to be later selected as the sensing element.

3.7.3. Fused silica glass

Silica glass is commonly referred in the literature as fused quartz or fused silica (or simply silica) interchangeably. Fused quartz is sometimes used to refer to ultra-high quality silica glass, while low-cost fused silica glass can have a high amount of impurities. Actually, both glasses have very similar physical properties and their principal difference lies in the manufacturing process. While fused silica is synthetically derived, fused quartz is obtained by melting naturally occurring crystalline quartz. In both cases the OH content can be controlled to the ppm level and hence the associated OH absorptions can be virtually removed. In this Thesis, it has been chosen to use the commercial Suprasil 300 [58] from Heraeus, which is fused silica made by flame hydrolysis. As in crystalline quartz, Suprasil 300 transmission extends continuously up to approximately 4 μm wavelength (transmission of around 6 dB/cm at 3.7 μm), as shown in Figure 3.7, unlike non-IR silica that has a strong deep in transmission around 2.8 μm (not shown here).

The high availability, low cost and good mechanical, chemical and thermal properties of fused silica made this material extremely attractive for the sensor purposes. The main advantage of silica over quartz crystal is that one can create Type I waveguides using femtosecond laser pulses. There is an extensive literature on 3DLW of waveguides and other elements in fused silica glass [2, 7,

8, 10, 13, 50], as well as fundamental research on it [8, 34, 59, 60]. This is explained by the fact that fused silica and silica-based glasses are materials with great scientific interest and broad applications in important industries such as semiconductor, microscopy or photonics.

Laser system	IMRA fiber laser
Polarization	Circular
Wavelength (λ)	1033 nm
Pulse width (Δt)	≈ 400 fs
Repetition rate (RR)	500 kHz
Lens Numerical Aperture (NA)	0.25
Number of scans/waveguide (NS)	76 and 32
Scan separation (SS)	0.4 μm
Expected width (W)	≈ 30 μm and 15 μm
Pulse energy (E)	0.45 to 0.51 μJ (13 energies)
Scan speed (SSp)	8, 4, 2, 1 mm/s (4 speeds)

Table 3.4. Fabrication parameters for the first set of 3DLW fused silica waveguides.

The first set of 3DLW Type I silica waveguides were fabricated at Heriot Watt University (Edinburgh, Scotland), as in the Gorilla Glass case. Two core width sizes (15 and 30 μm) were produced while testing different laser power and speeds (look at Table 3.4 for the complete list of parameters) for a total of 104 waveguides in a single silica substrate. An example of the transmission microscope images of structures obtained and their optical near-field output at λ = 3.39 μm is shown in Figure 3.11.

As with the Type III waveguides on α-quartz, mid-IR light transmission is verified together with an improved confinement (note they are single-mode) which may lead to better sensing performance. In this first set of fused silica waveguides, the maximum available pulse energy provided by the laser system was reached.

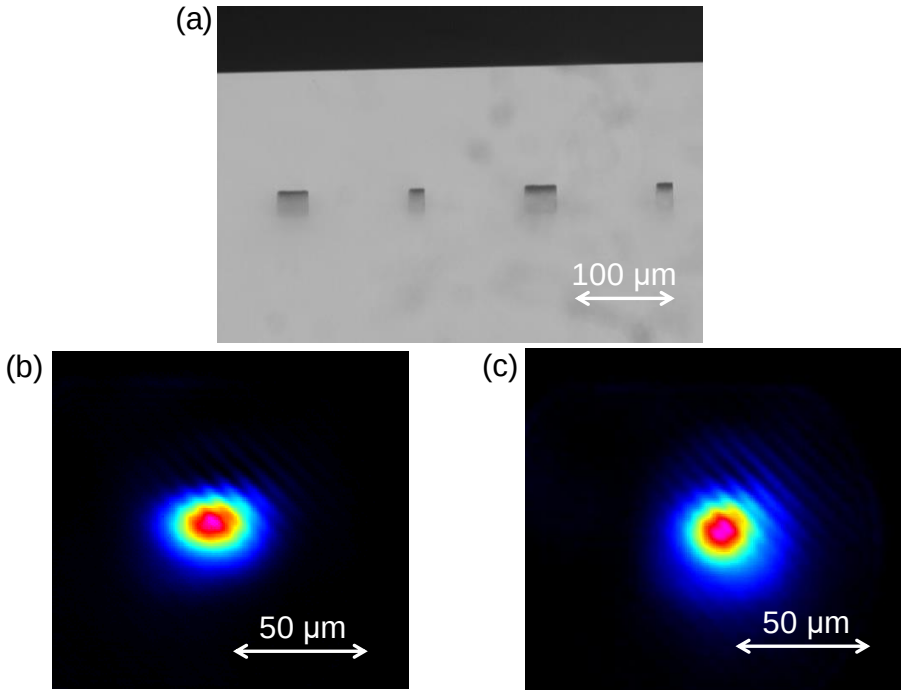

Figure 3.11. First set of 3DLW multiscan Type I waveguides on Fused Silica. (a) Transmission microscope view of some the waveguides cross-section. (b, c) Near-field output of a pair of waveguides at λ = 3.39 µm having width of 30 µm and 15 µm, respectively.

Since it was required to increase as much as possible the light confinement, a second set of improved waveguides was fabricated in the facilities of the Laser Processing Group (LPG) at the Instituto de Óptica Daza y Valdés of the Consejo Superior de Investigaciones Científicas (CSIC) in Madrid (Spain), led by Prof. Javier Solis, where a femtosecond fiber laser offering higher pulse energy was available. This novel high-contrast 3DLW waveguides for the 3.5 µm range were reported and thoroughly analyzed in [61] (see Paper I of Appendix E). Table 3.5 collects the 3DLW parameters for this second set of waveguides.

Laser system	Tangerine, Amplitude Systemes fiber
Polarization	Circular
Wavelength (λ)	1047 nm
Pulse width (Δt)	≈ 450 fs

Repetition rate (RR)	500 kHz
Lens Numerical Aperture (NA)	0.4
Number of scans/waveguide (NS)	26 and 12
Scan separation (SS)	0.4 μm and 0.8 μm
Expected width (W)	≈ 10 μm
Pulse energy (E)	0.80, 0.88, 0.92, 0.96 μJ (4 Energies)
Scan speed (SSp)	1.5 mm/s

Table 3.5. Fabrication parameters for the second set of 3DLW fused silica waveguides.

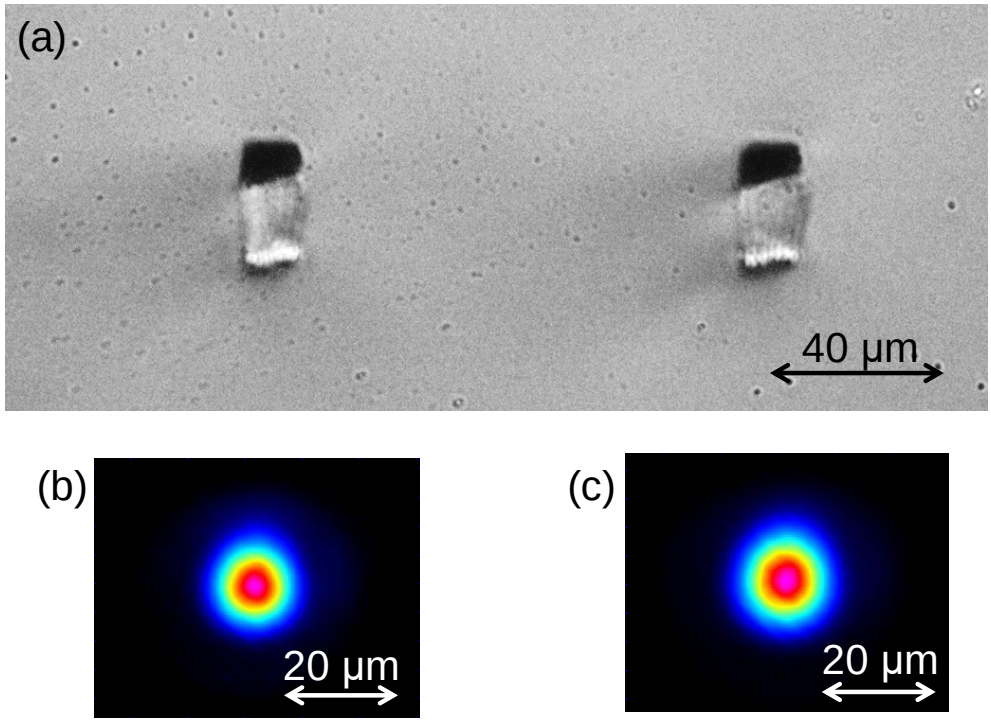

Figure 3.12. Second set of 3DLW multiscan Type I waveguides on Fused Silica. (a) Transmission microscope view of the waveguides cross-section with 0.4 μm (left) and 0.8 μm (right) scan separation. (b, c) Near-field output corresponding to each one of the previous waveguides at λ = 3.39 μm, respectively.

The range of the scan speed and the pulse energy was narrowed based on previous experience. Specifically, the pulse energy was kept higher than 0.8 μJ, and the scan speed fixed to 1.5 mm/s, which is relatively slow for this kind of

3DLW fabrication in glasses. On the contrary, the higher contrast obtained allowed decreasing the number of scans needed for smaller core sizes (note higher NA leading to shorter core height as well) and still support a guided mode. Likewise, a group of waveguides with double scan separation (see Figure 3.12(a)) was written so as to reduce even further the number of scans and consequently divide by two the waveguide fabrication time.

Figures 3.12 (b) and (c) show the mode confinement enhancement that was achieved by increasing the writing pulse energy, as compared with the waveguides shown in Figure 3.11. This greater light confinement at mid-IR wavelengths, as well as the much higher index contrast, which allows much tighter waveguide bending and better sensing sensitivity (see Chapter 2), led to choose this second set of waveguides as the transducing elements for the ice sensor. A deeper analysis of the variations of the fabrication parameters and their effects on the optical performance of the waveguides is next provided in Chapter 4.

References

1. R. Osellame, G. Cerullo, and R. Ramponi, Femtosecond Laser Micromachining: Photonic and Microfluidic Devices in Transparent Materials (Springer, 2012).
2. A. Marcinkevičius, S. Juodkazis, M. Watanabe, M. Miwa, S. Matsuo, H. Misawa, and J. Nishii, "Femtosecond laser-assisted three-dimensional microfabrication in silica," Optics Letters **26**, 277-279 (2001).
3. V. Maselli, R. Osellame, G. Cerullo, R. Ramponi, P. Laporta, L. Magagnin, and P. L. Cavallotti, "Fabrication of long microchannels with circular cross section using astigmatically shaped femtosecond laser pulses and chemical etching," Applied Physics Letters **88**, 191107 (2006).
4. Y. Cheng, K. Sugioka, K. Midorikawa, M. Masuda, K. Toyoda, M. Kawachi, and K. Shihoyama, "Three-dimensional micro-optical components embedded in photosensitive glass by a femtosecond laser," Optics Letters **28**, 1144-1146 (2003).
5. M. Haque, and P. R. Herman, "Chemical-assisted femtosecond laser writing of optical resonator arrays," Laser & Photonics Reviews **9**, 656-665 (2015).
6. K. Sugioka, Y. Cheng, and K. Midorikawa, "Three-dimensional micromachining of glass using femtosecond laser for lab-on-a-chip device manufacture," Applied Physics A **81**, 1-10 (2005).
7. G. Nava, F. Bragheri, T. Yang, P. Minzioni, R. Osellame, I. Cristiani, and K. Berg-Sørensen, "All-silica microfluidic optical stretcher with acoustophoretic prefocusing," Microfluidics and Nanofluidics **19**, 837-844 (2015).
8. K. M. Davis, K. Miura, N. Sugimoto, and K. Hirao, "Writing waveguides in glass with a femtosecond laser," Optics Letters **21**, 1729-1731 (1996).
9. K. Suzuki, V. Sharma, J. G. Fujimoto, E. P. Ippen, and Y. Nasu, "Characterization of symmetric [3 × 3] directional couplers fabricated by direct writing with a femtosecond laser oscillator," Optics Express **14**, 2335-2343 (2006).
10. H. Zhang, S. M. Eaton, and P. R. Herman, "Single-step writing of Bragg grating waveguides in fused silica with an externally modulated femtosecond fiber laser," Optics Letters **32**, 2559-2561 (2007).
11. S. M. Eaton, W. J. Chen, H. Zhang, R. Iyer, J. Li, M. L. Ng, S. Ho, J. S. Aitchison, and P. R. Herman, "Spectral Loss Characterization of Femtosecond Laser Written Waveguides in Glass With Application to Demultiplexing of 1300 and 1550 nm Wavelengths," Journal of Lightwave Technology **27**, 1079-1085 (2009).
12. Y. Liao, J. Xu, Y. Cheng, Z. Zhou, F. He, H. Sun, J. Song, X. Wang, Z. Xu, K. Sugioka, and K. Midorikawa, "Electro-optic integration of embedded electrodes and waveguides in LiNbO3 using a femtosecond laser," Optics Letters **33**, 2281-2283 (2008).
13. H. Zhang, S. Ho, S. M. Eaton, J. Li, and P. R. Herman, "Three-dimensional optical sensing network written in fused silica glass with femtosecond laser," Optics Express **16**, 14015-14023 (2008).

14. Y. Ren, G. Brown, A. Ródenas, S. Beecher, F. Chen, and A. K. Kar, "Mid-infrared waveguide lasers in rare-earth-doped YAG," Optics Letters **37**, 3339-3341 (2012).
15. A. Ródenas, G. Martin, B. Arezki, N. Psaila, G. Jose, A. Jha, L. Labadie, P. Kern, A. Kar, and R. Thomson, "Three-dimensional mid-infrared photonic circuits in chalcogenide glass," Optics Letters **37**, 392-394 (2012).
16. Y. Tan, A. Rodenas, F. Chen, R. R. Thomson, A. K. Kar, D. Jaque, and Q. Lu, "70% slope efficiency from an ultrafast laser-written Nd:GdVO4 channel waveguide laser," Optics Express **18**, 24994-24999 (2010).
17. G. A. Torchia, A. Rodenas, A. Benayas, E. Cantelar, L. Roso, and D. Jaque, "Highly efficient laser action in femtosecond-written Nd:yttrium aluminum garnet ceramic waveguides," Applied Physics Letters **92**, 111103 (2008).
18. L. Ding, R. I. Blackwell, J. F. Künzler, and W. H. Knox, "Femtosecond laser micromachining of waveguides in silicone-based hydrogel polymers," Applied Optics **47**, 3100-3108 (2008).
19. J. R. Grenier, L. A. Fernandes, and P. R. Herman, "Femtosecond laser inscription of asymmetric directional couplers for in-fiber optical taps and fiber cladding photonics," Optics Express **23**, 16760-16771 (2015).
20. R. G. H. van Uden, R. A. Correa, E. A. Lopez, F. M. Huijskens, C. Xia, G. Li, A. Schülzgen, H. de Waardt, A. M. J. Koonen, and C. M. Okonkwo, "Ultra-high-density spatial division multiplexing with a few-mode multicore fibre," Nature Photonics **8**, 865-870 (2014).
21. R. R. Thomson, R. J. Harris, T. A. Birks, G. Brown, J. Allington-Smith, and J. Bland-Hawthorn, "Ultrafast laser inscription of a 121-waveguide fan-out for astrophotonics," Optics Letters **37**, 2331-2333 (2012).
22. M. Ams, G. D. Marshall, P. Dekker, M. Dubov, V. K. Mezentsev, I. Bennion, and M. J. Withford, "Investigation of Ultrafast Laser--Photonic Material Interactions: Challenges for Directly Written Glass Photonics," IEEE Journal of Selected Topics in Quantum Electronics **14**, 1370-1381 (2008).
23. F. Chen, and J. R. V. de Aldana, "Optical waveguides in crystalline dielectric materials produced by femtosecond-laser micromachining," Laser & Photonics Reviews **8**, 251-275 (2014).
24. J. Burghoff, C. Grebing, S. Nolte, and A. Tünnermann, "Efficient frequency doubling in femtosecond laser-written waveguides in lithium niobate," Applied Physics Letters **89**, 081108 (2006).
25. A. Rodenas, and A. K. Kar, "High-contrast step-index waveguides in borate nonlinear laser crystals by 3D laser writing," Optics Express **19**, 17820-17833 (2011).
26. H.-D. Nguyen, A. Ródenas, J. R. Vázquez de Aldana, J. Martínez, F. Chen, M. Aguiló, M. C. Pujol, and F. Díaz, "Heuristic modelling of laser written mid-infrared LiNbO3 stressed-cladding waveguides," Optics Express **24**, 7777-7791 (2016).
27. A. Mermillod-Blondin, I. M. Burakov, Y. P. Meshcheryakov, N. M. Bulgakova, E. Audouard, A. Rosenfeld, A. Husakou, I. V. Hertel, and R. Stoian, "Flipping the sign of refractive index changes in ultrafast and temporally shaped laser-irradiated borosilicate crown optical glass at high repetition rates," Physical Review B **77**, 104205 (2008).

28. J. W. Chan, T. R. Huser, S. H. Risbud, J. S. Hayden, and D. M. Krol, "Waveguide fabrication in phosphate glasses using femtosecond laser pulses," Applied Physics Letters **82**, 2371-2373 (2003).
29. S. Gross, N. Jovanovic, A. Sharp, M. Ireland, J. Lawrence, and M. J. Withford, "Low loss mid-infrared ZBLAN waveguides for future astronomical applications," Optics Express **23**, 7946-7956 (2015).
30. S. Gross, and M. J. Withford, "Ultrafast-laser-inscribed 3D integrated photonics: challenges and emerging applications," Nanophotonics **4**, - (2015).
31. Y. Nasu, M. Kohtoku, and Y. Hibino, "Low-loss waveguides written with a femtosecond laser for flexible interconnection in a planar light-wave circuit," Optics Letters **30**, 723-725 (2005).
32. A. G. Okhrimchuk, A. V. Shestakov, I. Khrushchev, and J. Mitchell, "Depressed cladding, buried waveguide laser formed in a YAG:Nd3+ crystal by femtosecond laser writing," Optics Letters **30**, 2248-2250 (2005).
33. M. Lenzner, J. Krüger, S. Sartania, Z. Cheng, C. Spielmann, G. Mourou, W. Kautek, and F. Krausz, "Femtosecond Optical Breakdown in Dielectrics," Physical Review Letters **80**, 4076-4079 (1998).
34. D. J. Little, M. Ams, P. Dekker, G. D. Marshall, J. M. Dawes, and M. J. Withford, "Femtosecond laser modification of fused silica: the effect of writing polarization on Si-O ring structure," Optics Express **16**, 20029-20037 (2008).
35. C. B. Schaffer, J. F. García, and E. Mazur, "Bulk heating of transparent materials using a high-repetition-rate femtosecond laser," Applied Physics A **76**, 351-354 (2003).
36. B. Guan, R. P. Scott, C. Qin, N. K. Fontaine, T. Su, C. Ferrari, M. Cappuzzo, F. Klemens, B. Keller, M. Earnshaw, and S. J. B. Yoo, "Free-space coherent optical communication with orbital angular, momentum multiplexing/demultiplexing using a hybrid 3D photonic integrated circuit," Optics Express **22**, 145-156 (2014).
37. S. Gross, N. Riesen, J. D. Love, and M. J. Withford, "Three-dimensional ultra-broadband integrated tapered mode multiplexers," Laser & Photonics Reviews **8**, L81-L85 (2014).
38. R. R. Thomson, H. T. Bookey, N. D. Psaila, A. Fender, S. Campbell, W. N. MacPherson, J. S. Barton, D. T. Reid, and A. K. Kar, "Ultrafast-laser inscription of a three dimensional fan-out device for multicore fiber coupling applications," Optics Express **15**, 11691-11697 (2007).
39. J. C. Ng, C. Li, P. R. Herman, and L. Qian, "Femtosecond laser writing of a flat-top interleaver via cascaded Mach-Zehnder interferometers," Optics Express **20**, 17894-17903 (2012).
40. www.modularphotonics.com
41. www.optoscribe.com
42. A. D. Ellis, J. Zhao, and D. Cotter, "Approaching the Non-Linear Shannon Limit," Journal of Lightwave Technology **28**, 423-433 (2010).
43. D. J. Richardson, J. M. Fini, and L. E. Nelson, "Space-division multiplexing in optical fibres," Nature Photonics **7**, 354-362 (2013).
44. J. Bland-Hawthorn, and P. Kern, "Astrophotonics: a new era for astronomical instruments," Optics Express **17**, 1880-1884 (2009).
45. R. R. Thomson, T. A. Birks, S. G. Leon-Saval, A. K. Kar, and J. Bland-Hawthorn, "Ultrafast laser inscription of an integrated photonic lantern," Optics Express **19**, 5698-5705 (2011).

46. T. A. Birks, I. Gris-Sánchez, S. Yerolatsitis, S. G. Leon-Saval, and R. R. Thomson, "The photonic lantern," Advances in Optics and Photonics **7**, 107-167 (2015).
47. X.-d. Wang, and O. S. Wolfbeis, "Fiber-Optic Chemical Sensors and Biosensors (2013–2015)," Analytical Chemistry **88**, 203-227 (2016).
48. X. Bao, and L. Chen, "Recent Progress in Distributed Fiber Optic Sensors," Sensors **12** (2012).
49. M. C. Estevez, M. Alvarez, and L. M. Lechuga, "Integrated optical devices for lab-on-a-chip biosensing applications," Laser & Photonics Reviews **6**, 463-487 (2012).
50. Y. Bellouard, A. A. Said, and P. Bado, "Integrating optics and micro-mechanics in a single substrate: a step toward monolithic integration in fused silica," Optics Express **13**, 6635-6644 (2005).
51. G. M. Whitesides, "The origins and the future of microfluidics," Nature **442**, 368-373 (2006).
52. A. Crespi, Y. Gu, B. Ngamsom, H. J. W. M. Hoekstra, C. Dongre, M. Pollnau, R. Ramponi, H. H. van den Vlekkert, P. Watts, G. Cerullo, and R. Osellame, "Three-dimensional Mach-Zehnder interferometer in a microfluidic chip for spatially-resolved label-free detection," Lab on a Chip **10**, 1167-1173 (2010).
53. P. Paie, F. Bragheri, R. M. Vazquez, and R. Osellame, "Straightforward 3D hydrodynamic focusing in femtosecond laser fabricated microfluidic channels," Lab on a Chip **14**, 1826-1833 (2014).
54. M. Haque, K. K. C. Lee, S. Ho, L. A. Fernandes, and P. R. Herman, "Chemical-assisted femtosecond laser writing of lab-in-fibers," Lab on a Chip **14**, 3817-3829 (2014).
55. www.corninggorillaglass.com/
56. www.corninggorillaglass.com/en/technology/how-its-made
57. T. Gorelik, M. Will, S. Nolte, A. Tuennermann, and U. Glatzel, "Transmission electron microscopy studies of femtosecond laser induced modifications in quartz," Applied Physics A **76**, 309-311 (2003).
58. www.heraeus.com/media/media/hqs/doc_hqs/products_and_solutions_8/optics/Suprasil_and_Infrasil__Material_Grades_for_the_Infrared_Spectrum_EN.pdf
59. C. Corbari, A. Champion, M. Gecevičius, M. Beresna, Y. Bellouard, and P. G. Kazansky, "Femtosecond versus picosecond laser machining of nano-gratings and micro-channels in silica glass," Optics Express **21**, 3946-3958 (2013).
60. J. W. Chan, T. Huser, S. Risbud, and D. M. Krol, "Structural changes in fused silica after exposure to focused femtosecond laser pulses," Optics Letters **26**, 1726-1728 (2001).
61. J. Martínez, A. Ródenas, T. Fernandez, J. R. Vázquez de Aldana, R. R. Thomson, M. Aguiló, A. K. Kar, J. Solis, and F. Díaz, "3D laser-written silica glass step-index high-contrast waveguides for the 3.5 μm mid-infrared range," Optics Letters **40**, 5818-5821 (2015).

CHAPTER 4

Optical characterization of mid-infrared waveguides

In this chapter, the micro-characterization of 3DLW waveguides is described, focusing on those made in fused silica glass. Optical microscopy is first addressed as a tool for rapid waveguide morphology characterization. Next, waveguide guiding properties are retrieved using a customized optical setup for the mid-IR range. The imaged output near-field of waveguide modes and its matching with electromagnetic modal calculations is used to obtain estimations of the femtosecond laser induced refractive index changes in the mid-IR range, which are essential to model the waveguide sensor device. Moreover, waveguide propagation losses are also indirectly estimated, allowing to determine the power requirements for the prototype system, thus knowing its performance limitations. To finish, a fundamental micro-spectroscopic characterization (μ-luminescence and μ-Raman) of the waveguides is performed so as to understand the silica glass structural changes produced at the irradiated micro-volume which lead to a high and positive refractive index change.

4.1. Transmission and reflection microscopy

Visible light optical transmission microscopic observation of a 3DLW transparent sample allows to qualitatively know the type of modification induced in the material. The sample is illuminated from one side of the chip through a condenser while the opposite side is imaged with a magnifying objective together with a camera and eyepieces. Both cross-sectional images and top view of the waveguides can be achieved using transmission microscopy.

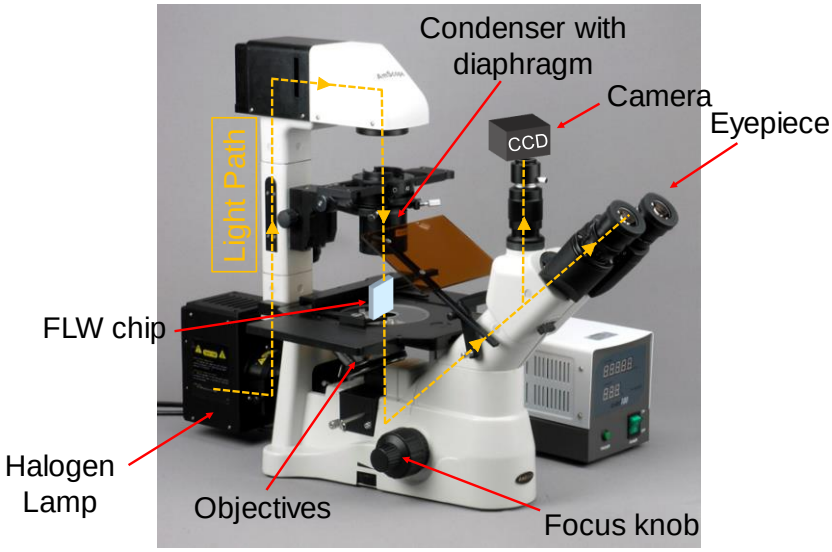

Figure 4.1. The inverted microscope used for the characterization of the waveguides in transmission.

The microscope model that was used in the laboratory featured an inverted configuration, that is the illumination is done from above the sample whereas the observation is from below (see Figure 4.1 for details). Images were also taken with a Leica DM2500 microscope (non-inverted) integrated in a Renishaw inVia Raman microscope that was later employed to obtain μ-photoluminescence and μ-Raman maps of the fused silica waveguides cross-section (Section 4.3.2).

Transmitted light microscopes (in bright-field mode) generate magnified images whose shapes and features are formed through the increased absorption of

certain elements in the sample. This also holds in the case of photonic chips with the difference that they are not a planar substrate but they have a third out-plane dimension that influence on the cross-section image obtained by the microscope. One can take advantage of this by varying the condenser and diaphragm such that the illuminating conditions can be approximately matched to the acceptance light cone of the waveguide being inspected and hence the obtained image emphasizes the core of the waveguide by the light guiding effect. This is showcased in Figure 4.2(b) where the core of the 3DLW fabricated waveguides in Gorilla Glass (see compression layer above) appear with an enhanced contrast. The rest of images shown in Figure 4.2 are examples obtained in transmission of fused silica waveguides. Note that Figure 4.2(d) is a top view of a 3DLW waveguide which was sometimes used to quickly assess the width of the fabricated waveguide. However, since this analysis is performed with visible light, no direct relation to the waveguide guiding properties in the mid-IR can be performed; i.e. in some cases waveguides can be seen to guide visible light, whereas not in others, even if all waveguides may feature low propagation losses at the longer wavelength mid-IR range.

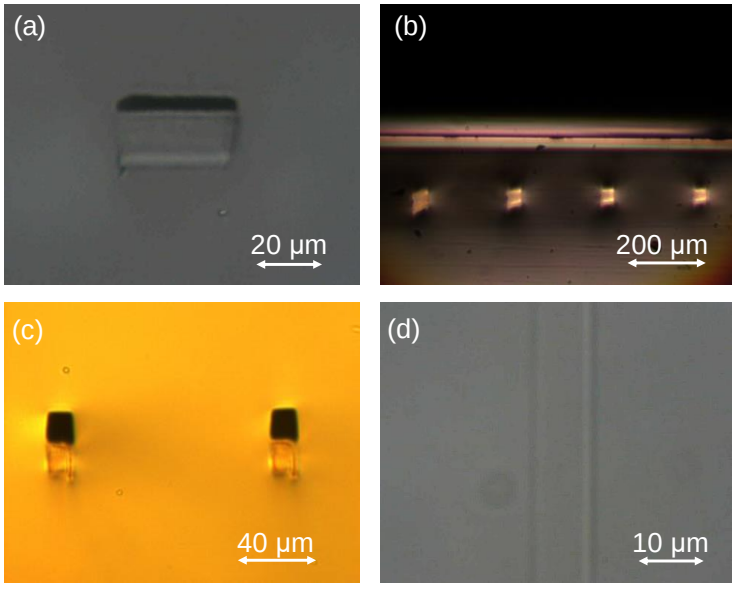

Figure 4.2. Transmitted light images of 3DLW waveguides made in fused silica (a, c) and Gorilla Glass (b, d). Note that (d) is a top view.

In some occasions, the waveguides surface cross-section was also imaged in reflection by means of a Sensofar PLμ 2300 confocal microscope. This allowed to observe certain surface details that were not noticeable in transmission. For instance, cracks and damage in cladding waveguides (Figure 4.3(b)) induced by femtosecond pulses. Likewise, in Figure 4.3(a), the shiny area above the core region of the Type I waveguide can be associated with an increased scattering whereas one cannot conclude the same just by looking at the dark area covering the core of similar waveguides in Figure 4.2(c). The nature of these zones will be studied later in detail, with the aid of μ-photoluminescence and μ-Raman analysis, in Section 4.3.

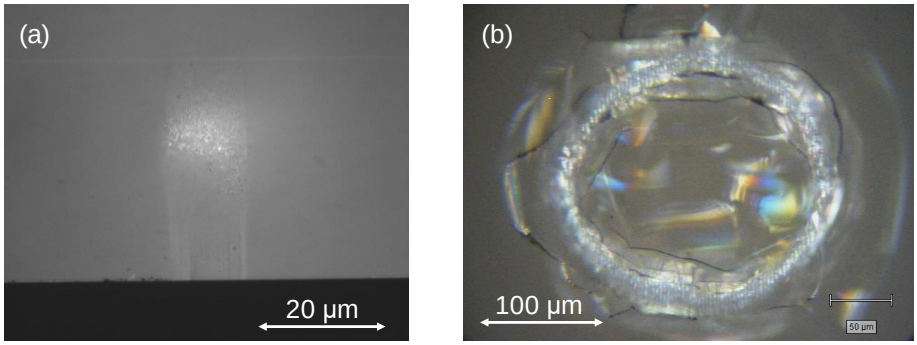

Figure 4.3. Microscope images of 3DLW waveguides in reflection in (a) fused silica and (b) quartz crystal.

4.2. Waveguide properties: mid-IR characterization

In this section, the guiding properties (near-field modes, index changes and waveguide losses) of 3DLW waveguides are studied using suitable mid-infrared optical setups and computer simulation tools.

4.2.1. Waveguiding setup description

The ability to confine and guide light in the mid-IR of the 3DLW waveguides together with their optical performance needs to be evaluated using a setup specifically designed for the characterization of waveguides at mid-IR wavelengths. Fundamentally, it consists of coupling laser light into one end of a

3DLW waveguide with the appropriate optic while imaging the other end with a lens and a camera.

As depicted in Figure 4.4, the launched mode field, which is usually Gaussian as the laser beam transversal profile, is focused onto the first waveguide facet and couples to the modes supported by the waveguide, inevitably undergoing a certain power loss. Ideally one wants to excite only waveguide's bound modes after the input optimization process (i.e. input NA and position). The coupled light then propagates through the waveguide until it reaches the waveguides second facet where it emerges again to the external air medium. A second lens images the waveguides output near-field onto an image sensor array (camera) which is highly sensitive to the working wavelength. By adjusting the output NA and the lens–camera distance one can control the image magnification.

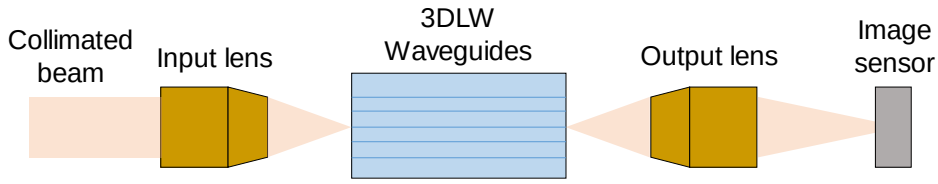

Figure 4.4. Simplified top view scheme of the waveguides characterization experiment: light excitation and output near-field imaging.

Figure 4.5 shows a sketch of the built setup for the free-space guiding configuration, which means that laser light propagates through the air from one element to the other, contrary to a fiber-coupled setup, later used. A pair of linearly polarized He-Ne lasers (REO) beams (λ = 1.52 µm and 3.39 µm, respectively) were alternatively routed through metallic mirrors to a set of three aligned optomechanical stages whose position was adjustable with micrometer accuracy. The first and third stage held the input and output optics, respectively. They could also hold other elements such as diaphragms or fiber clamps. The input/ouput lenses were aspheric so as to minimize aberrations, with moderately low NA at around 3.5 µm wavelength, and were made of IR transparent materials, specifically in chalcogenide (NA = 0.18, Thorlabs) and ZnSe (NA = 0.25, Innovation Photonics). Both types of lenses were used interchangeably at the

input or output depending on the particular NA and size of the analyzed 3DLW waveguide. The 3DLW photonic chip was held by the central stage which had angle adjustments to further optimize the coupling. After the third stage a semiconductor mid-IR camera (FLIR SC7000) which is sensitive from 1 to 5 μm wavelength was used to image the output facet of the chip. The spatial calibration of the captured images was carried out immediately after each group of measurements with calibration USAF patterns. Finally, mid-IR polarizers could be placed at the input and/or the output if necessary.

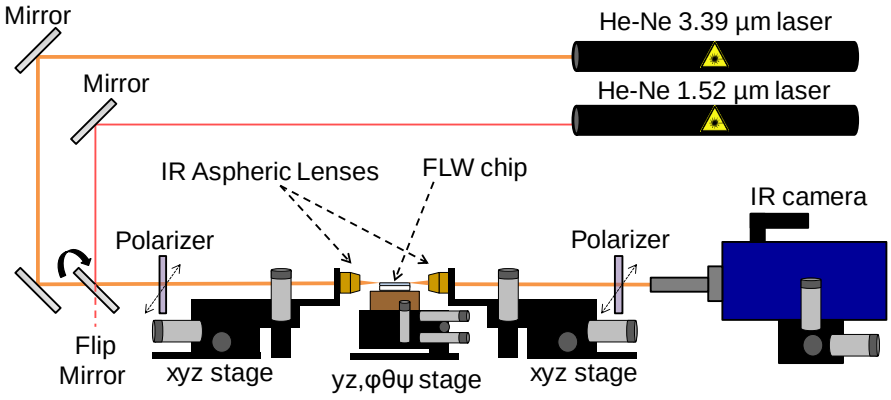

Figure 4.5. Free-space optical setup for IR waveguiding characterization.

A fibered configuration was also employed at the input stage as it is sketched in Figure 4.6. This setup helped when making the fiber to chip bonding in the integrated sensor development. For details about the mid-IR fiber preparation, bonding and packaging see Chapter 5, Section 5.2.2. A mid-IR interband cascade laser (ICL) emitting at λ = 3.68 μm was coupled to a ZBLAN IR fiber (Thorlabs), having 9 μm core size and 0.19 NA, whose output end was then butt-coupled to the corresponding waveguide under analysis. The rest of setup was the same as the free-space one. Note that it was possible to couple any of the lasers available to the fiber, not only the depicted ICL, as well as use the ICL in free-space mode.

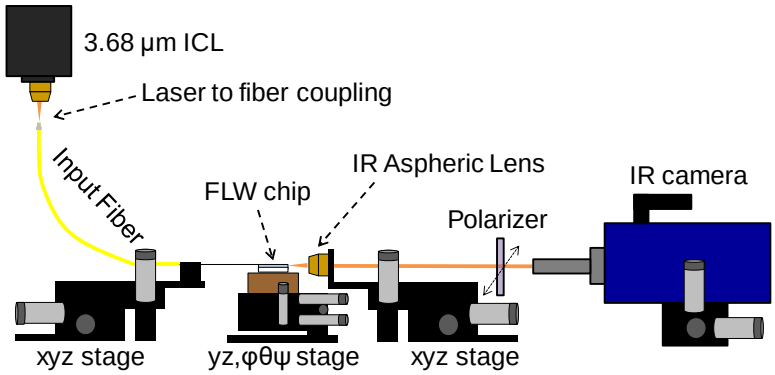

Figure 4.6. Fiber-coupled optical setup for IR waveguiding characterization.

4.2.2. Near-field analysis of fused silica waveguides

The modal analysis at mid-IR wavelengths of the Type I multiscan 3DLW sensing waveguides made in fused silica is presented below. The laser writing parameters were already provided in Chapter 3, Section 3.7.3, for the first and second set of waveguides. From now on they will be called low-contrast (LC) and high-contrast (HC), respectively, with regard to their refractive index change, which was estimated to be around $2 \cdot 10^{-3}$ and $9 \cdot 10^{-3}$, respectively (see Section 4.2.3 for the estimation method description).

A) Low-contrast fused silica waveguides

These LC were found to be single-mode in the 3 – 4 μm region in both width sizes (≈ 30 and 15 μm) as demonstrated in Figures 4.7(a) and (b), respectively. There an example of the measured near-field intensity output images of two waveguides is provided with the horizontal and vertical mode cross-section profiles. These profiles are normally enough to define the waveguides confinement through the evaluation the mode field diameters (MFD), which is taken at $1/e^2$ of the maximum intensity value.

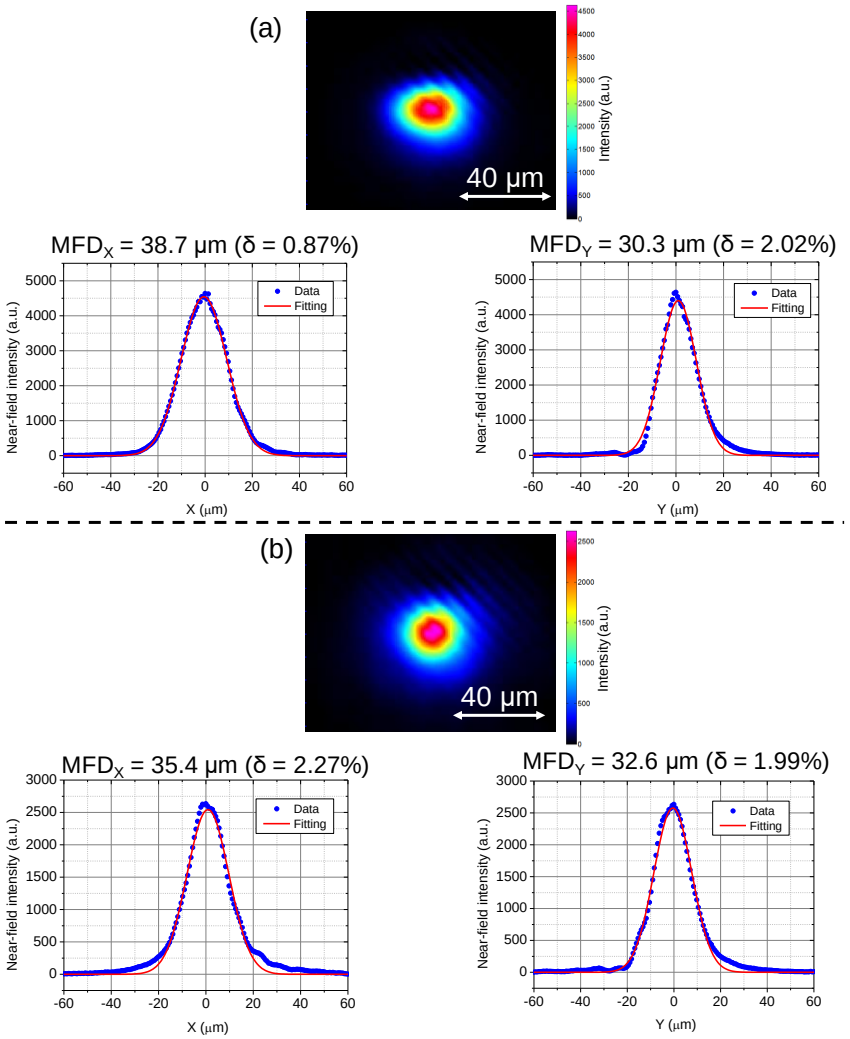

Figure 4.7. Measured output near-field at λ = 3.39 μm of a (a) 30 and (b) 15 μm LC waveguides. Horizontal and vertical profiles are depicted as well as their corresponding Gaussian fitting and the extracted MFD with the relative fitting error (δ).

Although the theoretical mode profile functions corresponding to channel waveguides are not Gaussian [1], one may find that a Gaussian fitting is still able to deliver a low fitting error (δ errors are shown in Figure 4.7) for the case of step-index rectangular core waveguides, as the ones fabricated in fused silica and Gorilla glass. It can be demonstrated that, from each one of the fitted Gaussian profiles, the associated MFD can be calculated as follows

$$MFD = 4\sigma \qquad \textit{Eq. 4.1}$$

where σ is the standard deviation of the corresponding Gaussian function which is defined as

$$I(x) = I_0 e^{-\frac{(x-\mu)^2}{2\sigma^2}} \qquad \textit{Eq. 4.2}$$

where I_0 is the maximum intensity, μ is the spatial point around which the function is centered (close to 0 μm in this case) and x is the horizontal spatial variable. For the vertical direction (y), the function is defined in the same way.

As mentioned in Chapter 3, variations on the laser writing parameters can strongly affect the morphology of the fabricated waveguides. This becomes evident in Figure 4.8(a), where it is shown the transmission microscope images of different waveguides (30 μm width) that were fabricated keeping the scan speed (SSp) at 8 mm/s and increasing pulse energy (E) from 0.45 to 0.51 μJ. The observed contrast of the core region growths for higher energies, which may indicate higher refractive index change, while at the same time a darker region starts to appear above it, which can be attributed the formation of nanocracks and nanogratings [2, 3] already at these energies.

Figures 4.8(b) and (c) show the evolution of the measured unpolarized MFD horizontal and vertical cross-sections at λ = 3.39 μm, respectively, with varying laser pulse energy and scan speed, of the 3DLW fused silica waveguides. As it can be noticed, the increase of the writing pulse energy has a major impact at fast scan speeds (8 mm/s), and low impact at medium-slow speeds (1 to 4 mm/s). Particularly, it produces a reduction in MFD, supporting the intuitive conclusion (already drawn before from Figure 4.8(a)) of increasing refractive index change for higher energies and fixed speed and core size, and within the short pulse energy range here studied (from 0.45 to 0.52 μJ). The MFD dependence on laser pulse energy for scan speed of 2 mm/s (Figure 4.8(d)) is seen to be particularly flat, this meaning that at that speed a laser photomodification stable regime is found where the induced index changes and feature sizes reach a local maximum for this energy regime. Finally, even though in all cases the observed dark area (nanogratings) becomes larger for higher energies, this is accompanied by a

generally larger guiding region as well, so that the effective core size is approximately maintained.

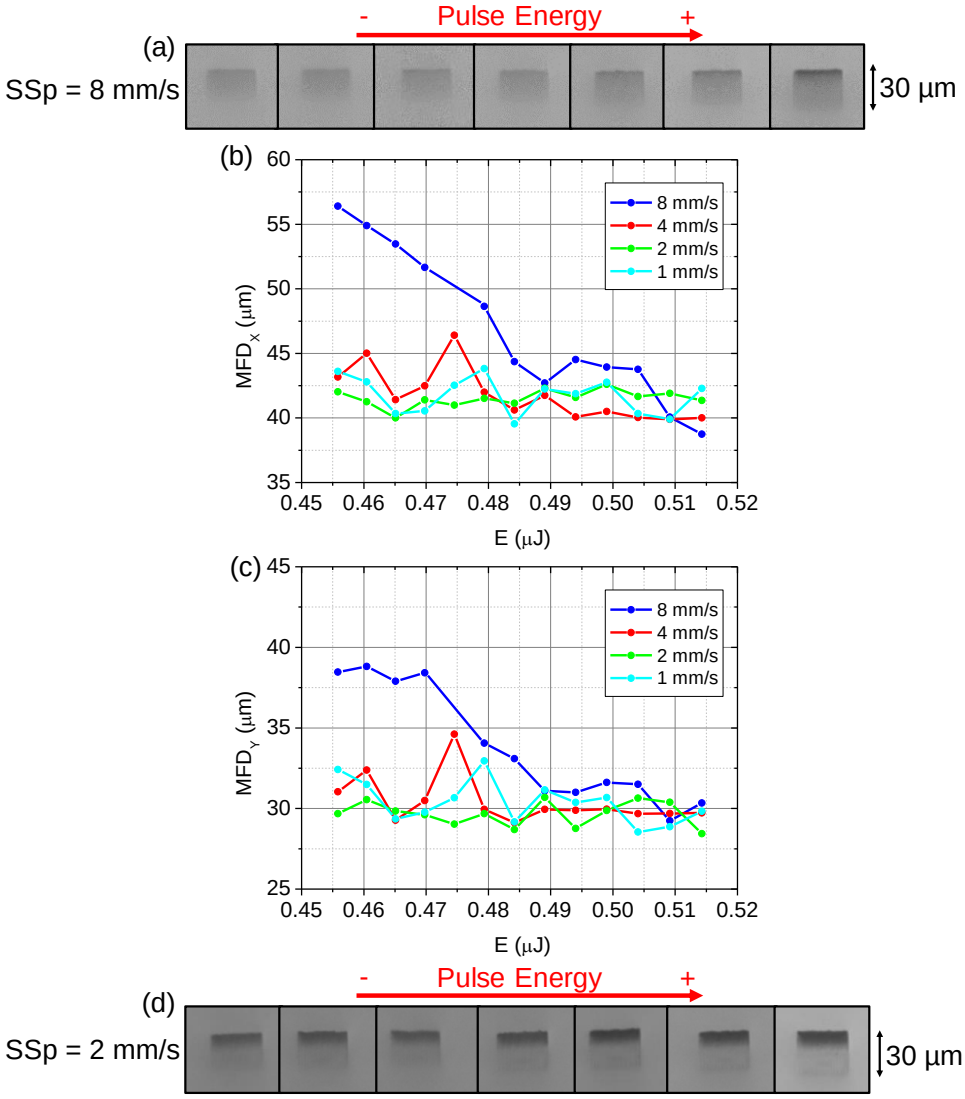

Figure 4.8. (a) Transmitted light microscope images of LC fused silica waveguides for SSp = 8 mm/s and increasing writing energy. (b, c) Evolution at $\lambda = 3.39$ µm of the horizontal and vertical MFDs, respectively, when varying the pulse energy and scan speed. (d) Same as (a) but for SSp = 2 mm/s.

B) High-contrast fused silica waveguides

By increasing the laser pulse energy above the 0.5 µJ range, a new regime of multiscan Type I HC waveguides in fused silica for the mid-IR range was found [4], as previously described at the end of Section 3.7.3 (fabrication parameters in Table 3.5 of Chapter 3). While keeping the scan speed at 1.5 mm/s, the higher laser pulse energy applied allowed for an increased material densification (see µ-Raman study below), thus leading to higher core index and improved light confinement. Another important milestone achieved was the ability to write waveguides 1.48 mm deep inside the bulk silica with similar optical performance, which demonstrates the 3D capability of the 3DLW fabrication technique. The low index of fused silica allows this deep laser writing as compared to other higher index optical materials, since it minimizes spherical aberration due to a minimized refractive index mismatch between air and glass.

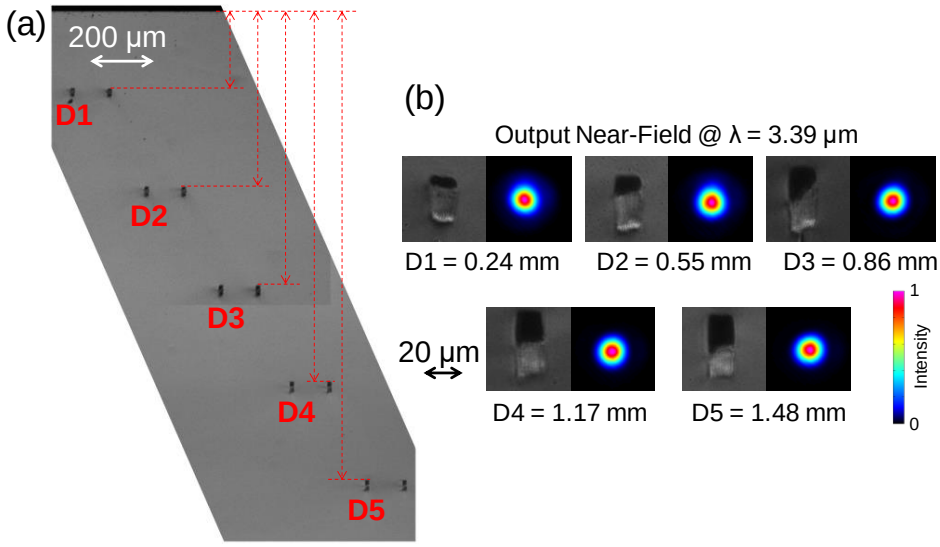

Figure 4.9. (a) Transmitted light microscope image of the HC 3DLW waveguides (0.8 µJ pulse energy) at different depths (D1 - D5) down to 1.48 mm. (b) Closer look of individual waveguides and their corresponding measured output near-field at λ = 3.39 µm.

Figure 4.9 clearly showcases the 3D capability of the fabrication technique together with the corresponding microscope images and experimental output

near-field profiles at λ = 3.39 µm. Note that, for a given pulse energy, the heavy variation of the core morphology (Figure 4.9(b)) when the fabrication depth is augmented does not affect significantly the output near-field especially in the vertical direction. Similarly, to the LC case, the elongation of the nanogratings area is accompanied by that of the guiding region as well. These variations are likely due to a combination of changes in the focusing conditions (i.e. optical aberrations and nonlinear pulse propagation effects) within the modified volume during the laser writing process [3]. For a spectroscopic analysis of the different modified regions of the laser written waveguides refer to Section 4.3.

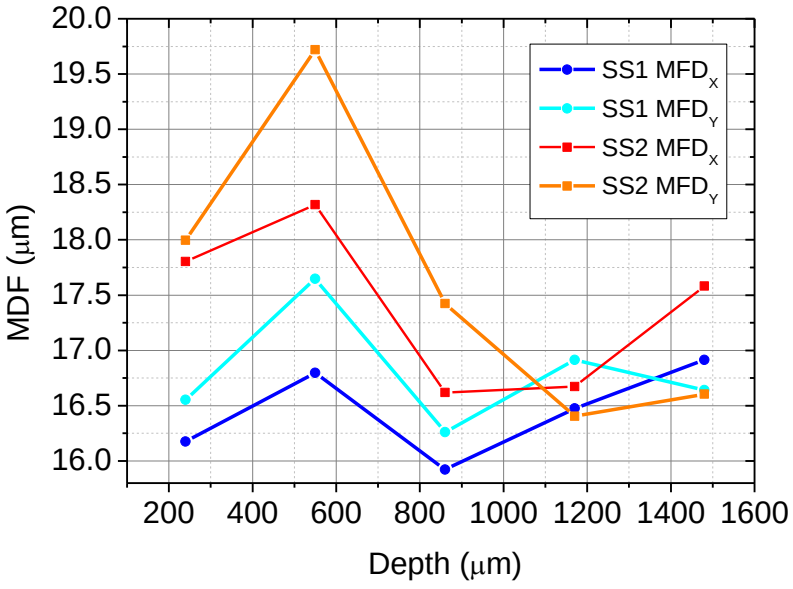

Figure 4.10. Measured vertical and horizontal MFDs at λ = 3.39 µm of HC waveguides for SS1 = 0.4 µm and SS2 = 0.8 µm and growing depth. Only waveguides corresponding to 0.8 µJ pulse energy are shown.

In 3DLW multiscan waveguides the scan separation parameter further determines the cumulative effects derived from laser scans irradiating a volume previously modified. Figure 4.10 shows the measured MFDs of the output near-field with increasing fabrication depth, for scan separations of 0.4 µm (SS1) and 0.8 µm (SS2). At first glance, an important improvement in light confinement can be observed when comparing these HC waveguides with the previous LC ones.

For instance, in absolute terms, the minimum mode field diameter products (MFD_X x MFD_Y) are $MFD_{LC,min}$ = 33.1 x 29.9 μm^2 (low contrast cores) against the $MFD_{HC,min}$ = 15.9 x 16.3 μm^2 (high contrast cores).

Although the number of scans were adjusted to obtain similar physical core widths, slight variations in them were still produced, as it can be observed. In general, the greater scan spacing (SS2) led to a larger MFD in both vertical and horizontal directions, at least for depths lower than ≈ 1 mm. Indeed, higher *SS* produces less cumulative interaction between light pulses and material so that material densification and thus increase of refractive index of the core region is reduced. Such variation of refractive index change will be addressed in Section 4.2.3. Regarding only the depth, one may notice variations in the MFD as the waveguide is written deeper inside the bulk. This is due to an interplay of optical aberrations and other effects in the 3DLW fabrication process, which cause change in the amount of material modification and the alteration of the size of the guiding region (see Figure 4.9(b)).

Of special interest are results for MFD of waveguides written at 1.2 mm depth (see Figure 4.10) and high pulse energy (0.8 μJ). At this focusing depth, multiscan waveguides fabricated with both 0.4 μm (SS1) and 0.8 μm scan spacing delivered approximately the same MFDs. This particular result has a direct application for writing Y-junction splitters with the multiscan writing technique, where the section before junction can be written with a given number N of scans, and the splitted waveguides can be smoothly written on the fly with N/2 scans without having to interrupt the fast laser writing at the Y-junction, which is important for achieving low-loss splitting transitions as first proved by Ródenas et al. [5]. Furthermore, since the focusing distance is so long (1.2 mm), large 3D waveguide architectures can be written within the silica glass bulk, far from the sample surface.

4.2.3. Indirect estimation of refractive index change

Having a good approximation of the waveguide 2D index profile is key to properly simulate the waveguide water-ice sensor (Chapter 2). Due to the lack of direct methods to measure the refractive index profiles at mid-IR wavelengths, an

estimation method involving numerical electromagnetic modal simulations and optical measurements was employed. The method encompassed the following steps.

1. The dimensions of the waveguide guiding region (core) were accurately measured from microscope images.
2. The MFDs at the desired wavelength of the output near-field were experimentally obtained as described in the previous chapter.
3. Multiple modal simulations were run using the physical dimensions found in step 1 as a fixed input, for an initial broad range of different refractive index changes (Δn).
4. The range of Δn was narrowed down according to the evaluation of the matching of the measured and simulated MFD.
5. Finally, the Δn providing the best match of the experimental and simulated MFD was chosen as the final estimation of index change.

Note that the waveguides were assumed to be single-mode and purely step-index, although the latter is just an approximation that might only hold for the horizontal direction. Moreover, the existence of the observed dark areas (nanogratings) above the waveguide cores was not taken into account when performing the experimental to theoretical matching. A precise μ-characterization of the waveguide morphology is performed with μ-spectroscopy tools in Section 4.3.2.

The used simulation software was RSoft BeamPROP, which is the same employed for the beam propagation method (BPM) simulations shown in Chapter 2. The iterative method for modes computation, which is based on the BPM, was employed because it is a fast, standardized and easy way to solve the modes of step-index channel waveguides [6].

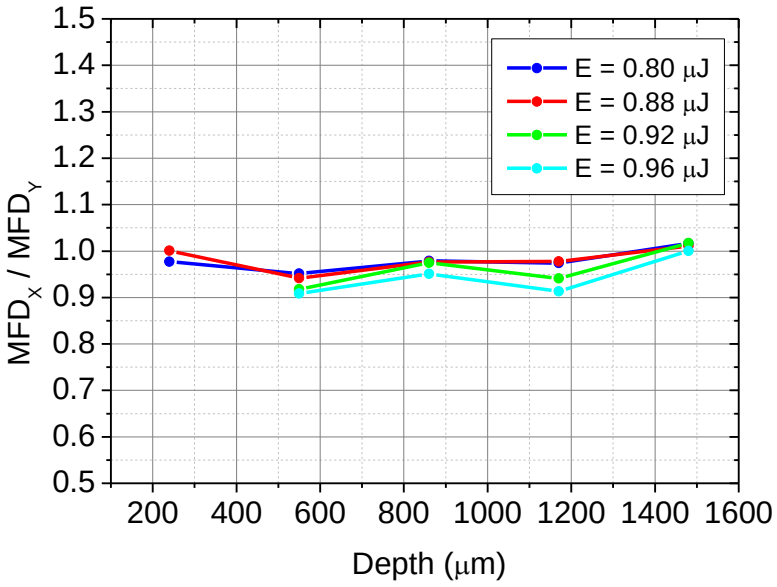

Figure 4.11. Ratio between horizontal and vertical MFDs at λ = 3.39 μm corresponding to the SS1 HC waveguides for all the fabrication pulse energies and depths (D1 – D5).

As the HC waveguides were the selected sensing waveguides, the index change estimation was performed systematically for all of them in order to get the most sensitive one (i.e. those with higher index contrast). Since it was not clear the physical extent of the core in the vertical direction (see Section 4.3.2 for detailed pictures and analysis), which in addition was varying for different depths, and because of the modes were highly symmetric, the core shape was approximated to a square. Such assumption is demonstrated in Figure 4.11, where the ratio of the horizontal and vertical MFDs is constantly close to unity. Note that although only the SS1 case is depicted (*SS* = 0.4 μm), the assumption is also valid for SS2 waveguides (*SS* = 0.8 μm). Furthermore, this core symmetry emphasizes the suitability of this type of waveguides for a fiber coupled device, as the one developed in this Thesis.

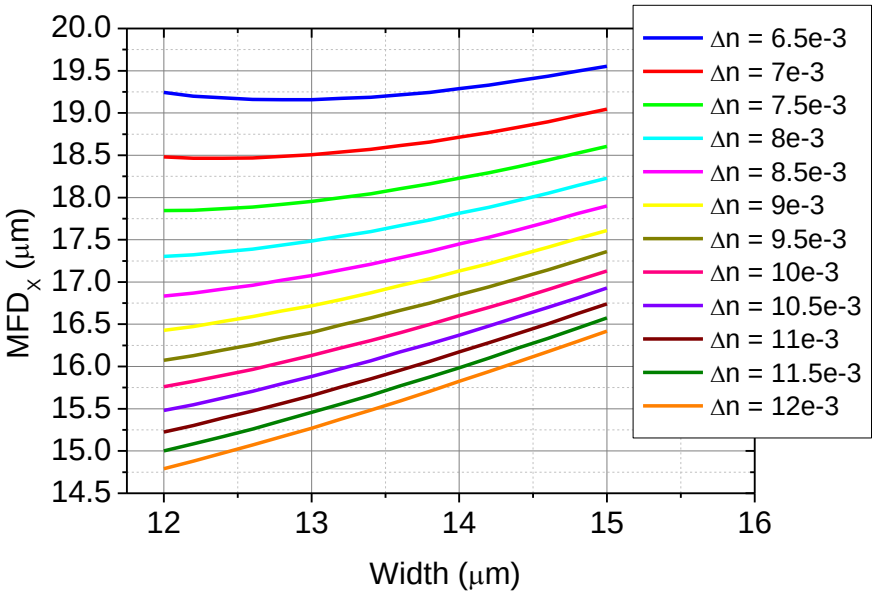

Figure 4.12. Simulated horizontal MFD (in this case equal to the vertical one) of a HC step-index square waveguide in fused silica for different widths and refractive index change (Δn) at λ = 3.39 μm.

Figure 4.12 shows the simulated MFD$_X$s, which in this case are equal to the MFD$_Y$s, for several selected Δn values and a specific short range of waveguide widths (from 12 to 15 μm). Using this graph allowed to straightforwardly find the Δn that made the simulated MFD to match the experimental one that had been measured previously together with the actual waveguide width. The maximum measured refractive index change was $\Delta n \approx 1 \cdot 10^{-2}$, which is a disruptive enhancement compared to the previously fabricated LC waveguides or to any other 3DLW multiscan waveguide in fused silica presented in the literature [7, 8]. Notice that there the given Δn values are only valid for visible or near-IR wavelengths, whereas here the estimated Δn are for the mid-IR range, for the first time to the author's knowledge. Regarding the estimation error, assuming that the main error source came from the width measurement of the waveguide, whose value was ε_W = 0.5 μm, the error in the estimated refractive index change became therefore $\varepsilon_{\Delta n} = 5 \cdot 10^{-4}$.

Figure 4.13 shows the variation of Δn against the waveguide fabrication depth for a couple of pulse energies (0.8 μJ and 0.96 μJ) and scan separations (SS1 and SS2). It is worth noting that for a given energy and scan separation the estimated Δn can vary as much as $2 \cdot 10^{-3}$ when writing deeper inside the bulk. As expected, smaller separation scan induced a larger effective index change but only up to some extent (Depth ≈< 1 mm). Similarly, higher pulse energies did not provide more contrasted waveguides except for the deepest ones.

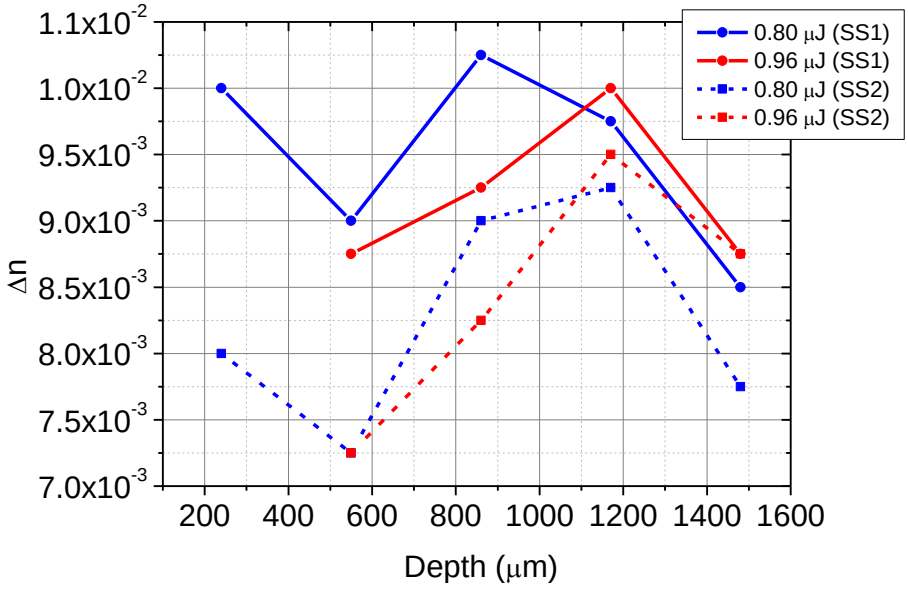

Figure 4.13. Estimated Δn at $\lambda = 3.39$ μm of HC waveguides as a function of the fabrication depth for two fabrication energies and scan separations (SS1 and SS2).

Generally, comparison with other 3DLW channel waveguides in terms of refractive index change is done by means of the refractive index contrast, which is defined as

$$C(\%) = 100 \cdot \frac{\Delta n}{n_0} \qquad \textit{Eq. 4.3}$$

where n_0 is the refractive index of the unmodified material which for fused silica is 1.4091 at $\lambda = 3.39$ μm, according to [9]. Taking the maximum estimated

refractive index change (≈$1 \cdot 10^{-2}$), the contrast of these HC waveguides is $\mathcal{C} \approx 0.71$ % at $\lambda = 3.39$ μm, which is superior to others 3DLW waveguides reported for the mid-IR range, such as those made in chalcogenide glass (≈ 0.55 %) [5] or borate crystals (0.29 %) [10].

4.2.4. Propagation loss measurements

Perhaps the most important figure of merit of optical waveguides is its propagation loss. Small propagation losses not only make integrated photonic devices more energy efficient by reducing the power requirements for sources and detectors but also improve their global performance in terms of signal to noise ratio (SNR). That is to say that for a given source power and total output noise of the system, the less propagation losses associated to the waveguide element, the more available free-noise signal at the output which contributes to less signal processing requirements and less output errors, namely bit error rate in communication devices or false alarms in sensors.

Direct methods for propagation loss measurements include destructive ones like the cut-back method, valid for single-mode and multimode waveguides, and interferometric methods, i.e. the Fabry-Pérot method valid only for single-mode waveguides [11]. The former was not applied for the present waveguides loss measurement because of the limited number of available samples; and the latter was discarded due to the low refractive index of fused silica which would have shrunk the eventual interference fringes involved in the experiment and hence would have made the loss measurement prone to large errors. Moreover, although the Fabry-Pérot method is common at telecommunication wavelengths (~ 1.55 μm), at mid-IR wavelengths the lack of high stability and low noise tunable sources makes it difficult to be applied.

The method employed consisted of the measurement of waveguide insertion losses, and of mode field diameters, for indirectly estimating the internal propagation losses. This method only requires the measurement of the input and output power of the waveguides, the launched laser mode field, the output near-field intensity profile of the waveguide, and the knowledge of the waveguide

effective refractive index. Since this method also entails propagation errors coming for the different measurements, the calculated values are taken as a first order approximation. The propagation losses in dB/cm are then calculated as

$$PL = \frac{-10\log\left(\frac{P_w}{P_{nw}C_1C_2}\right)}{L} \qquad \textit{Eq. 4.4}$$

where P_w is the power reaching the camera/detector when the waveguide is on the setup, P_{nw} is the power reaching the camera/detector when there is no waveguide, C_1 is a coefficient (0 to 1) accounting for the waveguide coupling losses, C_2 is a coefficient (0 to 1) accounting for out-coupling losses and L is the length of the waveguide in cm. C_1 encompasses firstly the Fresnel reflection factor at the input facet $(1-R)$, and secondly the mode coupling efficiency (η) between the launched laser mode and the waveguide's own mode, assuming that the waveguide is single-mode. On the other hand, C_1 only accounts for the Fresnel factor, since the used output lens numerical aperture (NA) is significantly larger than the waveguide's NA, and consequently no extra output coupling losses are considered in this case. Therefore, these two coefficients are expressed as follows

$$C_1 = (1-R)\eta \qquad C_2 = 1-R \qquad \textit{Eq. 4.5}$$

$$C_1C_2 = (1-R)^2\eta \qquad \textit{Eq. 4.6}$$

The reflectance R can be calculated by means of the corresponding Fresnel equation for normal incidence and assuming that the photonic chip is surrounded by air,

$$R = \left(\frac{1-n_{eff}}{1+n_{eff}}\right)^2 \qquad \textit{Eq. 4.7}$$

where n_{eff} is the effective refractive index of the excited mode, which is approximately the refractive index of the material ($n_{eff} \approx n_0$) due to the low index difference between the waveguide's core and the normal glass. The mode

coupling efficiency is calculated by the 2D normalized overlap integral of the complex transversal electric fields at the air-waveguide interface as follows

$$\eta = \frac{|\int \vec{E}_i^*(x,y)\vec{E}_w(x,y)dA|^2}{\int |\vec{E}_i(x,y)|^2 dA \int |\vec{E}_w(x,y)|^2 dA} \qquad \textit{Eq. 4.8}$$

where $\vec{E}_i$ is the launched electric field and $\vec{E}_w$ is the waveguide fundamental mode field. Although the formula involves complex field vectors, the calculation was carried out by considering scalar values since, experimentally, only intensity distributions were obtained with no phase nor polarization information. Therefore,

$$E_i(x,y) \approx \sqrt{I_i(x,y)} \quad \text{and} \quad E_w(x,y) \approx \sqrt{I_w(x,y)} \qquad \textit{Eq. 4.9}$$

where I_i is the measured input intensity distribution and I_w is the measured waveguide output intensity distribution.

For improved accuracy in the losses calculation, orthogonal polarizations (TE and TM) should have been treated separately so as to obtain the propagation losses corresponding to each polarization. Nevertheless, as it will be addressed in Section 4.2.5, the waveguides are inherently birefringent which promotes rotation of the polarization at the waveguide output when the launched light is not perfectly aligned with the corresponding optical axis. Hence, only the proper control of the light polarization implemented in the guiding setup can guarantee reliable polarized measurements. As this was not the case, the calculated propagation losses are considered an average of those produced for each one of the polarizations.

Figure 4.14 shows the calculated propagation losses at λ = 3.39 μm through Equation 4.4 for each one of the HC waveguides written using the minimum pulse energy (i.e. 0.8 μJ). Apart from the deviated value found for D2 depth and SS1 scan separation, the propagation losses appear to be quite constant for all the depths and scan separations. The minimum measured propagation loss is 1.33 dB/cm for the waveguide at D4 (1170 μm).

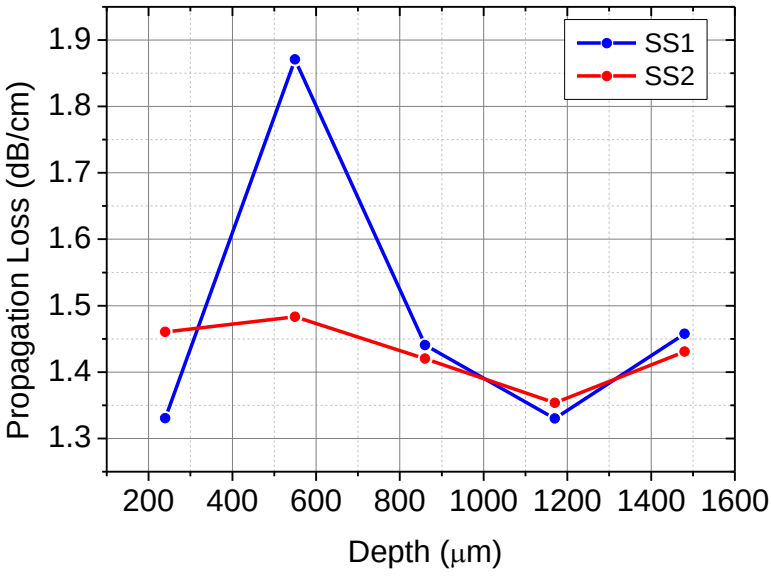

Figure 4.14. Experimental propagation losses of the HC waveguides for all the depths (D1 – D5) at λ = 3.39 μm fabricated with 0.8 μJ pulse energy and both scan separations (SS1 and SS2).

The losses were also measured close to the intrinsic limit of transparency of fused silica. To do so, the ICL emitting at 3.68 μm was employed instead of the He-Ne laser. Repeating exactly the same procedure, an increment of about 5 dB/cm was measured at this longer wavelength with respect to the shorter one. This can be also observed in Figure 4.15, where it has been compared the internal loss of the fused silica bulk with a pair of measured propagation loss points, corresponding to a D4 waveguide, at λ = 3.39 μm and 3.68 μm, respectively. Furthermore, by using the previous set of data, the waveguide propagation loss spectrum can be extrapolated (dashed cyan line in Figure 4.15). Note an average increase of about 1 dB/cm of the waveguide propagation loss over the bulk internal loss. This loss figure can be associated to scattering-induced losses due to e.g. defects or material inhomogeneities produced in the 3DLW fabrication process, whereas the rest is due to the material intrinsic absorption.

Lastly, together with the estimated high refractive index change (see Section 4.2.3), the relatively low propagation losses at $\lambda \approx 3.4$ μm makes these 3DLW

waveguides a robust platform for the surface sensor. What is more, still at the higher limit of material transparency the propagation losses are below 10 dB/cm, which means that a sensor working at these wavelengths is still feasible for short but sensitive interaction lengths (refer to Chapter 2 for engineering aspects of the sensor).

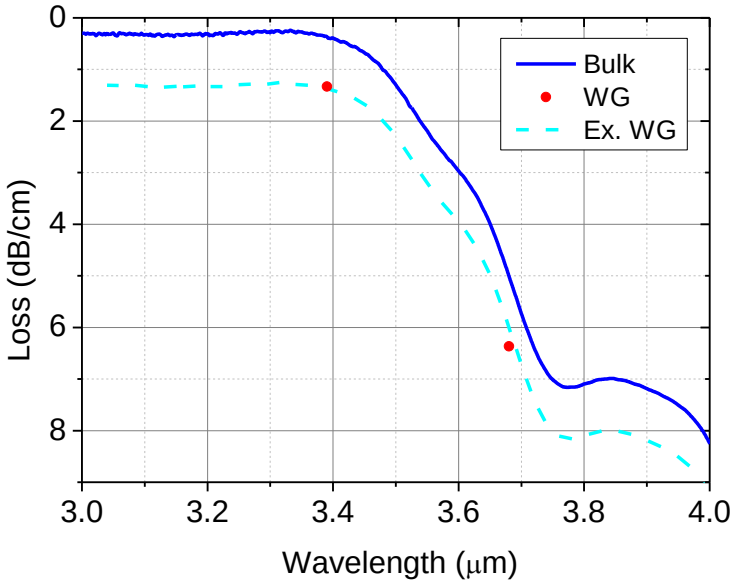

Figure 4.15. Comparison of the bulk fused silica internal loss and the HC waveguide propagation loss in the 3 - 4 μm mid-IR range (two experimental points in red and spectrum extrapolation in cyan).

4.2.5. Remarks about the waveguides birefringence

In all the previous sections, the possible birefringence (i.e. each one of the orthogonally polarized modes travelling at slightly different speed through the waveguide) of the 3DLW silica waveguides have been neglected. There are two main reason for this. Firstly, as it was mentioned in Chapter 2, the sensor performance did not depend on the polarization state of the launched light. Moreover, it was experimentally observed that the near-field output did not measurably change its shape when rotating the output polarizer placed before

the camera (Figure 4.5). Secondly, even in the case that the polarization would have influenced the sensor performance, the excitation and the interrogation of the sensing waveguide in the final device was done by means of optical IR fibers. The employed fibers were not polarization-maintaining fibers which entails that the polarization of the light coupled to the waveguide could not be controlled due to, for instance, random bend-induced mechanical stress producing optical birefringence [12].

In any case, the main cause of the waveguides birefringence is considered to be the darker area (nanogratings) above the guiding region (see Figures 4.2, 4.8 and 4.9). The birefringence nature of these laser induced nanostructures has been widely studied [13-15] and actually can have applications beyond integrated photonics [16]. As it was reported in [15], the presence of these nanogratings in close proximity to the guiding area directly affects the propagation characteristics of the modes by altering their effective refractive index and hence their phase velocity differently for each one of the polarizations, thus giving rise to birefringence.

4.3. Origin of refractive index change: μ-Raman and μ-Photoluminescence characterization

Normal microscope observation of the 3DLW waveguides together with their output near-field analysis and mode simulations are tools that when combined can provide a good estimation of the refractive index profile, as it has been shown in previous sections. From an exclusively engineering and practical point of view this is normally sufficient to fully characterize the fabricated waveguides in order to eventually integrate them into more complex devices. However, from a more fundamental perspective one often needs to know in-depth details about the local structural changes that the lattice has suffered. Studying the origin of the refractive index increase/decrease allows to understand the limitations of these type of 3DLW waveguides (i.e. maximum achievable index change, anisotropy, absorption), while at the same time provides hints for further tuning of their properties at will.

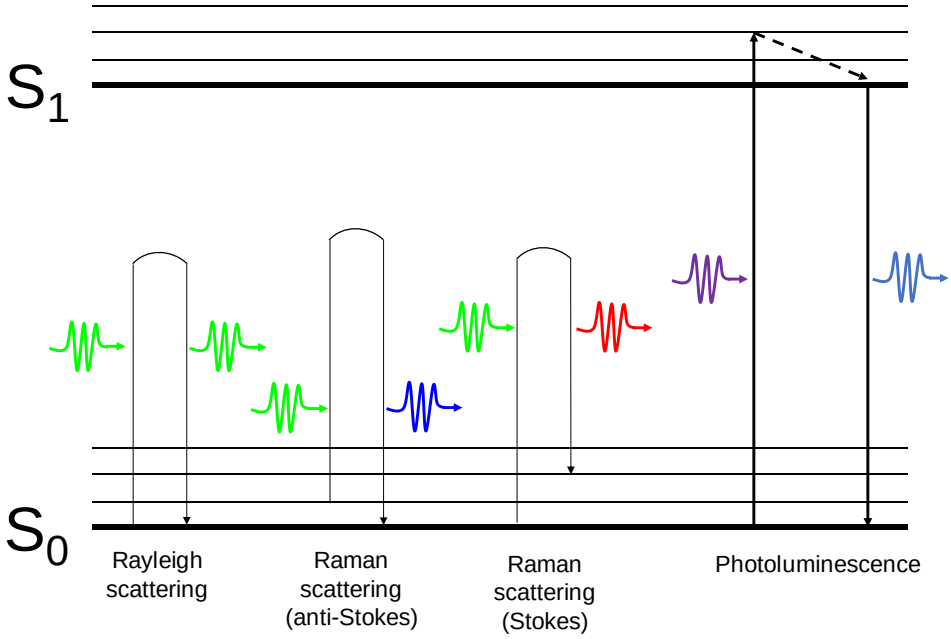

Figure 4.16. Different electronic energy transfer processes involving light emission when a photon reaches a hypothetical dielectric material: Rayleigh (elastic) and Raman (inelastic) scattering and photoluminescence (absorption, non-radiative and radiative relaxation).

4.3.1. Background

A common non-destructive optical technique used to investigate the structure of materials and their composition is Raman spectroscopy. The Raman effect is very weak: approximately only one photon out of a million (0.0001 %) will scatter at a wavelength slightly shifted from the original wavelength. This shifting, which can be either positive (scattered photon has more energy [anti-Stokes]) or negative (scattered photon has less energy [Stokes]) (see Figure 4.16), is due to the interaction of the photons with the discrete vibrational modes of the material molecules and/or bonds (i.e. the available lattice phonons modes) which are inherently linked to its atomic structure. Hence, Raman spectroscopy is a powerful tool to study the material micro-modifications which are induced by tightly focused femtosecond laser pulses.

Another popular spectroscopic method to investigate the material's structure is photoluminescence, which encompasses fluorescence (*fast* luminescence) and phosphorescence (*slow* luminescence). In contrast with Raman scattering, this effect is typically very efficient and involves the absorption of photons through the promotion of electrons to an excited energy state (see Figure 4.16). After a certain time (from femto to milliseconds) the excited electrons will return to a relaxed state emitting new photons with a wavelength corresponding to the electronic energy transition. In ion doped laser materials photoluminescence spectral analysis is employed to identify the absorption and emission bands of the dopant laser ions. If these materials are structurally photo-modified by focused femtosecond laser pulses, the luminescence associated with the doping ions will likely be modified as well, due to the induced lattice changes. Additionally, femtosecond laser pulses can create color centers or vacancy defects which introduce new energy levels, thus even if the material is not doped with luminescent or laser ions, finding luminescent lattice defects and studying their nature is proven to be useful to understand the origin of the refractive index changes induced by such ultrafast pulses.

The commercial setup employed to collect both Raman and photoluminescence data of 3DLW waveguides is the inVia Raman Microscope (Renishaw, Figure 4.17). It consists of a confocal microscope coupled to external lasers for Raman/photoluminescence excitation and to a spectrometer, based on a monochromator, that spectrally resolves the backscattered or emitted photons from the objective focal volume. Suitable optical filters are required to filter out the Rayleigh scattering and, in case of Raman measurements, the possible photoluminescence. For an exhaustive and general description of Raman optical setup and hardware as well as deeper insight into the Raman physics refer to the broad literature available on the topic like, for instance, [17] and [18].

Figure 4.17. Commercial inVia Raman Microscope used for Raman and photoluminescence characterization of 3DLW waveguides.

4.3.2. Spectroscopic analysis of a 3DLW waveguide

Next, a thorough spectroscopic analysis (photoluminescence and Raman) of a fused silica HC 3DLW multiscan waveguide is provided in order to gain understanding of the structural and electronic changes induced by the ultrafast laser pulses. The specific selected waveguide was fabricated using 0.8 µJ pulse energy and SS1 = 0.4 µm at 550 µm of depth. Figure 4.18 shows detailed micrographs of the chosen waveguide taken from an optical microscope and a scanning electron microscope (SEM). The waveguide facet was polished to optical quality so that a flat smooth surface was available showing the microfabricated waveguide cross-section.

Two kind of SEM images were recorded. Firstly, the common secondary electrons (SE) image (Figure 4.18(b)), corresponding to low energy inelastically scattered electrons and typically used for surface topography evaluation due to the small penetration depth (or emission volume beneath surface) of SE signal; and, secondly, the backscattered electrons (BSE) image (Figure 4.18(c)), corresponding to high energy elastically scattered electrons, which has a larger penetration depth and when using a monocompound homogeneous material,

such as SiO_2 glass, can be associated with local density changes (brighter areas corresponding to an effective higher density and darker areas to a reduced density).

From the comparison between visible light optical transmission, SE-SEM and BSE-SEM images, one can therefore clearly distinguish up to three different types of laser modified zones which are labeled in Figure 4.18(a). Two of them (Zones I and I*) consist of an area of refractive index increase (Type I modification), in which light guiding can occur as mentioned in previous sections, and which configures the waveguide core. The greater brightness of this regions seen in the BSE image therefore indicates that in principle, the primary mechanism of index increase is most probably glass densification [4]. Such a local densification could happen as a result of the fast local heating and melting of these volumes due to the femtosecond laser pulses localized ionization, which is followed by a fast cooling of the volume, which produces a silica glass with a higher density than the surrounding un-irradiated one.

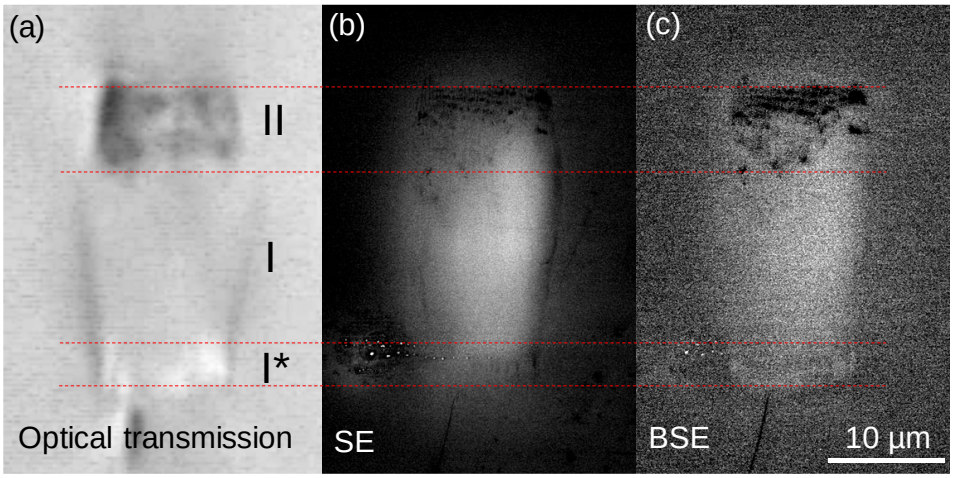

Figure 4.18. Cross-section images of the HC waveguide under spectroscopic characterization (energy 0.8 µJ and depth 550 µm). (a) Optical microscope transmission image, and SEM images: (b) secondary electrons and (c) back-scattered electrons.

On the other hand, above this guiding region a dark volume in all three types of images depicts a region where the glass has been damaged to the extent that light is strongly scattered, and the density is locally lowered with a complex nanostructured morphology (Zone II). The effective refractive index in this region is therefore assumed to be lowered, as a first order effective material approximation for waveguide simulation means. There is a very extensive literature on the study of these nanostructured damages zones, in which in some cases highly ordered nanogratings formation has been reported to occur [3, 19].

4.3.2.1. μ-Photoluminescence analysis

The different types of optical defects present on crystals and glasses give rise to varying photoluminescence spectrums. In the particular case of fused silica, the most commonly analyzed centers in the literature and those dominating the visible and near-IR photoluminescence of femtosecond laser irradiated silica are oxygen deficiency centers (ODC) and nonbridging oxygen hole centers (NBOHC) [20]. Both of these defects are induced by high intensity focused femtosecond pulses that produce bond breaking (via exciton trapping [19]) leading to either oxygen deficient or oxygen excess centers, respectively. A structural model of the characteristic tetrahedron (SiO_4) network of silica glass, as well as of ODC and NBOHC defects, is depicted in Figure 4.19(c), (d) and (e), respectively.

The recorded photoluminescence spectrums of the HC 3DLW waveguide under analysis for two different excitation wavelengths (514 and 532 nm) are also presented in Figures 4.19(a) and (b), respectively, together with deconvoluted emission band functions associated to the aforementioned defects, following previous bibliography [19]. In both cases, the Raman signal (note arrows in the graphs) is strongly masked by an intense photoluminescence which means that longer excitation wavelengths are needed to obtain a neat Raman spectrum free of luminescence background (Section 4.3.2.2). For each excitation wavelength, the emission was recorded at one spatial point within the guiding volume (Zone I), as well as far outside the modified structure for comparison purposes between the waveguide core material and un-irradiated glass.

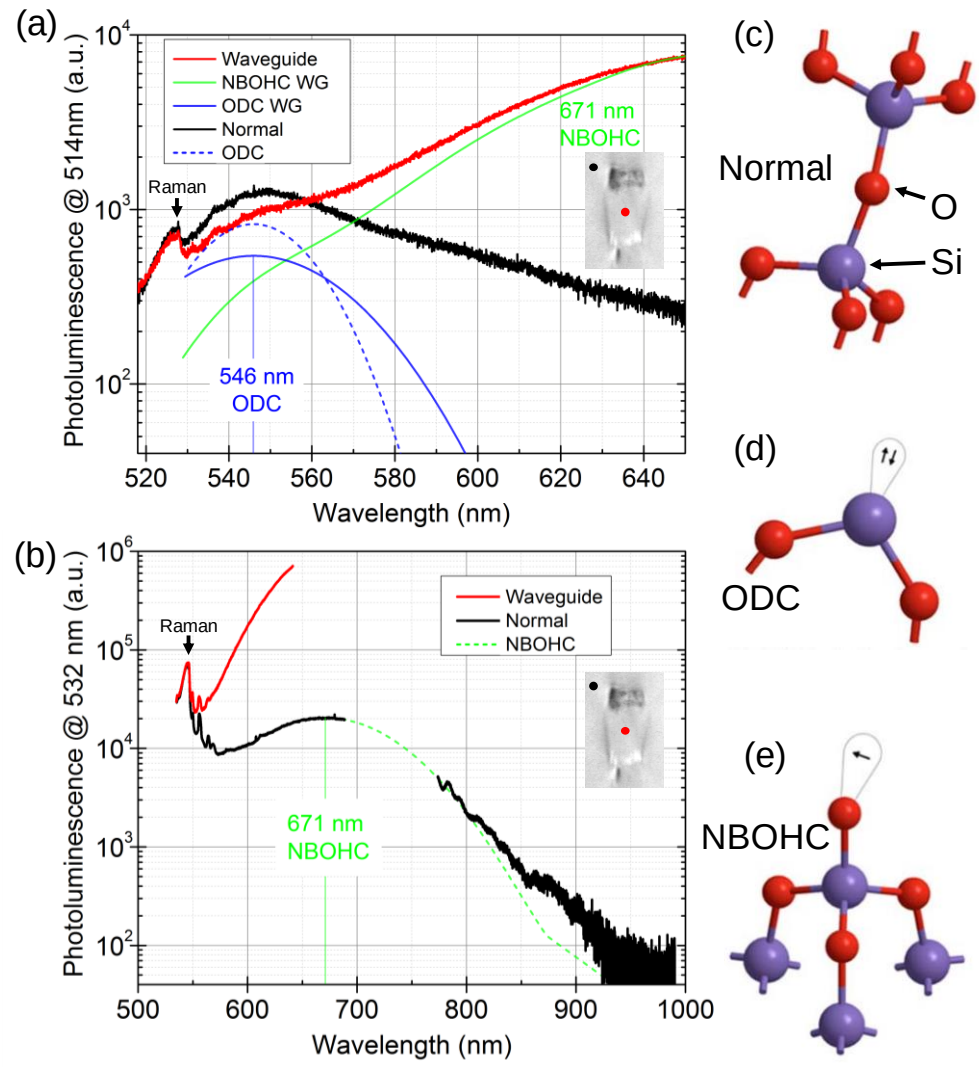

Figure 4.19. 3DLW silica waveguide photoluminescence excited at (a) 514 nm and (b) 532 nm. Red lines represent the modified core region (Zone I) whereas black lines are unmodified cladding surrounding. Deconvolved curves corresponding to relevant defects are also indicated on the graphs. Moreover, structural models (adapted from [20]) of (c) unmodified silica, (d) ODC and (e) NBOHC are depicted.

When exciting at 514 nm (Figure 4.19(a)), luminescence associated to ODCs (blue lines) is observed around 546 nm in both areas but not as strong as reported in [3], likely because ODC centers have an absorption peak at shorter

wavelengths (not available in the used setup). More importantly, the luminescence associated to NBOHC (671 nm, green line) is very clear in Zone I (waveguide core) which is in line with other works [3, 19, 20]. If the excitation is switched to the slightly longer wavelength of 532 nm (Figure 4.19(b)), the NBOHC emission is more efficiently excited and recorded, and it is seen to be almost two orders of magnitude higher in the waveguide core (Zone I) than in un-irradiated glass. Since NBOHCs background emission from the unmodified silica is also observed (straight green line) when exciting at 532 nm, we can conclude that a very small residual quantity of NBOHC defects is present in Suprasil 300 fused silica glass, and as a result of the 3DLW waveguide fabrication process the new glass structure in the waveguide core (Zone I) features a high density of NBOHC defects. Due to this, it could be concluded that the presence of NBOHC defects could also originate the refractive index increase which forms the waveguide. However, since the refractive index increments studied in this work correspond to the mid-IR (~ 3.5 μm wavelength) and not to the visible range (where these defects modify the susceptibility of the material), this assumption could be inaccurate.

With the aim of investigating this, the waveguides were submitted to a series of annealing steps, and the spatial distribution and emission intensity of NBOHCs was monitored for each step. The waveguides were also characterized in the optical guiding setup to evaluate their guiding characteristics, so that a direct prove of the increased index of refraction is obtained also, for each different annealing step.

Taking advantage of the μ-mapping technique, high resolution spatially resolved photoluminescence maps of the HC waveguide were obtained. Particularly, for each spatial point the peak intensity of the emission band associated to NBOHC centers was monitored (i.e. around 670 nm) and imaged (see Figure 4.20(a)). Additionally, the map was recorded two more times after subsequent one hour thermal annealings of the sample at 200 ºC and 400 ºC (Figures 4.20(b) and (c), respectively, in order to visualize possible variations of the defects with temperature [19]. Indeed, removal and creation of NBOHC defects from Zones I and I*, and Zone II, respectively, after each annealing process, took place as

Figures 4.20(a), (b) and (c) demonstrate. Note that a color scale has been used for the three maps, but the intensity maximum is different in each one of the three cases. To show these emission variations between annealing steps in a clearer way, a vertical cross-section of the emission map across the center of the waveguide is shown in Figure 4.20(d), where it is clearly noticeable the increase in NBOHCs emission in Zone II with respect to the other two areas.

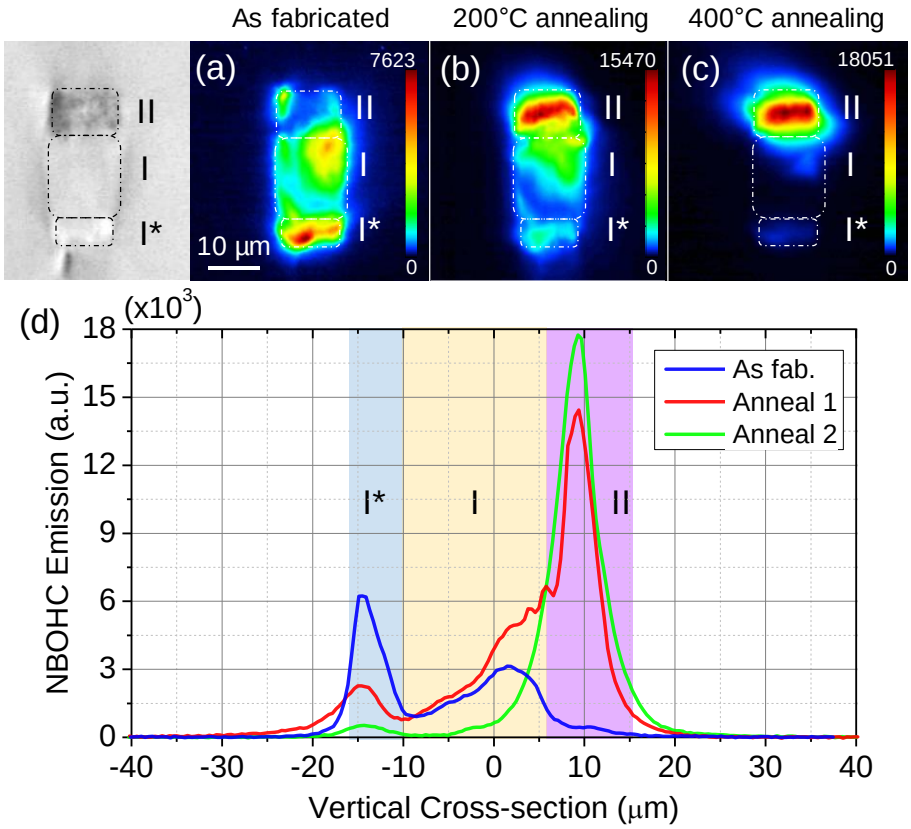

Figure 4.20. NBOHC luminescence (integrated area) µ-mapping of a HC 3DLW waveguide. (a) As fabricated waveguide, (b) after a 200 ºC annealing and (c) after a subsequent 400 ºC annealing. (d) Vertical cross-section of the previous µ-maps with indication of the different modified zones (I, I and II).*

Focusing only on the guiding region (Zone I), following the first annealing, the NBOHCs emission increases towards Zone II, whereas after the second one, it is almost erased, except close to Zone II. All these spatial variations in the µ-

maps suggest a complex rearrangement of the silica matrix after the heat treatment as pointed out in [19]. The removal of the NBOHCs in the positive index area was reported already in [19, 20] and [21], although in the latter, the annealing effect was effectively achieved by increasing the laser repetition rate producing heat accumulation effects.

Finally, it was checked if whether the waveguides kept the mid-IR confinement properties intact after the annealings. The result was positive with only an average decrease of the estimated index change of about $0.6 \cdot 10^{-3}$ at λ = 3.39 μm. Therefore, it can be concluded that the presence of NBOHC defects is not the origin of the mid-IR refractive index changes responsible for waveguide creation. Overall densification, as previously discussed at the light of BSE-SEM images, seems to be the cause of the index increase at the mid-IR wavelengths.

4.3.2.2 μ-Raman analysis

The spectroscopic Raman analysis of the 3DLW silica waveguide was carried out so as to evaluate the phonon network changes produced by the ultrafast laser irradiation and provide further evidences of the fundamental refractive index increase mechanism. As previously done in the photoluminescence experiments, firstly the Raman signal was recorded at individual points inside and outside the waveguide core (Zone I) to evaluate the local changes in the phonon modes of the glass. The employed excitation wavelength for Raman measurement was 785 nm, so that background luminescence was avoided and, as a result, neat Raman spectrums could be recorded.

Figure 4.21(a) shows the measured μ-Raman spectrums of un-irradiated glass (black spectrum) and waveguide core glass (red). Labelling of the different well-known phonons of the SiO_2 silica glass network are included following previous bibliography [22]. The different energies of these phonons are intrinsically linked to the particular way in which Si and O atoms are bonded to each other in the glassy network (e.g. bond angle and length). The characteristic SiO_4 tetrahedron basic structure of fused silica is not perfectly repeated itself in the volume of the material, like it would do in a crystalline lattice. In contrast, it is randomly

organized in the form oxygen rings [23], which are known as *n*-fold rings, where *n* is the order of the ring. Each one of these rings is characterized by a slightly different angle formed by the Si and O atoms which, in turn, determines the type of motion of the atoms and its frequency. In Figure 4.21(b), rings of different order (5, 4 and 3-fold) which are formed in the silica glass network are depicted so that one can observe that the ring order directly determines the bond angles and the size of the ring. Obviously, these angles are not deterministic but follow a given statistic which produces the measured phonon peaks associated to ring vibrations to be characteristically wide, as it is seen in Figure 4.21(a). Further detailed explanation of the dynamics involved in each one the measured vibrational modes of silica and in general of tetrahedral glasses can be found elsewhere [24].

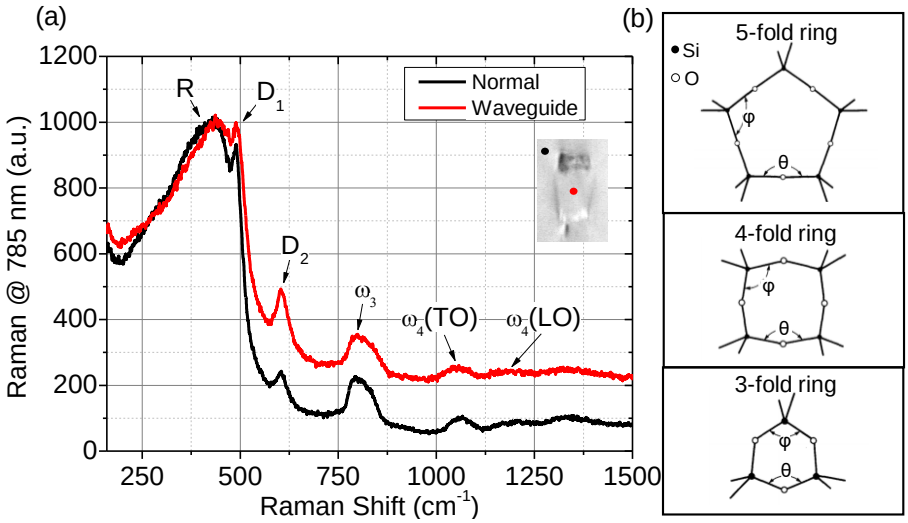

Figure 4.21. (a) Measured Raman Spectrum of a HC 3DLW silica waveguide: unmodified glass (black line) and core (red line). (b) Examples of 5-fold, 4-fold and 3-fold rings formed in silica with the bonding angles indicated (adapted from [25]).

In the particular case of the fabricated fused silica 3DLW waveguides, the relevant phonon modes are D_1 (≈ 495 cm^{-1}) and D_2 (≈ 606 cm^{-1}), which are associated to 4-fold [22] and 3-fold rings [25], respectively. Compared to the large low-energy phonon mode (R), these two modes are significantly narrow, which is attributed to the presence of highly regular rings [26] within the glass network,

and to the fact that their vibrations are independent of the rest of the lattice. Furthermore, it was demonstrated in [27] that the increase of the intensity of D_1 and D_2 peaks stems from an increased fictive temperature[1] (in the order of 1000's of ºC) of the material and, at the same time, a reduction of the Si-O-Si bridging angle which implies the formation of 4-fold and 3-fold rings. As a consequence, the region of the material with increased fictive temperature possesses a higher density, and therefore an increase in the intensity of D_1 and D_2 phonons would be expected following the previous assumption of an increased glass density at the waveguide core. Indeed, the measured Raman spectrum of the waveguide core region (red line) presented in Figure 4.21(a), shows that both D_1 and D_2 phonon modes have a greater intensity, thus confirming the glass densification first observed by the BSE image (Figure 4.18). In turn, the denser region leads to an increased refractive index volume which is ultimately responsible for the waveguiding effect. In fact, most of the published literature about ultrafast modification of fused silica point out the increase of the fictive temperature of the laser irradiated volume as the cause for densification and refractive index increase [3, 8, 20, 21]. However, the μ-luminescence and μ-Raman data here reported is the first to the author's knowledge reporting these effects in multiscan waveguides, and also the very high level of index increase, and therefore degree of densification, had not been previously observed.

Lastly, as it was done in the photoluminescence experiments, spatially resolved μ-Raman maps of the waveguide cross-section were recorded. For each point a complete Raman spectrum was obtained so as to generate a group of maps for each of the deconvolved phonon modes (phonon peak integrated area, peak intensity, energy shift and full width at half maximum FWHM). Figures 4.22(a-i) show these maps which analyze the spatial distribution over the waveguide surface of the R, D_1, D_2 and A_g phonons. The latter is a new phonon observed at Zone II, and which has been never reported before in SiO_2 glass to the author's knowledge.

[1] According to [27], fictive temperature is defined as a higher temperature at which SiO_2 is allowed to reach an equilibrium state before a rapid quench to room temperature.

In Figure 4.22(j), point Raman spectrums in the range from 350 cm^{-1} to 750 cm^{-1} corresponding to the different waveguide zones (Zones I, I*, II and unmodified cladding) are depicted. In general, both Zones I and I* have an increased Raman intensity of the broad R phonon, and D_1 and D_2 rings, whereas Zone II (nanogratings zone) presents a remarkably different and complex behavior.

The R phonon mode losses intensity significantly (around 26 %) within the nanostructured Zone II (Figure 4.22(a)) which may support the idea that fundamental network changes through the creation of multiple types of defects occur. Furthermore, as aforementioned, around 707 cm^{-1} (Figure 4.22(j)) a narrow crystal-like (FWHM = 13.5 cm^{-1}) A_g phonon mode arises, which might be associated to the Si-O-Si bending vibration found in Jadeite crystal ($NaAlSi_2O_6$) at 705 cm^{-1} [28, 29]. This further confirms the strong structural transformations happening in Zone II, which most probably present a very rich and complex structure at the nanometric level, thus going beyond the scope of the present study.

Figures 4.22(b-h) show the μ-Raman maps corresponding to the D_1 and D_2 ring phonon modes. Zone I and, particularly, Zone I* show an elevated integrated area of both modes (meaning material densification as explained before) together with a blue-shift in the phonon energy (Figures 4.22(g) and (h)). Zone II also follows such trends, but in the map corresponding to the ratio of the integrated areas of D_1 and D_2 (Figure 4.22(d)), the Zone II presents a higher value (≈ 3) than Zones I and I* (> 1.85). This ratio could be good indicator of the higher material densification in Zones I and I* and, hence, of the sign of the refractive index change, either negative (Zone II) or positive (Zones I and I*). Consequently, this ratio is a simple but effective way to reveal microstructural changes in the SiO2 matrix. Note, however, that especial care must be taken when performing the spectrum deconvolution since the peak associated to the R phonon has a very high influence on the D_1 and D_2 peaks and this could cause errors in their estimation.

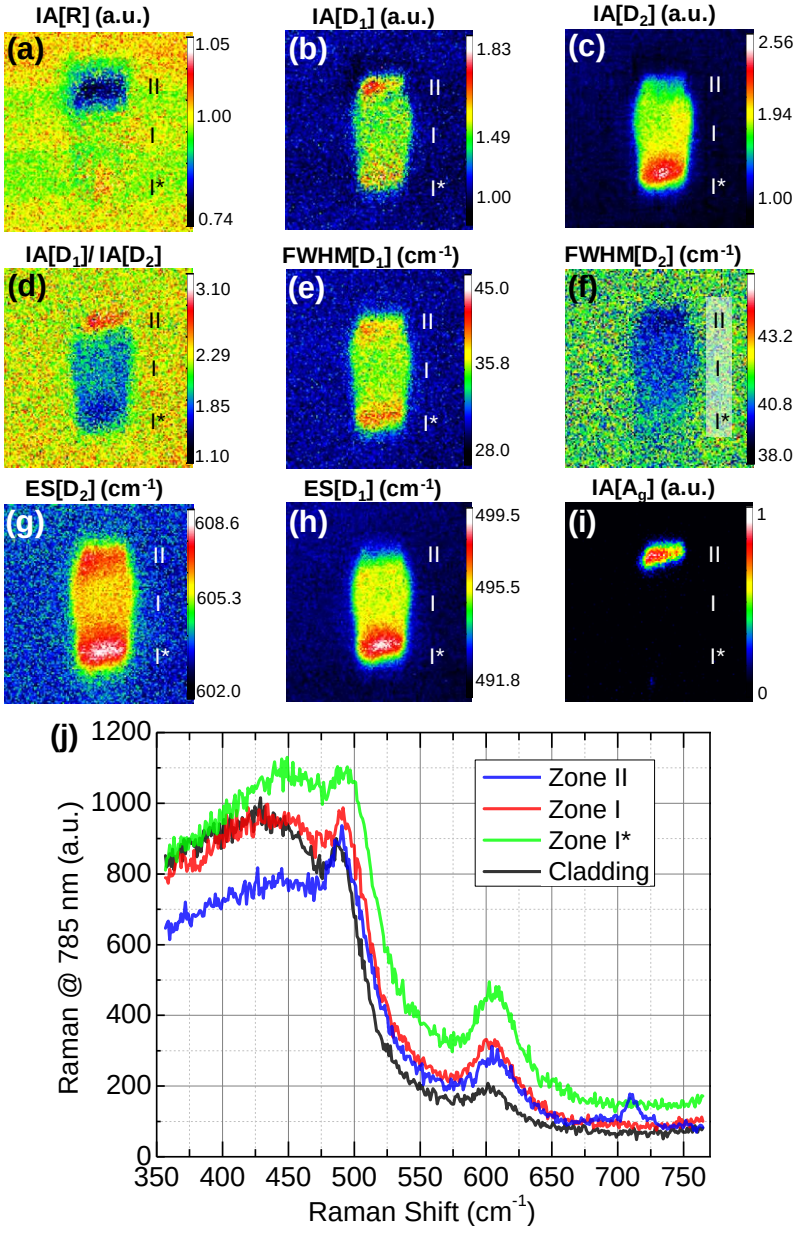

Figure 4.22. (a-i) μ-Raman maps of a 3DLW waveguide. The phonon associated to each map is indicated above it as well as the analyzed feature (i.e. IA = Integrated Area, FWHM = Full width at half maximum and ES = Energy shift). (j) Raman spectrums of a single point contained into each one of the waveguide zones.

All the presented Raman data reinforces the initial hypothesis that volume densification is the main responsible for refractive index increase within the 3DLW waveguide core. This densification is stable up to at least 400 ºC, according to the waveguiding experiments performed (no Raman spectrums after annealings presented here as they bear little variation with the original ones) although it has been reported that this type of permanent modification can withstand up to 1000 ºC [30]. This makes the 3DLW fused silica waveguides and, hence, the sensor presented in this Thesis extremely robust against large temperature variations.

References

1. G. Lifante, *Integrated Photonics: Fundamentals* (Wiley & Sons, 2003).
2. B. Poumellec, M. Lancry, A. Chahid-Erraji, and P. G. Kazansky, "Modification thresholds in femtosecond laser processing of pure silica: review of dependencies on laser parameters [Invited]," Optical Materials Express **1**, 766-782 (2011).
3. R. Stoian, K. Mishchik, G. Cheng, C. Mauclair, C. D'Amico, J. P. Colombier, and M. Zamfirescu, "Investigation and control of ultrafast laser-induced isotropic and anisotropic nanoscale-modulated index patterns in bulk fused silica," Optical Materials Express **3**, 1755-1768 (2013).
4. J. Martínez, A. Ródenas, T. Fernandez, J. R. Vázquez de Aldana, R. R. Thomson, M. Aguiló, A. K. Kar, J. Solis, and F. Díaz, "3D laser-written silica glass step-index high-contrast waveguides for the 3.5 μm mid-infrared range," Optics Letters **40**, 5818-5821 (2015).
5. A. Ródenas, G. Martin, B. Arezki, N. Psaila, G. Jose, A. Jha, L. Labadie, P. Kern, A. Kar, and R. Thomson, "Three-dimensional mid-infrared photonic circuits in chalcogenide glass," Optics Letters **37**, 392-394 (2012).
6. S. Jungling, and J. C. Chen, "A study and optimization of eigenmode calculations using the imaginary-distance beam-propagation method," IEEE Journal of Quantum Electronics **30**, 2098-2105 (1994).
7. W. Watanabe, Y. Note, and K. Itoh, "Fabrication of multimode interference waveguides in glass by use of a femtosecond laser," Optics Letters **30**, 2888-2890 (2005).
8. M. Lancry, B. Poumellec, A. Chahid-Erraji, M. Beresna, and P. G. Kazansky, "Dependence of the femtosecond laser refractive index change thresholds on the chemical composition of doped-silica glasses," Optical Materials Express **1**, 711-723 (2011).
9. I. H. Malitson, "Interspecimen Comparison of the Refractive Index of Fused Silica," Journal of the Optical Society of America **55**, 1205-1209 (1965).
10. A. Rodenas, and A. K. Kar, "High-contrast step-index waveguides in borate nonlinear laser crystals by 3D laser writing," Optics Express **19**, 17820-17833 (2011).
11. G. T. Reed, and A. P. Knights, *Silicon Photonics: An Introduction* (Wiley & Sons, 2004).
12. R. Ulrich, S. C. Rashleigh, and W. Eickhoff, "Bending-induced birefringence in single-mode fibers," Optics Letters **5**, 273-275 (1980).
13. E. Bricchi, B. G. Klappauf, and P. G. Kazansky, "Form birefringence and negative index change created by femtosecond direct writing in transparent materials," Optics Letters **29**, 119-121 (2004).
14. L. Sudrie, M. Franco, B. Prade, and A. Mysyrowicz, "Writing of permanent birefringent microlayers in bulk fused silica with femtosecond laser pulses," Optics Communications **171**, 279-284 (1999).
15. J. Canning, M. Lancry, K. Cook, A. Weickman, F. Brisset, and B. Poumellec, "Anatomy of a femtosecond laser processed silica waveguide [Invited]," Optical Materials Express **1**, 998-1008 (2011).
16. J. Zhang, M. Gecevičius, M. Beresna, and P. G. Kazansky, "5D Data Storage by Ultrafast Laser Nanostructuring in Glass," in *CLEO: 2013*

Postdeadline(Optical Society of America, San Jose, California, 2013), p. CTh5D.9.
17. J. R. Ferraro, K. Nakamoto, and C. W. Brown, *Introductory Raman Spectroscopy* (Academic Press, 2003).
18. E. Smith, and G. Dent, *Modern Raman Spectroscopy - A Practical Approach* (Wiley & Sons, 2005).
19. K. Mishchik, apos, C. Amico, P. K. Velpula, C. Mauclair, A. Boukenter, Y. Ouerdane, and R. Stoian, "Ultrafast laser induced electronic and structural modifications in bulk fused silica," Journal of Applied Physics **114**, 133502 (2013).
20. M. Beresna, M. Gecevičius, and P. G. Kazansky, "Ultrafast laser direct writing and nanostructuring in transparent materials," Advances in Optics and Photonics **6**, 293-339 (2014).
21. W. J. Reichman, D. M. Krol, L. Shah, F. Yoshino, A. Arai, S. M. Eaton, and P. R. Herman, "A spectroscopic comparison of femtosecond-laser-modified fused silica using kilohertz and megahertz laser systems," Journal of Applied Physics **99**, 123112 (2006).
22. S. K. Sharma, J. F. Mammone, and M. F. Nicol, "Raman investigation of ring configurations in vitreous silica," Nature **292**, 140-141 (1981).
23. S. V. King, "Ring Configurations in a Random Network Model of Vitreous Silica," Nature **213**, 1112-1113 (1967).
24. F. L. Galeener, "Band limits and the vibrational spectra of tetrahedral glasses," Physical Review B **19**, 4292-4297 (1979).
25. F. L. Galeener, "Planar rings in vitreous silica," Journal of Non-Crystalline Solids **49**, 53-62 (1982).
26. R. A. Barrio, F. L. Galeener, E. Martínez, and R. J. Elliott, "Regular ring dynamics in AX_2 tetrahedral glasses," Physical Review B **48**, 15672-15689 (1993).
27. A. E. Geissberger, and F. L. Galeener, "Raman studies of vitreous SiO_2 versus fictive temperature," Physical Review B **28**, 3266-3271 (1983).
28. M. Prencipe, "Simulation of vibrational spectra of crystals by ab initio calculations: an invaluable aid in the assignment and interpretation of the Raman signals. The case of jadeite (NaAlSi2O6)," Journal of Raman Spectroscopy **43**, 1567-1569 (2012).
29. M. Prencipe, L. Maschio, B. Kirtman, S. Salustro, A. Erba, and R. Dovesi, "Raman spectrum of NaAlSi2O6 jadeite. A quantum mechanical simulation," Journal of Raman Spectroscopy **45**, 703-709 (2014).
30. A. M. Streltsov, and N. F. Borrelli, "Study of femtosecond-laser-written waveguides in glasses," Journal of the Optical Society of America B **19**, 2496-2504 (2002).

CHAPTER 5

Experimental development of an icing sensor for the aircraft industry

This chapter describes the realization of the water-ice sensor concept presented in Chapter 2 for the specific case of the aircraft industry. The simulations predicting a very sensitive sensor capable of detecting the liquid-to-solid phase change of water in real-time are successfully corroborated experimentally. The 3DLW waveguides shown in Chapter 3 are used to obtain an experimental proof-of-concept of ice detection by exciting them with the appropriate mid-IR sources and observing the variation of their output while varying the temperature of the water/ice drops on the sensor surface. Furthermore, the sensor is flush-mounted on wing mock-up and coupled to mid-IR optical fibers to carry out realistic in-flight icing experiments and validate its sensing performance as well its capability of sustaining variable and harsh working conditions. This is an essential requirement to make the proposed sensor a feasible candidate to be implemented in future aircrafts.

Following the theoretical design of the water-ice sensor (Chapter 2), the fabrication of the main sensing elements, namely the 3DLW waveguides (Chapter 3) and their characterization (Chapter 4), the performance of the sensor needed to be experimentally validated. For this purpose, firstly, in a normal optics laboratory and under static conditions, a set of tests that evaluated the capability of the sensor of detecting phase changes of water drops placed on the sample were performed in free-space and fiber-coupled configurations (Section 5.1). Secondly, once the sensor was integrated into a wing mock-up, further tests with controlled in-flight icing conditions were carried out to verify the temporal evolution of the sensor output in different types of icing scenarios to prove its early-alert capability, as well as its robustness against the impact high-speed water droplets in liquid and solid state (Section 5.2). In both cases, the chosen building material for the device was fused silica because its better sensing performance as it has been demonstrated by simulations (see Chapter 2) as well as the possibility of writing mid-IR 3DLW step-index waveguides as it has been explained in Chapter 3.

5.1. Sensing demonstration in an optics laboratory

Experiments involving freezing water and ice on the sensor surface required upgrading the conventional waveguiding setup shown in Chapter 4. The sensor was placed on a Peltier thermoelectric cooler (TEC) instead of directly on the optomechanical stage. Then by applying the appropriate current to the Peltier unit, the surface in contact with the sensor was cooled down to the desired temperature. The heat generated on the opposite face of the cooler was dissipated by means of a copper cold plate with circulating water inside. In this manner, the temperature of the entire sensor could be brought down to a minimum temperature of about -30 ºC.

At this initial stage of the project, only the low-contrast (LC) 3DLW waveguides were available (see Section 4.2.2 of Chapter 4). Nevertheless, they were enough to prove the ice detection capability of the sensor. In particular, the selected waveguide to carry out the experiments described below had the following

parameters: W = 32 µm, H = 15 µm, G = 6 µm and $\Delta n = 2 \cdot 10^{-3}$. Only straight sensing waveguides with no bending sections were fabricated for the sake of simplicity. Physical polishing of the surface was performed to reduce the core-surface gap.

5.1.1. Proof of concept with free-space coupling

The free-space coupling setup was similar to that used for the characterization of waveguides which was already explained in Section 4.2.1, Chapter 4. As Figure 5.1(a) shows, the main modifications were the implementation of a TEC temperature control below the sensor substrate as well as enclosing part of the setup inside a PMMA chamber filled by N_2. This was required to purge the humidity that produced water condensation on the facets of the silica substrate when cooling it down and prevented from proper light coupling and imaging of the waveguides output. The employed source was either a mid-IR OPO or a mid-IR ICL, both with linear polarization. The state of the light polarization was not controlled at any point of the setup as no change in sensing performance was expected for different polarizations.

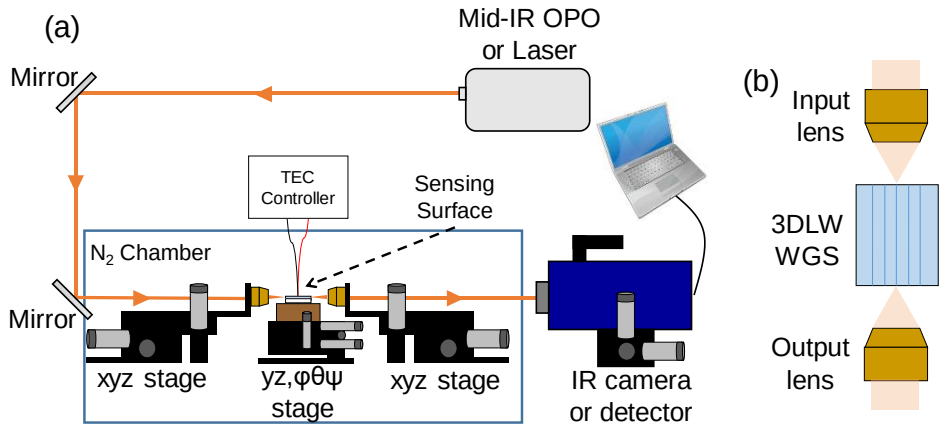

Figure 5.1. (a) Setup for the free-space coupling icing experiments in the optical lab. (b) Top view of the waveguide's light coupling and imaging using free-space optics.

Taking advantage of the short-term availability of a mid-IR OPO (Firefly-IR, M Squared Lasers) at the beginning of the project, the spectral response of the sensor could be measured. The mid-IR range covered by the OPO was λ = 3.3 μm to 3.7 μm. The experimental procedure carried out was as follows.

1) The waveguide of interest was identified and the light coupling to the photonic chip was optimized at a central wavelength within the range to sweep.
2) A wavelength sweep was done having the sensor surface clean at room temperature and the output intensity was recorded for each wavelength to get the output spectrum ($P_{o,a}(\lambda)$).
3) A millimeter-sized water drop was placed on the surface and its covering length (*L*) was measured in the propagation direction.
4) Surface temperature was set to the desired value. The temperature was monitored by a hand-held thermal camera and adjusted if needed.
5) Once the temperature was stabilized the light coupling into the waveguide was re-optimized in case of misalignments due to temperature changes.
6) Again, a spectral sweep with the water drop at the new temperature (and frozen if below 0 ºC) was performed to record $P_{o,i/w}(\lambda)$.
7) The attenuation spectrum $A_{i/w}(\lambda)$ of the ice/water drop relative to the clean sample was computed by using Equation 2.3 (see Chapter 2).

The experimental attenuation $A_{i/w}(\lambda)$ spectrum recorded using the OPO are shown in Figure 5.2 for liquid water at 20 ºC, clear (homogeneous) ice at -5 ºC and supercooled water (SW) at -5 ºC. The dotted raw data is accompanied by its corresponding fitting curves for the three cases. To obtain the SW no special means were employed. Since the sensor surface was polished with high quality and lacked significant nucleation centers, water could stay in a metastable liquid form (SW) well below 0 ºC.

For water and ice, the measured optimum wavelength at the particular temperature and sensor parameters studied were, respectively, $\lambda_{match,w}$ = 3.47 μm and $\lambda_{match,i}$ = 3.68 μm. As it was demonstrated in the

simulations of Chapter 2, the water curve $A_w(\lambda)$ has its maximum at a shorter wavelength than that of ice $A_i(\lambda)$, whereas the maximum of the curve associated to SW $A_{SW}(\lambda)$ is somewhere in between. This occurs because the optical constants of water vary with temperature making the complex refractive index of SW to approach progressively to that of ice [1]. Despite this, the attenuation spectrums of SW and ice at the same temperature can be clearly distinguished so that the sensor would be able to differentiate between both.

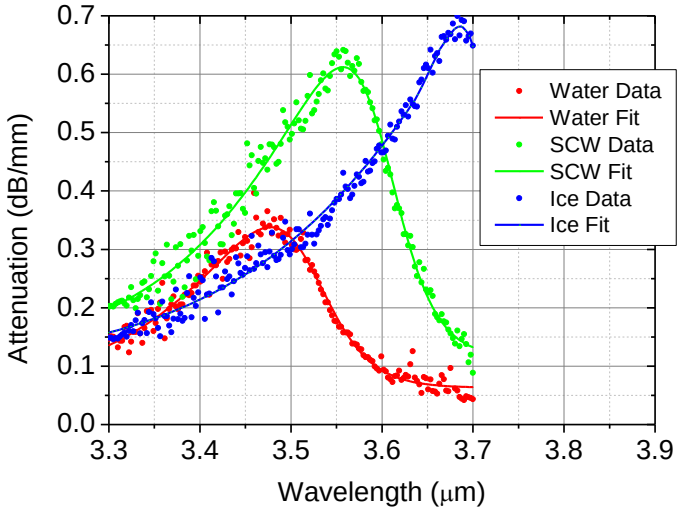

Figure 5.2. Experimental attenuation spectrum of the water-ice sensor (LC waveguide) measured with a mid-IR OPO for water, SW and ice: raw experimental data (dots) and fitting (lines).

A comparison of simulated and measured results can be found in Figure 5.3. The simulated curves were obtained in the same way as those shown in Chapter 2, but using the adequate parameters instead (i.e. *W* = 32 μm, *H* = 15 μm, G = 6 μm and $\Delta n = 2 \cdot 10^{-3}$). Overall, the shape of the simulated and experimental curves are similar although their magnitude (note that the simulation curve is divided by 2) and the maximum position vary. This can be attributed to errors in the optical constants taken from literature for ice and water and/or in the modelling of the waveguide structure not being accurate enough with respect to the actual fabricated waveguide. The importance of the matching of theoretical and

experimental results is relative, thus no further efforts were made in that sense. For this reasons, for the rest of the chapter, no more direct comparisons with the simulations will be done and strictly experimental results will be analyzed.

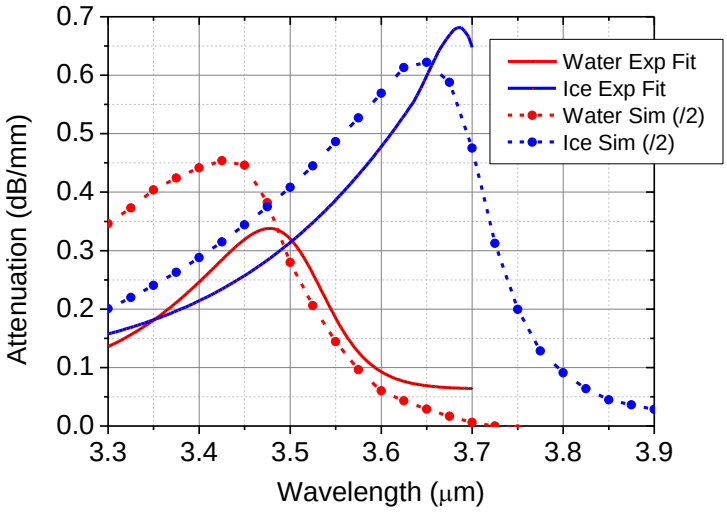

Figure 5.3. Experimental attenuation (fitting) of the water-ice sensor (LC waveguide) compared to the simulated one (divided by 2).

5.1.2. First fiber-coupled prototype

The first fiber-coupled water-ice sensor prototype working in normal optics laboratory conditions was still built employing the LC waveguides. ZBLAN mid-IR transparent fibers (FiberLabs Inc.) were bonded to the silica chip to couple the light into the sensing waveguide and gather the light out of it. The input single-mode fiber had 20 μm core diameter and NA = 0.12 for low coupling losses, whereas the multimode output one had 97 μm core diameter and NA = 0.30 that allowed maximum light collection and simplification of the bonding process. Prior to the bonding, cleaving of the fibers to obtain flat surfaces was done by a tension-adjustable fiber cleaver (Ericsson EFC 11) since standard fiber cleavers for telecom silica fibers operate at a much higher tension than the required for a soft glass like ZBLAN. Once cleaved, the fibers were placed on the respective optomechanical stages and their tips were covered by a small drop of NOA 61 optical adhesive. The process of fiber-waveguide coupling was done as usual

(i.e. optimizing the light intensity out of the output fiber by adjusting the position of the fibers and the chip with micrometer precision) and finally the adhesive was cured and solidified by UV light. Pictures of the cleaved fiber, the fiber-waveguide coupling and the completed first fiber-coupled prototype under icing conditions are shown in Figures 5.4(a-c), respectively.

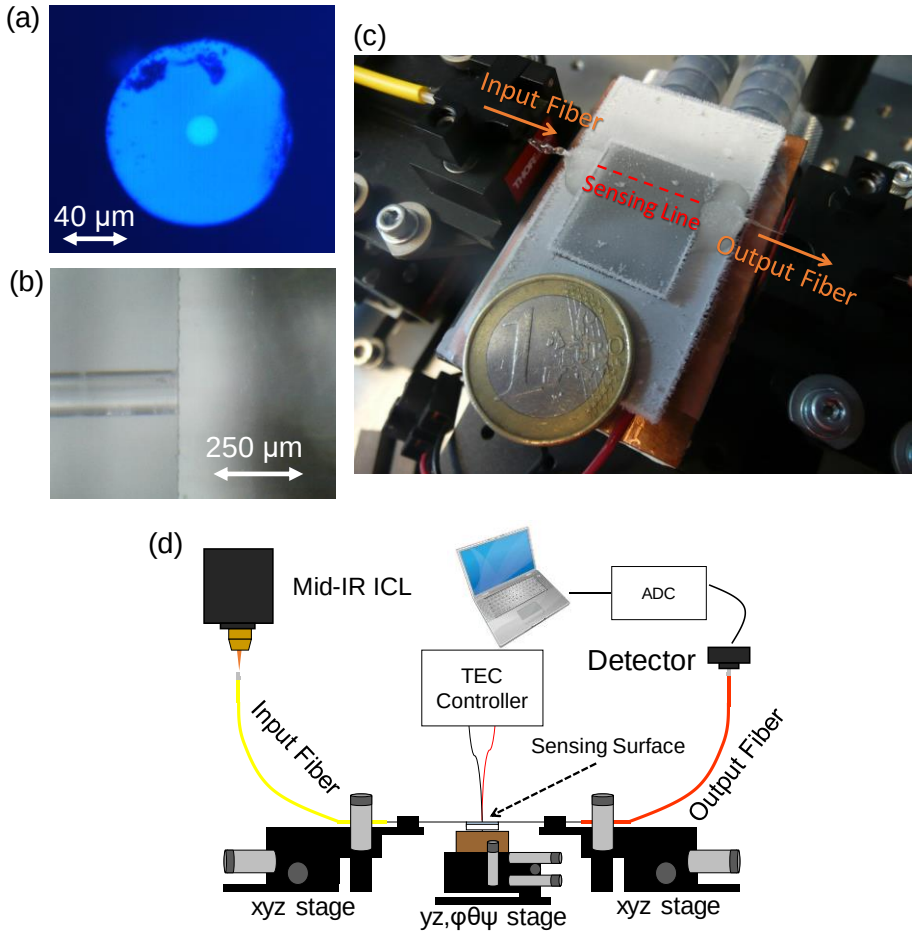

Figure 5.4. Pictures of (a) a ZBLAN cleaved fiber, (b) a fiber butt-coupling to a 3DLW waveguide and (c) the first fiber-coupled prototype of the water-ice sensor. (d) Fiber-based experimental setup for the sensor testing in the optics laboratory.

The experimental setup was adapted to the new coupling scheme (see Figure 5.4(d)). A mid-IR laser emitting at the appropriate wavelength was coupled into

the input ZBLAN fiber while the output fiber was coupled to a fast PbSe detector (Thorlabs) to monitor the output light intensity. The laser was electronically modulated at 2 kHz in order to improve the SNR at the output. The detectors output voltage was digitized by means of a DAQ connected to a PC and a simple LabVIEW interface allowed to demodulate the signal and record the temporal traces of the icing experiments. Note that it was not necessary to enclose the setup within a N_2 chamber since the fiber connections were waterproof thanks to the adhesive covering.

Figure 5.5 shows an example of the temporal evolution of the sensor output signal in an icing event in which the sensor surface was completely covered with water at room temperature (20 ºC) and, subsequently, cooled down to -20 ºC. The vertical axis corresponds to the output light power measured by the detector relative to that when the sensor is clean in logarithmic units. The laser source used was an ICL (Nanoplus) emitting at 3.68 μm which is the wavelength at which the attenuation is maximum for ice and these LC waveguides (see Figure 5.2). The water drop placed on the surface covered the whole waveguide extension.

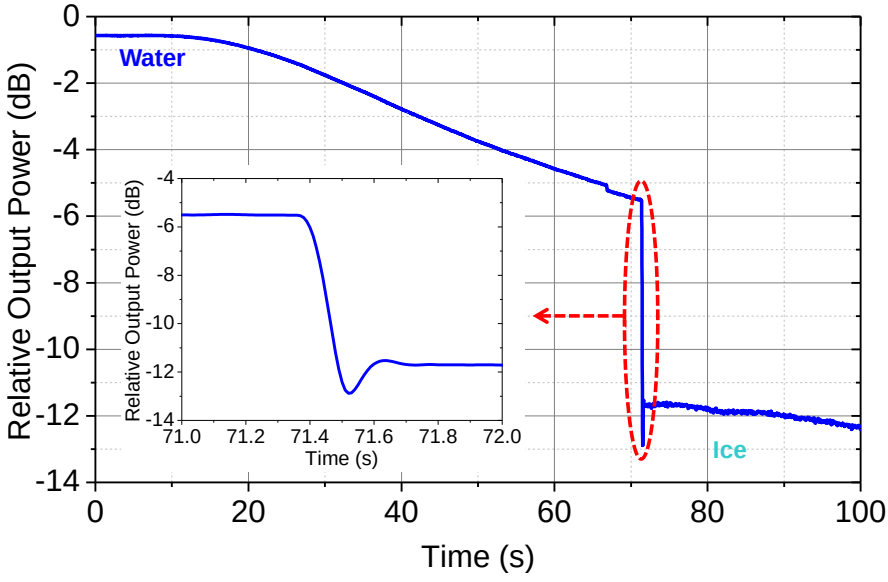

Figure 5.5. Temporal trace of the detected light intensity from the output fiber when the sensor surface was covered by water and it was cooled down from 20 ºC to -20 ºC. The phase transition from water to ice is shown in detail.

The detected waveguide output power decreased progressively as the sensor was cooled down due to the variation of the optical properties of water with the temperature. Close to the second 70 of the experiment, a sudden drop in the intensity was observed which was undoubtedly associated to the water phase change from liquid to solid. Direct visual inspection of the surface confirmed the water freezing process as well as the homogeneity of its structure (clear ice). In fact, the signal drop happened some seconds before the whole volume of water was frozen since the detection mechanism works already for the first μm's of ice as it was shown in Chapter 2 by simulations.

A closer look of temporal trace of the ice crystallization event reveals that the response time of the sensor is about 200 ms. This is mainly limited by the software and the signal acquisition electronics employed. Therefore, if required, this response time could be easily shortened by building a faster signal acquisition and processing system. In any case, this experiment proves that the sensor was able to detect water-ice phase changes in real-time with high sensitivity which is essential for an early-alert sensor.

5.2. Sensing demonstration in an icing wind tunnel

Once the sensor performance was tested in the static conditions of an optics laboratory, the next step was to test it in an environment closer to real in-flight conditions as the industry would require. For this reason, icing tests were conducted in the icing wind tunnel (IWT) facilities of the Fraunhofer IFAM in Bremen (Germany). A new fiber-coupled prototype directly flush-mounted on the leading edge of a wing model mock-up (NACA 0012) was specially fabricated for the tests. Below a description of the IWT, the new prototype and the tests conducted is provided.

5.2.1. Fraunhofer IFAM icing wind tunnel

The IFAM IWT can create wind speeds up to 350 km/h with a controllable temperature down to -30 ºC [2]. To mimic in-flight conditions, the turbulent airflow

created by the fans is converted into laminar by a system of vanes strategically placed within the tunnel structure. By means of a cooling/heating system the flow temperature is adjusted as needed. Lastly, in order to simulate the presence of clouds, the water is atomized and injected into the air stream by a couple of nozzles. The created droplets have median volume diameter (MVD) of 40 μm. The result is that the airflow arriving into the test section where the mock up is placed can be continuously modified in terms of temperature, speed and, indirectly, liquid water content (LWC).

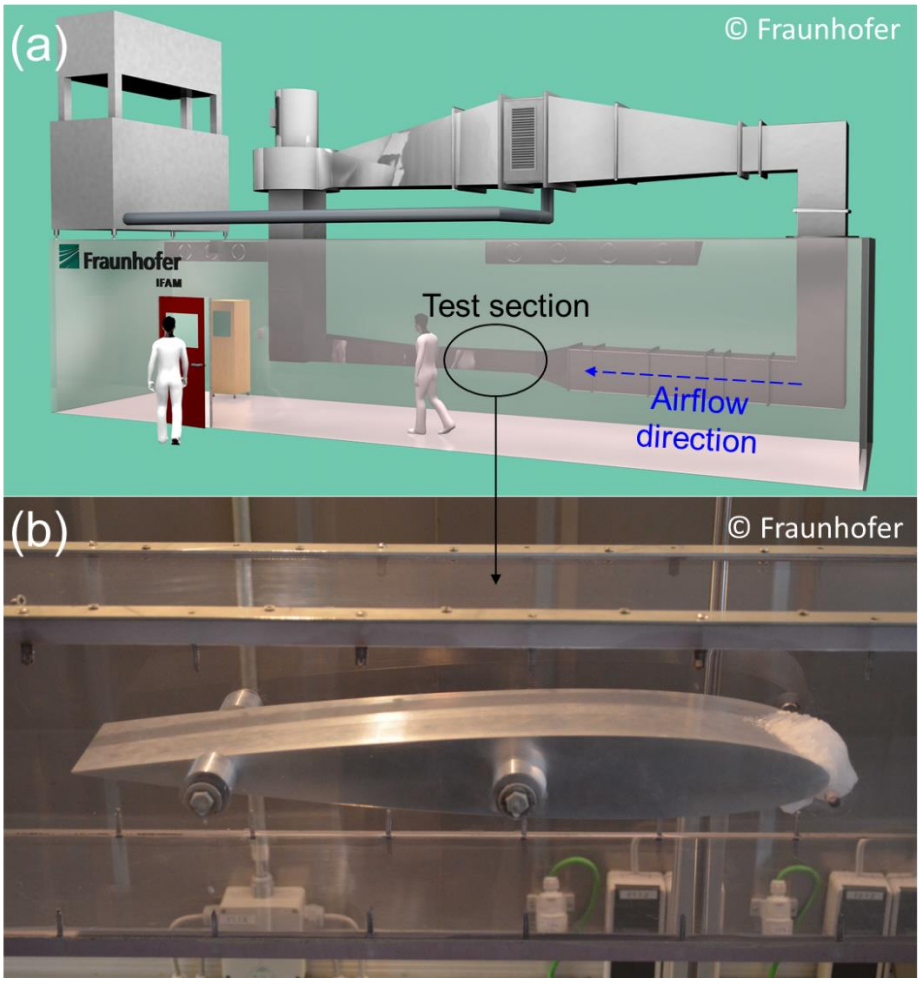

Figure 5.6. (a) 3D graphical model of the IWT facility. (b) Test section with a NACA 0012 aluminum wing mock-up inside.

Figure 5.6(a) shows a 3D model of the IWT facility. Essentially, from the aerodynamics point of view, its architecture is similar to that of others wind tunnels. A photograph of the real test section is shown in Figure 5.6(b) in which a NACA 0012 wing mock-up made of aluminum has been subjected to an icing experiment. The chord of the mock-up is 500 mm and the width 90 mm.

5.2.2. Sensor integration into a wing mock-up: second fiber-coupled prototype

High-contrast (HC) 3DLW silica waveguides were available at the time of building the second fiber-coupled prototype (see Section 4.2.2, Chapter 4). Thus, they were readily incorporated into the new prototype.

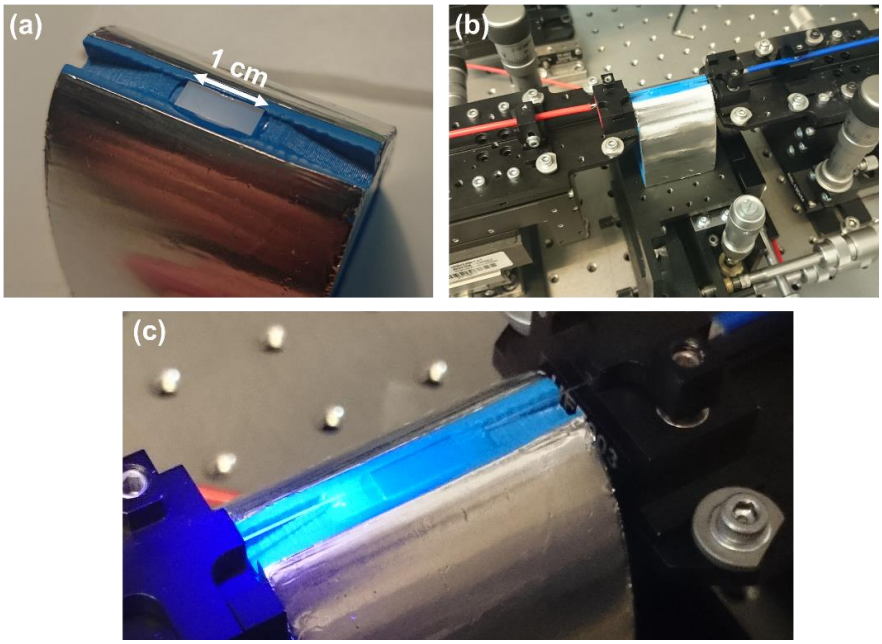

Figure 5.7. (a) 3DLW photonic chip placed on its corresponding slot of the leading edge of wing mock-up prior to the fiber bonding. (b) Process of fiber alignment and bonding to a 3DLW waveguide using optomechanical stages. (c) Closer look of the fiber to chip bonding with an UV-curable optical adhesive.

The specific morphological parameters of the chosen sensing waveguide were: W = 13 μm, H = 13 μm, G = 4 μm and $\Delta n = 8 \cdot 10^{-3}$. The waveguide length was 10 mm approximately, although the effective sensitive distance was reduced to 8 mm due to the optical adhesive partially covering the edges of the sensor-wing interface.

The wing model mock-up employed (NACA 0012) was fabricated with a 3D printer in polylactic acid (PLA) thermoplastic which was an economical and flexible platform in front of aluminum. To facilitate the integration process of the glass substrate together with the optical fibers into the mock-up, the wing was made in various pieces that could be joined together afterwards. The most important piece was the central one which accommodated the sensor body (see Figure 5.7(a)) and was small enough to be placed in a waveguiding setup for the fiber coupling procedure. A slot with a shape adapted to the glass substrate was fabricated on the leading edge so that the sensor could be flush-mounted with ease. At each side of this slot, the bare fibers (previously prepared as described in Section 5.1.2) were placed on a pair of sloped grooves which were meant to be filled with adhesive to completely seal the optical connection. Figures 5.7(b,c) show pictures taken during the ZBLAN fiber bonding process to the selected waveguide by means of NOA optical adhesive. The fibers were clamped on optomechanical stages and aligned to optimize the light transmission prior to the UV curing of the adhesive. The input single-mode fiber was slightly different with respect to the previous prototype. For better coupling to the HC waveguide, the fiber had a diameter of 9 μm and 0.19 NA.

Figure 5.8 shows a simple side view sketch of the concept of dividing the front part of the wing mock-up into three pieces. As aforementioned, the central part (CP) accommodated the photonic chip and the cleaved fiber ends. The input and output side pieces (ISP and OSP, respectively) had a tubular hole drilled with the same slope as the fiber grooves of the CP so that the corresponding fiber tubing could be introduced in it. Thus, once the fiber bonding was done and the fibers ends securely attached to the CP with an adhesive padding on them, the ISP and OSP could be assembled carefully to the CP by simply sliding them along the fiber tubing to the correct position and, subsequently, screwing the three pieces

together. Note that during all this process laser light was being coupled to the input fiber and monitored at the output end so as to ensure that the optical connection was not broken due to the soft nature of the involved ZBLAN fibers.

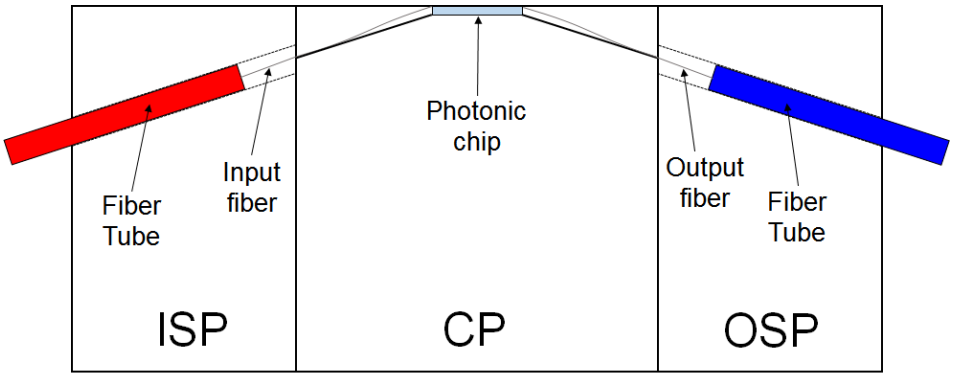

Figure 5.8. Side view of the wing mock-up front part divided into three pieces (ISP, CP and OSP) to facilitate the process of optomechanical integration of the fiber-coupled photonic sensor.

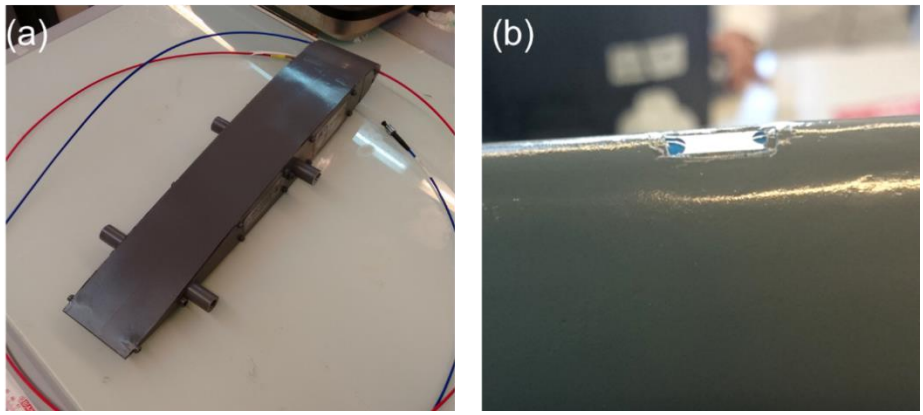

Figure 5.9. (a) Paint finish of the wing mock-up. (b) Detailed view of the flush-mounted water-ice sensor installed on the leading edge of the wing.

After assembling the three front pieces to the rest of the wing mock-up, a spray painting was applied to the whole body to make the surface uniform and improve aesthetics. The final look of the mock-up is shown in Figure 5.9(a). Beside it, a closer picture of the sensor finally integrated on the leading edge is provided in

Figure 5.9(b). Slight inhomogeneities and non-perfect flush-mounting of the glass substrate can be seen around its edges which might affect the ice formation pattern although not the sensing experiment.

Once the wing mock-up was finished, it was sent from Tarragona to the IFAM in Bremen (Germany) together with the laser, the detectors and the optics for fiber coupling mounted on a compact optical table. The wing was secured inside the test section by four lateral screws, just like any other wing mock-up designed for this IWT. Moreover, two extra holes were drilled on each one of the side walls so that the input and output optical fibers could be brought outside the test section through them and be coupled to the optical setup. Figure 5.10 shows some photographs of the installed wing mock-up ready for IWT experiments.

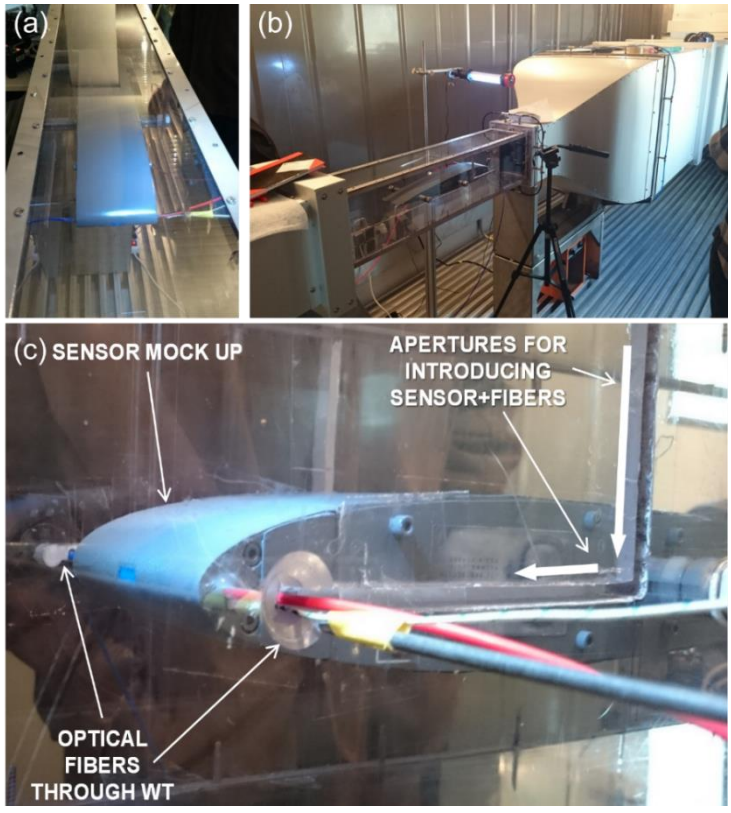

Figure 5.10. (a,b) Upper and lateral views of the second fiber-coupled sensor prototype integrated into a wing mock-up and installed in the IWT, ready for testing. (c) Close view of the fibers installation through the IWT walls.

Figures 5.10(a,b) show, respectively, an upper and side view of the mock-up inside the IWT. A more detailed picture of the fiber integration through the IWT walls is presented in Figure 5.10(c). Apart from the circular holes drilled on the walls, a couple of apertures with an L shape were also made to facilitate the installation of the mock-up while avoiding bending too much the soft ZBLAN fibers. Subsequently, they were covered by tape to minimize their possible effect on the generated airflow.

Following the installation of the wing, the fibers were coupled to the optical setup. Optical alignment for optimum fiber coupling was performed by maximizing the transmitted light through the fibers and sensing waveguide. The laser, detector and the signal acquisition system was identical to the one described in Section 5.1.2. Full technical specifications corresponding to this prototype are included in Appendix A.

5.2.3. IWT tests of the second sensor prototype

The tests conducted in the IWT consisted of recording the sensor output signal for different icing conditions. These conditions were varied each time by tuning the tunnel wind speed (WS) and temperature (T). Two WS's were tested, namely 55 m/s and 95 m/s, together with four T points which were 10 ºC, 0 ºC, -15 ºC and -25 ºC, resulting in a total of eight tests. As aforementioned, the MVD of the water droplets released by the nozzles was estimated to be 40 μm and the LWC, 2.1 g/m^3 and 0.8 g/m^3 for 55 m/s and 95 m/s WS's, respectively.

For each test the WS and T were stabilized for a few minutes prior to the cloud creation. Once the conditions were considered steady, the nozzles were opened and the water (SW depending on the temperature) droplets started to reach the wing mock-up. Figure 5.11 shows the look of the leading edge 3 s after the beginning of the spray of water. At positive temperatures (Figures 5.11(a,e)), no icing occurred and only a water film sliding towards the trailing edge can be observed. At 0 ºC (Figures 5.11(b,f)), both liquid water and clear ice can be spotted on the wing surface since this is the water freezing point and the temperature control system has a tolerance of ±0.5 ºC. At the negative

temperatures tested (Figures 5.11(c,g,d,h)), ice accretion of mostly transparent clear ice was evident at -15 ºC, whereas at -25 ºC, the accreted ice takes a milkier appearance (i.e. rime ice). The µm-sized water droplets reaching the wing are supposed to be SWD due to the low temperatures of the air. Some of them solidify upon contacting the surface while others run back along the surface before freezing. As it is explained in Chapter 1, this determines the nature of the accreted ice (clear, rime or mixed) and can be controlled by changing the icing conditions (T, WS and LWC) of the IWT experiments.

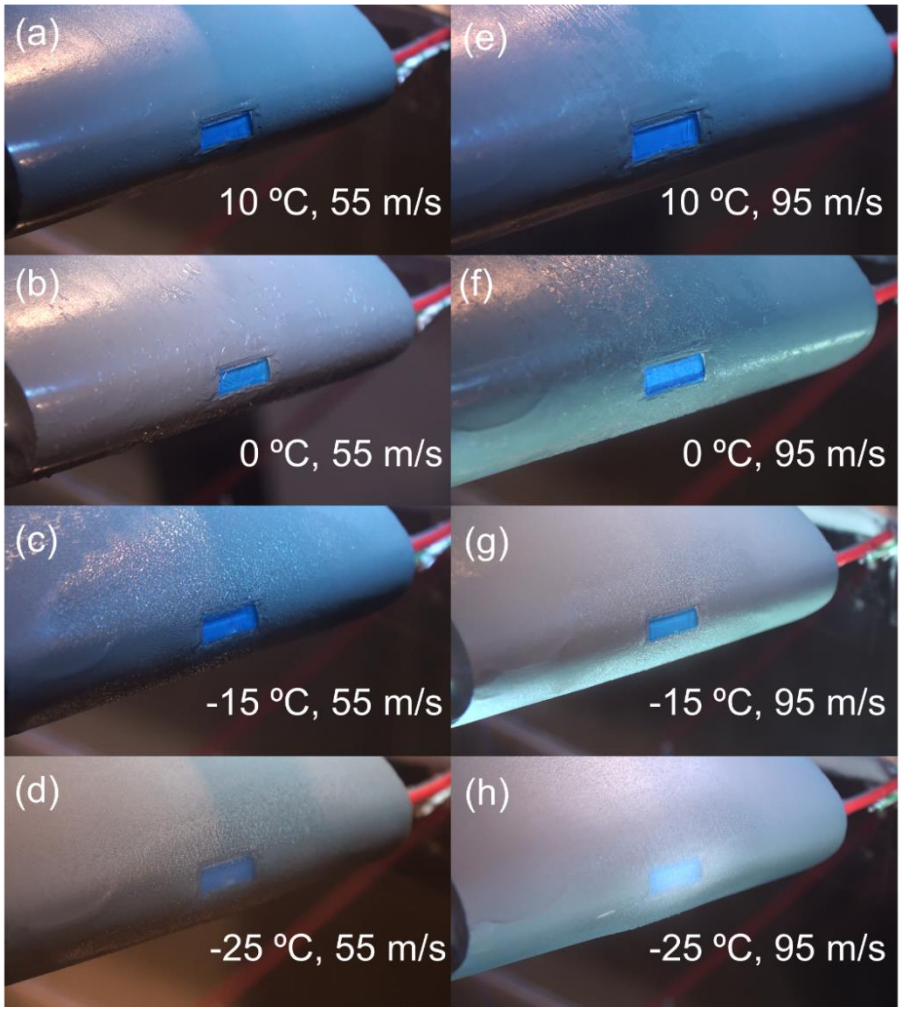

Figure 5.11. Wing mock-up appearance 3 s after starting water spray for all the tests performed.

Images of the accreted ice on the wing mock-up after 30 s are presented in Figure 5.12 for comparison purposes. Although thick ice layers are not relevant for the sensor performance, which is only sensitive to the first ice micrometers, it can serve as a visual aid for the reader since the different types of ice can be identified and thus associated to the sensor signals that will be provided later. For example, in the opposite cases of Figures 5.12(b) and 5.12(f), the differences in color and texture are more than evident. The first one could be associated to clear ice whereas the second to rime ice. Figures 5.12(c) and (e) represent an intermediate case in which clear and rime ice are both present in similar proportions, which is termed as mixed ice.

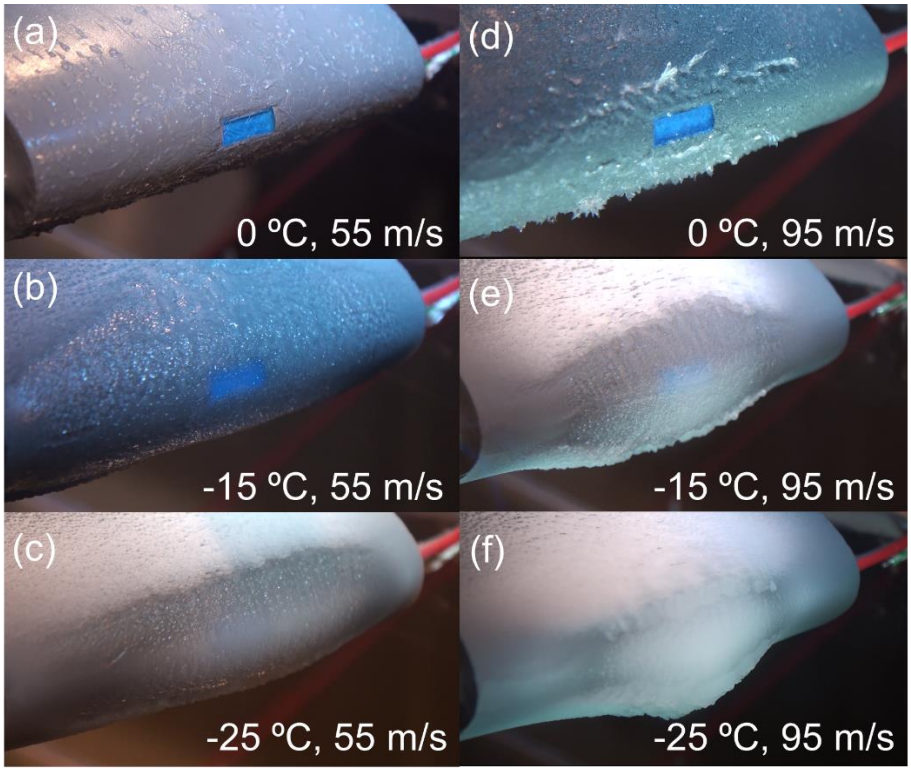

Figure 5.12. Wing mock-up appearance 30 s after starting the water spray for each one of the tested icing conditions.

A) <u>55 m/s tests</u>

The temporal traces of the sensor output signals recorded for WS = 55 m/s are shown in Figure 5.13. As it was done in previous experiments, the output signals depicted are relative to that corresponding to a clean sensor surface, i.e. just before the spraying starts, and expressed in logarithmic units. Furthermore, for easier comparison, the four curves are approximately synchronized with respect to the beginning of the water spray (second 0 of the temporal axis). Note that the ICL laser was emitting at 3.68 μm, as in the experiments involving LC waveguides, even though the maximum attenuation could have been shifted slightly to shorter wavelengths for the HC waveguides employed.

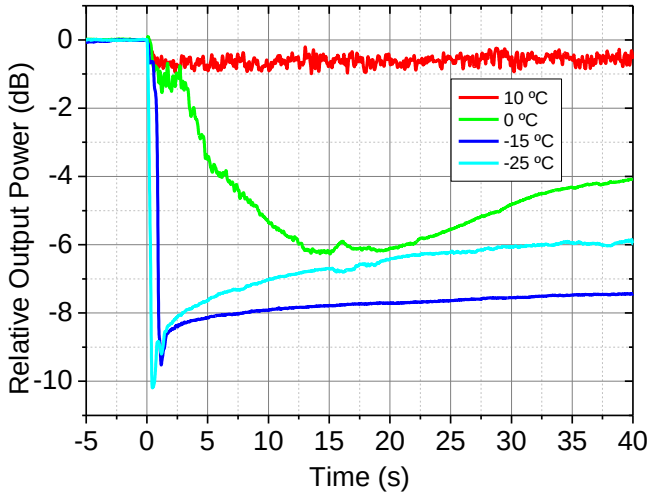

Figure 5.13. Temporal trace of the sensor output signals for WS = 55 m/s and four different temperatures in IWT tests.

For non-icing conditions (red curve), the sensor signal is slightly attenuated (about 0.65 dB) after the nozzles open due to the continuous presence of liquid water on the surface. Moreover, the signal has a characteristic “noisy” nature which stems from the droplets of the simulated cloud impacting the surface. For icing conditions, i.e. T = -15 ºC and -25 ºC, the signal rapidly drops about 10 dB for both temperatures. The elapsed time from the starting of the icing event to the maximum signal attenuation (called t_{icing} from now on) is 1.2 s and 0.4 s for -15 ºC and -25 ºC, respectively. Subsequent to the initial signal drop, both

curves evolve differently probably due to the different ice microstructure formed on the glass surface (see Figures 5.11(c,d) and Figures 5.12(b,c)). As it is observed, the -15 ºC curve undergoes greater attenuation after 40 s than that corresponding to -25 ºC. Finally, the 0 ºC curve reveals an initial slow freezing process of the droplets reaching the surface (6 dB and t_{icing} = 15 s), but from there, the signal recovers indicating ice melting. A plausible explanation for this is that small fluctuations of temperature around 0º C plus the continuous impacts of water droplets could prevent locally water from freezing on the glass surface, resulting in a mix of ice-water millimeter-sized films on it.

B) <u>95 m/s tests</u>

The WS was increased to 95 m/s and the tests were repeated for the same temperatures. The recorded curves are shown in Figure 5.14. The observed trends are similar to those of the previous counterparts. Still, for T < 0 ºC, the sensor output presents a sudden attenuation of almost 10 dB when the water spray starts indicating ice accretion with a t_{icing} of 0.8 s and 0.9 s for -15 ºC and -25 ºC, respectively. As before, a rise of the detected power occurs subsequently, being more pronounced for the -25 ºC case. At 0 ºC, t_{icing} is faster (4.3 s) and the attenuation slightly greater (7 dB).

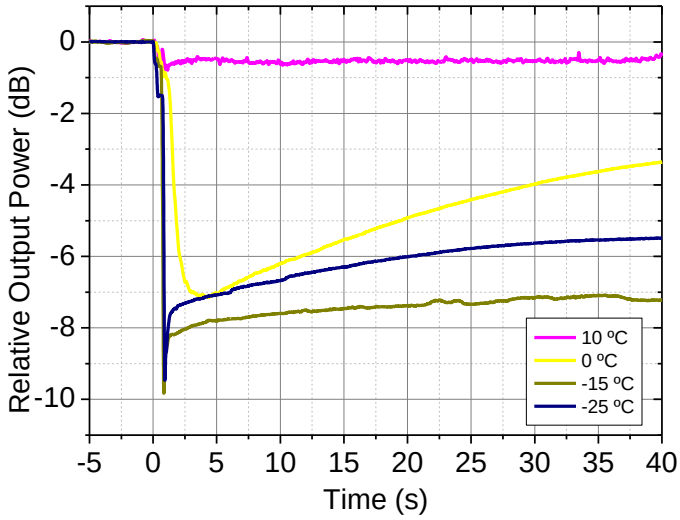

Figure 5.14. Temporal trace of the sensor output signals for WS = 95 m/s and four different temperatures in IWT tests.

C) 55 vs. 95 m/s tests

The curves corresponding to the whole set of experiments are depicted in Figure 5.15 for effortless comparison. Curiously, in non-icing conditions, at 55 m/s the signal presents a spikier behavior than at 95 m/s since, at this speed, the rate at which the water droplets impact the sensor surface is greater. Such high frequency signal is smoothed by the last digital low-pass filter of the demodulator block implemented in LabVIEW.

The T and WS parameters that produce a stronger attenuation (after the signals stabilization) are firstly, -15 ºC, 55 m/s and, secondly, -15 ºC, 95 m/s. The former conditions, produce a slightly clearer ice (see Figures 5.12(b) and (e)) layer which means that the sensor surface is more homogeneously covered by ice, thus producing a higher attenuation of the guided light. Among these couple of tests (-15 ºC, 55 m/s and -15 ºC, 95 m/s), the higher LWC occurring in the 55 m/s test (2.1 g/m^3) makes the accreted ice to be more homogenous which results in higher attenuation. In the 95 m/s case, although the LWC is much smaller, the higher wind speed counteracts such effect and the attenuation is still elevated, meaning a higher proportion of clear ice relative to that of rime ice.

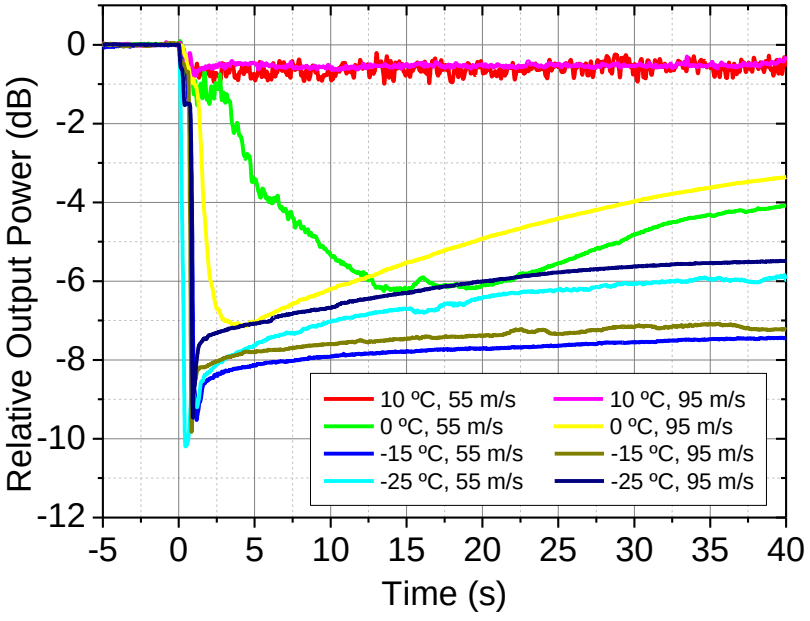

Figure 5.15. Temporal trace of the sensor output signals for all the IWT tests.

For T = -25 ºC, both 55 m/s and 95 m/s curves present about 1.5 dB less attenuation than its -15 ºC counterparts. As it is observed in Figures 5.12, the whiter color of the ice in (c) and (f) with respect to that in (b) and (e) indicates less homogeneous ice and, hence, the presence of more air bubbles within its structure which gives rise to less attenuation of the sensor output. This demonstrates that, at least in this particular group of experiments, the factor that has a major influence on the ice microstructure contacting the surface is temperature. Like in the -15 ºC case, the ice accreted at 95 m/s WS, produces less attenuation on the sensor signal which is attributed to the lower LWC of the simulated cloud at this speed. Indeed, Figures 5.11(h) and 5.12(f) show that for T = -25 ºC and WS = 95 m/s the accreted ice has the closer look to genuine rime ice which implies that it is the less dense, thus producing less attenuation of the guided light. Note that the reduced sensitivity of the sensor to rime ice is consistent with the simulations shown in Chapter 2, Section 2.2.6.

Regarding the results at T = 0 ºC, the signal evolution is similar for both, being faster for 95 m/s, as mentioned before. These kind of limit cases are relevant to study if looking for the optimum signal threshold that triggers an ice alarm to be sent to the corresponding anti-icing systems. For instance, if the threshold was placed at -5 dB relative to the dry sensor reference, it would be effective enough to trigger an ice alarm indicating ice accretion on the sensor surface and, a priori, on the surrounding wing surface for all the icing cases studied. While on strong icing conditions (T < 0ºC), the alarm could be sent about 1 s after entering the cloud, in both limit cases (T = 0ºC) it would happen a few seconds later (2 and 5 s). Notice, however, that this time is also proportional to the severity of the icing conditions which are monitored by the sensor in real-time. Thus, the magnitude of the signal attenuation could be used to modulate the intensity of the anti-icing action in order to minimize the energy consumption. The complete analysis on how to process the temporal information provided by the sensor (which might come from different points on the wing in an arrayed sensing scheme) and the subsequent activation the anti-icing devices is out of the scope of this Thesis.

D) Multiple wavelength sensing with a single laser

Taking advantage of the small wavelength tuning that the ICL allowed via temperature and current adjustment, the water/ice induced attenuation was investigated at two more wavelengths (i.e. 3.60 μm and 3.64 μm), apart from the main one (3.68 μm). Before (clean sensor reference) and after (covered sensor) each one of the tests presented previously, the wavelength was tuned twice to obtain output power values at both wavelengths, respectively. With this values, the attenuation for different T's and WS's conditions was computed for the new wavelengths. Note that the power values for the sensor covered by water or ice were taken when the signal was totally stable. Figure 5.16 presents the attenuation data for all the tests (and all three wavelengths) except for those performed at 0 ºC which were not included due to their lack of signal stability and the temporally variable nature of the accreted ice. Moreover, the attenuation data for a clear ice reference at -15 ºC which was measured in static conditions inside a refrigerator is included for comparison purposes.

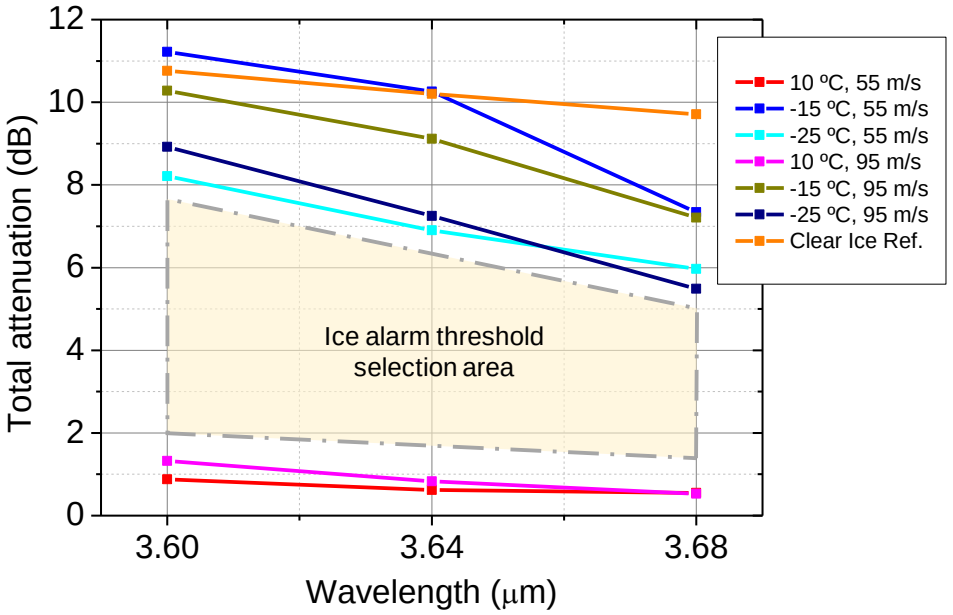

Figure 5.16. Measured attenuation for six of the eight IWT tests once the signal was stable for three different wavelengths obtained via tuning of the ICL emission wavelength.

From λ = 3.60 μm to 3.68 μm, the trend of the attenuation is to decrease with wavelength which is consistent with the spectrums recorded using the OPO (see Figure 5.2). As it is evident from the plot and was already observed in the time-resolved experiments (Figure 5.15), the attenuation in icing conditions is significantly stronger than that in non-icing conditions for the three wavelengths. This allows to choose the power threshold for ice accretion alert at each wavelength within a broad range of values as it is highlighted in Figure 5.16. The criterion of selection of this threshold should be based on the time for ice alarm vs. the false alarm probability trade-off.

Lastly, the ice accreted at -15 ºC in both WS cases generates an attenuation line resembling the static clear ice reference which is in accordance with the corresponding ice morphology visual observations presented in Figures 5.11 and 5.12. On the other hand, the ice formed at -25 ºC, induces an attenuation well below the clear ice reference, which again is consistent with the previous observations of milky and low density ice. As explained above in sub-sections A, B and C the reasons to get high or low relative attenuation and, therefore, have an attenuation pattern close or far from the static clear ice reference, respectively, come down to the microstructure of the ice in direct contact with the sensor surface. Obviously, the more homogeneous the ice, the closer the attenuation values to the clear ice reference for all the wavelengths inspected.

5.3. Conclusions, outlook and suggestions for improvements

To finish this chapter, the summary and conclusions regarding the building and testing of the different prototypes of mid-IR water-ice sensors that have been finally integrated into an aircraft wing model are presented below.

1) The free-space prototype based on 3DLW LC waveguides embedded in fused silica allowed to corroborate the sensing principle as well as the sensor design that had been simulated (see Chapter 2). A waveguiding setup with temperature control down to -30 ºC was built in the optics

laboratory to cool down the water drops placed on the sensor surface. By employing a tunable mid-IR source, the spectral behavior for water and ice was measured and observed to be consistent with the simulated one, although with some minor discrepancies. Thus, the capability of distinguishing the liquid and solid phases of water was demonstrated.

2) Subsequently, the first fiber-coupled prototype was successfully built. ZBLAN fibers were coupled to the 3DLW waveguides for robust integration on surfaces. Experimental verification that the sensor could sustain simple icing experiments over a large range of temperatures without the need of constant realignment required by free-space optics was performed. Moreover, it was demonstrated its early-alert nature (minimum response time of 200 ms) by temporally resolving the water-ice transition.
3) The sensor evolved through the use of HC waveguides as a sensing element which provided better sensitivity and water-ice discrimination as it was demonstrated with simulations (Chapter 2). In addition, the sensor was flush-mounted on a wing model and tested in the IWT facility of IFAM (Germany). There, several icing tests simulating SW clouds with varying temperature (down to -25 ºC) and wind speeds (up to 95 m/s) conditions were carried out. Fast reaction times to ice accretion (around 1 s) were observed for mild and strong icing conditions. Even for weak icing conditions (i.e. temperature fluctuating around 0 ºC) the sensor signal evolution was enough to determine that icing was occurring. Differences in sensor output signal at both single and multiple wavelengths were seen due to ice homogeneity and density variations, which enabled ice type differentiation in terms of being more clear- or rime-like ice. This capability had been already predicted by simulations.
4) Apart from the purely sensing performance aspects, the IWT experiments demonstrated, for the first time to the author's knowledge, the integration of a mid-IR 3DLW waveguide sensor on a surface undergoing the harsh conditions found in industry, specifically, in the aerospace industry. The sensor has sustained droplets impacts at 95 m/s and extreme temperature swings of about 40 ºC without loss of performance. The

glass surface of the sensor and the optical fiber connections were intact after the IWT set of experiments

Unlike some of the already existing commercial ice sensors manufactured by e.g. Goodrich [3] or New Avionics [4], the proposed sensor in this Thesis may be incorporated on aircraft structures with no protrusion which provides evident aerodynamic benefits. For that purpose, the last prototype tested in the IWT could be further improved by shrinking its size while maintaining good sensitivity. In the longitudinal direction, this could be achieved, for example, by making the fiber connection well below the surface (this would require bending sections of the waveguide) and closing the gap of the top of the core waveguide to the surface. In the transversal direction, the glass substrate could be made thinner to the point of still making possible its handling for the integration process. The author believes that the area of the external surface of the sensor could be safely shrunk to 5 x 1 mm^2. Reduction of the fabrication tolerances when flush-mounting the sensor substrate on the aircraft element to protect would also make the device less aerodynamically intrusive.

Regarding the sensitivity of the sensor, no other commercial ice sensor can nowadays detect the ice nucleation on a surface in such early stages (minimum detectable ice thickness was found to be lower than 1 μm by simulations considering the experimental available SNR). Because of this, the sensor is capable of triggering an ice alarm faster than others, thus minimizing the required time and energy that de-icing systems need to remove the accreted ice. Since ice accretion can be produced on different zones of the wings and the entire aircraft body, a multitude of point sensors like the one presented in here would be needed to have an effective aircraft early-alert sensor. The ideal position of each one of the sensors as well as the processing of all the signals to activate an ice alarm and monitor the ice removal process would require an in-depth study that is out of the scope of the present Thesis.

Finally, the extension of the IWT experiments would provide further data on the ice accretion in more varied environments. No only more temperatures and wind speeds should be considered but other variables such as the droplets MVD or the

arrangement of the nozzles should be modified in order to test diverse types of supercooled clouds or even clouds formed by ice micro-crystals. With a large enough amount of data and the corresponding generated statistics, threshold levels for ice alarm and ice identification could be defined more accurately.

References

1. R. Wagner, S. Benz, O. Möhler, H. Saathoff, M. Schnaiter, and U. Schurath, "Mid-infrared Extinction Spectra and Optical Constants of Supercooled Water Droplets," The Journal of Physical Chemistry A **109**, 7099-7112 (2005).
2. http://www.ifam.fraunhofer.de/content/dam/ifam/en/documents/Adhesive_Bonding_Surfaces/Paint_Lacquer_Technology/ice_lab_en_fraunhofer_ifam.pdf
3. http://utcaerospacesystems.com/cap/systems/sisdocuments/Ice%20Detection%20and%20Protection%20Systems/Ice%20Detector%20Model%200871NA.pdf
4. http://newavionics.com/dev/wp-content/uploads/2016/03/9732-STEEL.pdf

CHAPTER 6

Mid-IR hybrid waveguide-SPP sensor for contaminant identification in aqueous solutions

In this final chapter, an integrated photonics sensor based on the excitation of surface plasmons in the mid-IR for the detection of contaminants in water is presented. The sensor takes advantage of the elevated refractive index of water and the possible contaminants in the 3 – 4 μm wavelength range, due to the presence of strong molecular fingerprints in that band, to promote the coupling of a silica 3DLW waveguide mode with an ITO thin film plasmonic mode. This hybrid plasmonic mode is highly sensitive to the changes of the external aqueous analyte. The structure is firstly simulated by means of numerical modal analysis to assess the existence of such mode and, hence, the feasibility of the sensing mechanism. Then, after fabricating the sensor following standard techniques, its performance is spectrally characterized for the particular case of ethanol detection in water by using a homebuilt mid-IR supercontinuum generated in an IR fiber. Lastly, once the most suitable band is identified, a mid-IR ICL laser tuned accordingly is employed to drive the sensor to provide low-noise detection of small concentrations of ethanol in contaminated water samples.

6.1. Motivation and introduction to SPP sensing

The goal of the optical water-ice sensor designed in Chapter 2 and tested in Chapter 5 is to detect the presence of ice in its early nucleation stages on a surface that in principle will be exposed to a harsh environment. For this reason, the concept of the sensor must be kept as simple as possible by avoiding elements that could be rapidly eroded in such conditions which, in turn, might lead to the failure of the whole detection system. On the other hand, since sensing by taking advantage of the OH features of the water molecule in the 3 – 4 μm spectral range is a powerful tool, the developed sensor could be easily deployed in more controlled laboratory environments as a simple water quality sensor. However, such sensors normally require much higher sensitivity (i.e. ≈ 1 – 100 ppm of pollutant in water) than that of the previously presented water-ice sensor. An elegant and well-established way of increasing the sensitivity of chemical and biological optical sensors consists in the resonant excitation of surface plasmon polaritons (SPPs) on metallic thin films or nanostructures which are in direct contact with the analyte. In this chapter, a mid-IR SPP sensor for water quality control is proposed. The device takes advantage of the 3DLW fused silica waveguides to couple a mid-IR surface plasma wave on the surface in contact with an aqueous analyte. The published article arising from this work can be found in Appendix E (Paper II) Before presenting the device model (Section 6.2), a basic summary of the fundamentals of SPPs and their application in chemo/biosensing is provided below.

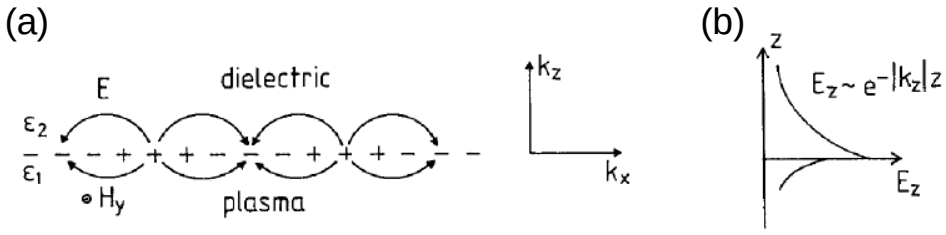

Figure 6.1. (a) Schematic showing the charge density oscillation on a single metal-dielectric interface together with the propagating TM field in the x direction and (b) decaying in z direction. Adapted from [1].

6.1.1. SPP very basics

Since the first theoretical investigations on surface plasmons [2] and its subsequent experimental verification [3, 4] back in the late 50's and beginnings of 60's, a huge number of researchers have investigated the SPP phenomenon from the very fundamental perspective to their application [1, 5] in many fields such as nanophotonic circuits [6, 7], surface-enhanced Raman spectroscopy [8] or chemo/biosensors [9, 10]. In particular, plasmonic sensors, either in propagating or localized (LSPP) form, have received substantial attention due to its inherent high sensitivity arising from the extraordinary field confinement (sometimes even below the diffraction limit) and enhanced light-matter interaction [11].

Essentially, a SPP is a charge density oscillation of the metal's free electron gas (*plasma*) at the metal-dielectric interface (*surface*) which is resonantly coupled to a light wave (*polariton*) which is tied to the surface and whose maximum intensity is located at the interface itself and decays exponentially into both mediums [1, 5], as it is shown in Figures 6.1(b). Normally the element enabling the SPP wave is made of metal, such as gold, silver or aluminum, or other materials presenting metallic behavior within a certain operating wavelength range, like some semiconductors or even graphene.

The simplest geometry supporting SPPs is the planar single metal-dielectric interface (see Figure 6.1(a)). Exact solutions of the surface confined waves can be retrieved by solving the Maxwell equations and using the appropriate boundary conditions on this geometry. In particular, the single-interface SPP dispersion relations of the TM solution (note that TE SPP solutions cannot exist) can be written as follows [1, 5, 12],

$$k_x = \frac{\omega}{c}\sqrt{\frac{\varepsilon_1\varepsilon_2}{\varepsilon_1+\varepsilon_2}} = \left\{\frac{\omega}{c}\sqrt{\frac{\varepsilon_1'\varepsilon_2}{\varepsilon_1'+\varepsilon_2}}\right\} + i\left\{\frac{\omega}{c}\sqrt{\left(\frac{\varepsilon_1'\varepsilon_2}{\varepsilon_1'+\varepsilon_2}\right)^3}\frac{\varepsilon_1''}{2(\varepsilon_1')^2}\right\} \qquad \textit{Eq. 6.1}$$

$$k_{zj} = \sqrt{\varepsilon_j \left(\frac{\omega}{c}\right)^2 - k_x^2} \quad , \quad j = 1, 2 \qquad \textit{Eq. 6.2}$$

where k_x is the SPP x wave vector, ω is the angular frequency of oscillation, c the speed of light, ε_1 the complex relative permittivity of the metal ($\varepsilon_1 = \varepsilon_1' + i\varepsilon_1''$), ε_2 is the relative permittivity of the dielectric, k_{zj} is the z wave vector where j can be either 1 (metal) or 2 (dielectric). Assuming that ε_2 is real (i.e. medium 2 is a lossless dielectric) and $\varepsilon_1'' < |\varepsilon_1'|$, one can demonstrate that k_x is complex [1] so that $k_x = k_x' + ik_x''$ as shown above. Moreover, in order to have real k_x', ε_1' must be negative and meet $|\varepsilon_1'| > \varepsilon_2$ which is true for most metals at visible and near-IR wavelengths [1, 5]. Likewise, as k_x'' will not become null, the SPP wave will attenuate as it propagates. On the other hand, given all the previous conditions, k_{zj} becomes purely imaginary which explains the exponential decay of the field in the direction perpendicular to the interface. Note the wavelength-dependence nature of SPPs, which implies that there is an optimum wavelength at which its performance is maximized in terms of losses and/or confinement.

The wave vectors defined in Equations 6.1 and 6.2 exactly determine the physical extent of the surface plasmon waves [1, 5]. Particularly, the propagation length L_x (referred to field intensity) and the transversal field confinement (or decay length) L_{zj} in the medium *j* are calculated as follows,

$$L_x = (2k_x'')^{-1} \qquad \textit{Eq. 6.3}$$

$$L_{zj} = |k_{zj}|^{-1} = \frac{c}{\omega}\sqrt{\frac{|\varepsilon_1'| + \varepsilon_2}{\varepsilon_j^2}} \quad , \quad j = 1, 2 \qquad \textit{Eq. 6.4}$$

From all these equations, it can be also deduced that the more the SPP field is bound to the surface the lower the distance that it can propagate before being fully attenuated. This tradeoff between localization and loss is something that applies to plasmonics in general [5]. There are many other geometries supporting SPPs modes, such as the commonly used planar thin metallic films of few nm surrounding by dielectric layers [3, 13]; 3D plasmonic waveguides [14, 15]

resembling their dielectric counterparts; or optical nanoantennas [16, 17], which have LSPP resonances and add a further localization down to the nanometer scale and sensitivity. Nevertheless, the general trends extracted from the single-interface SPP analysis are fully valid for the rest of cases. Furthermore, the exact properties of the SPP will depend on the particular geometry, the metal type and quality, the excitation wavelength and the type of interrogation system.

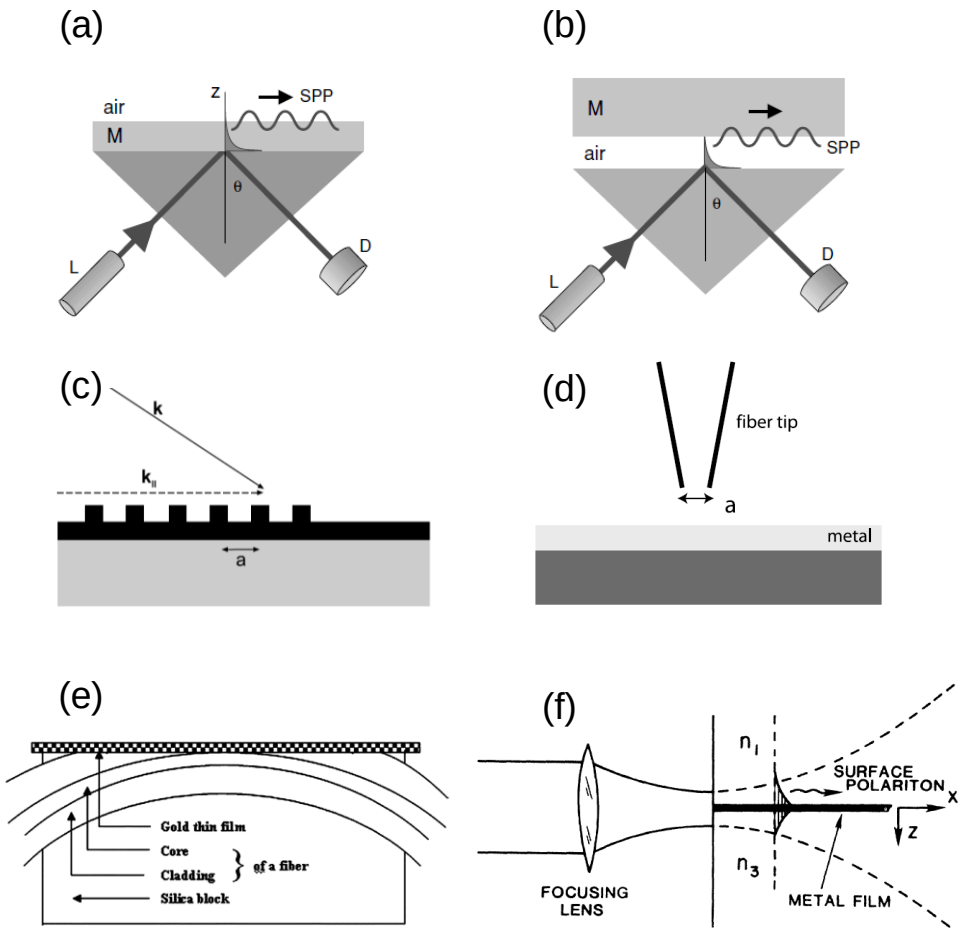

Figure 6.2. Some examples of different methods of SPP excitation. Prism coupling technique in the (a) Kretschmann and (b) Otto configuration (adapted from [12]), (c) grating coupling (adapted from [5]), (d) local near-field coupling (adapted from [5]), (e) side-polished (evanescent) coupling (adapted from [18]) and (f) end-fire coupling (adapted from [19]).

The increased confinement of surface plasmons comes at the expense of a greater propagation constant relative to that of a freely propagating wave would have had in the dielectric (i.e. $k = \omega / v_p$). For this reason, typically, special optical schemes need to be applied to excite SPP modes by light so as to match its lower phase velocity. The most commonly used for decades, particularly in biosensing [9], has been the prism coupling technique either in the Kretschmann [20] or Otto [21] configurations. Both take advantage of the total internal reflection produced within a prism which is in direct contact with a metallic film (Kretschmann) or separated from it by a small air gap (Otto). The produced evanescent wave penetrates into the metal and can couple into a SPP mode for certain angle that promotes the matching of propagation constants. When the surface plasmon has been effectively excited, a dip in the angular spectrum for monochromatic excitation or a dip in a wavelength spectrum for broadband excitation can be observed [9]. Other methods of excitation include grating couplers [1], local near-field methods [22], fiber-based excitation [18], and even efficient end-fire coupling for some particular type of surface plasmons called long-range SPP [15]. Schematics illustrating these examples are shown in Figure 6.2.

6.1.2. SPP sensing in the mid-IR

When a SPP is excited, the near-field intensity just around the interface is remarkably strong [12, 14] with respect to the incident field, making the SPP coupling extremely sensitive to even the slightest changes on the refractive index of the dielectric (i.e. the analyte in the case of sensors) in contact with the metal. Typically, in chemo/biosensors, these refractive index variations are produced by certain events such as a chemical change of the analyte or the presence of a particular biomolecule on the metallic surface. In most cases, the metallic surface needs to be chemically treated (i.e. functionalized) to immobilize a particular analyte [9], therefore configuring a so called *chemical sensor*. The coupling of the incident field with the SPP can be measured by monitoring and analyzing a certain sensor output, such us angular spectrums, wavelength spectrums, intensity changes, phase shifts, etc. The chosen sensor output depends basically

on the particular method of excitation, the configuration of the sensor and the expected variation on the refractive index of the substance under analysis.

For decades, the SPP effect for sensing applications have been intensively investigated in the visible and near-IR ranges since there conventional metals, such as gold or silver, can support highly confined plasmonic modes that provide high sensitivity by enhancing the interaction with the analyte. Moreover, SPP sensing in these short bands is purely based on refractive index sensing [9] which completely neglects the opportunities that the mid-IR range can provide. As explained at the beginning of this Thesis (Chapter 1, Section 1.4), in the mid-IR there are strong vibrational and molecular absorptions that might be used to boost optical chemo/biosensing mechanisms. In particular, if the wavelength is tuned appropriately, the SPP sensing effect might be enhanced by either detecting the mid-IR absorption of interest or the large refractive index variation associated to it. Furthermore, in some cases, one may not need to functionalize the surface as probing directly the molecular resonances naturally allows pure optical spectroscopic differentiation of different chemical constituents [23, 24].

Traditional plasmonic metals perform poorly in terms of confinement in the mid-IR given the degradation of their dielectric function at longer wavelengths [23, 25], as described below. The most promising route to overcome this problem is to use different materials that can mimic, in the mid-IR, the extraordinary optical properties that conventional metals have at shorter wavelengths [23]. These materials include, among others, doped semiconductors [26], conducting metal oxides [27], transparent conducting oxides [28, 29], and graphene [30].

Noble metals have excellent plasmonic characteristics in the visible and near-IR due to their intrinsic high carrier concentration and relative low losses [31]. The Drude model is an accurate way of describing the optical properties (i.e. the frequency-dependent complex relative permittivity $\varepsilon(\omega)$) of a metal, as it is shown in Equation 6.5 [5, 31],

$$\varepsilon(\omega) = \varepsilon' + i\varepsilon'' = \varepsilon_b - \frac{\omega_p^2}{\omega^2 + \gamma^2} + i\frac{\omega_p^2 \gamma}{(\omega^2 + \gamma^2)\omega} \qquad \textit{Eq. 6.5}$$

where ε_b is the background relative permittivity, ω_p is the plasma frequency and γ is the relaxation rate. The square of the plasma frequency is directly proportional the material's carrier concentration, whereas the relaxation rate accounts for the metal losses. Plasmonic sensing requires high field confinement with the minimum losses possible so as to achieve good spatial overlap between the surface field and the analyte thus obtaining sharp resonances leading to high sensitivity. For that reason, at the wavelength of interest the selected plasmonic material should have low $|\varepsilon'|$ compared to that of the surrounding dielectric in order to keep high confinement (see Equation 6.4).

Figure 6.3 shows the complex permittivity of gold, which is arguably the most popular plasmonic material used in the visible and near-IR ranges, from λ = 0.3 μm to 10 μm. This data is retrieved from [32] and consists of spectroscopic ellipsometry measurements of evaporated gold. As it is observed, below λ = 1 μm, gold has excellent plasmonic properties since its $|\varepsilon'|$ is comparable to that of common dielectric substrates while ε'' is kept small enough, around the unit. On the other hand, as the wavelength rises, both $|\varepsilon'|$ and ε'' grow rapidly so that around λ = 3.5 μm (region of interest is marked in green) they are about two orders of magnitudes higher than in the visible. This has a significant negative impact on the confinement capability of a hypothetical SPP gold sensor working in the mid-IR. For instance, considering a single-interface SPP (see Figure 6.1) involving gold and a dielectric having a refractive index of 1.5 (dispersion ignored), the decay length (Equation 6.2) within the dielectric would be approximately 0.4 μm, 9 μm and 70 μm for λ = 0.8 μm, 3.5 μm and 10 μm, respectively. The fact that gold, as most metals, has a high free carrier concentration (≈ 10^{22} cm^{-3}) makes ω_p^2 so large that the cross-over frequency (frequency above which ε' turns positive) lays in the UV. Conversely, the alternative materials mentioned previously have lower carrier concentration, which is sometimes tunable during fabrication or even electrically, leading to a redshifted cross-over frequency which, in turn, makes $|\varepsilon'|$ smaller around the

desired mid-IR range. For this reason, a transparent conductive oxide (TCO) having a reduced ω_p^2 relative to that of gold was used for the here proposed plasmonic device as shown in the next section.

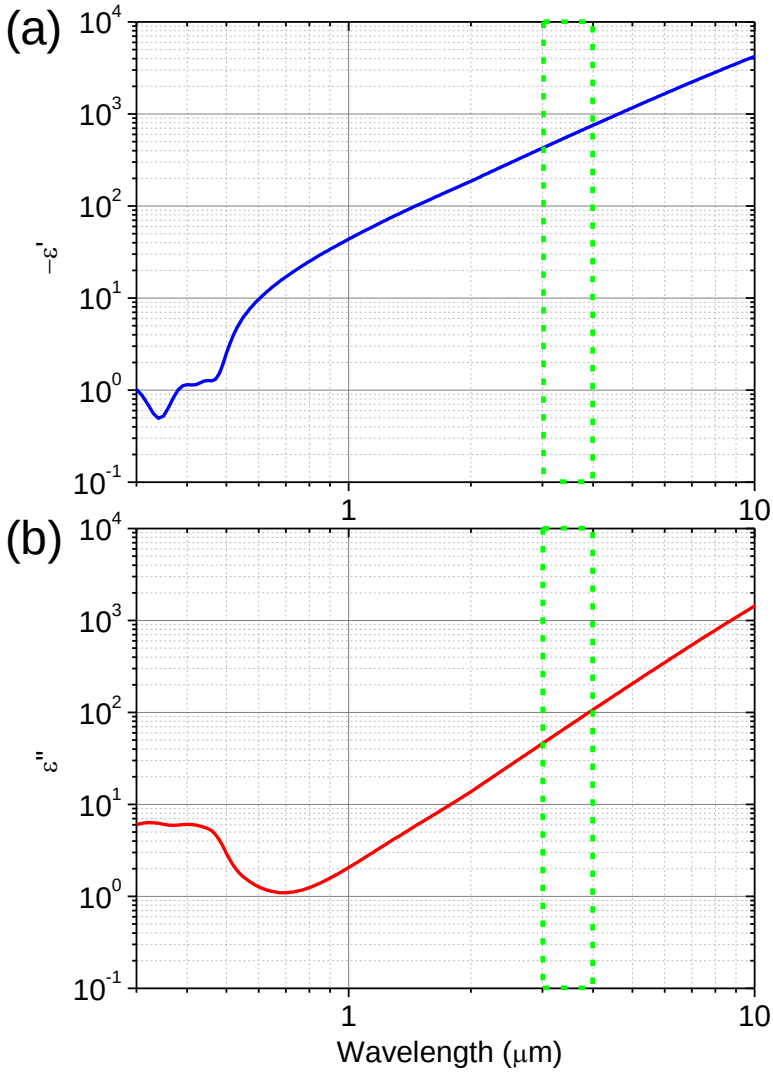

Figure 6.3. Relative permittivity of evaporated gold in the 0.3 μm to 10 μm range taken from [32]: (a) real (note opposite sign) and (b) imaginary part.

6.2. Concept development and fabrication

This section describes in detail the modelling process and the theoretical calculations carried out to evaluate the performance of the hybrid waveguide-SPP sensor. At the end, the fabrication process is also explained but in a brief way since the majority of the sensor hardware is inherited from the water-ice sensor presented in previous chapters.

6.2.1. Sensor model

Visually, the model of the mid-IR SPP sensor (Figure 6.4) is very similar to the ice sensor presented back in Chapter 2. In fact, the idea was to take maximum advantage of all the fabricated structures.

Essentially, it consists of a 3DLW step-index single-mode waveguide (core dimensions *W* x *H*) embedded in fused silica that routes narrow or broadband mid-IR light towards the sensing surface which is coated with an indium tin oxide (ITO) thin film with *TH* thickness that can support a SPP in the 3 – 4 μm wavelength range when covered by an aqueous analyte. ITO, a type of TCO, is chosen over gold because its superior properties within this range as well as its transparency in the visible that may be useful for certain applications. When the waveguide is brought a few microns close to the thin film (*G* parameter), the evanescent tail of the confined mode can effectively couple to a SPP mode under certain conditions, giving rise to a new coupled hybrid waveguide-SPP mode. This type of coupling technique is basically the same as the one illustrated in Figure 6.2(e). The loss associated to this mode directly depends on the coupling strength of the waveguide mode to the SPP (lossy) mode which, in turn, is determined by the refractive index of the analyte above, particularly, within the region limited by the plasmon penetration depth. After a certain interaction distance *L* with the analyte in which light propagates sustaining a certain loss, the waveguide routes the signal to the suitable detector that monitors its output power level. This output will be extremely sensitive to chemical changes of the aqueous sample.

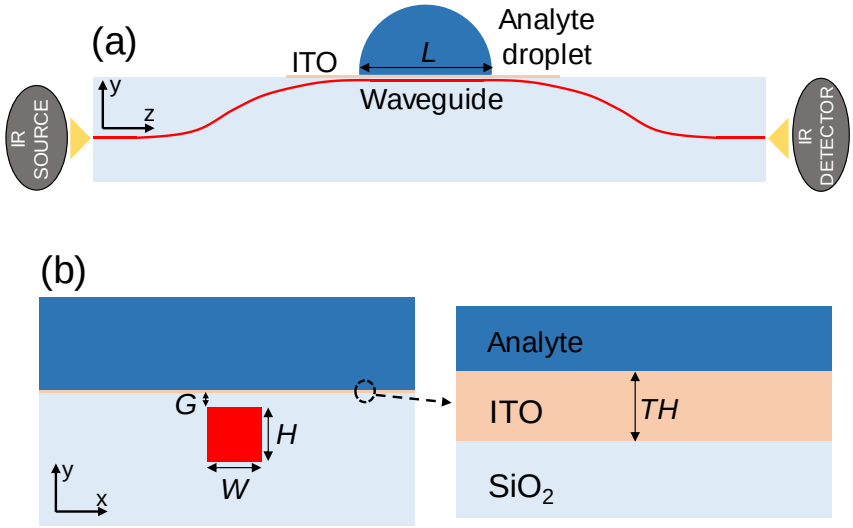

Figure 6.4. Sketch of mid-IR SPP chemical sensor proposed in this chapter covered by a droplet of an aqueous analyte. (a) Lateral view and (b) front view with a zoom of the droplet-substrate interface showing the ITO thin film.

So far, the working principle looks very similar to others SPP sensors found in the literature. However, here the existence of a mid-IR SPP mode confined to an ITO thin film is possible due to the abnormally (compared to that at visible and near-IR wavelengths) high refractive index of water, which is originated by the OH absorption of the H_2O molecule around 2.9 μm as explained in Chapter 2, which closely matches that of fused silica. Consequently, there is a symmetry between the two materials (i.e. silica and the aqueous analyte) surrounding the ITO thin film. This promotes an SPP mode to which a weakly guided mode can evanescently couple without requiring special methods such as grating coupling [33] or intermediate buffer layers [34]. Since the effective index of the 3DLW waveguide fundamental mode and that of the SPP mode supported by the ITO film closely match at a certain wavelength within the 3 – 4 μm range, a hybrid waveguide-SPP mode can exist when the waveguide core is brought close enough to the ITO film. It is known that metallic (or metallic-like) thin films surrounded by two dielectrics with similar optical properties support symmetric SPP modes [15] whose wave vector is not too large (obviously at the expense of

less confinement) compared to that of a plane wave propagating in one of the dielectrics. That is the reason why a simple low-contrast 3DLW waveguide mode can directly couple to a plasmonic mode.

For pure water, at a particular wavelength ($\lambda_{match,w}$), the waveguide-SPP coupling is optimum, meaning that the coupling from the waveguide mode to the SPP hybrid mode will be maximum and thus the output power will decrease as propagation losses of such new mode are higher. The existence of optical absorptions associated to other functional groups that water contaminants might contain introduce variations in the complex refractive index of the aqueous analyte. These variations are stronger around the mid-IR wavelength associated to the molecular resonance than at shorter wavelengths, thus enhancing the sensor's sensitivity [24]. These refractive index changes affect the SPP coupling and, hence, the intensity and the spectrum of the transmitted light as well. Later in Section 6.3, the case of sensing ethanol contaminants in water will be addressed.

6.2.2. Modal simulations setup

The sensor performance was investigated through electromagnetic finite element method (FEM) simulations using the commercial software COMSOL Multiphysics. Instead of solving the wave propagation as was done in Chapter 2 using Rsoft BeamPROP, only modal analysis in the frequency domain was performed employing COMSOL. This is due to the high computational cost that would have involved simulating a structure containing nanometric features (ITO thin film) for millimeters long propagation distances. Conversely, a simple modal analysis using the appropriate fine mesh around the thin film can reveal when the waveguide-SPP coupled mode occurs as well as the losses associated to it.

The cross-sectional view of the parametrized model that was built on the COMSOL interface is shown in Figure 6.4(b). The dielectric properties of the materials involved are found in Figure 6.5 for the wavelength band of interest (3 – 4 μm). The fused silica and water refractive indices and extinction coefficients were taken from the literature as in Chapter 2 (i.e. [35] and [36], respectively).

Regarding ITO, its complex refractive index was calculated through the Drude model to obtain its complex relative permittivity and applying the relation $n = \sqrt{\varepsilon}$. The parameters used (ε_b, ω_p and γ) were extracted from the fitting of transmittance measurements of the actual deposited thin film (see Section 6.2.5 for details about the deposition process). In Appendix C, the procedure followed to get the best fitting Drude parameters is thoroughly described. These are ε_b = 3.94, ω_p = 3.26·10^{15} rad/s and γ = 1.88·10^{14} rad/s.

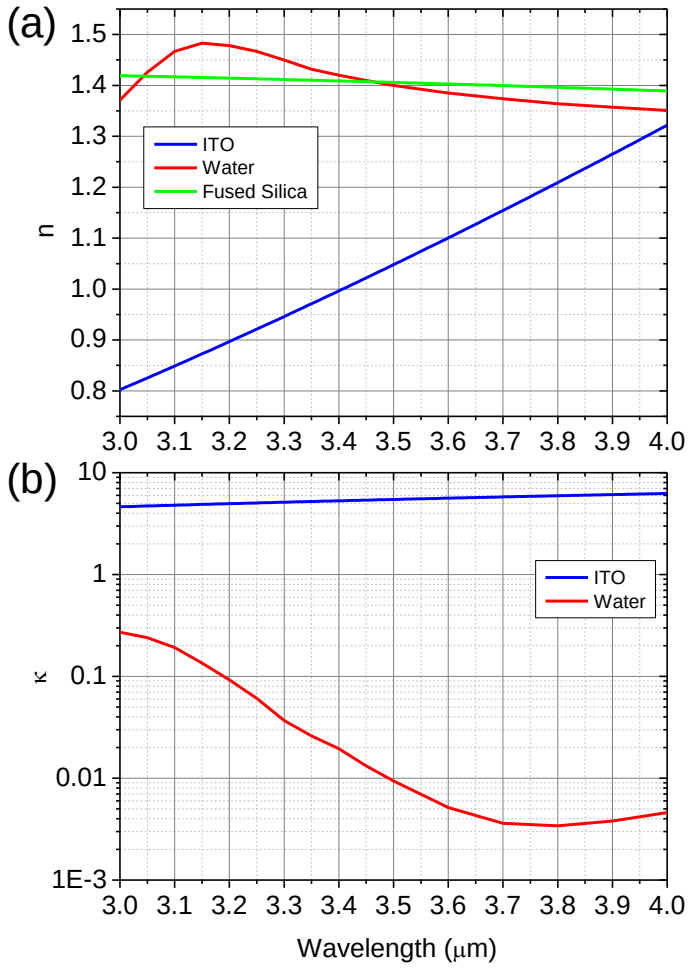

Figure 6.5. (a) Refractive index and (b) extinction coefficient dispersion of the materials involved in the COMSOL simulations. Fused silica curve is not depicted in (b) because it is assumed to be lossless in the whole range.

As it was seen in Chapter 2, the refractive indices of fused silica and water match around 3.5 μm. Regarding ITO, it is worth noting its metallic nature at these wavelengths. The fact that its extinction coefficient is larger than its refractive index makes its relative permittivity negative which is something that normally occurs in metals at visible and near-IR wavelengths. At 3.5 μm, ε_{ITO} = -28.7 + i11.4 which demonstrates that ITO is already a better plasmonic material than gold (ε_{gold} = -580.7 +i72.69) in terms of confinement and losses in this specific IR band. However, this particular ITO thin film is still far from being the perfect plasmonic material. The further optimization of the plasmonic characteristics of TCO thin films is nowadays under intense research, and is out of the scope of this Thesis.

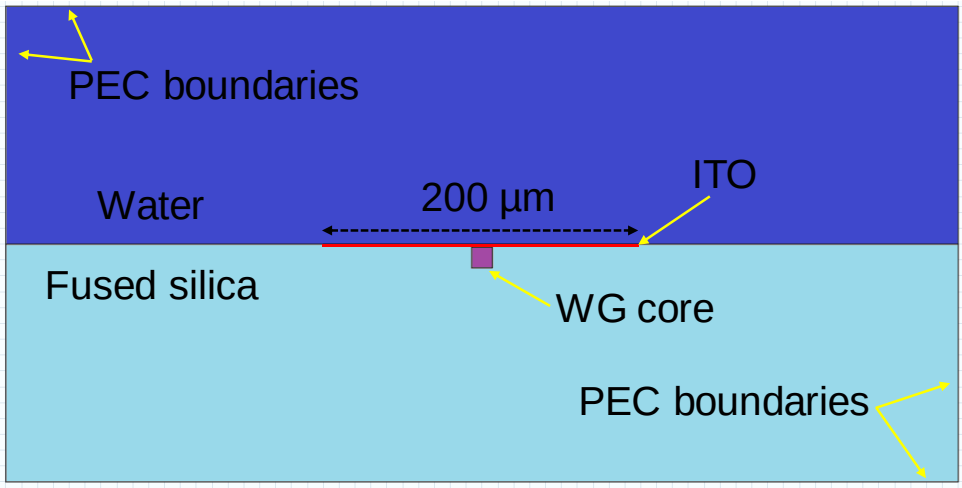

Figure 6.6. Sensor geometry built in COMSOL. The ITO layer is highlighted in red.

Figure 6.6 shows the COMSOL geometry employed which consists of an ITO thin film (in red) on a fused silica substrate covered by water. Just below the ITO layer, a step-index square waveguide (in purple) was placed. The simulation domain was limited by perfect electric conductor (PEC) boundaries. In order to limit the PEC effect on the calculated modes, the domain size was significantly larger than the waveguide core and thin film. Furthermore, note that the width of the thin film was chosen to be large (200 μm) compared to that of the waveguide underneath but still finite, as opposed to reality. As it will be described later (Section 6.2.5),

the actual deposited ITO thin film extended over the whole silica substrate forming a planar geometry. Given the PEC boundaries and their impact on the modes calculation, a limited width was needed. This was still a good approximation because only SPP bound modes around the waveguide core were being searched.

6.2.3. Hybrid waveguide-SPP coupled mode

The mode profiles corresponding to the ITO thin film and the dielectric silica waveguide when water is covering the structure were firstly calculated separately at λ = 3.49 µm (see Figures 6.7(a), (b) and (c)). The ITO layer thickness was set to *TH* = 54 nm as this was the thickness measured in the real deposited film (Section 6.2.5). The waveguide was assumed to be square and step-index with *W* = *H* = 13 µm and refractive index change of $\Delta n = 8 \cdot 10^{-3}$. The gap to the surface was set to *G* = 1 µm. The mesh was triangular and non-uniform given the large differences in size of the different components of the geometry, so that smaller features were resolved by a finer mesh (e.g. a 7 nm was used for the thin film).

Figure 6.7(a) shows that the structure water-ITO-silica supports a guided TM plasmonic mode. The horizontal confinement is due to the limited width of the ITO thin film that does not occur in reality, as aforementioned. In Figures 6.7(b) and 6.7(c), the intensity profiles corresponding to the TE and TM modes of the dielectric waveguide (no ITO on the water-silica interface) are shown. Note the similarity between the real part of the effective indices of the SPP mode and the waveguide TM mode, which implies phase matching when combined.

Subsequently, the whole structure (waveguide plus thin film) was simulated at the same wavelength (Figure 6.7(d)). The mode field profile shows the effective coupling between the SPP and waveguide modes. The electric field is spatially shifted slightly upwards and its evanescent tail penetrates well into the water. Although this hybrid mode is not purely plasmonic, it is still sensitive to dielectric changes in the aqueous analyte above. Furthermore, it has the advantage of being coupled from a TM waveguide mode (Figure 6.7(c)) with low mode

overlapping losses. The field penetration depth into the water is measured to be 3.2 μm after an exponential fitting.

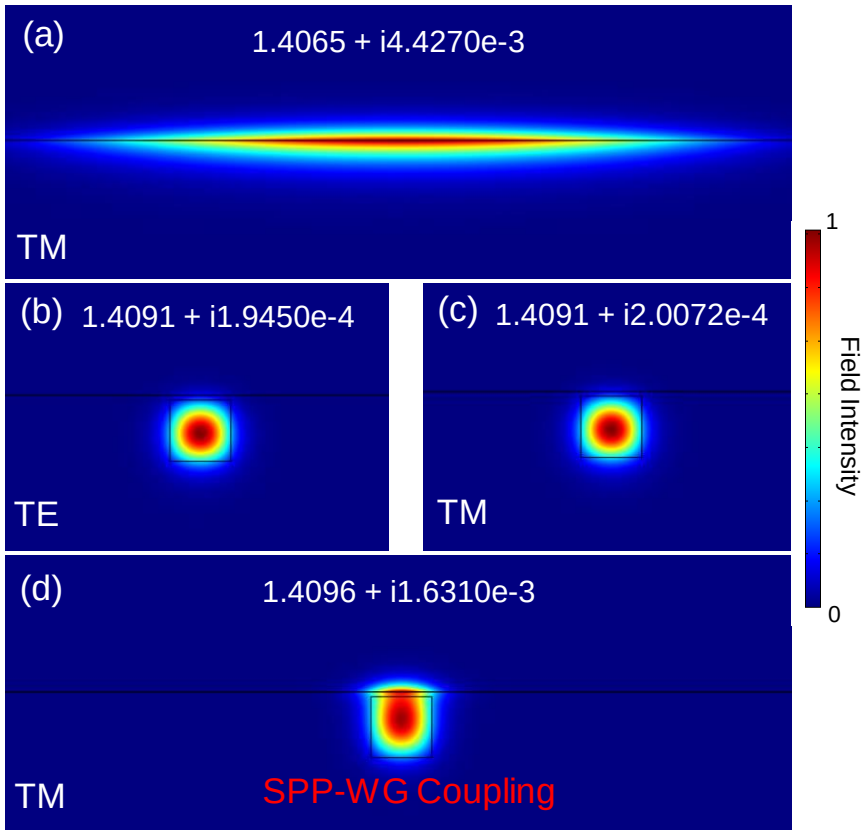

Figure 6.7. Calculated electric field intensity profile at λ = 3.49 μm of (a) the isolated ITO thin film SPP mode, the isolated waveguide (b) TE mode and (c) TM mode, and (d) the hybrid waveguide-SPP mode. The mode effective index is indicated in the upper part of each image. Water covers the sensor in all the cases.

Figure 6.8 demonstrates that the hybrid waveguide-SPP mode only exists when water or an aqueous analyte covers the sensor for TM polarized light. If the cover material is air (Figures 6.8(a) and (b)) only a waveguide mode is supported by the structure for TE and TM polarizations which is spatially shifted towards the silica substrate due to the presence of a metallic layer (ITO) and a low index material (air) on top of it. Similarly, for a water cover and TE polarization (Figure 6.8(c)) no

SPP mode exists since plasmonic modes are intrinsically TM polarized. Lastly, for water and TM polarization, phase matching is achieved and the hybrid mode is supported, (Figure 6.8(d)).

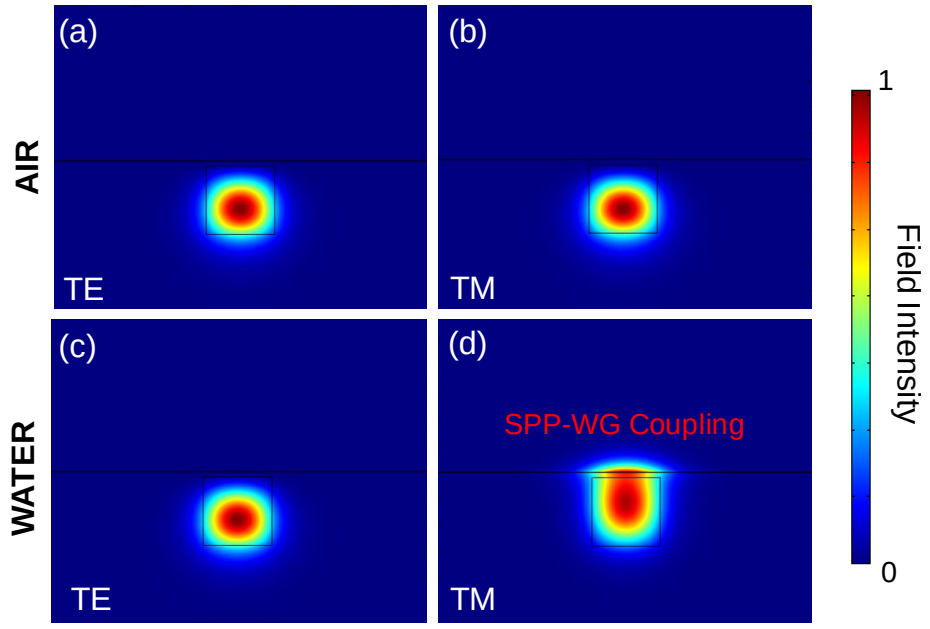

Figure 6.8. Calculated electric field intensity profile at λ = 3.49 µm of the (a) TE mode and (b) TM mode of the structure when air covers it. (c) TE mode and (d) TM (hybrid) mode of the structure when water covers it. Note that the ITO thin film is present in all four cases.

6.2.4. Mode dispersion and gap effect

Operation out of the wavelength of maximum waveguide-SPP coupling was simulated in order to find out the width of the resonance.

The TM field intensity mode profiles provided in Figure 6.9 allow to clearly see how the coupled mode behaves below and above the optimum matching wavelength ($\lambda_{match,w}$ = 3.49 µm). Note that the field is evenly distributed over both dielectric waveguide and thin film at this optimum point. Moreover, the spectral trend is not symmetric around the optimum point due to the particular dispersion of water around this wavelength (see Figure 6.5).

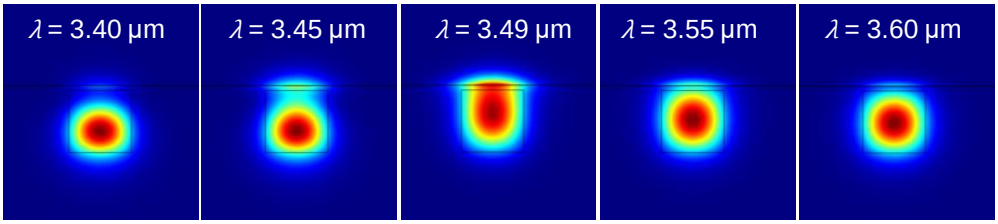

Figure 6.9. Calculated electric field intensity profile of the waveguide-SPP mode for various particular wavelengths within the 3.40 μm to 3.60 μm range. Gap set to 1 μm.

For each particular wavelength, one can calculate the corresponding modal attenuation in logarithmic units per unit length just from the obtained extinction coefficient. The light associated to a given mode propagates with a certain attenuation coefficient α_m which is defined as,

$$\alpha_m = \frac{4\pi\kappa_m}{\lambda} \qquad \textit{Eq. 6.6}$$

where κ_m is the mode extinction coefficient and λ the free-space wavelength. This attenuation coefficient determines an exponential decay of the light intensity after a certain propagation length L:

$$\frac{P_o}{P_i} = e^{-\alpha_m L} \qquad \textit{Eq. 6.7}$$

where P_o/P_i is the output to input light power ratio. If the L and α_m units are mm and mm^{-1}, respectively, the mode attenuation MA expressed in dB/mm becomes

$$MA = \frac{-10\log\left(\frac{P_i}{P_o}\right)}{L} = \frac{-10\log(e^{-\alpha_m L})}{L} = 10\alpha_m \log(e) \qquad \textit{Eq. 6.8}$$

Then by combining Equation 6.6 and 6.8 and having λ in mm one gets

$$MA = \frac{10 \cdot 4\pi\kappa_m \log(e)}{\lambda} \qquad \textit{Eq. 6.9}$$

Now the mode attenuation for water (MA_w) covering the sensor (i.e. the TM mode corresponding to Figure 6.8(d)) relative to that (MA_a) when nothing, only air (e.g.

the TM coupled mode corresponding to Figure 6.8(b)), is on it can be calculated simply as follows,

$$MA_{w-a} = MA_w - MA_a \qquad \textit{Eq. 6.10}$$

The relative mode attenuation MA_{w-a} is a useful theoretical figure of merit that allows fast comparison of the attenuation undergone by the different modes supported by the sensing structure. The experimentally measured attenuation per unit length due to the presence of an aqueous substance is closely related to this value but it is not exactly the same as it will be explained later Section 6.3. Nevertheless, MA_{w-a} is still a valid tool to study the theoretical sensing performance of the device.

By applying Equations 6.9 and 6.10 to the extinction coefficients of the computed modes at various wavelengths, one is able to obtain a relative attenuation spectrum that visually helps to identify the wavelength at which the coupled waveguide-SPP mode gives maximum attenuation. This may not coincide to that giving optimum waveguide-SPP coupling at $\lambda_{match,w}$. Figure 6.10 shows the relative mode attenuation spectrum for the only gap studied so far (*G* = 1 μm) as well as for larger gaps.

For *G* = 1 μm the maximum mode attenuation occurs at 3.47 μm due to the larger portion of field around the lossy ITO layer. However, the mode to which a TM waveguide mode (e.g. those shown in Figure 6.7(c) and 6.8(b)) will be able to couple more efficiently, since their better overlapping, is the one at $\lambda_{match,w}$ = 3.49 μm which has substantially lower mode attenuation. Although, one may need a wave propagation analysis to exactly determine the position of the maximum attenuation undergone by broadband light launched into the sensing waveguide, it would be expected to be within these range (i.e. 3.45 – 3.50 μm).

Regarding the rest of curves corresponding to larger gaps, the maximum attenuation obtained is significantly lower and the resonance width is broader which means that the sensing performance is degraded as the gap increases. The reason for this is the reduced overlap between the waveguide and the SPP modes which prevents a good waveguide-SPP coupling. Anyhow, these

calculations are still convenient since 1 μm gap was difficult to obtain later in the fabrication stage due to tolerance issues, whereas gaps of around 3 μm were obtained without risking the integrity of the dielectric waveguide.

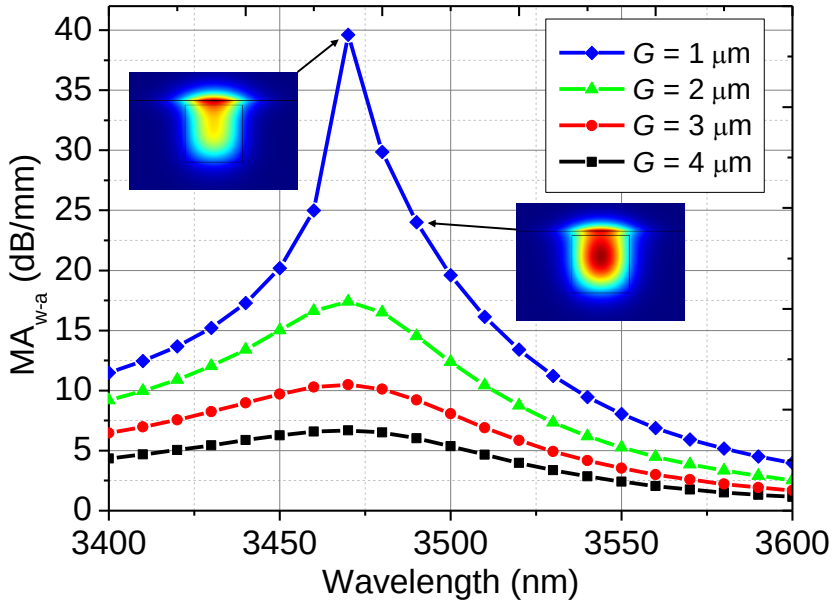

Figure 6.10. Calculated relative (water to air) mode attenuation spectrum for different gaps between the waveguide and the ITO thin film. Mode profiles for λ = 3.47 μm and 3.49 μm depicted for comparison purposes.

6.2.5. Hybrid waveguide-SPP sensor fabrication: 3DLW and ITO coating

The fused silica waveguide was fabricated employing the 3DLW technology described in Chapter 3 so as to obtain step-index channel waveguides. The laser writing parameters used can be found in Section 3.7.3. Straight waveguides were fabricated for the sake of simplicity since this does not affect the sensing performance evaluated afterwards due to the measurements being always normalized to an air reference. After the writing process, the fused silica sample was physically polished so that the gap between the top of the core and the surface was minimized without breaking the waveguide. Moreover, slight angular

deviation in the polishing process caused a non-constant gap from side to side of the sample. The average gap corresponding to the input and output faces of the sample was $G = 3.3$ μm for the particular waveguide employed in the experiments.

The ITO thin film was deposited on the silica surface via DC magnetron sputtering following similar processes to those found in the literature [37, 38]. The sputtering target was an indium-tin alloy having a In_2O_3/SnO_2 weight ratio of 90/10 %. The chamber was oxygen-free and the sample was kept at room temperature during the deposition. The sputtering power density was set to 2 W/cm^2 which provided a 54 nm thick ITO film for 24 minutes of deposition. By means of a previous deposition of ITO on a silicon substrate that was characterized using a precision optical profilometer with an error of ±5 nm, the thickness measurement could be correctly calibrated. This thickness was further corroborated in the fitting of transmittance measurements [39] described in Appendix C which were conducted in order to find out the actual electro-optical properties of the ITO thin film (already given in Section 6.2.2).

Following the deposition of the ITO thin film, the whole sample was annealed at 400ºC for one hour in a N_2 atmosphere as described in [40]. The 3DLW waveguides kept good guiding properties after the annealing as it was demonstrated in Chapter 4. The annealed film had improved properties (i.e. higher carrier concentration and mobility) enabling SPP modes in the range of interest as well as higher transparency. The estimated thin film optical properties were provided in Figure 6.5.

A sketch of the sensor tested in the experimental stage is depicted in Figure 6.11. Notice that ITO was not sputtered over the whole sensor surface but only on the central part. Furthermore, a microscope image of the selected sensing waveguide reveals its true size, which is $W \times H = 11.8 \times 12.7$ μm^2.

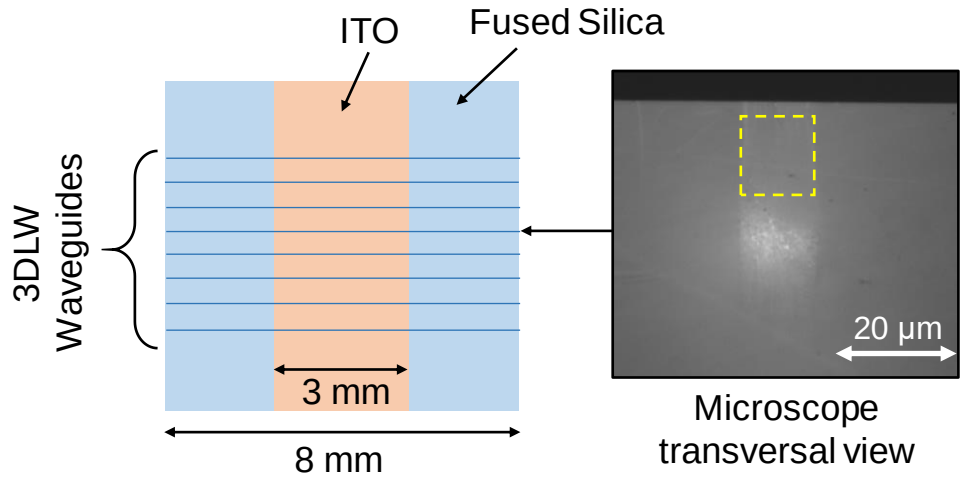

Figure 6.11. Sketch of the top view of the fabricated SPP sensor together with a microscope image showing the 3DLW waveguide (core marked in yellow) chosen for the experimental stage.

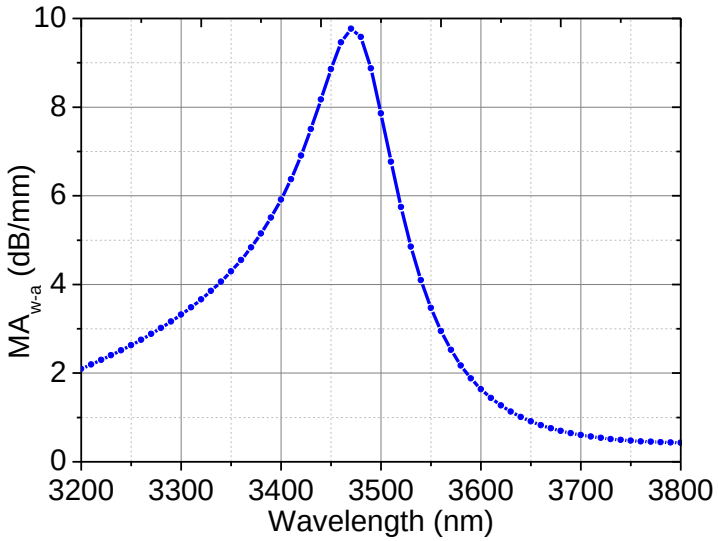

Figure 6.12. Calculated relative (water to air) mode attenuation spectrum taking the parameters from the real device, namely $\Delta n = 8 \cdot 10^{-3}$, W x H = 11.8 x 12.7 µm^2, G = 3.3 µm and TH = 54 nm.

Finally, a simulation to calculate the relative mode attenuation for the real fabricated SPP sensor was run (Figure 6.12). A greater number of spectral points were taken as well as a broader range. This theoretical curve will be compared to the measured attenuation spectrum obtained later in the experimental section.

6.3. Sensing performance evaluation by detecting ethanol contamination in water

The water-ethanol mixture is an appealing topic to engineers and researchers of many fields either from the fundamental [41, 42] or the applied [43, 44] point of view. Hence, sensors able to detect small variations of ethanol or water within the mixture are of special interest. The molecular structure of the water-alcohols systems in general is complex and still subject of scientific debate nowadays [45]. For this reason, it is not the aim of this chapter to study such complex system, but just the performance of the sensor itself without explaining or searching for the primary causes of the obtained results.

Just by examining the dielectric properties of water [36] and ethanol [46] one may understand why working in the mid-IR range can improve the sensing capabilities the optical sensor. Figure 6.13 shows the real part and imaginary parts of the complex refractive index of each liquid at room temperature. Roughly, for wavelengths lower than 2.5 μm the dispersion curves remain quite parallel. On the contrary, when approaching to the broad OH stretching band around 2.9 μm the curves start to deviate from each other. In the range of interest (3 - 4 μm) the dielectric function of ethanol differs considerably from that of water. In addition, a narrow absorption band from ≈ 3.36 μm to 3.47 μm associated to the CH-stretching vibrations of ethanol further emphasize these differences.

Regarding the optical properties of the water-ethanol solutions in the mid-IR, there are studies reporting their IR absorbance and Raman scattering [42]. They demonstrate through spectral deconvolution that when water and ethanol are mixed, up to four components make contributions to the measured spectrums, namely pure water, pure ethanol and two type of hydrates [42]. Thus, for the

different concentrations of ethanol in water, the refractive index of the resulting substance would vary in a complex manner making very difficult a theoretical study via simulations of the sensor performance as it was done for the pure water case.

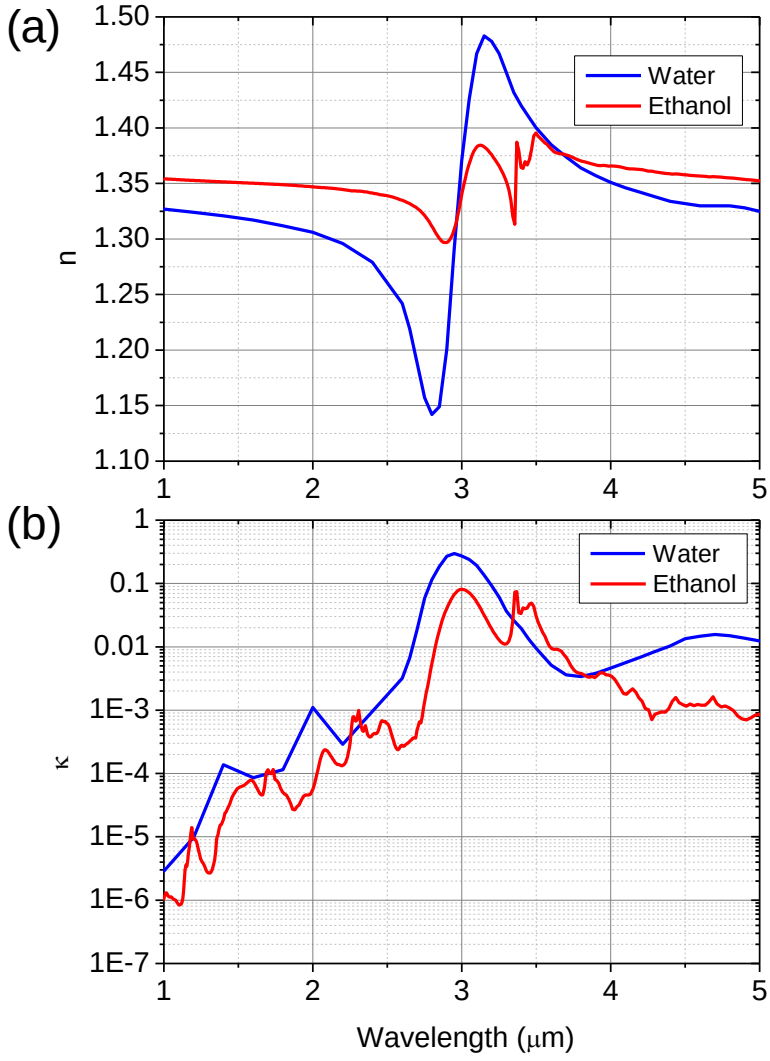

Figure 6.13. Complex refractive index of water and ethanol: (a) real and (b) imaginary parts.

To asses that the fabricated hybrid waveguide-SPP sensor is able to detect ethanol contamination in water samples, two main experiments were conducted.

Firstly, by employing a homebuilt fiber-based IR supercontinuum source and a spectrometer, the modification of the spectrum of polychromatic light transmitted through the sensing waveguide due to variations in the ethanol concentration was measured (Section 6.3.1). Secondly, a mid-IR laser whose wavelength is close to the one giving significant variation with rising ethanol concentration was utilized as a source for a monochromatic precision experiment (Section 6.3.2). The greater stability of the laser light allowed to find a better estimation of the minimum concentration of ethanol that the sensor was able to detect.

Regardless the source and the light detector, in both experiments the procedure carried out was as follows.

1) The reference spectrum/intensity of the light coming out of the sensing waveguide was recorded. The selected reference was the clean ITO surface, i.e. only air covering the sample. This is denoted as $V_{o,a}$ and is measured in volts as provided by the detector's amplifier.
2) A drop of water-ethanol solution (deionized water and 96 % pure ethanol) was placed on the ITO surface, covering around 2 mm of the waveguide total length. The waveguide output spectrum or power is again recorded and denoted as $V_{o,s}$. At the same time, a photograph from the top of the sample is taken so as to exactly measure the length of the solution drop (L).
3) The attenuation (A_{s-a}), expressed in dB/mm, due to the presence of the water-ethanol solution relative to the reference and normalized to the covered distance was then calculated as

$$A_{s-a} = \frac{-10 \log\left(\frac{V_{o,s}}{V_{o,a}}\right)}{L} \qquad \textit{Eq. 6.11}$$

The normalization to the drop length allowed to compare different results from different experiments. However, it also introduced an additional uncertainty factor which was estimated to be ± 50 μm which meant a ± 2.5 % error to the relative attenuation A_{s-a}. Other than thoroughly cleaning the ITO film after the evaluation of each analyte, no further surface treatment of functionalization was performed.

6.3.1. Evaluation with an unpolarized mid-IR supercontinuum light source in a broad range

The supercontinuum light source employed for the SPP sensing broadband experiments is based on the one designed and fabricated in [47]. Basically, it consisted of a two-stage erbium fiber amplifier driven by a diode laser emitting at 1.55 μm that was intensity-modulated to provide ns pulses. The peak power of the pulses was amplified from mW to kW level before coupling them to a short section of standard single-mode silica fiber in which the ns pulses broke into short fs pulses with increased peak power in a process known as modulation instability [47]. Then these fs pulses were coupled into a single-mode IR ZBLAN fiber and due to the high peak power reached inside and various material nonlinear effects, the resulting spectrum is broadened continuously up to around 4 μm. Figure 6.14 shows a sample of the spectrum corresponding to the generated mid-IR light. In Appendix B, a detailed description of the supercontinuum light source setup is provided.

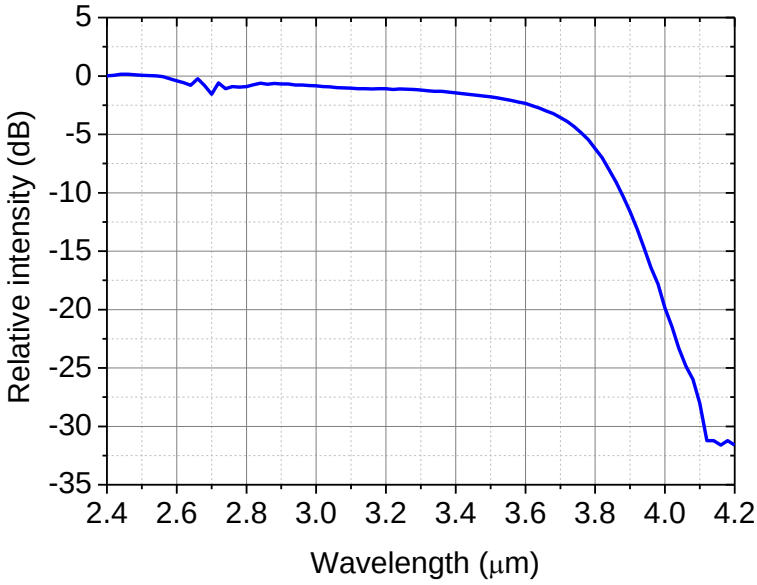

Figure 6.14. Sample of the spectrum of the generated supercontinuum light source.

The supercontinuum light is advantageous over blackbody thermal light in terms of spatial coherence. Since the supercontinuum light is generated within the small core of a single-mode fiber, the coupling to the subsequent sensing waveguide is significantly more efficient. In contrast, typical blackbody sources are mm-sized, radiate omnidirectionally and, consequently, the relative amount of photons that can be coupled into a single-mode fiber are fundamentally limited [48].

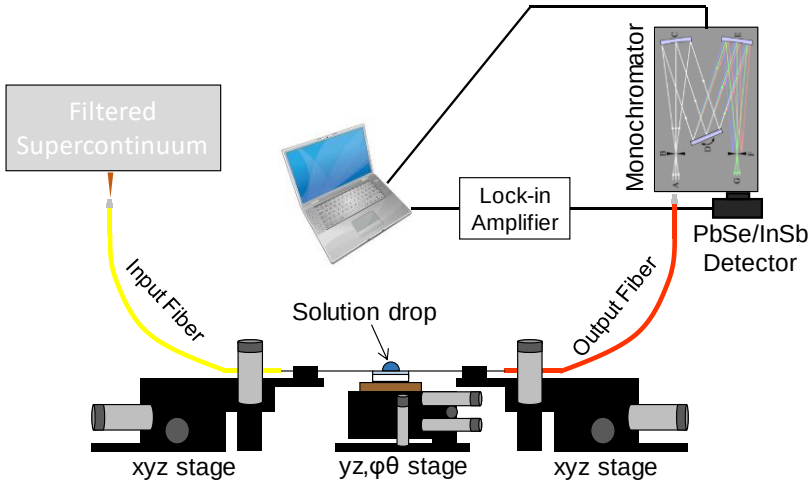

Figure 6.15. Fiber-based setup for the sensor evaluation with broadband unpolarized supercontinuum light.

A schematic showing the setup for the experiment is provided in Figure 6.15. The coupling and collection of light was done by butt-coupling to the sensing waveguide input and output ports single-mode (Thorlabs, core diameter 9 μm, NA = 0.19) and multimode ZBLAN fibers (Thorlabs, core diameter 100 μm, NA = 0.20), respectively. Note that the source is referred as “filtered” supercontinuum because a long-pass germanium filter (2.4 μm cut-off wavelength) was employed just after the IR broadening fiber in order to remove shorter wavelength components that could interfere with the measured spectrum in the region of interest (3 – 4 μm) as well as to reduce the peak intensity reaching the sensing waveguide, thus avoiding damage of the chip. The output spectrum was retrieved by a PC-controlled Jobin-Yvon Horiba HR460 monochromator equipped with a 300 gr/mm IR ruled grating together with PbSe or InSb infrared

detectors and their respective transimpendance amplifiers. The detection was synchronized to the repetition rate of the light source (5.12 kHz) via a lock-in amplifier which provided maximum SNR.

Since the polarization of the supercontinuum source could not be controlled and the optical fibers employed were not polarization-maintaining fibers, the experiment was carried out without a certain knowledge of the polarization state of the input and output light. Even though the SPP sensing mechanism only works for TM polarization, still one should expect changes on the measured spectrums for varying ethanol concentration.

The first analyte to test was pure water. The measured relative attenuation spectrum (A_{s-a}) is shown in Figure 6.16 with the corresponding simulated TM mode attenuation (MA_{w-a}), which was already provided in Figure 6.12, divided by ten. The experimental and simulated curves have similar trend and the maximum is close to λ = 3.5 μm although the values of the latter are around ten times greater.

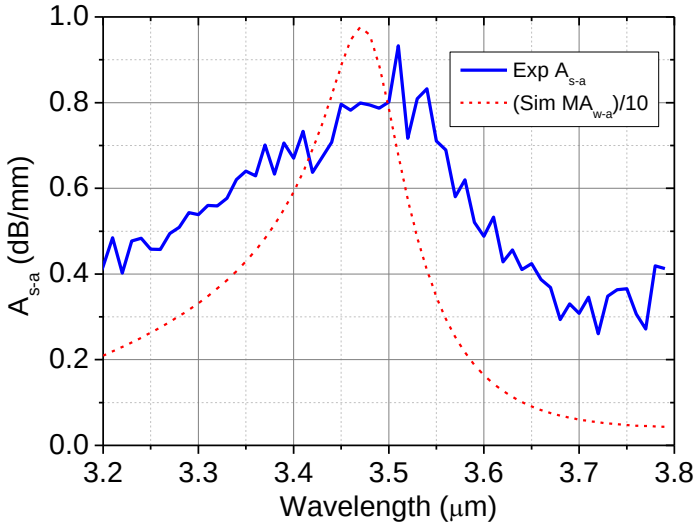

Figure 6.16. Experimental relative attenuation spectrum (blue line) compared to the simulated mode attenuation spectrum (red dashed line) for pure water.

The observed discrepancies stem mainly from the fact the theoretical calculation was done for TM polarization whereas experimental data was taken with a setup lacking polarization control and using 3DLW silica waveguide which are known to be birefringent (see Section 4.2.5 of Chapter 4). Consequently, the output spectrum is an unknown weighted combination of the attenuation suffered by TE and TM light through the waveguide. In addition, even though the mode attenuation is one of the factors determining the attenuation of the guided light, it is not the only one. For example, the light scattering losses due to the small distance between waveguide core and surface might vary from air to water.

Next, various samples with increasing concentration of ethanol in water (volume/volume) were evaluated. The measured relative attenuation spectrums are shown in Figure 6.17 for ethanol concentrations lower or equal than 5 % in steps of 1 %. Slight variations can be observed as the concentration rises in the 3.45 – 3.50 μm range (attenuation decreasing) and in the 3.60 – 3.65 μm range (attenuation increasing).

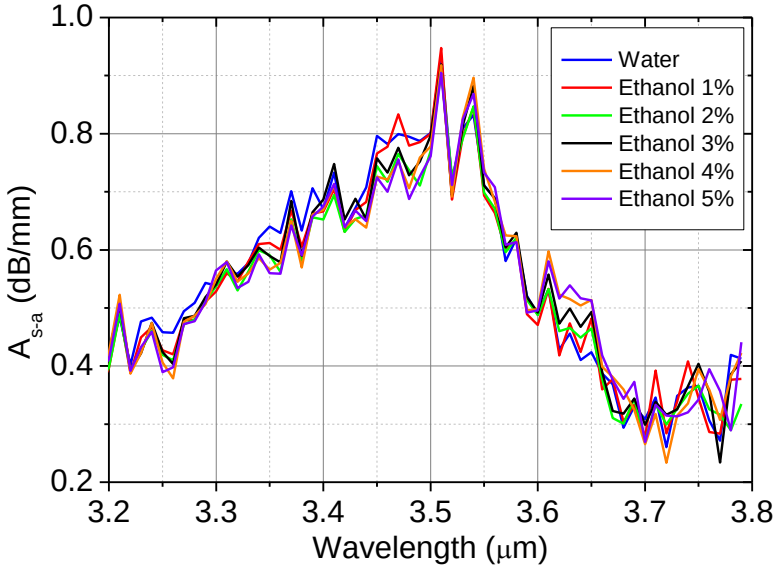

Figure 6.17. Measured relative attenuation spectrum for low ethanol concentrations (1 % - 5 %) using an unpolarized supercontinuum source.

When the ethanol concentration was further increased up to 50 % more relevant spectral variations were observed as it is shown in Figure 6.18. Three distinct bands in which the spectral changes seem to be stronger are highlighted in color.

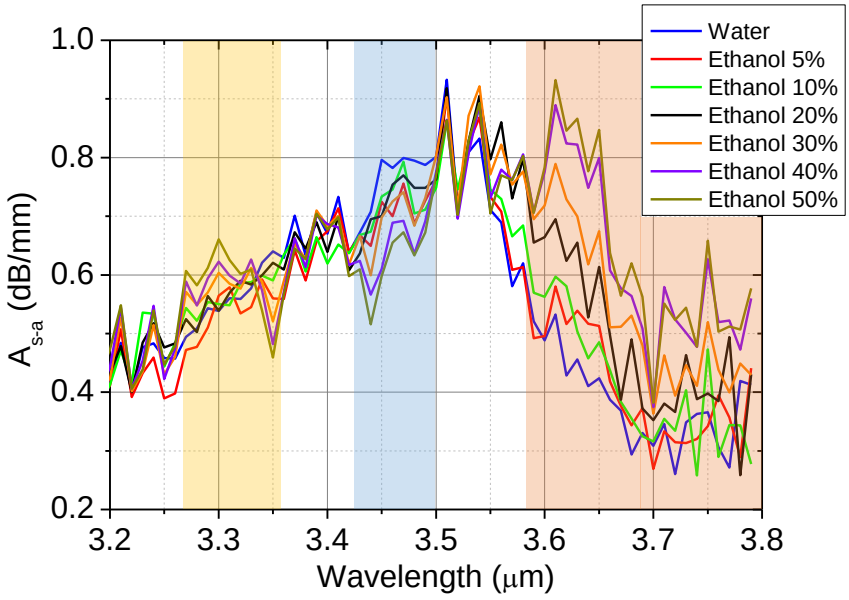

Figure 6.18. Measured relative attenuation spectrum for high ethanol concentrations in water (5 % - 50 %) using an unpolarized supercontinuum source.

The shorter band in yellow (≈ 3.27 – 3.36 μm) indicates an increase of the substance attenuation especially above 20 % of ethanol concentration. This might be associated directly to the higher absorption of the analyte due to the rising contribution of the CH-stretching vibrations associated to ethanol occurring around 2980 cm^{-1} [42].

On the other hand, the contribution of the OH groups diminishes as it is seen in the drop of attenuation in the range ≈ 3.42 – 3.50 μm highlighted in blue. As demonstrated through simulations, the maximum mode attenuation for pure water is found within this range (see Figure 6.16) due to the elevated refractive index of water. Consequently, if the attenuation here decreases for higher ethanol

concentrations, it means that the contribution of the pure water compound along the interaction length is lower.

Finally, the longer band (≈ 3.58 – 3.80 μm) in orange shows major variations for different ethanol concentrations, particularly for the peak emerging around 3.62 μm. As in the pure water case, ethanol has an index increase due to its characteristic CH absorption produced at 3.30 μm approximately. However, this index increase makes the waveguide-SPP phase matching to occur at longer wavelengths. Therefore, the author speculates that the increased measured attenuation around 3.62 μm might be due to the higher ethanol compound contribution which makes the resulting solution's refractive index larger at this band along the sensor interaction length.

In short, the spectral variations seen in the experimental attenuation curve within the yellow band might be associated to an absorptive phenomenon (i.e. κ increase of the solution due to CH vibrations), whereas those within the blue and orange bands might correspond to a refractive phenomenon that derives from the refractive index swings stemming from the solution's OH and CH resonances, respectively, and giving rise, in turn, to a waveguide-SPP phase matching effect.

Although the results have a strong potential for ethanol sensing, the observed spiky spectral curves imply an uncertainty that can limit the accuracy of the sensing. For this reason, a low-noise mid-IR laser providing rapid interrogation of the samples at the suitable wavelength within one of the studied bands was employed subsequently. Moreover, the experiment could be carried out in a polarization-controlled setup, thus increasing the sensitivity for low ethanol concentration samples.

6.3.2. Evaluation with a polarized mid-IR laser at a single wavelength and LOD estimation

The mid-IR interband cascade laser (ICL) that was employed in the experimental works of Chapters 4 and 5 was chosen again as a suitable driving source for the waveguide-SPP sensor evaluation at a single wavelength. Although the laser was

designed for λ = 3.68 μm emission, it could be tuned within a certain range by modifying the diode temperature. Specifically, the emitting wavelength was blueshifted to λ = 3.60 μm which is close to the point of maximum sensitivity to ethanol concentration as demonstrated in Figure 6.18.

The optical setup was built with no optical fibers involved and linear polarizers before and after the photonic chips as it is shown in Figure 6.19. Coupling the light in and out of the sensing waveguide was done by means of IR aspheric lenses and the output intensity was monitored by an IR camera. Further details on the equipment can be found in the waveguiding setup description (Chapter 4, Section 4.2). Placing both polarizers perpendicular to the chip surface allowed to observe the response of the sensor for TM polarized light.

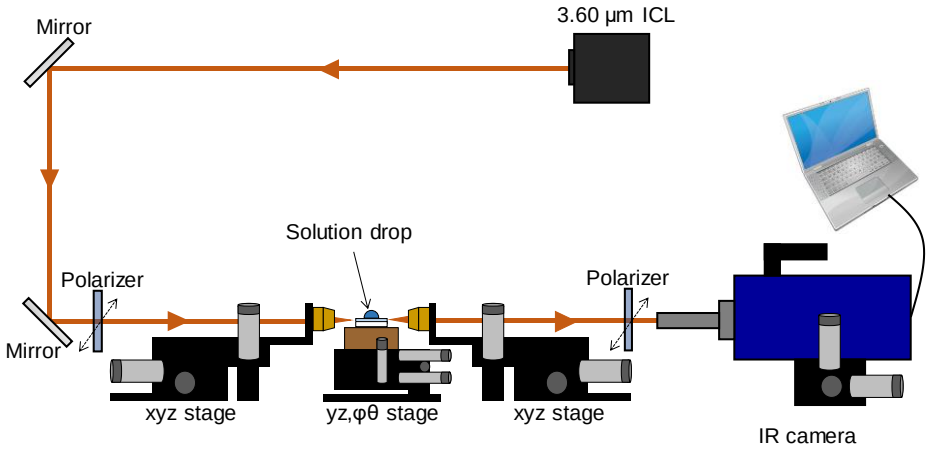

Figure 6.19. Experimental setup for the sensor evaluation with a mid-IR polarized laser emitting at λ = 3.60 μm.

The same measurements were repeated so as to obtain the relative attenuation for TM polarization at λ = 3.60 μm. The resulting A_{s-a} curve is shown in Figure 6.20 for ethanol concentrations from 0 % (water) to 50 %. At first glance, one can observe the significantly greater attenuation compared to the corresponding values of Figures 6.17 and 6.18 at the same wavelength. This is attributed to the removal of the TE component of the launched light into the input port which cannot couple to a plasmonic mode and, hence, is not sensitive to the changes of the

external analyte. This was not possible in the previous fiber setup and consequently the performance was being deteriorated. Error bars (2.50 %) accounting for the uncertainty in the drop length measurement are placed over each experimental point. Regarding the slope of the curve, which determines the sensitivity of the sensor, it is maximum between 10 % and 30 % of ethanol concentration and progressively declines from there. Figure 6.20 also demonstrates that the sensor is sensitive at least from 1 % up to 50 % of ethanol in water which is already a wide range of pollutant concentration for this type of sensors

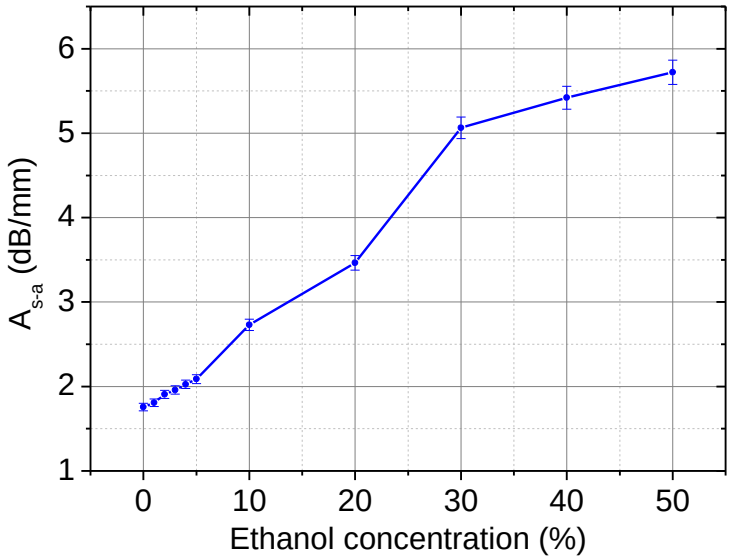

Figure 6.20. Measured relative attenuation spectrum for all the ethanol concentrations in water tested (0 % - 50 %) at $\lambda = 3.60$ μm for TM-polarized light.

Focusing on the low concentration results, Figure 6.21 shows the relative attenuation for the 0 % - 5 % range. A linear fitting is provided which can be used as a calibration curve for the ethanol limit of detection (LOD) calculation when expressed in terms of output voltage as it is explained below. In particular, the LOD was calculated following the guidelines of the first method described in [49]. This calculated LOD was not a definitive number, but only an approximate lower

limit since the uncertainty introduced by the determination of the drop length (error bars in figures) was neglected for the sake of simplicity. This means that it was considered a hypothetical perfect case in which the analyte-waveguide covering length was exactly determined and constant from measurement to measurement so that no uncertainty was added to the measurement. This could had been achieved by adding more complexity to the built device by means of, for example, a microfluidic channel deposited on the fused silica substrate. The equation employed for the LOD (%) calculation was [49],

$$\mathrm{LOD} = \frac{t_{\alpha,k-1}\sigma_{V_o}}{|r|} \qquad \textit{Eq. 6.12}$$

where $t_{\alpha,k-1}$ is the α quantile of the Student t-function with $(k-1)$ degrees of freedom, σ_{V_o} is the standard deviation (measured in V) of the k measurements performed on the output voltage for a certain sample and r is the slope of the calibration curve (measured in V/%) extracted from the output voltage corresponding to the low concentration samples and a given drop length.

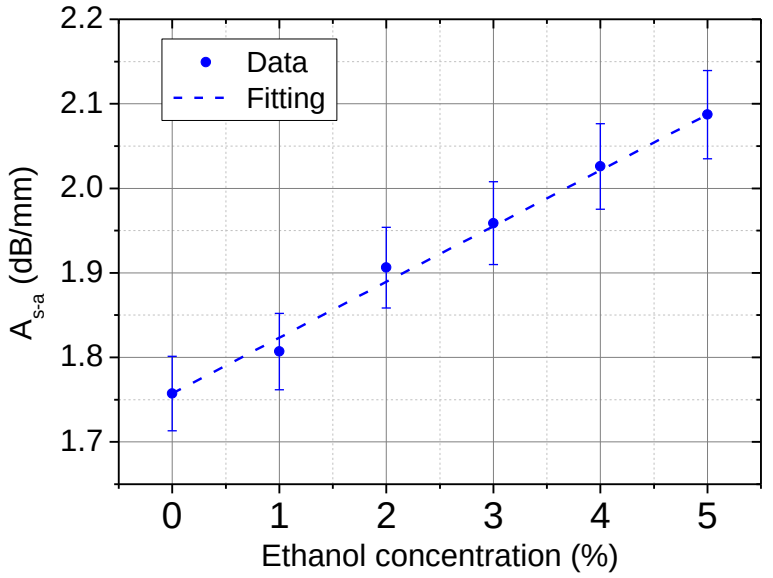

Figure 6.21. Measured relative attenuation spectrum for the lower ethanol concentrations in water tested at λ = 3.60 μm for TM-polarized light.

Once the equation was applied as it is described in detail in Appendix D, the resulting estimated LOD was 0.022 % (i.e. 220 ppm) of ethanol in water. This value closely matches that of other published sensors, namely [50] and [51], which are based on electronics and plasmonics technology, respectively.

The polarization-controlled setup also allowed to check the sensor response for TE light just by rotating the polarizers by 90º. For pure water, the measured attenuation for TE light was 0.02 dB/mm which is negligible when compared to the 1.76 dB/mm for TM light. If instead of placing the drop of water on the ITO surface, it was placed on one of the adjacent non-coated area (i.e. bare silica surface), the results were 0.34 dB/mm and 0.41 dB/mm, respectively. Note that in the latter case, the sensing mechanism is not plasmonic, but the one exploited for the water-ice sensor which shows no dependence on the light polarization. This data clearly demonstrates that the plasmon-mediated nature of the sensing mechanism is enabled by the ITO thin film placed between the silica substrate and the aqueous analyte.

6.4. Conclusions and outlook

In this final chapter, a simple mid-IR hybrid waveguide-SPP sensor has been conceived, simulated, fabricated and tested for detecting contaminants in an aqueous analyte. It has not been the main goal of this work to produce the most sensitive sensor, but only to show a proof of the (still fully unlocked) potential of plasmonic sensors in the mid-IR by just employing well-stablished fabrication techniques such as 3DLW of waveguides and sputtering of semiconductor thin films.

Even though the presented mid-IR waveguide-SPP sensor was only experimentally evaluated for the specific case of ethanol contaminant in water, other substances might be detected as well. For example, there are insecticides such as Aldrin or Lindane whose presence in water poses serious risks and since they have molecular fingerprints in the 3 – 4 μm range [52, 53] as well, they might be detected in a similar way to ethanol. Also, hydrocarbon pollutants in water such as toluene have important CH resonances there. Likewise, the same

principle may apply for many other (bio)molecules having resonances in the said range.

Several upgrades could be implemented on the device to improve the sensitivity below the ppm range that sometimes is required for the detection some hazardous substances. For instance, by means of surface functionalization techniques on the ITO thin film, which were not needed in this work, the molecules of interest could be attached to the surface in order to boost the sensor performance. Moreover, optimization of the optoelectronic properties of the ITO thin film by changing the deposition conditions would also lead to improved sensor sensitivity. Additionally, the reduction of the fabrication tolerances could reduce the gap between the waveguide core and the ITO/surface which would strengthen the waveguide-SPP coupling thus significantly enhancing the sensing sensitivity as it was demonstrated by simulations. Finally, with a laser source providing finer and broader tunability, the wavelength could be further adjusted to the optimum one depending on the analyte.

The fact that both ITO and fused silica are transparent makes the sensor particularly appropriate for devices requiring transversal optical clarity. Given its small footprint, the sensor could be embedded into microscope ITO-coated silica slides appropriately connected to polarization-maintaining fibers transporting the mid-IR light into and out of the slide. This would enable real-time micrometric-resolved sensing of chemicals with no interference on the experiment being performed. Lastly, as mentioned before, the ITO-coated fused silica platform is completely compatible with microfluidic chips (made of e.g. PDMS). The precise control of the analytes that microfluidics permit combined with the sensitivity and discrimination of integrated mid-IR sensors will ultimately improve the biochemical analysis of lab-on-a-chip devices in a not too distant future.

References

1. H. Raether, Surface Plasmons on Smooth and Rough Surfaces and on Gratings (Springer, 1988).
2. R. H. Ritchie, "Plasma Losses by Fast Electrons in Thin Films," Physical Review **106**, 874-881 (1957).
3. C. J. Powell, and J. B. Swan, "Origin of the Characteristic Electron Energy Losses in Aluminum," Physical Review **115**, 869-875 (1959).
4. E. A. Stern, and R. A. Ferrell, "Surface Plasma Oscillations of a Degenerate Electron Gas," Physical Review **120**, 130-136 (1960).
5. S. A. Maier, Plasmonics: Fundamentals and Applications (Springer, 2007).
6. Y. Fang, and M. Sun, "Nanoplasmonic waveguides: towards applications in integrated nanophotonic circuits," Light: Science & Applications **4**, e294 (2015).
7. E. Ozbay, "Plasmonics: Merging Photonics and Electronics at Nanoscale Dimensions," Science **311**, 189 (2006).
8. B. Sharma, R. R. Frontiera, A.-I. Henry, E. Ringe, and R. P. Van Duyne, "SERS: Materials, applications, and the future," Materials Today **15**, 16-25 (2012).
9. J. Homola, "Surface Plasmon Resonance Sensors for Detection of Chemical and Biological Species," Chemical Reviews **108**, 462-493 (2008).
10. J. N. Anker, W. P. Hall, O. Lyandres, N. C. Shah, J. Zhao, and R. P. Van Duyne, "Biosensing with plasmonic nanosensors," Nature Materials **7**, 442-453 (2008).
11. W. L. Barnes, A. Dereux, and T. W. Ebbesen, "Surface plasmon subwavelength optics," Nature **424**, 824-830 (2003).
12. L. Novotny, and B. Hecht, Principles of Nano-Optics (Cambridge University Press, 2006).
13. E. N. Economou, "Surface Plasmons in Thin Films," Physical Review **182**, 539-554 (1969).
14. S. Lal, S. Link, and N. J. Halas, "Nano-optics from sensing to waveguiding," Nature Photonics **1**, 641-648 (2007).
15. P. Berini, "Long-range surface plasmon polaritons," Advances in Optics and Photonics **1**, 484-588 (2009).
16. P. Bharadwaj, B. Deutsch, and L. Novotny, "Optical Antennas," Advances in Optics and Photonics **1**, 438-483 (2009).
17. T. H. Taminiau, R. J. Moerland, F. B. Segerink, L. Kuipers, and N. F. van Hulst, "λ/4 Resonance of an Optical Monopole Antenna Probed by Single Molecule Fluorescence," Nano Letters **7**, 28-33 (2007).
18. A. K. Sharma, R. Jha, and B. D. Gupta, "Fiber-Optic Sensors Based on Surface Plasmon Resonance: A Comprehensive Review," IEEE Sensors Journal **7**, 1118-1129 (2007).
19. J. J. Burke, G. I. Stegeman, and T. Tamir, "Surface-polariton-like waves guided by thin, lossy metal films," Physical Review B **33**, 5186-5201 (1986).
20. E. Kretschmann, and H. Raether, "Radiative Decay of Non Radiative Surface Plasmons Excited by Light," Zeitschrift für Naturforschung **23a**, 2135-2136 (1968).

21. A. Otto, "Excitation of nonradiative surface plasma waves in silver by the method of frustrated total reflection," Zeitschrift für Physik **216**, 398–410 (1968).
22. B. Hecht, H. Bielefeldt, L. Novotny, Y. Inouye, and D. W. Pohl, "Local Excitation, Scattering, and Interference of Surface Plasmons," Physical Review Letters **77**, 1889-1892 (1996).
23. Y. Zhong, S. D. Malagari, T. Hamilton, and D. Wasserman, "Review of mid-infrared plasmonic materials," Journal of Nanophotonics **9**, 093791-093791 (2015).
24. J. W. Cleary, G. Medhi, R. E. Peale, W. R. Buchwald, O. Edwards, and I. Oladeji, "Infrared surface plasmon resonance biosensor," Proc. SPIE 7673, Advanced Environmental, Chemical, and Biological Sensing Technologies VII **7673**, 767306 (2010).
25. S. Law, V. Podolskiy, and D. Wasserman, "Towards nano-scale photonics with micro-scale photons: the opportunities and challenges of mid-infrared plasmonics," Nanophotonics **2**, 103 (2013).
26. Y.-B. Chen, "Development of mid-infrared surface plasmon resonance-based sensors with highly-doped silicon for biomedical and chemical applications," Optics Express **17**, 3130-3140 (2009).
27. E. Sachet, C. T. Shelton, J. S. Harris, B. E. Gaddy, D. L. Irving, S. Curtarolo, B. F. Donovan, P. E. Hopkins, P. A. Sharma, A. L. Sharma, J. Ihlefeld, S. Franzen, and J.-P. Maria, "Dysprosium-doped cadmium oxide as a gateway material for mid-infrared plasmonics," Nature Materials **14**, 414-420 (2015).
28. J. Martínez, A. Ródenas, M. Aguiló, T. Fernandez, J. Solis, and F. Díaz, "Mid-infrared surface plasmon polariton chemical sensing on fiber-coupled ITO coated glass," Optics Letters **41**, 2493-2496 (2016).
29. F. Khalilzadeh-Rezaie, I. O. Oladeji, J. W. Cleary, N. Nader, J. Nath, I. Rezadad, and R. E. Peale, "Fluorine-doped tin oxides for mid-infrared plasmonics," Optical Materials Express **5**, 2184-2192 (2015).
30. D. Rodrigo, O. Limaj, D. Janner, D. Etezadi, F. J. García de Abajo, V. Pruneri, and H. Altug, "Mid-infrared plasmonic biosensing with graphene," Science **349**, 165 (2015).
31. G. V. Naik, V. M. Shalaev, and A. Boltasseva, "Alternative Plasmonic Materials: Beyond Gold and Silver," Advanced Materials **25**, 3264-3294 (2013).
32. R. L. Olmon, B. Slovick, T. W. Johnson, D. Shelton, S.-H. Oh, G. D. Boreman, and M. B. Raschke, "Optical dielectric function of gold," Physical Review B **86**, 235147 (2012).
33. Ó. Esteban, A. González-Cano, B. Mizaikoff, N. Díaz-Herrera, and M.-C. Navarrete, "Generation of Surface Plasmons at Waveguide Surfaces in the Mid-Infrared Region," Plasmonics **7**, 647-652 (2012).
34. C. R. Lavers, and J. S. Wilkinson, "A waveguide-coupled surface-plasmon sensor for an aqueous environment," Sensors and Actuators B: Chemical **22**, 75-81 (1994).
35. I. H. Malitson, "Interspecimen Comparison of the Refractive Index of Fused Silica," Journal of the Optical Society of America **55**, 1205-1209 (1965).
36. G. M. Hale, and M. R. Querry, "Optical Constants of Water in the 200-nm to 200-μm Wavelength Region," Applied Optics **12**, 555-563 (1973).
37. T. Ocal, S. Yusuf, A. Gulnur, and O. Lutfi, "High quality ITO thin films grown by dc and RF sputtering without oxygen," Journal of Physics D: Applied Physics **43**, 055402 (2010).

38. H.-C. Lee, and O. Ok Park, "The evolution of the structural, electrical and optical properties in indium-tin-oxide thin film on glass substrate by DC reactive magnetron sputtering," Vacuum **80**, 880-887 (2006).
39. F. Lai, L. Lin, R. Gai, Y. Lin, and Z. Huang, "Determination of optical constants and thicknesses of In2O3:Sn films from transmittance data," Thin Solid Films **515**, 7387-7392 (2007).
40. Y. Hu, X. Diao, C. Wang, W. Hao, and T. Wang, "Effects of heat treatment on properties of ITO films prepared by rf magnetron sputtering," Vacuum **75**, 183-188 (2004).
41. F. Franks, and D. J. G. Ives, "The structural properties of alcohol-water mixtures," Quarterly Reviews, Chemical Society **20**, 1-44 (1966).
42. S. Burikov, T. Dolenko, S. Patsaeva, Y. Starokurov, and V. Yuzhakov, "Raman and IR spectroscopy research on hydrogen bonding in water–ethanol systems," Molecular Physics **108**, 2427-2436 (2010).
43. T. Kurihara-Bergstrom, K. Knutson, L. J. DeNoble, and C. Y. Goates, "Percutaneous Absorption Enhancement of an Ionic Molecule by Ethanol–Water Systems in Human Skin," Pharmaceutical Research **7**, 762-766 (1990).
44. I. Vieitez, C. da Silva, G. R. Borges, F. C. Corazza, J. V. Oliveira, M. A. Grompone, and I. Jachmanián, "Continuous Production of Soybean Biodiesel in Supercritical Ethanol−Water Mixtures," Energy & Fuels **22**, 2805-2809 (2008).
45. Y. Koga, K. Nishikawa, and P. Westh, ""Icebergs" or No "Icebergs" in Aqueous Alcohols?: Composition-Dependent Mixing Schemes," The Journal of Physical Chemistry A **108**, 3873-3877 (2004).
46. E. Sani, and A. Dell'Oro, "Spectral optical constants of ethanol and isopropanol from ultraviolet to far infrared," Optical Materials **60**, 137-141 (2016).
47. C. Xia, M. Kumar, O. P. Kulkarni, M. N. Islam, J. F. L. Terry, M. J. Freeman, M. Poulain, and G. Mazé, "Mid-infrared supercontinuum generation to 4.5 μm in ZBLAN fluoride fibers by nanosecond diode pumping," Optics Letters **31**, 2553-2555 (2006).
48. D. H. McMahon, "Efficiency limitations imposed by thermodynamics on optical coupling in fiber-optic data links*," Journal of the Optical Society of America **65**, 1479-1482 (1975).
49. H.-P. Loock, and P. D. Wentzell, "Detection limits of chemical sensors: Applications and misapplications," Sensors and Actuators B: Chemical **173**, 157-163 (2012).
50. D. L. McCorkle, R. J. Warmack, S. V. Patel, T. Mlsna, S. R. Hunter, and T. L. Ferrell, "Ethanol vapor detection in aqueous environments using micro-capacitors and dielectric polymers," Sensors and Actuators B: Chemical **107**, 892-903 (2005).
51. B. Schwarz, P. Reininger, D. Ristanić, H. Detz, A. M. Andrews, W. Schrenk, and G. Strasser, "Monolithically integrated mid-infrared lab-on-a-chip using plasmonics and quantum cascade structures," Nature Communications **5**, 4085 (2014).
52. http://webbook.nist.gov/cgi/cbook.cgi?ID=C309002
53. http://webbook.nist.gov/cgi/cbook.cgi?ID=C58899

Conclusions

- An innovative, ultrasensitive surface icing sensor for the aviation industry and other industries with similar needs has been theoretically demonstrated. Numerical simulations have proven the proposed sensing mechanism in which a sub-surface waveguide embedded in a glassy or crystalline material can be used to detect phase changes undergone by water and ice films. The waveguide is driven by a mid-IR source whose wavelength is tuned to be nearby the OH-stretching vibration (3 – 4 μm) of the water molecule so that when the core of the waveguide passes just below the external medium, the waveguide attenuation is sensitive to the state of water (liquid, supercooled or ice) because of variations of its complex refractive index. Operating wavelength, waveguide material and design parameters are chosen so that light is no longer guided through the waveguide core but leaked out when ice is formed. Apart from being sensitive to the water phase, it has been shown that the spectral attenuation of the waveguide also varies according to the thickness and microstructure of the ice formed so that non-homogeneous ice like rime ice can be detected as well. It has been calculated that the sensor could detect ice films with thickness lower than 1 μm.
- The sensor has been fabricated on fused silica glass by 3DLW technology resulting in a monolithic, flat, mm-sized device connected to the light source and detector via mid-IR optical fibers. Static experiments have corroborated the capability of the sensor to clearly detect the freezing of liquid water when cooling it down given the sharp and sudden time response when ice nucleates. Moreover, if monitoring its spectral response, the detector can distinguish supercooled water from room-temperature water and ice as well. Moving into the sensor integration, a fiber-coupled prototype has been flush-mounted into the leading edge of an aircraft wing mock-up. Although the result has not been the less aerodynamically intrusive possible, it has been enough to test the ice sensing performance and its robustness against the impact water droplets at

high speed in an icing wind tunnel. The accretion of different types of ice composed of varying proportions of clear and rime ice have been successfully detected and different behaviors of the sensor output for different ice densities has been observed. Response times of about 1 s to the icing event have been measured which confirms the high-sensitivity and early-alert nature of the sensor. No reliability issues concerning the fiber-waveguide connection, the water erosion or the strong temperature swings undergone by the prototype have been detected. Further icing wind tunnel tests considering the variation of more icing parameters, such as droplets MVD, and additional experimental points are required to fully unravel the limits of the sensor.

- By using 3DLW waveguides embedded in IR grade fused silica for the water-ice sensor fabrication, it has been shown that is possible to employ this material beyond 2.5 μm (conventional fused silica operating limit) for mid-IR devices. High index contrast (0.7 %) 3DLW multiscan waveguides have been achieved with extended transparency up to around 3.5 μm (6.5 dB/cm loss at 3.68 μm) and low coupling loss to commercially available mid-IR single-mode fibers. Consequently, an excellent material like fused silica in terms of mechanical, chemical and thermal properties could be employed in this low part of the mid-IR range for integrated photonic sensors as well as astrophotonic integrated circuits requiring continuous transparency from the visible to almost the long edge of the L band. Furthermore, fundamental studies involving high temperature annealings to find out the mechanism giving rise to the increased refractive index of the 3DLW waveguide core have been carried out by means of μ-Raman and μ-photoluminescence analysis. They have revealed that the main mechanism of refractive index change is volume densification of the modified material rather than network (luminescent) defects, both induced by highly intense femtosecond laser pulses.
- The same type of 3DLW silica waveguides have been employed to build a proof-of-concept hybrid waveguide-SPP surface sensor working again at mid-IR wavelengths (3 – 4 μm) capable of detecting ppm contaminants in water. The device has been demonstrated via simulations for pure water in which case its elevated refractive index within this range (due to its strong OH-

stretching vibration) allows for the coupling of the confined mode of the sub-surface waveguide with the plasmonic mode sustained by an ITO thin film covering the silica substrate. This coupling is promoted by the refractive index symmetry achieved between the substrate material and the analyte. At a specific wavelength (around 3.5 μm) this coupling is maximized and so the sensitivity to the presence of water. Experimentally, this hybrid mode has been demonstrated exciting the waveguide with a homebuilt fiber-based unpolarized supercontinuum source while monitoring its spectral output. Similarly, testing of water samples contaminated by ethanol has given rise to different spectral responses proving that the waveguide-SPP coupling is also affected by the CH features of the ethanol. Finally, tuning the excitation of a mid-IR polarized laser (TM polarization to only excite the plasmonic mode) to the proper wavelength for maximum CH-sensitivity, a limit of detection in the order of 100's of ppm of ethanol in water has been demonstrated. Further optimization of the waveguide and thin film as well as microfluidic-based upgrades should improve this result. The fact that the sensor is fabricated on an ITO-coated silica substrate might be of interest for integrated chemical sensing devices (not only of ethanol) requiring transversal optical clarity such as smartphones screens or microscope slides.

APPENDIX A

Technical specifications of the flush-mounted icing sensor

This appendix contains the technical specifications corresponding to the icing sensor prototype flush-mounted on the leading edge surface of a wing mock-up and tested in the icing wind tunnel (see Chapter 5).

Technical specifications

- Ice sensing characteristics
  - Water and ice type discrimination capability: yes
  - Minimum detectable ice thickness: < 0.001 mm (simulated)
  - Response time: ≈ 1 s for ice alert, ≈ 3 s for ice identification
- Optical system specifications
  - Laser: Distributed Feedback (DFB) Laser
    - Nominal operating wavelength: 3.68 µm
    - Forward voltage: 3.5 V
    - Max. current: 100 mA
    - Light modulation frequency: 1-10 kHz
  - Detector: PbSe Amplified Photodetector
  - Input optical fiber: SM ZBLAN, NA 0.19, FC connector
  - Output optical fiber: MM ZBLAN, NA 0.20, FC connector
- Electrical specifications
  - Laser current driver
    - Supply voltage (Max. current): 5 V (400 mA), -15 V (250 mA), +15 V (250 mA)
    - Max. power consumption: 9.5 W
  - Laser TEC driver
    - Supply voltage (Max. current): 5 V (1 A)
    - Max. power consumption: 5 W
  - Detector amplifier circuit
    - Supply voltage (Max. current): +12 V (200 mA), -12 V (200 mA)
    - Max. power consumption: 5 W
- System control and communications
  - Remote control via provided software

- USB connection to PC
- Real-time monitoring of detector voltage signal
- Easy calibration for ice identification

- Physical characteristics
  - Probe material: glass
  - Probe plus optical fibers weight: 0.1 kg
  - Optical system plus electronics weight: 2 kg
  - Probe dimensions: 8 mm by 3.5 mm
  - Optical fiber length: 1.5 m each
  - Optical system plus electronics dimensions: 250 mm by 300 mm by 100 mm
- Environmental considerations
  - Probe and fibers operating temperature: -50 ºC to + 80 ºC
  - Optical system and electronics operating temperature: +5 to +40 ºC (non-condensing)
  - Maximum tested wind speed: 95 m/s

Sensor general arrangement

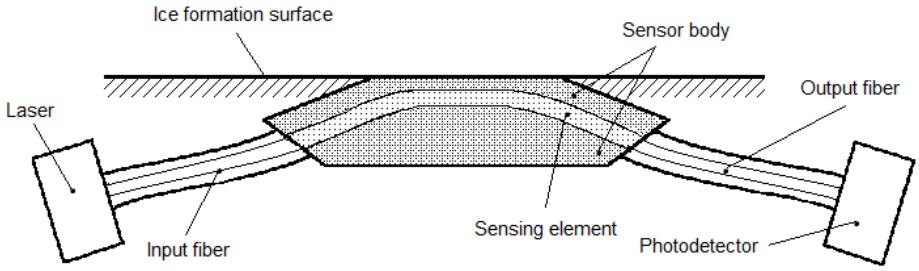

APPENDIX B

Development of a fiber-based mid-IR supercontinuum source

The design of the homebuilt fibered supercontinuum source developed for the experimental work described in Chapter 6 is fundamentally based on [1]. Although recently other researchers have published broader and more powerful supercontinuum sources (e.g. [2, 3]) by employing different pumping wavelengths and nonlinear IR materials, the source that was built was enough to cover the wavelength range of interest (3 – 4 μm). This source had the additional advantage of only requiring standard telecom single-mode components, such as diode lasers, multiplexers, filters, isolators and doped fibers, apart from the IR fiber.

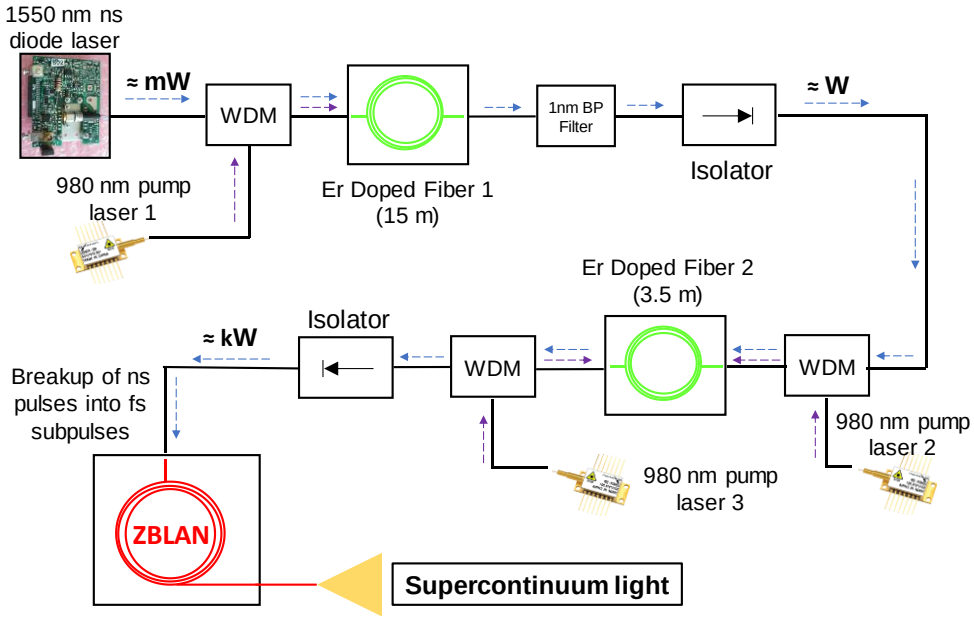

Figure B.1. Setup of the homebuilt fiber-based supercontinuum source.

The schematic of the setup employed is shown in Figure B.1. The first element is a seed intensity-modulated laser diode (Optilab DFB laser driven by Optical Pulse Machines high-speed current modulator) emitting at 1551.7 nm, producing 2 ns wide (FWHM) pulses at a tunable 1 – 20 kHz repetition rate with peak power of approximately 20 mW. The measured temporal pulse shape and the optical spectrum corresponding the seed laser are shown in Figure B.2.

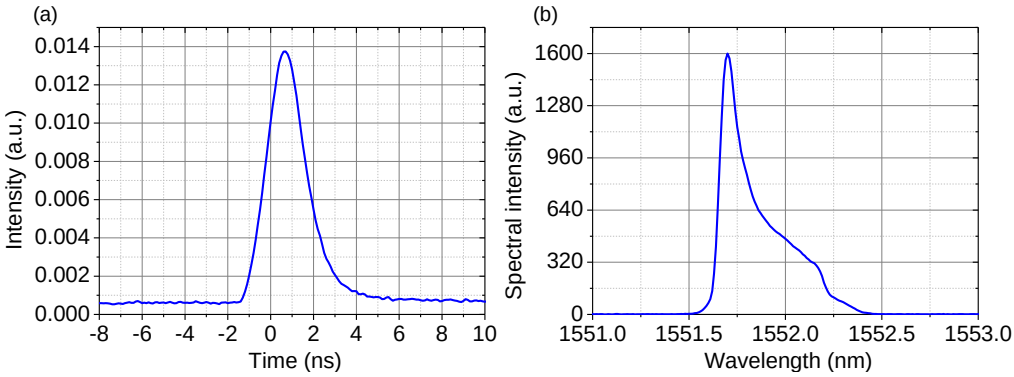

Figure B.2. (a) Example of the temporal trace of one pulse emitted by the seed laser. (b) Seed laser optical spectrum.

By means of a wavelength division multiplexer (WDM), the light coming from the seed laser (i.e. the signal) and the CW 980 nm light (i.e. the pump) emitted by a relatively low-power (maximum 250 mW at 450 mA) pump laser (II-VI Laser Enterprise) are combined within the same fiber core. Then the light is launched into a 15 m erbium-doped fiber (Fibercore MetroGain M-5) where the signal is amplified in a three-level system scheme with the 980 nm pump exciting the erbium ions so that the energy stored along the fiber can be transferred to the short signal pulses. At the output of this first amplifier stage a 1 nm band-pass removes the amplified spontaneous emission (ASE) and an isolator protects the setup from back-reflections. Roughly this first stage provides around 30 dB of gain that elevate the pulse peak power up to the 10's of W.

Still following the light path of Figure B.1, the second stage starts with a bi-directional pumping scheme using two high power CW 980 nm pump lasers (maximum of 750 mW at 1200 mA) coupled to a highly doped-erbium fiber (Liekki

Er80-8/125) with shorter length (3.5 m) which further amplify the signal intensity up to the kW level (20 dB of gain approximately). Again a high power optical isolator prevents back-reflections from damaging the amplifier. Before coupling the light into the final IR fiber, a short section of standard single-mode telecom fiber is needed in order to break the ns pulses into fs ones and achieve the high peak powers required to trigger the broadening nonlinear effects. This effect occurring when pumping the silica fiber in its anomalous dispersion range is known as modulation instability [1].

Finally, the energetic fs pulses reach the IR ZBLAN fiber (FiberLabs Inc.). After a propagation length of about 7.5 m, the supercontinuum light emerges from the output end, ready to be used. The high peak power of the fs pulses together with the proximity of the signal wavelength to the zero dispersion wavelength of the ZBLAN fiber (i.e. around 1.65 μm [4]), triggers an intense self-phase modulation (SPM) nonlinear effect on the ultrafast pulses along the length of the fiber which effectively add new frequencies to the spectrum while greatly broadening it [5].

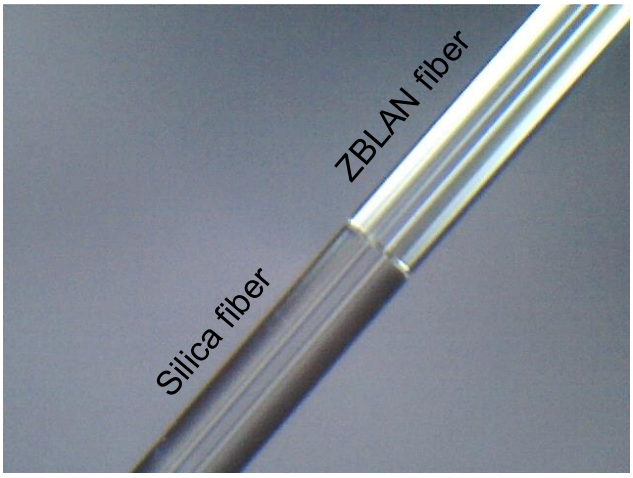

Figure B.3. Micrograph of the silica-zblan fiber mechanical join.

The telecom fiber and the ZBLAN fiber were directly butt-coupling by precision mechanical stages (see Figure B.3 for a micrograph) since no fusion splicing could be done with the available splicer device due to the totally different melting temperature of both glasses. Nevertheless, recently it has been successfully

demonstrated the splice of this type dissimilar fibers by the engineering of the splicing process [6]. No optical adhesive or index matching fluid was used to prevent scattered light from burning and damaging the fiber join. The mechanical splice resulted in a 1.3 dB loss which is a good figure given the core size and NA mismatch. In particular, according to the specifications the silica fiber has 8.2 μm core diameter and 0.14 NA whereas the ZBLAN has 7.1 μm core diameter and 0.265 NA.

A few parameters could be adjusted to tune the source performance, namely seed repetition rate and the driving current of each one of the three pumping lasers. Decreasing the repetition rate allowed, for the same pumping power, to obtain higher peak power pulses reaching the ZBLAN fiber which made the output spectrum broader, at the expense of reduced average power. In addition, by varying the driving current of the pumping lasers, the gain of each amplifier stage could be modified at will.

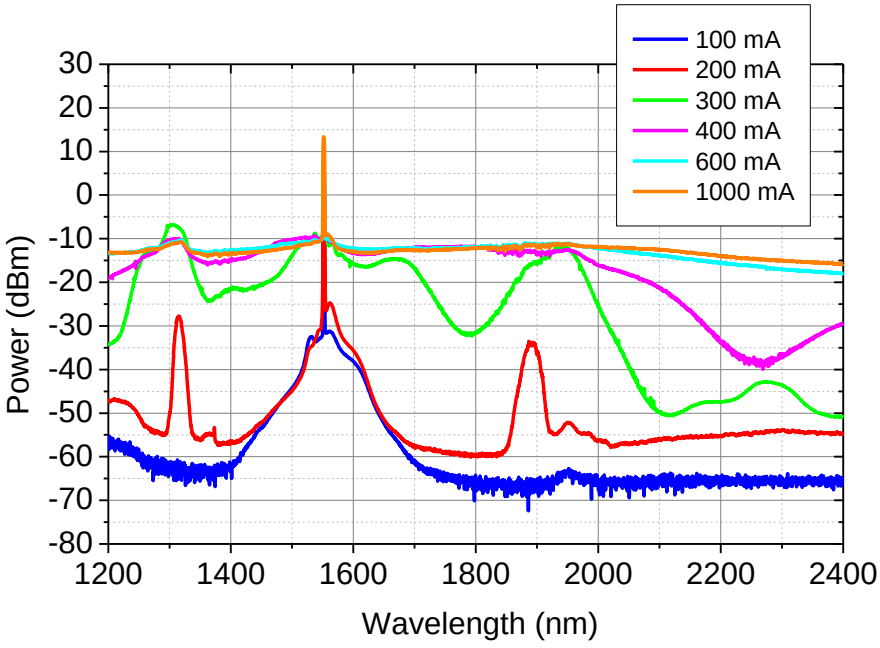

Figure B.4. Supercontinuum light spectrum measured from 1200 to 2400 nm for different levels of pumping currents (100 to 1000 mA) of the second stage pump lasers and a seed repetition rate of 16.10 kHz.

Figure B.4 shows part of the spectrum (1200 to 2400 nm) of the generated supercontinuum light for a seed repetition rate of 16.10 kHz. It was measured with a Yokogawa AQ6375 optical spectrum analyzer (OSA) in terms of absolute power. Various curves are depicted corresponding to increasing pumping currents of the second stage pump lasers. On the other hand, the pumping of the first stage is set constant at 200 mA for all the cases. For the lowest pumping (100 mA) the amplifier gain is small so that no broadening occurs and the observed spectrum coincides with that of the seed. If the pumping is increased, symmetric lobes start to appear around the signal wavelength giving rise progressively to the formation of a flat supercontinuum spectrum below and above 1550 nm.

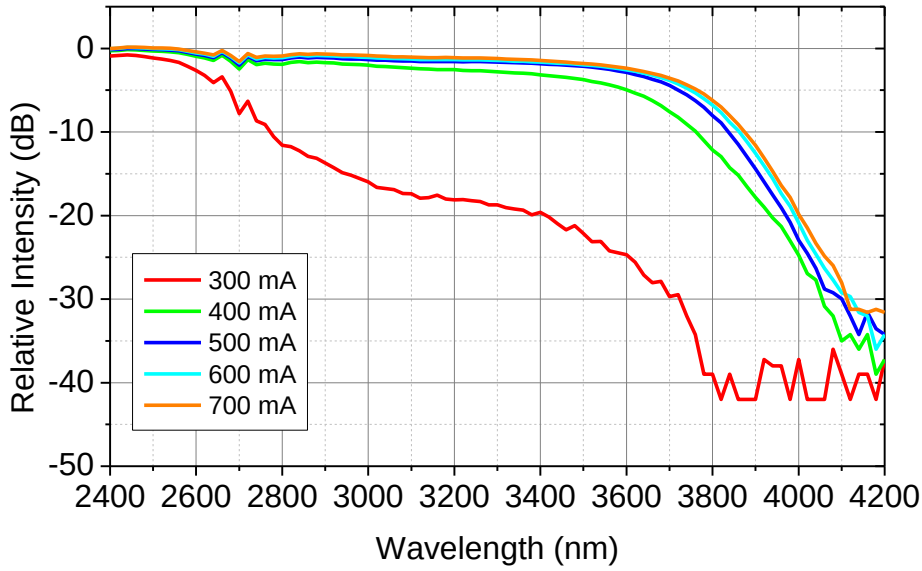

Figure B.5. Supercontinuum light spectrum measured from 2400 to 4200 nm for different levels of pumping currents (300 to 700 mA) of the second stage pump lasers and a seed repetition rate of 5.12 kHz.

Due to the spectral limits of the OSA, the longest part of the spectrum could not be measured in the same way. For that reason, a PC-controlled Jobin-Yvon Horiba HR460 monochromator equipped with a 300 gr/mm IR ruled grating together with PbSe or InSb detectors at the output slit was employed. By means

of a lock-in amplifier, the detection was synchronized to the seed repetition rate. To prevent higher diffraction orders from leaking into the range of interest, a long-pass germanium filter (2400 nm cut-off wavelength) was placed just before the detectors. Figure B.5 shows the supercontinuum spectrum measured by the monochromator from 2400 to 4200 nm. In this case, the seed repetition rate was 5.12 kHz which made the supercontinuum broader for the same pumping so that the maximum driving current required was lower (i.e. 700 mA). The -30 dB intensity drop relative to that at 2400 nm is produced at 4100 nm, approximately. Therefore, the built supercontinuum source is a solid platform to develop integrated mid-IR sensors working in the 3 – 4 μm range such as that presented in Chapter 6.

References

1. C. Xia, M. Kumar, O. P. Kulkarni, M. N. Islam, J. F. L. Terry, M. J. Freeman, M. Poulain, and G. Mazé, "Mid-infrared supercontinuum generation to 4.5 μm in ZBLAN fluoride fibers by nanosecond diode pumping," Optics Letters **31**, 2553-2555 (2006).
2. Y. Yu, X. Gai, P. Ma, K. Vu, Z. Yang, R. Wang, D.-Y. Choi, S. Madden, and B. Luther-Davies, "Experimental demonstration of linearly polarized 2-10 μm supercontinuum generation in a chalcogenide rib waveguide," Optics Letters **41**, 958-961 (2016).
3. D. D. Hudson, M. Baudisch, D. Werdehausen, B. J. Eggleton, and J. Biegert, "1.9 octave supercontinuum generation in a As_2S_3 step-index fiber driven by mid-IR OPCPA," Optics Letters **39**, 5752-5755 (2014).
4. M. Monerie, F. Alard, and G. Maze, "Fabrication and characterisation of fluoride-glass single-mode fibres," Electronics Letters **21**, 1179-1181 (1985).
5. G. Agrawal, *Nonlinear Fiber Optics* (Academic Press, 2001).
6. K. Yin, B. Zhang, J. Yao, L. Yang, S. Chen, and J. Hou, "Highly stable, monolithic, single-mode mid-infrared supercontinuum source based on low-loss fusion spliced silica and fluoride fibers," Optics Letters **41**, 946-949 (2016).

APPENDIX C

Determination of the optical properties of the sputtered ITO thin films

In order to obtain accurate simulations of the plasmonic structure presented in Chapter 6, a good estimation of the optical properties of the sputtered ITO thin films is required. The Drude model (see Equation 6.5 in Chapter 6) seamlessly links the optical properties (i.e. permittivity ε) to the electrical ones (i.e. carrier concentration N and carrier mobility μ) of a semiconductor in the spectral range where the material has a "metallic" behavior. This means that the Drude model can be employed with low error at longer wavelengths than the zero-crossing one where the real part of the permittivity turns negative.

N and μ can be directly retrieved via Hall effect measurements. From them one can calculate the Drude model parameters, namely plasma frequency ω_p and relaxation rate γ, by employing the equations below [1].

$$\omega_p = \sqrt{\frac{Ne^2}{m^*\varepsilon_0}} \qquad \textit{Eq. C.1}$$

$$\gamma = \frac{e}{m^*\mu} \qquad \textit{Eq. C.2}$$

where e is the electron charge, m^* is the carrier effective mass (for ITO is 0.4 times the free electron mass [2]) and ε_0 the free-space permittivity. Given Equations C.1 and C.2, one can notice that N and μ together with the background permittivity ε_b define the dielectric function at mid-IR wavelengths via the Drude model of Equation 6.5. Although the Hall effect measurements allow to know the parameters N and μ, not always the necessary equipment is available.

Alternatively, optical measurements such as transmittance or reflectance can be also employed to characterize semiconductors thin films giving results close to those obtained by electrical Hall measurements. In particular, in this Thesis work, near-UV to near-IR transmittance measurements of the sputtered ITO thin films on fused silica substrates were performed and subsequently fitted to a theoretical model so as to retrieve their electro-optical properties.

The followed procedure is described in detail in [2]. As it is explained there, the Drude model alone does not provide good enough fitting to the measured transmittance spectrums in the observed wavelength range. For that reason, two models are combined, the modified Drude model and the Forouhi-Bloomer model [2] (denoted as FBD from now on) that accounts for the shorter wavelength range. The model contains up to 11 parameters that need to be fitted to the experimental transmittance of the ITO-silica system. The transmittance is measured by a Cary 5000 UV-Vis-NIR spectrometer from 250 to 2500 nm. Then by means of MATLAB scripting, the particular parameters that minimize the difference between the model and the experiment are calculated via the least square method. The minimization of the nonlinear objective function is done with the built-in *fmincon* MATLAB function after applying the suitable constraints. The fitting process is repeated for various thicknesses around the experimentally measured one in order to find the one giving the lowest residual error.

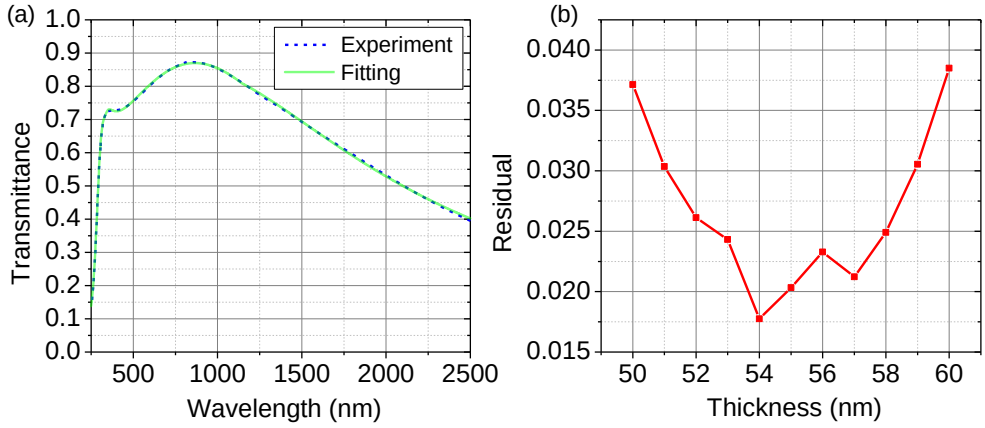

Figure C.1. (a) Experimental and fitted transmittance curve from 250 to 2500 nm for a 54 nm thick ITO thin film. (b) Fitting residuals for various thin film thicknesses.

Figure C.1(a) shows the measured transmittance curve (dashed line) corresponding to the definitive ITO thin film employed for the sensing experiments presented in Chapter 6. The overlaying solid line is the fitted curve for 54 nm thickness. Both lines show quite good agreement as it is demonstrated in Figure C.1(b), where the fitting residuals are depicted for various thicknesses. As it can be observed, the minimum residual occurs indeed for the thickness of 54 nm. The obtained values of the most relevant fitting parameters are ε_b = 3.94, N = 13.37·10^{20} cm^{-3} and γ = 23.36 cm^2/Vs. N and γ give rise, through Equations C.1 and C.2, to the parameters ω_p and γ presented in Section 6.2.2 of Chapter 6.

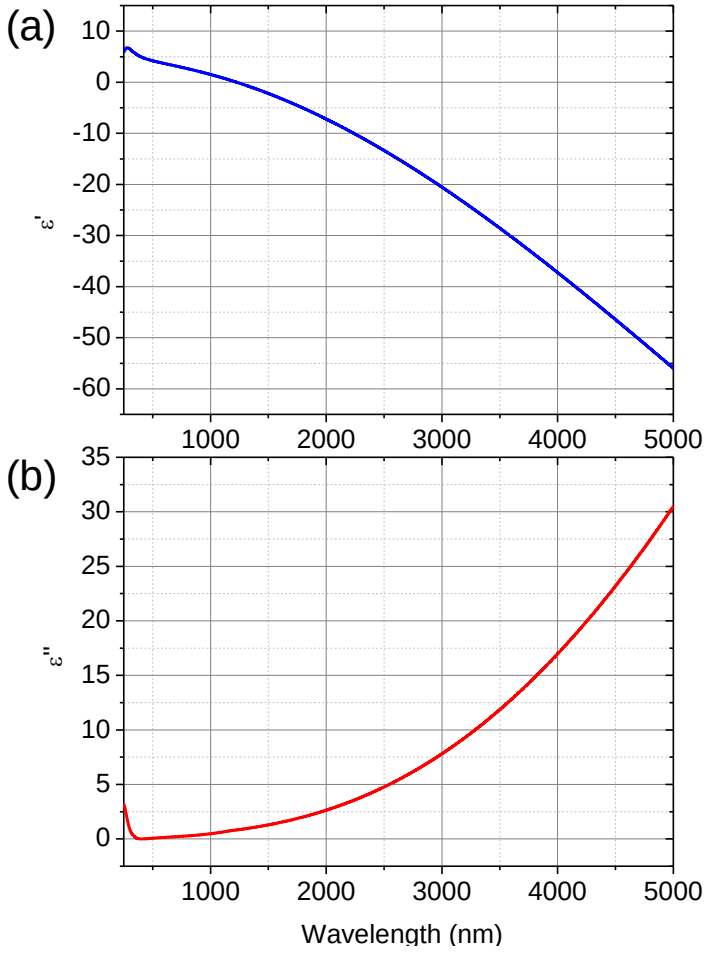

Figure C.2. (a) Real and (b) imaginary part of the permittivity of a 54 nm thick ITO film retrieved by fitting optical transmittance data.

Once the best fitting parameters are found, the dielectric function can be computed over the desired range by introducing them in the model. Figure C.2 shows the dielectric function of the 54 nm thick ITO film from 250 nm to 5000 nm. It can be demonstrated that at mid-IR wavelengths the model used for the fitting (FBD model) coincides with the Drude model alone which only requires ε_b, ω_p and γ instead of the 11 parameters of the former. For instance, at λ = 3.5 μm, the FBD model gives ε_{ITO} = -28.7 + i11.4, whereas the Drude model alone gives ε_{ITO} = -28.5 + i11.9. The deviations of electromagnetic modal simulations due to this error are negligible. Therefore, the Drude model was the one employed for the simulations of Chapter 6 given its simplicity and accuracy in the 3 – 4 μm range.

References

1. S. Basu, B. J. Lee, and Z. M. Zhang, "Infrared Radiative Properties of Heavily Doped Silicon at Room Temperature," Journal of Heat Transfer **132**, 023301-023301 (2009).
2. F. Lai, L. Lin, R. Gai, Y. Lin, and Z. Huang, "Determination of optical constants and thicknesses of In_2O_3:Sn films from transmittance data," Thin Solid Films **515**, 7387-7392 (2007).

APPENDIX D

Estimation of the hybrid waveguide-SPP sensor LOD

In this appendix, the procedure for obtaining a first-order estimation of the limit of detection (LOD) of the ethanol in water waveguide-SPP sensor presented in Chapter 6 is described. As it was mentioned there, the uncertainty of the measurements due to the determination of the sample drop is not taken into account. The procedure is based on the first method provided in [1] which relies on the measurement of a calibration curve and standard deviations at a particular concentration. As mentioned in Chapter 6, the LOD is computed as

$$\mathrm{LOD} = \frac{t_{\alpha,k-1}\sigma_{V_o}}{|r|} \qquad \textit{Eq. D.1}$$

where $t_{\alpha,k-1}$ is the α quantile of the Student t-function with $(k-1)$ degrees of freedom, σ_{V_o} is the standard deviation (measured in V) of the k measurements performed on the output voltage for a certain sample and r is the slope of the calibration curve (measured in V/%) extracted from the output voltage corresponding to the low ethanol concentration samples (0 – 5 %) and a given drop length (*L*).

The confidence interval is directly $(1-\alpha)$. This means that a measurement at the LOD has a probability of $(1-\alpha)$ of being larger than the one corresponding to a blank sample [1] which corresponds to the 0 % ethanol concentration in water. In this case, $(1-\alpha)$ is chosen to be 0.9973 which together with k = 10 measurements make the t-function to be t = 3.640. Next, the calculation of r is carried out by finding the calibration curve corresponding to lowest concentration samples (0 – 5 %). Taking the experimental attenuation data A_{s-a} (see Figure 6.21 of Chapter 6), one can then calculate the output voltage V_o of the detector

for each concentration and for a constant L = 2 mm long analyte drop considering that the voltage when nothing covers the sensor is 1 V. The relation required can be directly retrieved from Equation 6.11. The obtained data is summarized below in Table D.1.

Ethanol (%)	A_{s-a} (dB/mm)	V_o(V)
0	1.757	0.4452
1	1.807	0.4351
2	1.906	0.4157
3	1.959	0.4057
4	2.026	0.3934
5	2.087	0.3824

Table D.1. Sensor attenuation and output voltage for low ethanol concentration samples and L = 2 mm.

By plotting these points (see Figure D.1), one can easily find a linear fitting curve whose slope is directly the r parameter of Equation D.1. Specifically, r = - 0.01256 V/%.

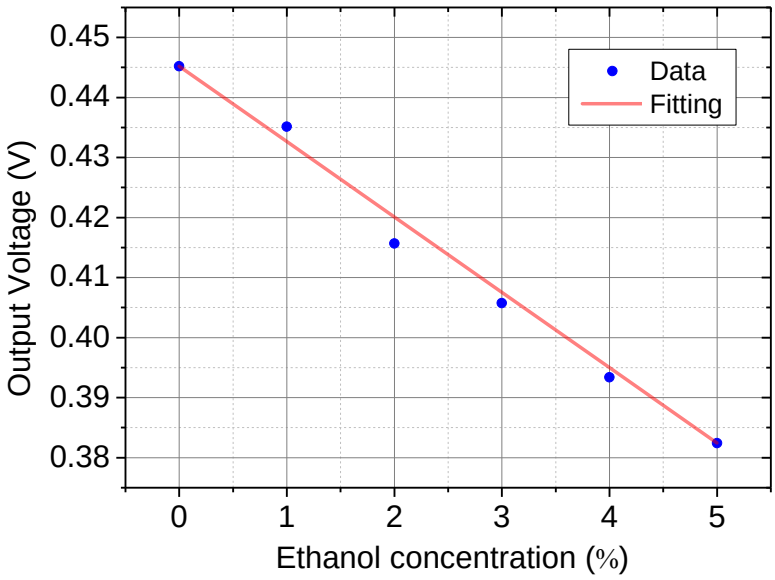

Figure D.1. Sensor output voltage and corresponding linear fitting for low ethanol concentration samples and L = 2 mm.

The standard deviation σ_{V_o} of the 10 measurements is calculated for one of the samples. In this case, the 5 % concentration sample is chosen although a lower one might give a more accurate estimation of the LOD. Following the same procedure, from the experimental A_{s-a} corresponding to each one of the 10 different measurements, the output voltage V_o is computed for a constant L = 2 mm. Each measurement is taken several seconds after the previous one. Ideally, though, the measurements should have been done independently from each other and from different batches, but in that way the drop length determination uncertainty would have affected the final result. Table D.2 contains the output voltages for each measurement, from which the calculated deviation is σ_{V_o} = 7.514·10^{-5} V.

Measurement #	V_o(V)
1	0.3824
2	0.3823
3	0.3824
4	0.3822
5	0.3823
6	0.3822
7	0.3823
8	0.3821
9	0.3823
10	0.3823

Table D.2. Sensor output voltage of 10 different measurements for the 5 % ethanol sample.

Lastly, from the values of t, r and $\sigma_{V_o}$and applying Equation D.1, the limit of detection for the particular sensor configuration shown in Section 6.3.2 of Chapter 6 is LOD = 0.022 %

References

1. H.-P. Loock, and P. D. Wentzell, "Detection limits of chemical sensors: Applications and misapplications," Sensors and Actuators B: Chemical **173**, 157-163 (2012).

APPENDIX E

Related publications and patent

Next the -first author- papers arising from the Thesis development are attached. Subsequently, the patent document written in Spanish is included as well.

PAPER I

Optics Letters

3D laser-written silica glass step-index high-contrast waveguides for the 3.5 μm mid-infrared range

Javier Martínez,[1] Airán Ródenas,[1,*] Toney Fernandez,[2,5] Javier R. Vázquez de Aldana,[3] Robert R. Thomson,[4] Magdalena Aguiló,[1] Ajoy K. Kar,[4] Javier Solis,[2] and Francesc Díaz[1]

[1]Física i Cristal•lografia de Materials (FiCMA), Departament de Química Física i Inorgànica, Universitat Rovira i Virgili, 43007 Tarragona, Spain
[2]Laser Processing Group, Instituto de Óptica-CSIC, Madrid 28006, Spain
[3]Laser Microprocessing Group, Facultad de Ciencias, Universidad de Salamanca, 37008 Salamanca, Spain
[4]Institute of Photonics and Quantum Sciences, Heriot-Watt University, Edinburgh EH14 4AS, UK
[5]Currently at Dipartimento di Fisica, Politecnico di Milano, Milano, Italy
*Corresponding author: arodenas@gmail.com

Received 21 September 2015; revised 17 November 2015; accepted 17 November 2015; posted 19 November 2015 (Doc. ID 250479); published 11 December 2015

We report on the direct laser fabrication of step-index waveguides in fused silica substrates for operation in the 3.5 μm mid-infrared wavelength range. We demonstrate core-cladding index contrasts of 0.7% at 3.39 μm and propagation losses of 1.3 (6.5) dB/cm at 3.39 (3.68) μm, close to the intrinsic losses of the glass. We also report on the existence of three different laser modified SiO_2 glass volumes, their different micro-Raman spectra, and their different temperature-dependent populations of color centers, tentatively clarifying the SiO_2 lattice changes that are related to the large index changes.

OCIS codes: (130.2755) Glass waveguides; (140.3390) Laser materials processing; (220.4000) Microstructure fabrication.

http://dx.doi.org/10.1364/OL.40.005818

The advent of intersubband cascade lasers in the mid-90s [1–3] and of interband cascade lasers (ICL) more recently [4] played a crucial role in the development of mid-infrared (IR) optical instruments (from around 2.5 to 20 μm) [5]. Likewise, due to the high interest in deploying remote mid-IR sensors, huge work has also been done in the field of fiber growth, with fluoride and chalcogenide glasses as the most widespread solid-fiber materials [6–8]. Yet these glasses have mechanical and corrosion limitations that make them unsuitable for long exposure to the environment. Chalcogenide glasses have a much lower fracture stress limit than fused silica glass, are susceptible to water corrosion, have low optical-damage thresholds, and typically have toxic arsenic as a primary component. Fluoride glasses also share similar mechanical, water-corrosion, and optical-damage limitations [9]. Fused silica glass on the other hand is well known to be mechanically and thermally resilient; chemically resistant to nonfluorinated acids, solvents, or plasmas; and is currently ubiquitous in many industries, from optical fibers to microfluidic systems, microelectromechanical systems (MEMS), high temperature glassware, microscope slides, or in thermonuclear reactors as long-lifetime vacuum windows capable of withstanding high neutron and gamma irradiation levels [10–12]. Fused silica glass is, however, also frequently thought to be "opaque" for wavelengths above around 2.5 μm, though this is not the case for high-purity fused silica glass, which maintains its high transparency to around 3.5 μm wavelength. Since novel surface-sensing schemes based on dielectric loaded plasmonics [13] allow for short optical path lengths, the benefits of having a robust fused-silica-glass chip as a light loading interface for point sensing could outweigh the limitations of intrinsic absorption losses of the material. In this Letter, we explore the fabrication of 3D waveguides (WGs) inside silica for single-mode operation around 3.5 μm wavelength, with capability for bends with radii below 15 mm, and low numerical aperture so as to provide low-loss fiber interconnects.

To have embedded WGs with 3D architectures capable of interconnecting fibers as well as having on-chip functional WG circuits, the 3D direct laser writing technique (DLW) has become the standard technique after almost 20 years of research, with fused silica being the most frequently studied material [14–20]. Our DLW setup consisted of an fs-fiber-laser amplifier (Tangerine, Amplitude Systemes) delivering ~450 fs pulses at 1047 nm and at a rate of 500 KHz. The laser power was kept at 400 mW by means of neutral density filters, and the beam was circularly polarized. The laser beam was focused inside Suprasil 300 (S300, Heraeus) high-purity silica using an aspheric lens with 0.4 NA. The sample was translated at a speed of 1.5 mm/s, and the multiscan approach was used [16], with a scan separation of 0.4 μm. For this work, we performed a study of WG depth fabrications down to 1480 μm so as to evaluate the potential for inscribing "on the fly" 3D circuits. After WG fabrication, the sample facets were polished to optical quality, characterized under bright-field microscopy, and characterized in a mid-IR guiding setup. Our guiding setup consisted of a 1.5 mW HeNe laser (3.39 μm) and a 3 mW ICL tunable laser (from 3.57 to 3.68 μm). Both lasers provided vertically polarized beams. A pair of lenses with NA = 0.18 (Thorlabs

0146-9592/15/245818-04$15/0$15.00

C021TME-E) were used for in- and out-coupling laser light from the WGs. A Thorlabs (PDA20H-EC) PbSe amplified detector was used in combination with a FLIR SC700 camera for imaging the output WG modes. COMSOL software was used to simulate the WGs modes assuming step-index profiles and the measured core sizes from bright-field microscopy: by changing the core refractive index, the simulated mode field diameters (MFDs) could be made to match the experimentally found values, therefore obtaining approximate inferred values for the core index changes $\Delta n = n_{\text{core}} - n_{\text{cladding}}$ for all WGs, where the n_{cladding} value is assumed to be the index of unmodified glass. Figure 1 shows a summary of the characterization results performed at 3.39 μm. Figure 1(a) shows the measured MFDs for horizontal (x) and vertical (y) directions and for 5 different WG depths. As can be seen, the MFDs only changed within ±1 μm for all depths. Figure 1(b) shows the near-field images of the 5 WGs and the MFDs vertical to horizontal ratios (R). The mode ratios are measured to be almost constant at $R = 1 \pm 5\%$, which is fundamental for ensuring low-loss coupling to optical fibers. Figure 1(c) shows the bright-field images of the WGs at different depths. Three different zones observed in the WGs are labeled II, I, and I*. The first two zones (II and I) are believed to correspond to Type II and Type I index modifications, respectively [21,22]. Type I modifications consist of index increased volumes, and Type II regions are typically depressed index zones with nanoscale features. The core waveguiding region is therefore assumed to be only zone I and I*. Finally, Fig. 1(d) shows the corresponding estimated mid-infrared Δn values for different fabrication depths, which on average is of 0.01 ± 0.0015.

The estimated NA of these WGs, $\text{NA} = (n_{\text{core}}^2 - n_{\text{clad}}^2)^{1/2}$, is NA ~ 0.17, therefore allowing for low-loss coupling to commercial fluoride optical fibers, which adds to the advantage of reduced Fresnel losses between fused silica and fluoride glasses. Importantly, an index change of $\Delta n = 0.01$ with the low cladding index of 1.4095 of silica at 3.39 μm indicates that these WGs have a high index contrast $C\% = \Delta n / n_{\text{core}}$ of ~0.7%, a value significantly high for a DLW WG. This contrast value at 3.39 μm is higher than other previously reported values for mid-infrared DLW WGs in chalcogenide glass (~0.55%) [23] and borate crystals (~0.29%) [24], allowing for tighter bend radii without significant losses. It is also appropriate to indicate here that although the typical values found in the literature for the Δn of multiscan DLW WGs in silica are lower at around ~2E − 3 [25], these values are typically measured at visible or near-infrared wavelengths, far from the long-wavelength transmission edge of silica, which is associated to multiphonon excitations. In this sense, a straight comparison with previously reported Δn values can therefore be misleading [26]. The significance of this high index contrast of ~0.7% with step-index WGs was estimated by performing a comparison of two equivalent s-bent WGs using the beam propagation method (BPM). The simulation of a WG with core size of 13 μm, $\Delta n = 0.01$ and a normalized frequency parameter $V = 2.026$, which for two s-bends with radii of 15 mm yielded a total radiation loss of only 0.5 dB, whereas a step-index WG with the same V parameter but a standard index of $\Delta n = 2\text{E} - 3$ would lose all the light at the start of the first bend. The reported WGs therefore allow for smaller DLW footprint circuits than previously envisaged, thus allowing for shorter optical paths and therefore significantly reduced propagation losses at mid-IR wavelengths than previously thought for silica WGs.

The insertion losses (IL) were measured for all the WGs. The coupling losses (CL) were estimated using the overlap integral between the measured WG mode and the measured focal spot of the input/output lenses. The propagation losses (PL) were then obtained from $\text{PL} = (\text{IL} - 2\text{CL})/L$, where L is the WG length. Figure 2 shows the measured transmission spectrum of the S300 sample and the WG PLs of WGs fabricated at 550 μm depth. The PLs follow closely the transmission of S300, being of 1.3 (6.5) dB/cm at 3.39 (3.68) μm wavelength. To evaluate the thermal resistance of the WGs, the sample was submitted to a two-step annealing process: a first annealing step for 2 h at 200°C and a second one at 400°C were performed. After the annealing, the WGs were found to be almost unchanged, the index change was found to be maintained within the ±1E − 3 error, and only the PL at 3.68 μm was observed to slightly deteriorate by +0.55 dB/cm. The fact the WG PLs are 0.5 dB larger than the glass intrinsic absorption at 3.39 μm, and even 1.0 dB larger at the longer wavelength of 3.68 μm, suggests that a larger mode would have a further extension in the defect zone I, where light scattering and absorption is likely to occur. To better understand the morphology of the multiscan WGs, a detailed analysis of the WGs was performed. Figure 3 shows optical bright-field, back-scattered electrons (BSE), and secondary electrons (SE) micrographs of the WG output facet. These images allow to better differentiate volume II (nanostructured defects region), I (index increased core), and I*. The BSE

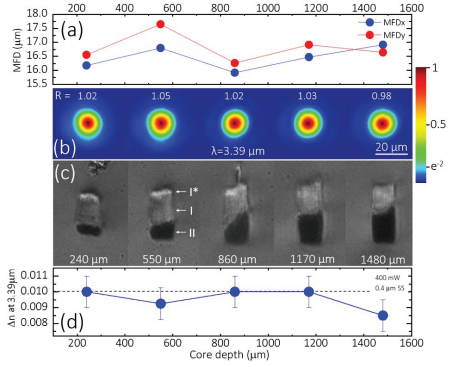

Fig. 1. (a) Horizontal (x) and vertical (y) mode field diameters, (b) output near-field images, (c) bright-field transmission images of WGs, (d) inferred approximate core index changes.

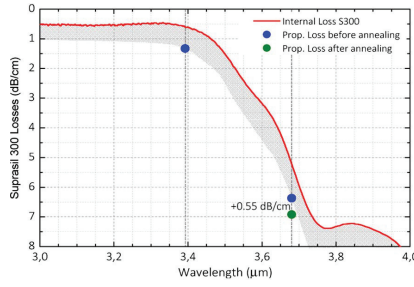

Fig. 2. Measured transmission spectrum of S300 sample together with the WG propagation loss values at different wavelengths.

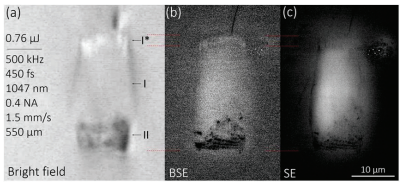

Fig. 3. (a) Optical bright-field, (b) back-scattered electrons, and (c) secondary electrons images of a WG. Volumes II, I, and I* indicated.

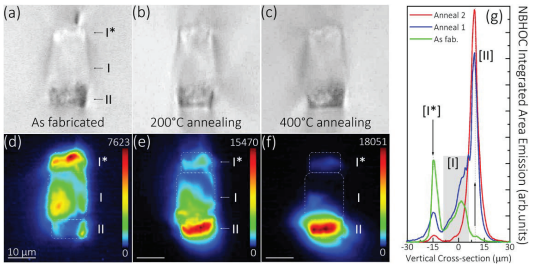

Fig. 5. (a, d) As fabricated WG, (b, e) after 200°C first annealing, (c, f) 400°C second annealing, (g) vertical cross-sections of the three maps.

image shows that the core region I + I* corresponds to densified SiO_2 glass due to the increased brightness. Densification is therefore a main contribution to the large observed mid-infrared index increase.

Further information on the performed laser micromodifications can be obtained from microspectroscopy mapping of the WG facet. With this aim, we first performed micro-Raman confocal measurements at the center of the WG core (zone I) and in unmodified glass volume (see Ref. [23] for further experimental setup details). Figure 4 shows the Raman and luminescence spectra obtained at three different excitation wavelengths. Gaussian fits were used to deconvolute the different broad emission bands of luminescent centers. Excitation at 514 nm [Fig. 4(e)] in unmodified S300 produces broad emission of oxygen deficiency centers (ODCs) with peak intensity at 546 nm (2.27 eV), as well as of an unidentified laser-induced defect (LID) at 576 nm (2.15 eV) [22]. At the WG core, however, strong emission from nonbridging oxygen-hole centers (NBOHCs) is also observed. When exciting at 532 nm [Fig. 4(b)], only NBOHC defects are observed to emit both from unmodified glass and from the WG core, although the peak intensity coming from the core is almost 20-fold more intense than from unmodified glass. Lastly, when exciting at 785 nm [Fig. 4(c)], no luminescence is observed, and the Raman spectrum can be accurately measured.

To obtain a better image of the presence and distribution of NBOHC defects, Fig. 5 presents luminescence 2D micro-mapping of the WG cross section performed before and after the annealing process, revealing that, in the as-fabricated WG NBOHC, defects are mostly present in the WG core with the highest concentration located at region I*, but after the two-step 400°C thermal annealing, NBOHCs are remarkably activated at region II (defect nanofeatures) and almost completely erased from other volumes, this being in line with previous observations by Mishchik *et al.*, even if they were performed at the low repetition rate regime and without multiscan overwriting [27]. Since the index change at the WGs was not observed to change significantly as a result of the annealing process, these experiments confirm that the mid-infrared Δn at the WG core (zone I) is not driven by the presence of NBOHCs, this observation being also in line with previous findings by Reichman *et al.* for the visible range [28]. The obtained mid-IR high index change would then be due at least to the higher glass density observed in the brighter BSE images [see Fig. 3(b)], while other lattice changes such as an increased polarizability could also contribute to the effect.

A micro-Raman mapping (see Fig. 6) was also performed in the WG, before and after annealings, to evaluate the phonon lattice changes produced at each modified volume. Results were very similar in both cases, so after-annealing results are not shown for the sake of brevity. Figure 6(k) shows representative spectra at unmodified S300 glass, top of the core (region I*), core (region I), and at the bottom (nanogratings) region II. The integrated area map of the broad R phonon band [Fig. 6(b)] shows a decrease of 26% from normal glass to zone II, but not at the positive index volumes, thus indicating that, at zone II (nanofeatures defects), indeed strong lattice defect creation

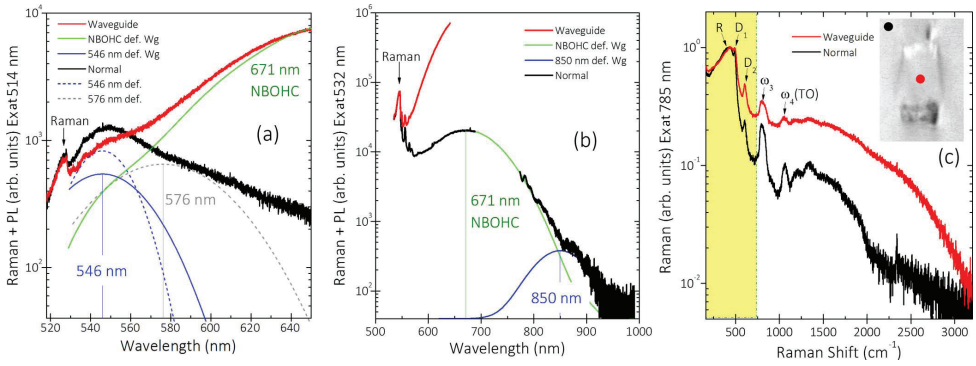

Fig. 4. Micro-Raman spectra inside and outside of the WG: (a) excitation at 514 nm yields a dominant emission of three color centers, (b) excitation at 532 nm yields Raman and emission from NBOHCs, (c) excitation at 785 nm yields clear Raman with no luminescence background. All graphs are in logarithmic scale for clarity of all spectral features.

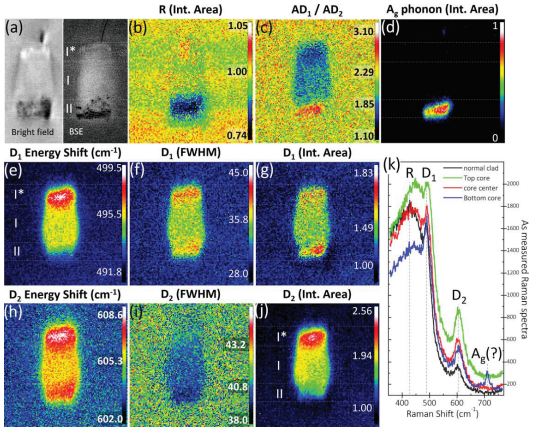

Fig. 6. (a) Bright-field and BSE images; (b) integrated area of R mode; (c) ratio of D_1 and D_2 modes areas; (d) area of the 707 cm^{-1} (A_g) mode; (e) and (h) energy shifts of D_1 and D_2, respectively; (f) and (i) FWHM of D_1 and D_2, resepectively; (g) and (j) areas of the D_1 and D_2, respectively; and (k) representative Raman spectra at nonmodified normal point and at each of the three modified zones.

occurs. This behavior is, however, not observed for the rest of phonon modes. A phonon at 707 cm^{-1} with narrow crystal-like full width at half-maximum (FWHM) of only 13.5 cm^{-1} is also detected at zone II only [Fig. 6(d)] (and which disappeared after 400°C annealing), indicating that indeed fundamental structural transformations of the SiO_2 glass structure occur at this nanostructured volume. This phonon has never been reported in SiO_2 glass to our knowledge, and we tentatively assign it to the identified A_g mode at 705 cm^{-1} from Si-O-Si characteristic bending vibrations of ordered SiO_2 polyhedra in Jadeite [29]. Figures 6(e)–6(j) show maps of phonon energy, FWHM, and integrated area of D_1 and D_2 ring modes. At regions I and I*, a blueshift of both D_1 and D_2 modes is observed, indicating a probable higher compaction level of these ring defects as compared to the surrounding glass and which could be also related to the observed index changes at the long wavelength limit of transparency of the glass, related to multiphonon absorptions. Finally, we also analyzed the ratio of integrated areas of D_1 and D_2 rings, finding a clear trend in which the depressed index zone II has a high ratio value of ∼3, while positive Δn zones I and I* show a lower value of ∼1.85 down to ∼1.1. The use of this ratio coefficient could prove useful as an indicator of refractive index increased areas in DLW fused silica glass. Further in depth analysis of these observations is being prepared and will be published elsewhere.

In conclusion, we have demonstrated the DLW of step-index WGs in SiO_2 glass capable of guiding at around the 3.5 μm range. We have proved these WGs can sustain temperatures of up to 400°C and can provide low-loss coupling to mid-IR fluoride fibers. We have also studied the microstructural changes associated with the femtosecond pulse laser modified glass, identifying three different states of SiO_2 glass state.

Funding. Spanish Government (MAT2013-47395-C4-4-R, TEC2014-55948-R, TEC2014-52642-C2-1-R, FIS2013-44174-P); Catalan Government (2009SGR235, 2014FI_B 00274); European Commission (EC) (ACP2-GA-2013-314335-JEDI ACE).

Acknowledgment. F. D. acknowledges additional support 2010ICREA-02 for excellence in research.

REFERENCES

1. J. Faist, F. Capasso, D. L. Sivco, C. Sirtori, A. L. Hutchinson, and A. Y. Cho, Science **264**, 5158 (1994).
2. Y. Yao, A. J. Hoffman, and C. F. Gmachl, Nat. Photonics **6**, 432 (2012).
3. M. S. Vitiello, G. Scalari, B. Williams, and P. De Natale, Opt. Express **23**, 5167 (2015).
4. W. Zeller, L. Naehle, P. Fuchs, F. Gerschuetz, L. Hildebrandt, and J. Koeth, Sensors **10**, 2492 (2010).
5. C. R. Webster, P. R. Mahaffy, S. K. Atreya, G. J. Flesch, and K. A. Farley, and the MSL Science Team, Science **342**, 355 (2013).
6. M. Saad, Proc. SPIE **7316**, 73160N (2009).
7. V. Fortin, M. Bernier, S. T. Bah, and R. Vallée, Opt. Lett. **40**, 2882 (2015).
8. B. Bureau, C. Boussard-Plédel, V. Nazabal, J. Adam, and J. Lucas, "Chalcogenide optical fibers for mid-infrared sensing: state of the art and future strategies," in *Advanced Photonics*, OSA Technical Digest (online) (Optical Society of America, 2014), paper SeTh1C.1.
9. N. Caron, M. Bernier, D. Faucher, and R. Vallée, Opt. Express **20**, 22188 (2012).
10. Y. Bellouard, A. Said, and P. Bado, Opt. Express **13**, 6635 (2005).
11. Y. Bellouard, Opt. Mater. Express **1**, 816 (2011).
12. I. I. Orlovskiy, K. Y. Vukolov, E. N. Andreenko, and T. R. Mukhammedzyanov, J. Nucl. Mater. **442**, S508, Supplement 1, 508 (2013).
13. B. Schwarz, P. Reiniger, D. Ristanic, H. Detz, A. M. Andrews, W. Schrenk, and G. Strasser, Nat. Commun. **5**, 4085 (2014).
14. K. M. Davis, K. Miura, N. Sugimoto, and K. Hirao, Opt. Lett. **21**, 1729 (1996).
15. A. Marcinkevičius, S. Juodkazis, M. Watanabe, M. Miwa, S. Matsuo, H. Misawa, and J. Nishii, Opt. Lett. **26**, 277 (2001).
16. Y. Nasu, M. Kohtoku, and Y. Hibino, Opt. Lett. **30**, 723 (2005).
17. G. D. Marshall, M. Ams, and M. J. Withford, Opt. Lett. **31**, 2690 (2006).
18. R. R. Thomson, H. T. Bookey, N. D. Psaila, A. Fender, S. Campbell, W. N. MacPherson, J. S. Barton, D. T. Reid, and A. K. Kar, Opt. Express **15**, 11691 (2007).
19. S. J. Beecher, R. R. Thomson, B. P. Pal, and A. K. Kar, IEEE Sens. J. **12**, 1263 (2012).
20. G. Cheng, C. D'Amico, X. Liu, and R. Stoian, Opt. Lett. **38**, 1924 (2013).
21. Y. Shimotsuma, P. G. Kazansky, J. Qiu, and K. Hirao, Phys. Rev. Lett. **91**, 247405 (2003).
22. R. Stoian, K. Mishchik, G. Cheng, C. Mauclair, C. D'Amico, J. P. Colombier, and M. Zamfirescu, Opt. Mater. Express **3**, 1755 (2013).
23. A. Ródenas, G. Martin, B. Arezki, N. Psaila, G. Jose, A. Jha, L. Labadie, P. Kern, A. Kar, and R. Thomson, Opt. Lett. **37**, 392 (2012).
24. A. Rodenas and A. K. Kar, Opt. Express **19**, 17820 (2011).
25. W. Watanabe, Y. Note, and K. Itoh, Opt. Lett. **30**, 2888 (2005).
26. S. M. Eaton, M. L. Ng, R. Osellame, and P. R. Herman, J. Non-Cryst. Solids **357**, 2387 (2011).
27. K. Mishchik, C. D'Amico, P. K. Velpula, C. Mauclair, A. Boukenter, Y. Ouerdane, and R. Stoian, J. Appl. Phys. **114**, 133502 (2013).
28. W. J. Reichman, D. M. Krol, L. Shah, F. Yoshino, A. Arai, S. M. Eaton, and P. R. Herman, J. Appl. Phys. **99**, 123112 (2006).
29. M. Prencipe, J. Raman Spectrosc. **43**, 1567 (2012).

PAPER II

Letter Vol. 41, No. 11 / June 1 2016 / Optics Letters 2493

Optics Letters

Mid-infrared surface plasmon polariton chemical sensing on fiber-coupled ITO coated glass

Javier Martínez,[1] Airán Ródenas,[1,*] Magdalena Aguiló,[1] Toney Fernandez,[2] Javier Solis,[3] and Francesc Díaz[1]

[1]Departament de Química Física i Inorgànica, Universitat Rovira i Virgili, Tarragona, Spain
[2]Dipartimento di Fisica, Politecnico di Milano, Milano, Italy
[3]Laser Processing Group, Instituto de Óptica-CSIC, Madrid, Spain
*Corresponding author: arodenas@gmail.com

Received 11 April 2016; revised 28 April 2016; accepted 28 April 2016; posted 29 April 2016 (Doc. ID 262883); published 20 May 2016

A novel fiber-coupled indium tin oxide (ITO) coated glass slide sensor for performing surface plasmon polariton chemical monitoring in the ~3.5 μm mid-infrared (IR) range is reported. Efficient mid-IR fiber coupling is achieved with 3D laser written waveguides, and the coupling of glass waveguide modes to ITO surface plasmon polaritons (SPPs) is driven by the varying phase matching conditions of different aqueous analytes across the anomalous dispersion range determined by their molecular fingerprints. By means of using both a mid-IR fiber supercontinuum source and a diode laser, the excitation of SPPs is demonstrated. The sensor sensitivity is tested by discriminating CH from OH features of ethanol in water solutions, demonstrating an instrumental ethanol limit of detection of 0.02% in a wide concentration range of at least 0%–50%. The efficient optical monitoring of mid-IR SPPs in smart glass could have a broad range of applications in biological and chemical sensing.

OCIS codes: (240.6680) Surface plasmons; (300.6340) Spectroscopy, infrared; (130.3060) Infrared; (130.6010) Sensors.

http://dx.doi.org/10.1364/OL.41.002493

Since the introduction of the quantum cascade laser [1], the rapid development of mid-infrared (IR) technology has fostered research in novel photonic devices for sensing [2]. In the mid-IR range, the strong molecular absorption features associated with vibrational resonances allow for distinction of different chemical species within a substance [3]. Moreover, the sensing performance of mid-IR devices can be enhanced by incorporating field enhancement and confinement techniques that effectively increase the strength of the light-analyte interaction [4]. A widely extended mechanism for sensing in the VIS and NIR ranges is the surface plasmon polariton (SPP) [5,6]. However, the plasma frequency of noble metals typically used in SPP devices lies on the visible part of the spectrum, making them less appealing plasmonic materials at IR wavelengths [7]. For this reason, and because the properties of metallic thin films cannot be tuned, other materials have been considered in recent years, such as semiconductors, silicides, germanides, transparent conductive oxides, or graphene. On the other hand, particular methods like prism interrogation [6,8], waveguide gratings and tapers [6,9], or nanoantenna arrays [10], are typically used to access plasmonic modes as normally done in the VIS and NIR regions, but highly efficient direct fiber-coupling schemes are still lacking in the mid-IR.

In this Letter, a simple yet robust concept for sensing at mid-IR wavelengths through the excitation of SPPs is explored. The concept is numerically investigated and also fabricated using 3D laser writing (3DLW) of waveguide circuits and thin film sputtering. The experimental observation of mid-IR SPP excitation is presented together with an evaluation of the sensing potential for a specific analyte. The proposed mid-IR SPP sensor consists of a fiber-coupled waveguide inside an indium tin oxide (ITO) covered silica slide. ITO is chosen for its superior plasmonic properties within the spectral range of interest ~3.5 μm [7]. A sketch of the device is shown in Fig. 1. The width of the thin film is considered infinite for modeling purposes. Mid-IR light is coupled into the 3DLW waveguide, which then routes the light to the analyte interaction area and a detector monitors the output power of the waveguide. An interferometric scheme could be further applied on a Mach–Zehnder configuration, although this is out of the scope of the present Letter.

The mechanism of SPP excitation is the phase matching of the dielectric waveguide mode and the SPP mode, as well as the

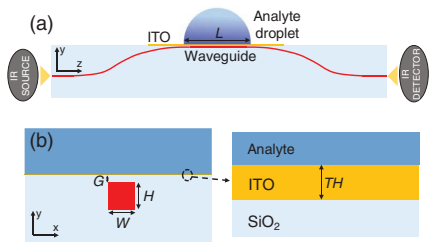

Fig. 1. Sketch of the (a) proposed fiber-coupled mid-IR SPP glass sensor and (b) detailed waveguide cross-section design.

spatial overlapping between the evanescent field of the waveguide mode and the thin film mode [5]. The intense and broad optical absorption of liquid water associated with the stretching of OH groups is accompanied by a large refractive index variation around 3.5 μm, shown in Fig. 2, which enables index matching between liquid water and silica glass. This fact ensures the refractive symmetry needed between the *substrate* (silica) and the *superstrate* (water), which, in turn, allows the existence of a SPP mode and hence the aforementioned phase matching. Following the same reasoning, other substances added to the analyte having molecular groups with mid-IR resonances will modify the SPP coupling condition. Note that the presented scheme avoids the need for structuring the surface to achieve phase matching, which notably simplifies the fabrication process.

As sketched in Fig. 1, the waveguide parameters are its width and height (W and H) and its index increases with respect to the unmodified bulk surrounding silica (Δn). Details of the fabrication and characterization of these 3DLW mid-IR waveguides were recently published [11]. Between the core and the thin film there is also a gap (G) of unmodified silica. The interaction length of the generated plasma wave and the liquid is defined as L, which will be ~2 mm. Regarding the thin film, a thick layer of ITO (TH) was deposited onto the silica substrate by direct current magnetron sputtering of a commercial ITO target [12]. Optical constants, as well as the TH of the deposited ITO thin film, were retrieved through the fitting of its transmittance data to a hybrid Forouhi–Bloomer plus Drude model [13]. For the particular thin film deposited, these are carrier concentration $N = 13.4 \times 10^{20}$ cm^{-3}, mobility $\mu = 23.4$ cm^2/(V · s) and $TH = 54$ nm. From the said model one can extrapolate the complex ITO mid-IR relative permittivity.

With the aid of COMSOL Multiphysics software the electro-magnetic transversal bound modes of the mid-IR SPP structure were solved via the finite element method. The mid-IR relative permittivity of the rest of different materials involved (liquid water and silica glass) was taken from literature [14,15]. For example, at $\lambda = 3.47$ μm they become, respectively, $\epsilon_{\text{water}} = 1.98 + i0.03$, $\epsilon_{\text{silica}} = 1.98$, and $\epsilon_{\text{ITO}} = -28.23 + i11.17$. Note that silica losses are here considered negligible in comparison with water and ITO. Calculated transverse-magnetic (TM) mode profiles at $\lambda = 3.49$ μm are shown in Fig. 3(a) with the corresponding complex effective index ($n + ik$) for two different silica gaps and when air or water are covering the chip. It can be seen that a coupled waveguide-SPP mode appears when the superstrate is water, and not air. This coupling becomes the more evident the smaller the gap (G), leading to increased mode losses as well.

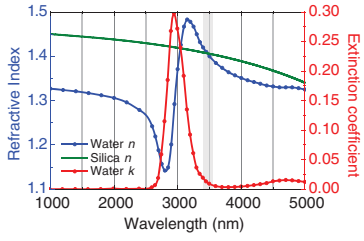

Fig. 2. Refractive index of water and fused silica and extinction coefficient of water in the 2–4 μm band.

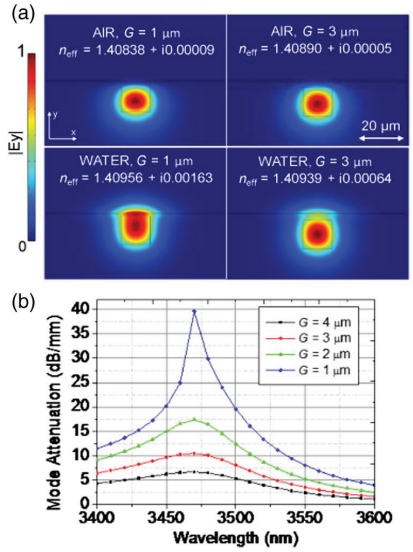

Fig. 3. (a) Simulated TM electric field profile magnitude at $\lambda = 3.49$ μm for different superstrates and gaps. (b) Calculated SPP relative MA spectrum for different gaps.

The case $G = 3$ μm is also displayed here because it is a closer value to the one here experimentally reported. The calculated field penetration into the liquid was numerically computed to be 1.6 μm, taking the intensity as an exponentially decaying function [6].

From the simulated effective extinction coefficients one can calculate the relative mode attenuation (MA) which is here defined as $MA(\text{dB/mm}) = 4\pi \cdot \log(e) \cdot 10^4 (k_{\text{water}} - k_{\text{air}})/\lambda(\mu\text{m})$, where k_{water} and k_{air} are the mode extinction coefficients when the *superstrate* is water and air, respectively, and λ is the free-space wavelength in mm. The MA spectrum for the SPP coupled mode is shown in Fig. 3(b) for various gaps G. As mentioned, the waveguide-SPP coupling and, therefore, the attenuation are stronger for shorter gaps leading to a decreasing width of the resonance, which makes the device more sensitive and selective. The maximum MA is located at $\lambda = 3.47$ μm, which may not necessarily coincide with the maximum measured attenuation.

For the correct experimental demonstration of the SPP excitation, a broadband mid-IR source is needed. A home-built high brightness fiber-based IR supercontinuum source (SCS) was therefore used [16]. The small core (7.5 μm) and numerical aperture (0.265) of the fiber guarantees low-loss mid-IR coupling with the waveguide. The resulting 2.4 to 4.1 μm spectrum (see Fig. 4) of the light generated by the SCS was recorded by a Jobin-Yvon Horiba HR460 monochromator equipped with a 300 gr/mm IR ruled grating and having a lead selenide detector at the output slit. The detection system was synchronized to the seed laser repetition rate (5.12 kHz) by means of a lock-in amplifier for maximum SNR.

Because only the longest wavelengths (>2.4 μm) are relevant, a germanium-based long-pass filter was placed between a pair of aspheric lenses that collimated the light from the SCS and coupled the filtered light to another single-mode

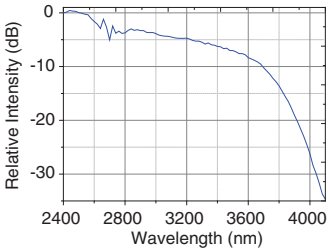

Fig. 4. Long-wavelength spectrum generated by the home-built SCS.

transporting fiber. This also protects the chip from the high intensity residual seed at $\lambda = 1.55$ μm that had been greatly amplified in the SCS. The measured average output power of the transporting fiber is 500 μW. The transporting fiber and an output fiber were carefully aligned to their corresponding sensor chip ports. When the waveguide insertion loss was minimized, the second end of the output fiber was placed in front of the input slit of the monochromator in order to measure relative spectral variations of the light emerging from the mid-IR SPP sensor. Note that no polarizing elements were used here so no isolation of TM light was performed.

Spectra with and without water drops covering the ITO thin film were measured so as to evaluate the relative light attenuation (*LA*) associated with a SPP excitation. Precisely, $LA(\mathrm{dB/mm}) = -10\log(V_{\mathrm{water}}/V_{\mathrm{air}})/L$, where V_{water} is the detector voltage when a water drop is covering the sensor, V_{air} is the clean reference voltage and L is the drop length (in mm), which acts as a normalization factor. L was determined by taking a top view image of the analyte drop, which introduced a ±50 μm uncertainty in the measurement [a microfluidic poly(dimethylsiloxane) cover would eliminate this uncertainty but is also out of the scope of the present Letter]. An example of a *LA* spectrum using pure deionized water at 20°C is shown in Fig. 5(a). The curve has a resonant-like behavior that peaks at $\lambda = 3510 \pm 10$ nm, thus hinting a SPP excitation.

Direct analogy with the simulated *MA* [dashed line in Fig. 5(a)] may be done cautiously and taking into account that in the experimental setup the polarization is not controlled, and that the device transmission not only depends on the polarized modal attenuation but on other processes such as the mode coupling efficiency dispersion between the pure waveguide mode and the hybrid waveguide-SPP mode. These factors may explain the lower attenuation obtained in this SCS experiment, that is 0.9 dB/mm versus 9.8 dB/mm (simulated) TM mode attenuation. The parameters used for this simulation were $W \times H = 11.8 \times 12.7\ \mu\mathrm{m}^2$, $\Delta n = 8 \cdot 10^{-3}$, $G = 3.3$ μm, and $TH = 54$ nm, which were extracted from the previous characterization of the fabricated device.

Following the same procedure of that with pure water, drops of a solution of water and ethanol at 20°C were tested on the SPP sensor. In Fig. 5(b), the measured spectra for different volume concentration of ethanol in water (from 0% to 50%) are shown. Differences in several CH and OH bands for increasing ethanol concentration are observed. For instance, a rise of *LA* occurs around $\lambda \approx 3.3$ μm and, more intensively, from $\lambda \approx 3.6$ to 3.8 μm. These spectral variations can be associated to the

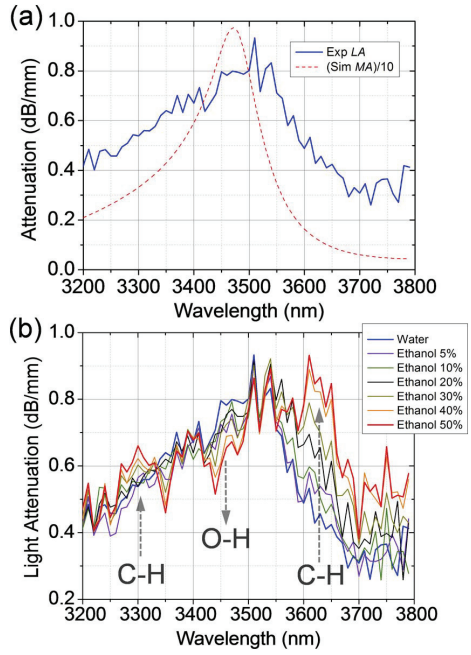

Fig. 5. (a) Unpolarized *LA* spectrum (solid line) when a drop of water is placed on the sensor. The calculated TM *MA* spectrum (divided by 10) is superimposed (dashed line) for comparison purposes. (b) Unpolarized *LA* spectra corresponding to different solutions of water and ethanol with increasing ethanol concentrations.

increasing presence of the CH stretching band around ~2970 cm^{-1} [17], which can produce SPP coupling at different wavelengths due to absorption increments or index increments, i.e., both real and imaginary parts of the dielectric and the hybrid-SPP mode effective indices affect the coupling ratios and hence the measured attenuation.

The higher attenuation at $\lambda \sim 3.3$ μm is directly produced by a stronger optical absorption (CH stretch), whereas the growing attenuation in the 3.6–3.8 μm band is due to the refractive index increase (around the anomalous dispersion range) associated with the CH resonance. As already explained for the pure water case, such index increase facilitates the symmetry condition for a SPP excitation and the modes coupling, with the difference that for the CH stretch it happens at a longer wavelength as it can be clearly observed in the new peak emerging at $\lambda \sim 3610$ nm, for the higher concentration case (30%–50%). Conversely, at the same time the *LA* at $\lambda \sim 3450$ nm is reduced indicating a diminishing presence of the OHs against CHs within the SPP near-field. In short, the complex refractive index of the water–ethanol solution has a spectrally complex nature in this region, which allows for SPP excitation around two distinct bands corresponding with the OH and CH stretching molecular vibrations.

The mid-IR SPP sensor was further tested for the water–ethanol specific case by using a 3.60 μm narrow-band low-noise interband cascade laser (ICL) in a TM-polarized setup, therefore allowing for a much more precise reading of the SPP effect.

For these tests the waveguide output was imaged into a FLIR SC7000 mid-IR camera, which allowed for direct monitoring of the output power temporal evolution. Polarizers in TM direction were placed before and after the waveguide to isolate the SPP effect. The same experiment as with the SCS was repeated but adding low ethanol concentration samples down to 1%.

As shown in Fig. 6(a), an increasing *LA* associated to the CH feature at 3.60 μm for higher ethanol concentration was observed in the spectral measurements. The included ±2% relative error bars correspond to the ±50 μm uncertainty in the drop size determination. Furthermore, the maximum ethanol measurable concentration was estimated to be at least of 50%, having a higher slope (i.e., higher sensitivity) in the range 0%–30%, and a decreasing one from 30% to 50%. As expected, higher attenuation is obtained than in the preceding experiment because only TM light was coupled into the waveguide. At 0% ethanol (i.e., pure deionized water) the experimentally measured *LA* is 1.75 dB/mm, in very good agreement with the simulated *MA* at $\lambda = 3.60$ μm of 1.63 dB/mm. It was also verified that *LA* is negligible when launching TE polarized light regardless of the analyte, because no TE SPP mode can exist.

Focusing on the lower concentrations, Fig. 6(b) shows the measured *LA* from which a clear linear trend can be deduced. Using this as a calibration curve, and using mean and standard deviation values derived from the several measurements, the instrumental limit of detection (LOD) of ethanol of this SPP sensor can be estimated [18]. It is important to note that for this calculation the *L* uncertainty (drop length) of our laboratory experiments is neglected, because adding a microfluidic channel on the ITO surface would allow to easily fix the interaction length. For $L = 2$ mm, 3σ criterion, and 10 measurements, the LOD is calculated to be 0.02%. The LOD of this mid-IR SPP sensor matches that of other sensors fabricated with more complex techniques like the ones found in [4] (0.06%) and [19] (0.004%), which are based on plasmonic and capacitive micro-electro-mechanical systems technology, respectively. Moreover, our prototype sensor has a waveguide to surface distance of 3.3 μm gap (*G*), and by reducing this gap to 1 μm, the sensor attenuation would be enhanced by a factor of ∼33 dB/mm, i.e., a 2000-fold increase.

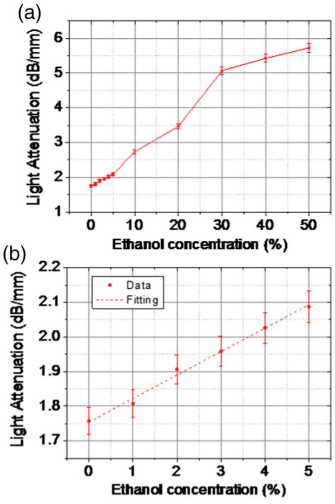

Fig. 6. (a) TM polarized *LA* induced by the water–ethanol solution drops on the sensor at $\lambda = 3.6$ μm for increasing ethanol concentrations. (b) *LA* for low ethanol concentrations and linear fitting of the data.

In conclusion, the excitation of a mid-IR SPP on an ITO thin film covered by an aqueous analyte via a 3DLW silica glass waveguide has been demonstrated. The device has been modeled through finite element method simulations, then fabricated with well-established microfabrication techniques, and finally experimentally validated using broad and narrowband spatially coherent light. The attenuation due to the SPP excitation has been used to sense the presence of water and the concentrations of ethanol in water, taking advantage of the anomalous dispersion range of the liquids at their molecular resonances. The highly efficient mid-IR fiber-to-SPPs coupling on common ITO coated silica glass could find wide applications in biological and chemical sensing, and could be directly implemented in portable smart phone screens, microscopy slides, or any other glass surface used in everyday life.

Funding. Spanish Government (MAT2013-47395-C4-4-R, TEC2014-52642-C2-1-R, TEC2014-55948-R); Catalan Government (2009SGR235, 2014FI_B00274); European Commission (EC) (ACP2-GA-2013-314335-JEDI ACE).

Acknowledgment. F. D. acknowledges additional support 2010-ICREA-02 for excellence in research.

REFERENCES

1. J. Faist, F. Capasso, D. L. Sivco, C. Sirtori, A. L. Hutchinson, and A. Y. Cho, Science **264**, 553 (1994).
2. B. Mizaikoff, Chem. Soc. Rev. **42**, 8683 (2013).
3. B. H. Stuart, *Infrared Spectroscopy: Fundamentals and Applications* (Wiley, 2004).
4. B. Schwarz, P. Reiniger, D. Ristanic, H. Detz, A. M. Andrews, W. Schrenk, and G. Strasser, Nat. Commun. **5**, 4085 (2014).
5. J. Homola, Chem. Rev. **108**, 462 (2008).
6. H. Raether, *Surface Plasmons on Smooth and Rough Surfaces and on Gratings* (Springer, 1988).
7. G. V. Naik, V. M. Shalaev, and A. Boltasseva, Adv. Mater. **25**, 3264 (2013).
8. M. Golosovsky, V. Lirtsman, V. Yashunsky, D. Davidov, and B. Aroeti, J. Appl. Phys. **105**, 102036 (2009).
9. O. Esteban, A. González-Cano, B. Mizaikoff, N. Díaz-Herrera, and M.-C. Navarrete, Plasmonics **7**, 647 (2012).
10. L. Baldassarre, E. Sakat, J. Frigerio, A. Samarelli, K. Gallacher, E. Calandrini, G. Isella, D. J. Paul, M. Ortolani, and P. Biagioni, Nano Lett. **15**, 7225 (2015).
11. J. Martínez, A. Ródenas, T. T. Fernandez, J. R. Vázquez de Aldana, R. R. Thomson, M. Aguiló, A. K. Kar, J. Solis, and F. Díaz, Opt. Lett. **40**, 5818 (2015).
12. H.-C. Lee and O. Ok Park, Vacuum **80**, 880 (2006).
13. F. Lai, L. Lin, R. Gai, Y. Lin, and Z. Huang, Thin Solid Films **515**, 7387 (2007).
14. G. M. Hale and M. R. Querry, Appl. Opt. **12**, 555 (1973).
15. I. H. Malitson, J. Opt. Soc. Am. **55**, 1205 (1965).
16. C. Xia, M. Kumar, O. P. Kulkarni, M. N. Islam, and F. L. Terry, Jr., Opt. Lett. **31**, 2553 (2006).
17. S. Burikov, T. Dolenko, S. Patsaeva, Y. Starokurov, and V. Yuzhakov, Mol. Phys. **108**, 2427 (2010).
18. H.-P. Loock and P. D. Wentzell, Sens. Actuators B **173**, 157 (2012).
19. D. L. McCorkle, R. J. Warmack, S. V. Patel, T. Mlsna, S. R. Hunter, and T. L. Ferrell, Sens. Actuators B **107**, 892 (2005).

PAPER III

Submitted to Advanced Functional Materials on the 14th of February 2017

Harsh-Environment Resistant OH-Vibrations Sensitive Water-Ice Photonic Sensor

Javier Martínez, Airán Ródenas, Andreas Stake, Miquel Traveria, Magdalena Aguiló, Javier Solis, Roberto Osellame, Taro Tanaka, Benoit Berton, Shigueo Kimura, Nadine Rehfeld, and Francesc Díaz

Whereas water is the most common liquid on Earth, its plethora of anomalous and counterintuitive properties still puzzle scientists and engineers from a wide diversity of fields [1]. Possibly the most abundant state of water in the universe is its solid glass form present in interstellar dust and comets (polyamorphous ice) [1], while on Earth it appears in liquid form, its crystalline hexagonal phase, or in its cubic phase below -80 ºC [2]. Yet, there also exists a metastable state of liquid water within the crystalline domain between 0 and -32 ºC in which its thermodynamical anomalies manifest most strongly; Supercooled water (SCW) [3] is of importance for cell research and the understanding of life at its lower temperature limit, the food and pharmaceutical industries, environmental and climate research sciences, and the aviation industry, amongst others.

Natural SCW is largely present in cold clouds and it is a recognized hazard for commercial aviation, ultimately hampering achievement of the zero operational accidents international safety goal [4]. When micrometer SCW cloud droplets impinge on a wing surface they immediately freeze, promoting a fast-growing ice accretion layer which can degrade wing performance within seconds with potential loss of control and aircraft stall [5], a process commonly known as in-flight icing. As modern aircraft design evolves towards adopting advanced wing concepts such as the blended wing body and low-drag end surfaces for greener and fuel efficient aircrafts, in-flight icing phenomena not only poses a challenge to coming safety regulations but also to the development of next-generation aircrafts. Among the priorities in aeronautics icing research, besides the development of icephobic anti-icing and de-icing coatings [5, 6], is the development of highly-reliable ice sensors that can be embedded and distributed across wing surfaces for the automatic control of electro-thermal de-icing systems. Current aircraft ice sensors are large, heavy, airflow intrusive, are installed in the aircraft fuselage rather than at aerodynamic control elements (wings and stabilizers), cannot detect a fast growing ice layer until it reaches a sub-mm thickness (>0.2 mm), and are limited in response time (>3 s). The development of small footprint and lightweight, ultrasensitive ice sensors that yet do not disturb the airflow and resist environmental erosion is therefore a clear need in aeronautics icing research.

State-of-the-art nanophotonic sensors rely on the exposure of engineered nanostructured devices such as evanescent-field enhanced waveguides, whispering gallery mode resonators, photonic crystal cavities or nanoplasmonic structures [7]. However, these devices are not monolithic but made of heterogeneous materials and rely on their nanometer precision design to achieve maximal sensitivities, this implying that they are fragile and rely on careful calibrations, becoming either catastrophically damaged or dysfunctional if systematically exposed to harsh environmental conditions (i.e. contamination, chemical corrosion, erosion, vibrations and large temperature variations >200 ºC). As a result, the goal of designing sensitive surface sensors that can yet sustain long-term operation in harsh environments has hitherto not been achieved.

Here we demonstrate a harsh-environment resistant photonic water-ice sensor that probes external molecular changes through resonant light transfer across the infrared OH-stretch vibrational mode, which is a known sensitive probe of the intermolecular distances between water molecules [8]. The sensor was designed on the basis of being resistant to large temperature changes, moderate surface erosion and vibrations, and yet being not-intrusive to aerodynamic flow and highly sensitive to water ice layers. It is based on a mid-IR waveguide which is seamlessly formed inside a transparent glass substrate and low-loss interconnected to external optical fibers for remote optical monitoring. Fast differentiation between water, SCW and crystalline ice was first evaluated through both numerical simulations and laboratory experiments. To prove the sensor robustness and response in a relevant environment, extensive tests were done in an icing wind tunnel in conditions ranging from in-flight cold rain to fast accretion of different types of microstructured rime and glaze ices. Lastly, the tuning of sensitivity to an ultra-wide range of water layer thicknesses from sub-mm down to nanometric widths (≤100 nm) is demonstrated by varying the waveguide parameters. Overall, this type of robust and sensitive photonic water-ice sensor could find application in the aircraft industry as well as in other fields where precise monitoring of the phase or composition of water molecules within micro- to nanometric layers is needed, such as for biogenic ice nucleation research, the freeze-drying food and pharmaceutical production, wind turbines, the nuclear fission industry, for in-field medical analysis, in cryogenic high-vacuum space-simulation testing chambers, or for fundamental atmospheric science [9-15].

The sensing mechanism of the mid-IR waveguide sensor is 3D rendered in Figure 1A. The waveguide follows an in-depth bent path so as to pass several microns below the surface to be sensed, and deepens away from it to achieve low-loss direct interconnection with embedded commercial fibers. The phase state of water droplets in the sensing region determines the efficiency and frequency of the resonant transfer condition as a result of the large complex refractive index changes of water around its OH-stretch vibrational fingerprint. The mid-IR waveguide circuit is embedded by means of sub-picosecond 3D direct laser writing (3DLW) in commercially available IR-grade fused silica glass ($aSiO_2$), which has well-known mechanical and chemical stability, besides it´s widespread use in many technologies. Light tunnelling can take place even if the sensing waveguide is buried tens of microns inside the glass, so that the sensor has the unique feature of being erosion resilient while also highly specific and sensitive. Figure 1B shows the sensor cross-section scheme and its main design parameters: the core width (W), height (H) and the gap to surface (G). Additional

Submitted to Advanced Functional Materials on the 14th of February 2017

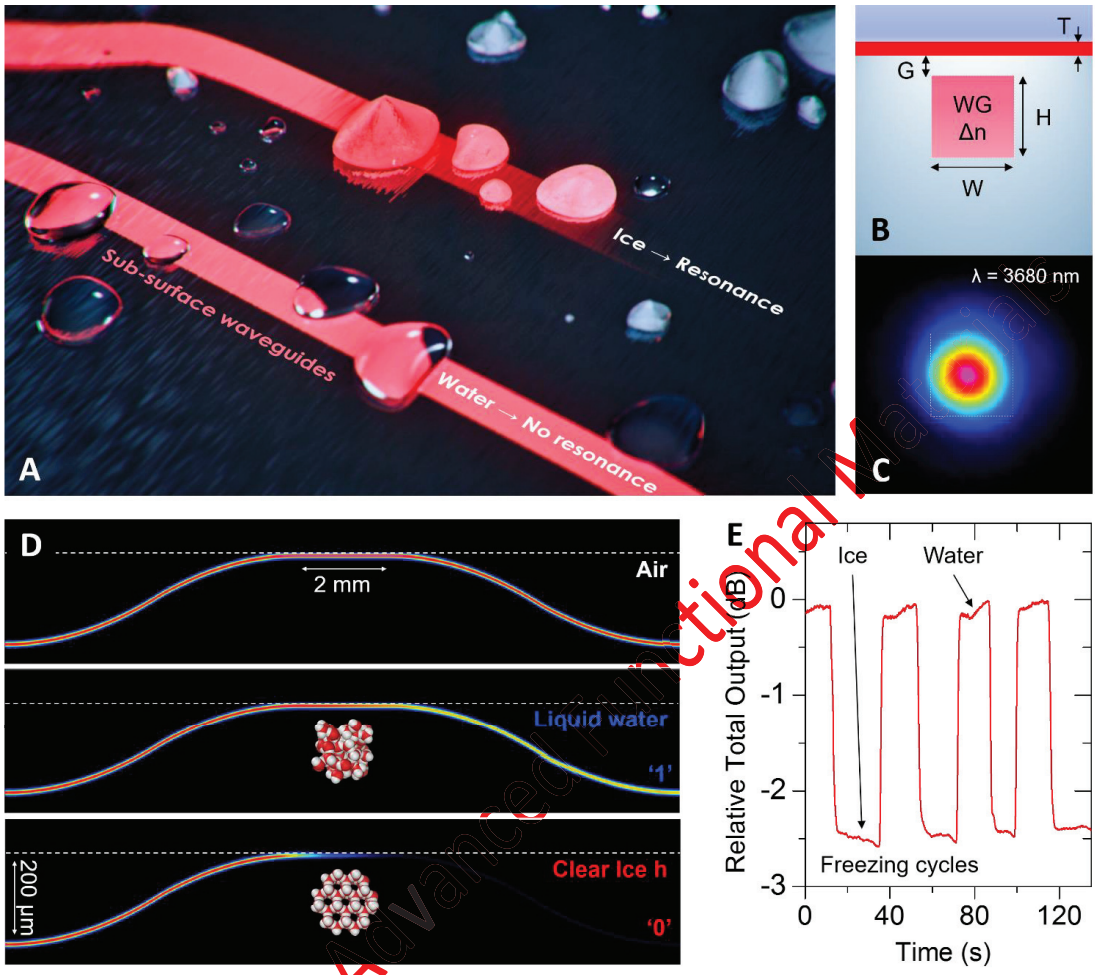

Figure 1. Mid-IR water ice phase surface sensor. (A) Conceptual view of the photonic sensor working mechanism. When water droplets are present on the sensor surface detection occurs by means of resonant light transfer to droplets whose index of refraction produces a phase matching condition implying a sudden dip on transmitted light. By spectrally tunning light across the OH vibrational band of water the phase state of the water layer is obtained. Since waveguides propagate below surface the sensor is immune to erosion or scratches smaller than its depth gap (B) Sensor design cross-section parameters (typical values W=15 µm, H=15 µm and G=5 µm) which can be changed to maximise the light coupling sensitivity to a given layer thickness T (from ~100 nm to ~500 µm). (C) Measured near-field of the waveguide output at 3.68 µm wavelength. (D) Electromagnetic beam propagation simulations of light travelling the 2 mm long sensing waveguide for air, room temperature water and clear -7 ºC homogenous ice surface layers. (E) First tests on experimental detection of freezing cycles of a water droplet with the glass sensor temperature controlled by a peltier unit and detection with a thermal power meter. The measured output intensity is evaluated as relative output power (dB) between ice and liquid water states.

parameters are the waveguide core index difference with the glass surrounding ($\Delta n=n_{core}-n_{aSiO2}$), and the length of the interacting path (L). All these parameters can be tailored at the fabrication stage so as to optimize the sensor for a given application (layer thickness of interest or level of attenuation) as discussed below. Figure 1C shows an experimental image of the waveguide mode near-field intensity at 3.68 µm, before it is bonded to optical fibers (see Figure S2.1 and Supporting Information for further experimental details).

Several electromagnetic beam propagation simulations based on the beam propagation method (BPM) were carried out to show the waveguide output photon flux as a function of the external medium being air, liquid water at room temperature or homogenous clear ice at -7 ºC using data from Hale [16] and Warren [17] for the index of refraction of water and ice, respectively (see Supporting Information for further details). Figure 1D shows the obtained field intensity ($|E|^2$) profiles, for a glass sample of 16 mm total length with an interaction (sensing) waveguide length of 2 mm. The waveguide core size is W=H=14 µm, the gap G=2 µm and the refractive index change relative to the silica cladding is $\Delta n=8\cdot10^{-3}$. These parameters give single mode behaviour at wavelengths between 3 to 4 µm (see experimental mode in Figure 1C). It can be clearly observed that the presence of ice induces a strong power attenuation of the guided light due to resonant light tunnelling, and which does not occur when water is in liquid state or there is air. The detection principle relies on the evanescent coupling between the waveguide mode and available light modes in the external water layer, a process which occurs most efficiently at a different wavelength depending on the phase state of water and its

Submitted to Advanced Functional Materials on the 14th of February 2017

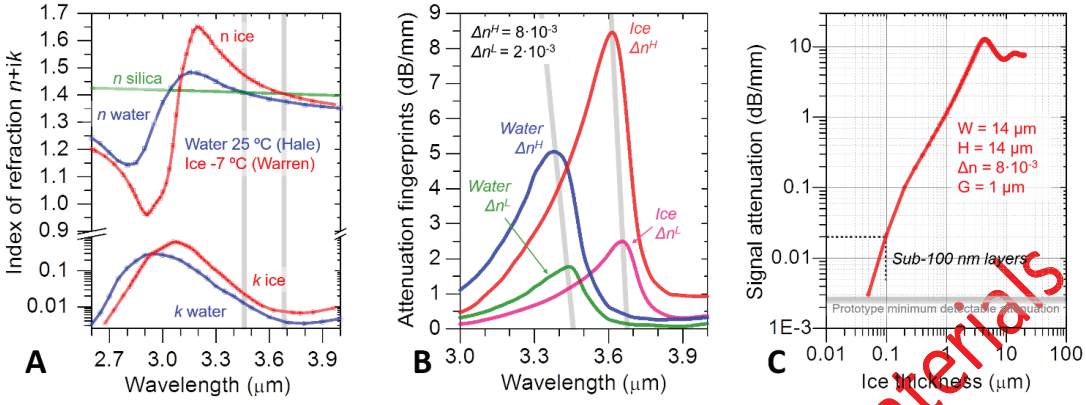

Figure 2. Directional coupling (light tunnelling) conditions and simulation of sensor performance across the anomalous-to-normal dispersion range of water. (A) Complex refractive index of liquid water (25 ºC) from Hale [16], and ice at -7 ºC from Warren [17], and index of refraction of fused silica glass. The phase matching wavelengths between water and silica are indicated with grey vertical bars at around 3.46 μm (liquid water) and 3.68 μm (ice). (B) Simulated sensor spectral output response for ice and water layers (normalized to air and per mm of sensing length). For small gaps (G<5 μm), the differential attenuation levels (sensitivity) between ice and water depend on the waveguide refractive index change Δn, due to the change in waveguide propagation constant. No light tunnelling occurs across the 3 μm wavelength region due to the 2 orders of magnitude increase of the imaginary part $k(\lambda)$ of the complex index of refraction of water (see A). (C) Simulation of sensor output attenuation as a function of ice layer thickness in water. Maximum attenuation occurs for single mode ice layers of around 3 μm thickness. Due to the large differential absorption of liquid water and ice the sensor can also detect formation of nanometric (100 nm) ice layers below liquid water (the minimum detectable attenuation with our experimental setup is of 0.0026 dB, given our SNR of 32 dB. See Supporting Information for further details).

complex index refraction [18]. The selectivity of this process also allows to easily distinguish between ice and metastable SCW, which has a maximal structural similarity to ice [1-3]. Figure 1E shows the measured sensor output when the sensor is temperature controlled to perform cyclic freezing and melting phase changes of water droplet on top of the sensor just below and around the freezing point (see Supporting Information for further details).

Since the waveguides have a low index contrast to surrounding glass (less than 1%) [19], the effective index of the waveguide mode is only marginally higher than the refractive index of fused silica and phase matching regions can be first identified by evaluating the spectral dispersion of the complex index of refraction of all involved materials. Figure 2A shows the index of refraction n and extinction coefficient k dispersion values for aSiO$_2$ glass [20], clear ice at -7ºC [17] and liquid water at 25ºC [16] in the 2.6 to 4 μm wavelength region across the OH-stretching vibrational mode of water. Resonant light transfer is allowed for wavelengths where the n index matching condition is fulfilled (~3.46 μm for warm water and ~3.68 μm for -7 ºC clear ice), while the extinction coefficient is low ($k \leq 10^{-2}$). At shorter wavelengths where the anomalous dispersion of water takes place (~3 μm) no light transfer occurs due to the large water k increment of almost 2 orders of magnitude [18]. To fully evaluate these assumptions, wavelength sweeps of BPM simulations of the sensor response across the 3 to 4 μm wavelength range were performed with the sensor surface covered with infinite thickness layers of air, water or ice, which allows to qualitatively evaluate the sensitivity of the device to liquid/solid phase transitions of water (see Figure 1D as BPM example for λ=3.62 μm light), and the expected spectral response across the anomalous-to-normal water dispersion range. Figure 2B shows the sensor spectral output response for ice and water layers (normalized to air and per mm of sensing length) and for sensing waveguides of low (Δn^L) and high index change (Δn^H). The parameters for Δn^H are the same as those for Figure 1D, and the parameters defining the waveguides for the Δn^L case are W=H=28 μm, G= 5 μm and $\Delta n = 2 \cdot 10^{-3}$, which result in the same waveguide normalized V number (1.89) [18] associated to the Δn^H waveguides, so that direct comparison can be made. A set of simulations with λ=3 μm to λ=4 μm have been implemented in order to determine the optimum wavelength (i.e. perfect index matching conditions) at which the power attenuation is maximum when ice is formed on the surface. As seen in Figure 2B, maximal light attenuation when ice forms at -7 ºC happens at around 3.68 μm as expected before from Figure 2A, but at slightly lower wavelengths of 3.62 μm for the Δn^H case, and 3.65 μm for Δn^L due to the increase of the mode effective index with respect to bulk silica. The spectral attenuation corresponding to room temperature liquid water as external medium also peaks at around the expected wavelength of 3.46 μm from Figure 2A, but again slightly blue-shifted due to the higher values of mode effective index with respect to bulk silica. These results demonstrate the impact of the waveguide index contrast on the sensitivity and selectivity of the sensor to ice and liquid water. For a higher sensitivity and selectivity, higher contrast waveguides are required, at the cost of a reduced gap (G) which can make the sensor weaker in harsh environments due to a reduced erosion resistance.

All previous simulations were done for infinite layer thicknesses, so that no evaluation of the sensor response against layer thickness was performed. To evaluate this, layer thickness simulation sweeps were performed for various sensor configurations (see Figure S1.12 in Supporting Information). The attenuation levels (in normalized dB/mm units) for ice layers against water are shown in Figure 2C for the case of a sensor with small gap G =1 μm and Δn^H. The sensor surface was covered by room temperature water and layers of ice with decreasing thickness (T) from 20 μm down to 50 nm were computed. Maximal attenuation is obtained for ice layer thickness of micrometer size around the wavelength size (12.6 dB/mm for T ~4 μm) with an oscillating behaviour as T increases, due to the creation of a higher number of modes available on it, stabilizing at around 7.5 dB/mm for T ≥ 20 μm. Towards the nanometer range the sensitivity for ice against water decreases reaching a computed value of ~0.02 dB/mm attenuation for ice layers of 100 nm thickness. This small attenuation level in the output signal is ~8 times above the

Submitted to Advanced Functional Materials on the 14th of February 2017

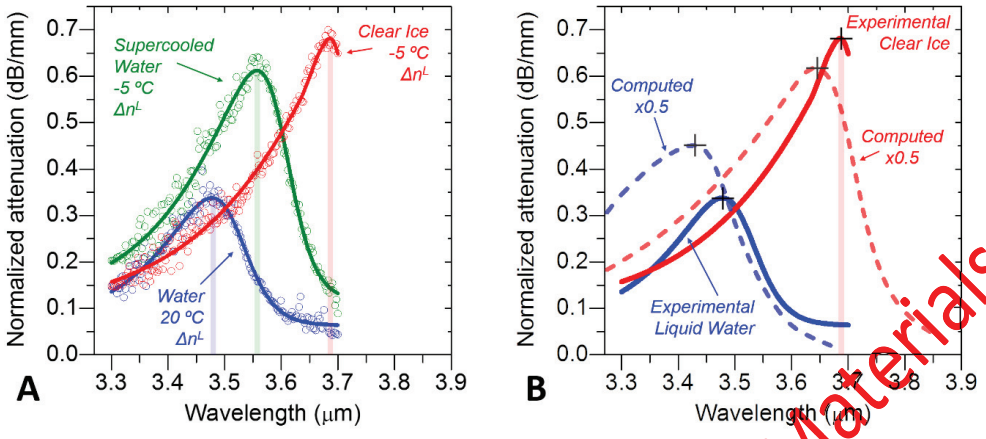

Figure 3. Experimental spectral fingerprints for warm water, SCW and clear ice with a low contrast (Δn^L) waveguide sensor. (A) Experimental normalized attenuation spectra for deionized water drop at 20 ºC (blue data), and at -5 ºC for both its SCW (green data) and solid state (red data). Solid lines are best fits to experimental points. Data noise is mostly arising from random output power oscillations of the tunable mid-IR OPO laser used for the experiments. Peak attenuation wavelengths are marked for each water phase state. (B) Evaluation of the matching between experimental normalized attenuation sensor data (asymmetric peak fits) and BPM simulations. Experimental data is the same as in (A), simulations used same water index of refraction data as in Figure 2, and normalized attenuation is divided by two. Good qualitative agreement on the powerful selectivity on ice against water is found, which validates the sensor 3DLW fabrication technique.

experimentally determined minimum detectable attenuation (~0.0026 dB) given by the detection noise floor of our prototype (SNR of ~32 dB, so that we can detect signal attenuations as small as ~0.06%; see Supporting Information for further details), so that this type of sensor could also be used for fundamental studies of nanometer confined water dynamics, although this goes beyond the scope of this report where we focus only on micrometer scale icing.

The experimental development of a sensor laboratory prototype was initiated using 3DLW low contrast waveguides (Δn^L), which allowed for the proof-of-concept demonstration under static water layer conditions in an optical bench with the sensor itself as temperature changing element. Three mid-IR lasers were used, a tunable OPO for broad wavelength tuning from 3.3 to 3.7 μm, a HeNe gas laser at 3.39 μm, and an ICL diode at 3.68 μm (see Supporting Information for further details). High contrast waveguides (Δn^H), which were experimentally developed later on [19], were integrated in a wing mock-up model for dynamic icing wind tunnel tests for simulation of in-flight aircraft icing conditions. The first goal of experimental developments was the verification of the simulated attenuation spectral fingerprints of room temperature liquid water and clear ice (see Figure 2B), as well as of metastable SCW layers. For these experiments, a waveguide with the following parameters was used: W=32 μm, H=15 μm, G=6 μm and an estimated $\Delta n=2\cdot10^{-3}$. The total waveguide length was 18.2 mm, but deionized water droplets with only 1 mm diameters were used. The experimental setup with a tunable mid-IR OPO laser is shown in Figure S2.1, for which static droplet measurements were recorded by covering the chip with a mm-sized water droplet, stabilizing the temperature of the surface at a given value, and running a fast laser wavelength sweep of a few seconds from 3.3 μm to 3.7 μm in order to obtain a spectral water fingerprint at that given temperature and water phase. To obtain SCW, cyclic droplet freezing/melting steps were done, so that measurements at a same nominal temperature could be repetitively performed for both metastable and solid phases before transitions occurred. All output spectral measurements were normalized to an air reference obtained previously at the same nominal temperature, so that potential chromatic effects associated to the whole opto-mechanic and photonic system were removed. The raw normalized attenuation results as well as their fits to asymmetric double sigmoidal peaks are shown in Figure 3A. The noise in the data arises from the output power fluctuations when changing the OPO laser wavelength. At 3.68 μm wavelength, a maximal selectivity of 0.54 (0.60) dB/mm between -5 ºC solid ice and -5 ºC SCW (20 ºC warm water) is found. The spectral fingerprint of SCW (green data) resembles a water structure in between normal liquid water and ice, with a large peak red-shift of ~80 nm with respect to 20 ºC water due to its structural similarity with ice, although solid ice peaks with a further red-shift of ~130 nm from SCW, clearly depicting the higher crystalline order and associated polarizability change at the OH-stretch vibrational resonance which drives the large index change (see Figure 2A). In order to evaluate the validity of BPM computations, a simulation set was performed for the exact waveguide parameters of Figure 3A, and which is shown in Figure 3B, using the same complex index of refraction data as in Figure 2. For the sake of visual comparison all attenuation values for the simulation results are divided by 2, so that one of the first conclusions is that at least for the low contrast waveguides (Δn^L), relative attenuation values between ice and water are overestimated by an order of ~2 or lower. Besides this, a very good qualitative agreement is found in the ice/water fingerprints, although it is worth noting that a much better agreement is found for -5 ºC ice, than for 20 ºC liquid water. There are many factors that can explain the found discrepancies, such as the mismatch between used dispersion data from Warren [17] and Hale [16] for simulations and real values, non-perfect modelling of the photonic structure (e.g. inaccurately estimated Δn) or defects in the fabrication along the waveguide. An in-depth refinement of these issues is currently in development.

Once the experimental spectral fingerprints of each water phase were determined, the temporal response of the sensor was studied at three different wavelengths: 3.39 μm, 3.64 μm, and 3.68 μm. The initial sensor tests were performed at 3.64 μm wavelength with an OPO laser system, and the output power measurement was done with a thermal power meter. Fast liquid-solid phase transitions of a 5 mm long water droplet were performed in a laboratory sensor

Submitted to Advanced Functional Materials on the 14th of February 2017

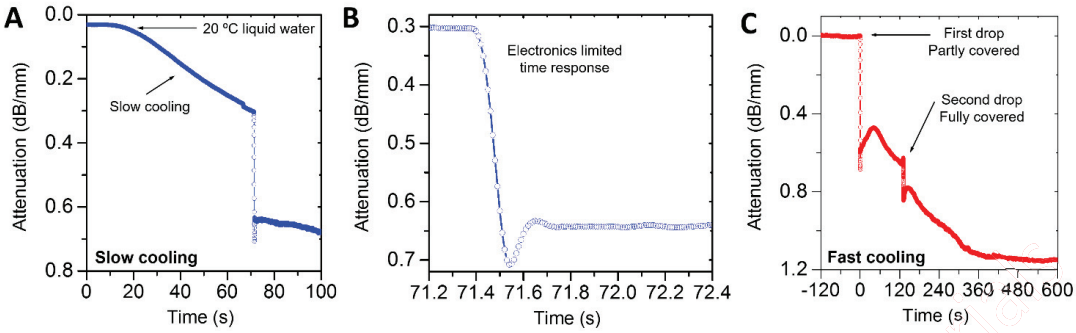

Figure 4. Characterization of the sensor prototype response time. (A) Time record in slow cooling and freezing of a room temperature +20 ºC liquid deionized water droplet down to -20 ºC. (B) Detail of the time response at the freezing point of the water-sensor surface area. The response time is given by the electronics slow response, of around ~300 ms. (C) Time record of fast cooling experiment for +20 ºC deionized water droplets when in contact with the sensor at -15 ºC temperature, inside a freezer chamber. Two droplets were used, a first one which covered around a 75% of the sensor surface, and a second droplet covering the remaining sensor area. The sensor response time at the freezing transitions have the same electronics limited time response as in slow-cooling experiments, proving that the sensor response can be improved by using faster electronics and signal analysis.

configuration with low thermal inertia (i.e. direct contact between a peltier unit and the sensor glass chip) (see Supporting Information), and in the surface temperature range from -5ºC to +5ºC calibrated with a FLIR thermal imaging camera. These experiments were performed first freezing the whole droplet until its top tip, and afterwards cycling the sensor temperature preventing the full frozen droplet from becoming liquid entirely, i.e. with only the droplet surface contact area melting before the temperature was again decreased so freezing occurs within seconds and cycles were of around 40 s. Figure 1E shows this water phase change cycling at 3.64 µm wavelength.

In a second round of tests at 3.68 µm wavelength with an ICL, the configuration was slightly modified: direct laser coupling of light was done by means of bonded optical fibers and the glass sensor chip was attached with thermal silver paint on a thick piece of metal which added thermal inertia to the system. In this experiment, the sensor response when a room temperature (+20 ºC) liquid water drop is slowly cooled to -20 ºC is monitored. Figure 4A shows the evolution of the temporal power loss with respect to the uncovered sensor. The zero seconds time is set when temperature is started to decrease at around 20 ºC/min. It can be observed that signal starts to decrease for colder water as it was also seen in the recorded spectrums of Figure 3A. At some point a sudden fall of the signal (of about 0.35 dB/mm) indicates the liquid-solid phase transition at freezing point. Figure 4A shows the detail of this transition, where it can be seen that its apparent duration is measured to be of ~300 ms, although this is a response time given by the used electronics and signal processing system.

A third set of freezing drop experiments was performed with a fiber-coupled sensor prototype inside a freezing chamber, so that the same transition as in Figure 4A could be done instantaneously. This prototype was integrated on the leading edge of a 3D printed wing model for ice detection in real in-flight icing conditions (see Fig. S2.7 and Supporting Information). In this prototype 3DLW waveguides have a high contrast (Δn^{H}). Specifically, the core parameters were W=13 µm, H=13 µm, an estimated $\Delta n=8\cdot10^{-3}$ and G=4 µm. Before sensing tests, the waveguide technology and its optical bonding to fibers had to be tested at low temperatures and for large and fast temperature changes. The sensor was first continuously tested at -30ºC for 24h, without observing any change in its output signal levels, and afterwards was exposed to fast temperature changes performed by moving the sensor from inside the freezer at -30ºC to a water bath at +20ºC. Once the sensor prototype resistance to temperature changes and low temperatures was verified, tests were performed inside the freezer. In this case the sensor was fully maintained at -15 ºC and drops of warm deionized water at +20 ºC where dropped on it. Figure 4C shows the time signal evolution, in which the zero seconds time is set when the first drop contacts the sensor. First, a small water drop (covering around 25 mm of the sensor) freezes instantaneously in its bottom in contact with the cold sensor and produces the first strong signal drop (of ~60 % signal, or 0.6 dB/mm). Secondly, another drop fills the rest of the sensor and the signal goes further down by around -0.2 dB/mm more, being followed by a very slow signal drift probably due to the gradual cooling of the whole ice layer down to -15 ºC of the freezer environment. The results of Figure 4C corresponding to the second sensor prototype sensing clear ice at -15 ºC will be later compared to results from the icing wind tunnel tests, labelled as laboratory clear ice reference.

So far, only homogeneous ice (i.e. no air micro-bubbles inside) has been considered. However, aircraft icing typically takes place in mixed conditions, where ice layers feature a heterogeneous microstructure with air grains of variable size, giving rise to different types of phenomenological macroscopic ice types such as frost or rime ice. These microstructured ices are characterized by a non-homogeneous microstructure which will therefore have a different optical properties and affect the sensor's principle of operation. A simple model was used to simulate rime ice consisting of ice and air blocks with average lengths along the light propagation direction of 80 µm and 20 µm. The ice blocks had a thickness of 50 µm and an infinite width perpendicular to the propagation direction. As before, the attenuation spectrum was calculated and the comparative results between liquid water, ice and frost/rime can be seen in Figure 5A. Note that here we refer to rime or frost ices as similar cases of microstructured ice (air and ice grains with any given volume filling fractions, sizes and distributions), even if these are terms for types of ices which form in completely different circumstances and physical parameters. The main differences of the simulated sensor attenuation output spectra for rime/frost curve with respect to the ice and water curves is that its peak wavelength is located in between the other two maximums (at λ~3.58 µm), that this maximum value is lower than all other water phases or states, and that the resonance has a very damped behaviour with a very large full width at half maximum, probably caused by the presence of the air blocks which induce scattering in the ice/air

Submitted to Advanced Functional Materials on the 14th of February 2017

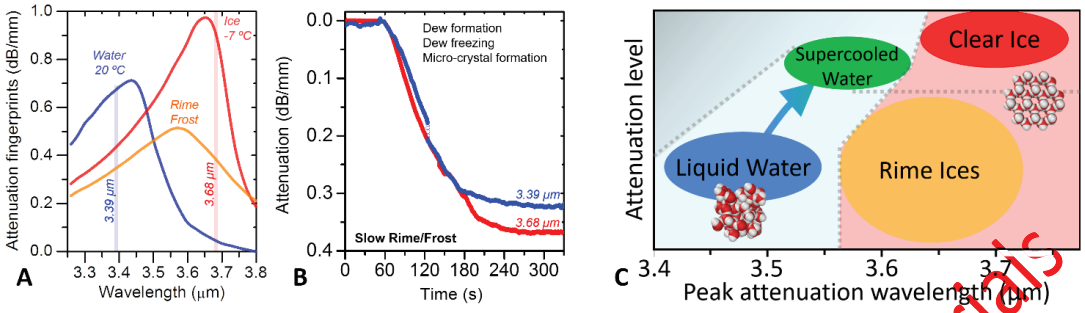

Figure 5. Simulation and experimental formation of frost microstructured ice. (A) Simulation of liquid water, homogenous clear ice, and air/ice microstructures (frost/rime). Microstructured ice is clearly identified by an increased full width at half maximum of its attenuation fingerprint and a peak intensity reduced to around a 50% with respect to homogenous clear ice. (B) Experimental time-response of the sensor for the slow formation of frost by first allowing dew to condense at room temperature conditions and slow sensor cooling, dew freezing, and ice microcrystals formation across the sensor area. Good agreement for attenuation values at 3.39 μm and 3.68 μm is found between simulation (A) and experiments (~0.35 dB/mm). (C) Conceptual sketch on the sensor response parameter space – attenuation peak level against wavelength-, and the different regions corresponding to each water phase and microstructured rime ice types. A third parameter (not shown here) is the spectra full width at half maximum, which allows to differentiate between homogeneous (liquid or solid water) and microstructured ice (rime or frost) (see A).

interfaces. Depending on the ice microstructure the attenuation spectrum can therefore vary substantially, but ice microstructures with air pores are clearly identified by a strong fingerprint blue-shift with respect to homogenous clear ice and a low attenuation value as well as very large width. To simulate this type of microstructured frost-like ice in the laboratory a series of experiments were performed using the same setup as for slow water cooling (see Figure 4A). Frost ice was created on the surface by slowly cooling down the sensor at room temperature, allowing dew formation due to vapour water condensation. At a given time, the dew freezes, and ice micro-crystals (frost) start to grow (see Figure 5B). In this condition and within a few minutes ice crystals had grown to enough size to be seen by the naked ice, showing the characteristic white aspect of frost. These experiment was performed in the laboratory for the wavelengths of 3.39 μm and 3.68 μm, which lie both out of the maximal fingerprint attenuation. The two independent experiments were performed under the same protocol and are plotted on the same time scale in Figure 5B. The initial and final temperature is 20ºC and -15ºC, respectively. Both curves show a gradual fall of the output power which corresponds to freezing of the dew across the sensor surface area, as well as a saturation region at the end indicating no further growth of micro-crystals on the glass surface. A very good agreement is found between experiments and rime-frost simulation (Figure 5A), with attenuation levels of around ~0.35 dB/mm for both wavelengths, and slight higher at the longer wavelength of 3.68 μm.

Overall, these findings demonstrate that these novel type of mid-infrared water ice sensor allow to clearly distinguish between the structural phases of water, as well as its microstructure with regard to rime-type or frost structures with given percentages of micro-porosity. The main detection parameters to effectively identify these different icing conditions are the operating wavelength (which allows to tune the sensor for an improved selectivity of a given water phase against other) and the attenuation values spectral dependence. A clear trend is observed for which liquid water is detected for wavelengths gradually shifting from ~3.45 μm (+20 ºC) to ~3.55 μm (-5 ºC, metastable SCW), clear ice peaks at much longer wavelengths ~3.68 μm and with higher attenuation levels, and rime ices do peak in a wide region between SCW and clear ice, but with a reduced attenuation to half the level of clear ice. These observations are summarized in a hypothetical parametric table in Figure 5C.

To fully confirm this sensor capability further experiments must however be performed under more sophisticated experimental conditions covering the whole range from liquid to solid water, as well as microstructured ice types

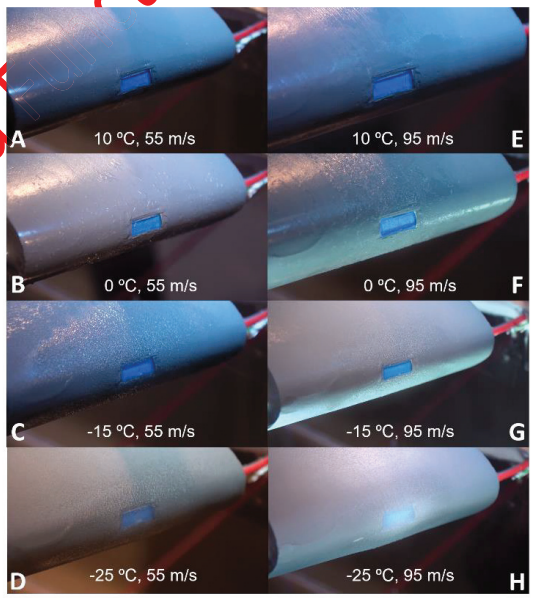

with varying air pore densities from low to high density rime ices.

Fig. 6. Wing model leading edge appearance for different temperatures and wind speeds inside the IWT. Only in the case of -25 ºC and 95 m/s air speed can the first layers of ice be detected by the naked eye.

To further prove that this sensor can operate in harsh in-flight conditions, under high speed water impact and at low temperatures, we performed a series of tests inside an icing wind tunnel (IWT) at the Fraunhofer IFAM icing facilities (see Fig. S2.6 and Supporting Information). The sensor prototype used is the same as that tested in freezing conditions as previously described (see Figure 4C). Regarding the icing testing facility, it consisted of a wind tunnel capable of simulating dangerous in-flight icing

Submitted to Advanced Functional Materials on the 14th of February 2017

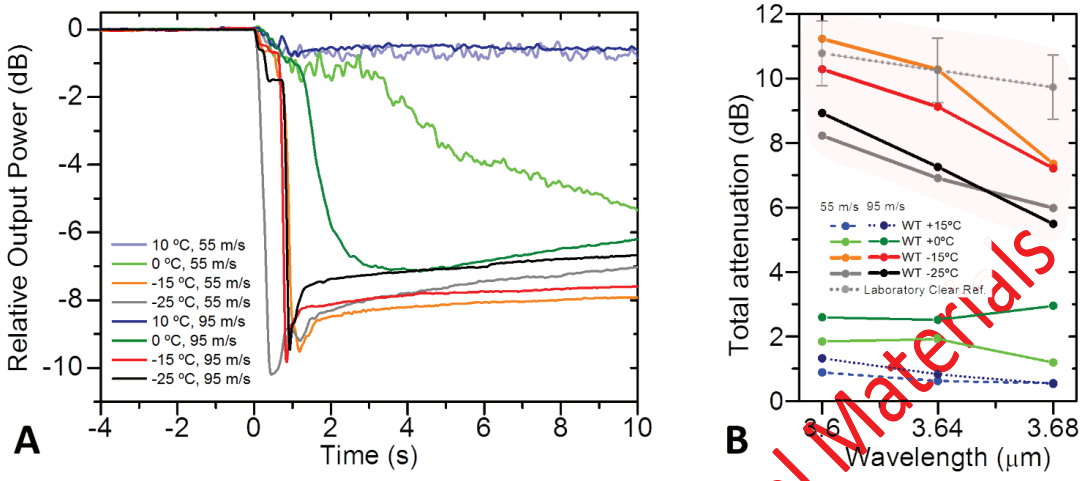

Figure 7. In-flight icing detection. Icing wind tunnel tests. (A) Time signal detection at +10, 0, -15 and -25 ºC (±2 ºC) and wind speeds of 55 and 95 m/s. Fast micrometric ice layer accretion is detected in less than 1 s. Afterwards ice layers evolve towards a steady state depending on the air temperature and wind speed. At freezing point temperatures, a thin ice layer forms slowly at a time scale of around 4-20 s, and afterwards gradually melts within various minutes (not shown for the sake of brevity). Above freezing temperatures only impacting drops are measure which produce an oscillating signal with almost no attenuation. (B) The final steady states are summarized and compared with homogenous clear ice detection -out of the wind tunnel- in a freezing chamber (see Fig. 4C) as a reference for -15 ºC clear ice.

environments, such as clouds being composed of supercooled water droplets, and where wind speed, temperature, liquid, water droplet size could be accurately controlled. The sensor mock-up was first tested at various temperatures at 55 m/s speeds, in order to check that there were no material failures after prolonged use (3h continuous test). Signal stability and repeatability between air, water and ice cycles was very high. The temperatures to test were +10 ºC, 0 ºC, -15 ºC and -30 ºC (±2 ºC), the wind speeds were of 55 m/s and 95 m/s. The liquid water content (LWC) was of 2.1 and 0.8 gr/m^3, for 55 and 95 m/s respectively. Mean droplet volume diameter (MVD) was of 40 μm. Figure 6 shows the visual appearance of the leading edge of the wing model were the sensor was embedded, 3 seconds after the cloud was created. The sensing waveguide was driven by the ICL diode at its nominal wavelength (3.68 μm) and the output signal was measured by the PbSe detector (see Figure S2.10 and Supporting Information for further details). The temporal evolution of the sensor's output signal is depicted in Figure 7A, where output power values are given in dB for the whole sensor waveguide length of 8 mm. At temperatures above the freezing point, the signal output power decreases by a very small margin. A noise component is added to the signal indicating the impact of the water droplets on the glass surface, which is more evident at 55 m/s than at 95 m/s, probably meaning that in the latter case a continuous film of water remains on the surface. In the opposite case, when the temperature is well below 0 ºC (at -15 and -25ºC), the output signal quickly falls around 10 dB within 1 second as a consequence of ice accretion. At 3.68 μm wavelength, the detection of ice is therefore characterized by a clear and fast signal attenuation, of the order of 10 dB. However, this attenuation level evolves to a steady state more characteristic of microstructured rime ice, with a lower attenuation values of around 7 dB. Lastly, at temperatures around the freezing point, the sensor response differs in its slow response. Although not immediately, the signal still decreases more than when having positive temperatures and hence icing conditions might be inferred. A plausible explanation for this is the fact that small fluctuations of temperature around ±2 ºC could prevent locally the water droplets from freezing on the glass surface, resulting in a mix of ice-water millimetre-sized films. In any case, the sensor can clearly detect when there is running water (droplets impact) from the measured noise fluctuations, and in the case that an ice layer is blocking the sensor this is so identified by the absence of noise. By using the ice sensor in conjunction with de-icing electro-thermal systems which could fast remove any detected ice layer icing safety would therefore be largely increased.

The attenuation values in the steady state for each IWT test were also measured at three different wavelengths. Although the ICL laser is not continuously tunable, three current-temperature set-points that provided single-frequency lasing (3.60, 3.64 and 3.68 μm) were used. In Figure 7B, the final steady states are summarized and compared with homogenous clear ice detection in a freezing chamber (see Figure 4C) as a reference for -15 ºC clear ice. All the ice films created inside the wind tunnel produced a different spectral sensor response from the one corresponding to the reference ice. In general, the lower attenuation observed at any of the spectral points, the higher proportion of low-density rime-like microstructured ices present on the sensor surface. In our experimental set of icing parameters, temperature was the dominant factor, having the ices accreted at -25 ºC a less dense nature than those at -15ºC. At 55 m/s speeds, high-density microstructured ice formed only at -15 ºC temperature (orange line), which gave a fingerprint very similar to that of clear ice but with decreased attenuation at 3.68 μm wavelength, while lower density microstructured ice (with milky appearance as seen by the naked eye) with reduced attenuation formed at -25 ºC (grey line). At 95 m/s speeds a similar trend can be observed to occur: high-density and slightly lower density microstructured ices also formed for -15 and -25 ºC temperatures, respectively; and with similar attenuation values to 55 m/s. At the freezing points (0 ºC), all attenuation curves correspond to cold liquid water. The reason for this is that the values were taken in a stationary regime when the output power had increased relative to the initial sudden fall. Such increase is probably due to high speed water droplet

impacting on the sensor surface and detaching the first layer of accreted ice before forming a thin layer of very cold liquid water film below an igloo-like ice structure surrounding the sensor area. We therefore show here that the ice contact surface layer can fundamentally change in sub-second time scales, and this type of sensor can continuously monitor these changes, thus enabling the development of future fast-response automated active de-icing electro-thermal systems.

In conclusion, we have introduced a novel concept for photonic surface sensors capable of withstanding harsh environments and yet be sensitive enough to detect water molecule phase changes with layer thicknesses within the micron scale and nanometric scale. The concept has also been fully developed in prototypical form and tested on industrially relevant environments, such as in icing wind tunnel for replicating in-flight icing conditions. We have shown that this novel type of mid-infrared sensors can be exploited for detecting both structural phase changes of water, as well as microstructural arrangements of porous ices such as rime ice, which pose a serious threat to aircraft transport. Furthermore, the use of silica glass as surface sensor allows to open various research avenues with could have a strong impact in both applied and fundamental sciences. A new field for instance opens for studying the sensor behaviour in combination with hydrophobic or icephobic microstructured surface ends. In a similar way to how the sensor detects microstructured ice with air pores, the detection of water or biological matter in contact with microstructured silica could be investigated, for which the sensor would perform as an element of inbuilt monitoring capability for the automated feedback control of other systems. Additionally, bio-functionalizing the SiO_2 sensor surface [20] would also enable to exploit the sensor in the novel field of mid-infrared biosensors. In parallel, the current rapid development process of mid-infrared photonic technology (such as tunable or supercontinuum laser sources, optical fibers and detectors) will undoubtedly lead this type of glass embedded surface sensors of a wide range of scientific and engineering applications.

Experimental Section

Sensor simulations: BPM simulations of the waveguide sensor performance were carried out by means of the commercial RSoft BeamPROP software package. Complex refractive index dispersion data was taken from [16], [17] and [20] for liquid water at 25 ºC, ice at -7 ºC and fused silica, respectively. The geometry of the structure was parametrized according to Figures 1B and S1.1 (see Supporting Information). Only scalar simulations were performed as the sensing performance did not depend on the light polarization. In all cases, the excitation field was the waveguide's own fundamental mode. For the broadband results presented, individual simulations at different wavelengths were carried out taking into account the optical dispersion of materials. Extensive details about all the aspects of the simulations can be found in Supporting Information (PART I).

Photonic sensor fabrication: The waveguides were fabricated using the 3DLW multiscan technique on commercial low-OH fused silica glass substrates (Suprasil 300). For the low contrast waveguides (estimated $\Delta n^L \sim 2 \cdot 10^{-3}$), a 1033 nm circularly polarized laser beam, giving 400 fs pulses with an energy of 0.5 µJ at a repetition rate of 500 kHz was focused inside the sample trough an aspheric lens of 0.25 NA. The sample was translated at a speed of 1 mm/s to produce rectangular cores with approximate 32 x 14 μm^2 size. For the high contrast waveguides, the fabrication parameters were, respectively, 1047 nm laser wavelength, circular polarization 450 fs pulse width, 0.9 µJ pulse energy, 500 kHz repetition rate, 0.4 NA and 1.5 mm/s scan speed. The obtained waveguide core had a size of around 13 x 13 μm^2 with an estimated $\Delta n^H \sim 8 \cdot 10^{-3}$ at 3.68 µm wavelength. Further details about the fabricated waveguides were reported elsewhere [19]. After the 3DLW process, the samples were physically polished to reduce the waveguide-surface gap to the desired values. Bonding the waveguides to mid-IR ZBLAN cleaved fibers was done using optical adhesive NOA 61. The connection area was covered by adhesive prior to carefully aligning the cleaved facets of the fibers with the corresponding ports of the waveguide. UV light was then applied to cure the adhesive and make permanent connection. For the integration of the sensor on an aircraft structure, a wing mock-up (NACA 0012) 3D printed in PLA was properly modified to host the glass substrate on the leading as well as the optical fibers. See further details in Supporting Information (PART II).

Sensing Experiments: Ice sensing demonstration in an optical laboratory was carried out in a standard optical waveguiding setup for mid-IR guiding. The sources used were a Firefly-IR OPO (M Squared Lasers), a 3.68 µm ICL laser (Nanoplus) and a 3.39 µm He-Ne laser (REO). The detectors were a Thorlabs S302C thermal power meter, a Thorlabs PDA20H-EC PbSe amplified detector and a FLIR SC7000 InSb camera. For free-space experiments, a pair of chalcogenide aspheric lenses with NA = 0.18 (Thorlabs C021TME-E) coupled the light in and out the waveguide, respectively. A peltier unit controlled the temperature of the sensor while the temperature was constantly monitored by a calibrated thermal camera. The setup was enclosed in a N_2-purged PMMA chamber to avoid water vapor condensation on the photonic chip facets. In the fiber-coupled case, this was not needed. The ZBLAN fibers used were provided by FiberLabs and Thorlabs and their core size and NA closely matched that of the 3DLW waveguide coupling light into it in order to achieve low coupling losses. For collecting light out of the waveguides, a multimode fiber was used instead. The precise protocol followed to characterize the sensor performance in the optics laboratory and the IWT is explained in detail in Supporting Information (PART II).

Supporting Information

Supporting Information is available from the Wiley Online Library or from the author.

Acknowledgements

This work was funded by the European Union's Seventh Framework Program for research, technological development and demonstration, Japanese-European De-Icing Aircraft Collaborative Exploration project (JEDI ACE, http://www.jediace.net/) under grant agreement no. 314335, and the Japanese Ministry of Economy, Trade and Industry. This work was also supported by the Spanish MINECO and FEDER (MAT2016-75716-C2-1-R), Spanish Ministry of Economy, Industry and Competitiveness (TEC2014-55948-R and TEC2014-52642-C2-1-RF), and Generalitat de Catalunya (2014SGR1358). A. R. and R. O. acknowledge that the research leading to these results also received funding from LASERLAB-EUROPE (grant agreement no. 654148, European Union's Horizon 2020 research and innovation programme). F. D. acknowledges additional support 2010-ICREA-02 for excellence in research.

Received: ((will be filled in by the editorial staff))
Revised: ((will be filled in by the editorial staff))
Published online: ((will be filled in by the editorial staff))

[1] (a) O. Mishima, H. E. Stanley, Nature 1998, 396, 329; (b) J. R. Errington, P. G. Debenedetti, Nature 2001, 409, 318; (c) F. Mallamace, C. Branca, M. Broccio, C. Corsaro, C.-Y. Mou, S.-H. Chen, Proceedings of the National Academy of Sciences 2007, 104, 18387; (d) B. Pamuk, J. M. Soler, R.

Ramírez, C. Herrero, P. Stephens, P. Allen, M.-V. Fernández-Serra, Physical Review Letters 2012, 108, 193003; (e) C. Colosi, M. Costantini, A. Barbetta, C. Cametti, M. Dentini, Physical Chemistry Chemical Physics 2013, 15, 20153; (f) F. Mallamace, C. Corsaro, H. E. Stanley, Proceedings of the National Academy of Sciences 2013, 110, 4899; (g) A. Nilsson, L. G. Pettersson, Nature communications 2015, 6; (h) P. Gallo, K. Amann-Winkel, C. A. Angell, M. A. Anisimov, F. Caupin, C. Chakravarty, E. Lascaris, T. Loerting, A. Z. Panagiotopoulos, J. Russo, J. A. Sellberg, H. E. Stanley, H. Tanaka, C. Vega, L. Xu, L. G. M. Pettersson, Chemical Reviews 2016, 116, 7463; (i) L. G. M. Pettersson, R. H. Henchman, A. Nilsson, Chemical Reviews 2016, 116, 7459.

[2] (a) E. Mayer, A. Hallbrucker, 1987; (b) B. J. Murray, D. A. Knopf, A. K. Bertram, Nature 2005, 434, 202.

[3] F. Frank, Nature 1946, 157, 267.

[4] (a) S. M. Jones, M. S. Reveley, J. K. Evans, F. A. Barrientos, 2008; (b) P. Appiah-Kubi, 2011; (c) in 2014-25789, Vol. 79 FR 65507 (Ed: F. A. Administration), Federal Aviation Administration, 2014, 65507.

[5] S. Jung, M. K. Tiwari, N. V. Doan, D. Poulikakos, Nature communications 2012, 3, 615.

[6] (a) S. Kimura, Y. Yamagishi, A. Sakabe, T. Adachi, M. Shimanuki, SAE Technical Paper, 2007; (b) J. C. Bird, R. Dhiman, H.-M. Kwon, K. K. Varanasi, Nature 2013, 503, 385; (c) K. Morita, H. Sakaue, T. Tanaka, T. Yoshida, N. Rehfeld, A. Brinkmann, K. Lummer, G. Pauly, SAE Technical Paper, 2015; (d) K. Golovin, S. P. Kobaku, D. H. Lee, E. T. DiLoreto, J. M. Mabry, A. Tuteja, Science advances 2016, 2, e1501496.

[7] (a) M.-C. Estevez, M. Alvarez, L. M. Lechuga, Laser & Photonics Reviews 2012, 6, 463; (b) C. Fenzl, T. Hirsch, O. S. Wolfbeis, Angewandte Chemie International Edition 2014, 53, 3318. (c) Zhi, Y., Yu, X. C., Gong, Q., Yang, L., & Xiao, Y. F. (2017). Adv. Mater, 2017

[8] F. Perakis, L. D. Marco, A. Shalit, F. Tang, Z. R. Kann, T. D. Kühne, R. Torre, M. Bonn, Y. Nagata, Chemical Reviews 2016, 116, 7590.

[9] R. Pandey, K. Usui, R. A. Livingstone, S. A. Fischer, J. Pfaendtner, E. H. Backus, Y. Nagata, J. Fröhlich-Nowoisky, L. Schmüser, S. Mauri, Science advances 2016, 2, e1501630.

[10] S. L. Nail, S. Jiang, S. Chongprasert, S. A. Knopp, in Development and manufacture of protein pharmaceuticals, Springer, 2002, 281.

[11] M. C. Homola, P. J. Nicklasson, P. A. Sundsbø, Cold regions science and technology 2006, 46, 125.

[12] T.-S. Kim, H. Park, K. Ko, G. Lim, Y.-H. Cha, J. Han, D.-Y. Jeong, Applied Physics B 2010, 100, 437.

[13] "Introduction to body composition assessment using the deuterium dilution technique with analysis of saliva samples by Fourier transform infrared spectrometry". International Atomic Energy Agency, 2010, IAEA human health series, ISSN 2075-3772; no. 12) STI/PUB/1450, ISBN 978–92–0–103210–2.

[14] (a) D. Lynch, DTIC Document, 2005; (b) J. M. Labello, University of Tennesse, 2011; (c) T. M. Moeller, L. Smith, F. G. Collins, J. M. Labello, J. P. Rogers, H. S. Lowry, D. H. Crider, "Further results in measuring water ice build-up on optical components in cryogenic vacuum chambers", presented at SPIE Optical Engineering+ Applications, 2013.

[15] Sastry, S. (2005), Nature, **438** (7069), 746-747.

[16] S. G. Warren, Appl. Opt. 23, 1206-1225 (1984).

[17] G. M. Hale and M. R. Querry, Appl. Opt. 12, 555-563 (1973).

[18] Snyder, A. W., & Love, J. (1983). "Optical waveguide theory". Springer Science & Business Media.

[19] Martínez, J., Ródenas, A., Fernandez, T., de Aldana, J.R.V., Thomson, R.R., Aguiló, M., Kar, A.K., Solis, J. and Díaz, F. Opt. Lett. 40(24), pp.5818-5821 (2015)

[20] Clechet, P., & Jaffrezic-Renault, N., "Silica surface sensitization and chemical sensors", Adv. Mater., 2(6-7), 293-298, 1998.

UNIVERSITAT ROVIRA I VIRGILI
Mid-Infrared Integrated Photonic Sensors of Water and Ice Films for Harsh Environments
Javier Martínez García

PATENT

SENSOR ÓPTICO, SISTEMA, Y PROCEDIMIENTO PARA DETECTAR LA PRESENCIA DE HIELO EN SUPERFICIES

DESCRIPCIÓN

La presente invención se refiere a un sensor óptico para detectar la presencia de hielo en superficies.

También se refiere a un sistema para detectar la presencia de hielo que comprende al menos uno de dichos sensores, y a un procedimiento para detectar la presencia de hielo en superficies.

ESTADO DE LA TÉCNICA ANTERIOR

Existen varias aplicaciones en las que es necesario detectar la formación de hielo o la presencia de hielo sobre una superficie.

Por ejemplo, la presencia de hielo en cualquier elemento aerodinámico de un avión o un helicóptero altera la forma, el peso y la distribución de masas del mismo: cuando se inicia la formación de hielo, generalmente en un borde de ataque, se produce una distorsión de flujo laminar y se generan turbulencias, de modo que se incrementa la resistencia y disminuye la sustentación. La formación de hielo supone por tanto un riesgo para la seguridad, y de hecho ha tenido un papel importante en accidentes de aviación, y además afecta el control de la aeronave y hace aumentar el consumo de combustible.

Otro campo en el que conviene controlar la formación de hielo en una superficie es por ejemplo el de los aerogeneradores, ya que la formación de hielo en las palas reduce el rendimiento, puede provocar cargas excesivas, etc. También en buques, estructuras navales y otras aplicaciones submarinas en las cuales puede ser conveniente detectar la formación de hielo. También puede ser útil detectar la presencia o la ausencia de hielo en frigoríficos, cámaras frigoríficas y similares, o en conducciones de agua.

Para abordar este problema se han propuesto distintos tipos de sensores ópticos, por ejemplo sensores que comprenden una fibra óptica a lo largo de la cual se propaga una

onda electromagnética, configurados y montados de modo que la propagación de la onda se vea afectada en alguna medida, por fenómenos de reflexión, refracción y dispersión de la luz (*scattering)*, por la presencia de agua o hielo.

Sin embargo, los sensores ópticos conocidos tienen diferentes limitaciones que hacen que su aplicación no sea del todo satisfactoria y fiable: algunos sensores conocidos en general no son capaces de discriminar entre la presencia de hielo y la presencia de agua, por lo que en la práctica para saber si se forma hielo se requieren sensores adicionales de temperatura o de otro tipo; algunos sensores requieren elementos que sobresalen de la superficie, con lo que afectan la aerodinámica de la misma, o se pueden instalar sólo en determinadas posiciones y por tanto no miden directamente en la zona de interés; en otros casos las características de los sensores hacen que no sean resistentes a la erosión.

La presente invención proporciona un sensor que resuelve al menos en parte las limitaciones de los sensores conocidos.

EXPLICACIÓN DE LA INVENCIÓN

De acuerdo con un primer aspecto, la presente invención proporciona un sensor óptico para detectar la presencia de hielo en superficies, que se caracteriza porque comprende:

- una guía de ondas con un material de revestimiento óptico cuyo índice de refracción $n_{material}$ cumple la relación $n_{agua} \leq n_{material} < n_{hielo}$ a una longitud de onda de trabajo λ_T para la cual $n_{agua} < n_{hielo}$, y con una zona de núcleo contenida en el material de revestimiento y apropiada para la propagación de una señal óptica que tiene la longitud de onda de trabajo, presentando la guía de ondas un tramo sensor apropiado para ser instalado en una superficie en la que se debe detectar la presencia de hielo de modo que una cara del material de revestimiento del tramo sensor quede expuesta ;
- medios para inyectar en la guía de ondas una señal óptica con una longitud de onda de trabajo λ_T para la cual $n_{agua} < n_{hielo}$; y
- medios para detectar la señal óptica transmitida por la guía de ondas curso abajo de dicho tramo sensor.

Con estas características del sensor, la atenuación de la señal óptica a lo largo del tramo de la guía de ondas que está próxima a la cara expuesta del cuerpo es significativamente

diferente si hay presencia de hielo sobre la superficie, y por tanto sobre la cara expuesta del cuerpo, o si hay únicamente presencia de aire o agua. A continuación se explica con más detalle de qué manera el sensor permite detectar hielo de modo fiable, y más particularmente diferenciar entre la presencia de hielo y la presencia de agua.

En la propagación de la señal óptica a lo largo de la guía de ondas, existen uno o varios modos electromagnéticos guiados.

En la cara del tramo sensor que está expuesta, es decir, sobre la que se puede depositar agua o hielo, hay un salto en el índice de refracción: si el índice de refracción del medio exterior es mayor que el de la guía, puede surgir un acoplamiento evanescente entre los modos electromagnéticos guiados y el medio exterior, que se traduce en una pérdida de potencia de los modos guiados.

Debido a que la guía de ondas es apropiada para trabajar en la región espectral donde se cumple la condición $n_{agua} \leq n_{material} < n_{hielo}$, en presencia de hielo habrá acoplamiento evanescente y se producirá la pérdida de señal óptica, mientras que en presencia de agua o aire no lo hará, ya que sólo en presencia de hielo hay un aumento del índice de refracción entre el material y el exterior.

En realizaciones de la invención se aprovechan estos fenómenos para la detección unívoca del hielo frente al agua, de manera eficiente y sin necesidad de ulteriores parámetros. Además el sensor se puede montar sin necesidad de que sobresalga de la superficie, por lo que es particularmente apropiado en aplicaciones en que es importante no afectar la aerodinámica de las superficies, y la zona de núcleo de la guía de ondas queda protegida de la erosión porque no está expuesta directamente.

Preferiblemente, el índice de refracción del material cumple la relación $n_{agua} < n_{material} < n_{hielo}$ a la longitud de onda de trabajo λ_T.

En algunas realizaciones, especialmente cuando la aerodinámica de la superficie es importante, el tramo sensor es apropiado para ser instalado en la superficie de modo que la cara del material de revestimiento del tramo sensor quede expuesta a través de una

abertura en la superficie; de este modo el sensor se puede montar nivelado con la superficie, y no afecta sus características aerodinámicas.

La guía de ondas puede comprender una fibra óptica, de la cual se ha retirado el recubrimiento exterior al menos en el área del tramo sensor destinada a quedar expuesta durante el uso, y opcionalmente se ha retirado además una parte del espesor del revestimiento óptico.

Alternativamente, al menos en el tramo sensor de la guía de ondas la zona de núcleo puede estar fabricada dentro de un cuerpo de material apropiado, de modo que varíe en esta zona el índice de refracción; es decir, el resto de la guía de ondas a ambos lados del tramo sensor puede estar configurado de otro modo.

Por ejemplo, a un extremo de entrada y a un extremo de salida de la guía de ondas que incluye el tramo sensor pueden estar acopladas unas fibras ópticas. Esto permite situar el emisor y el detector a cualquier distancia del tramo sensor, y siguiendo cualquier camino, gracias a la flexibilidad de la fibra óptica, cosa que puede ser particularmente útil en aplicaciones en las que conviene minimizar el espacio ocupado por el sistema en la superficie, como puede ser por ejemplo el ala de un avión.

En algunas realizaciones concretas, la longitud de onda de trabajo es de entre 3000 y 5000 nm, preferiblemente entre 3200 y 4000 nm; y el material se puede seleccionar entre cuarzo cristalino, cuarzo vítreo, fluoruro de indio, o compuestos de los mismos.

En realizaciones de la invención el espesor entre la zona de núcleo y la cara del material de revestimiento destinada a quedar expuesta es inferior a 250 µm, preferiblemente inferior a 50 µm; estos rangos permiten que los sensores tengan dimensiones reducidas.

El sensor puede comprender además un recubrimiento anti-erosión aplicado sobre la cara del material de revestimiento del tramo sensor destinada a quedar expuesta. Este recubrimiento permite alargar la vida útil del sensor, y será adecuado sobre todo en condiciones en que la superficie esté sometida a fricciones elevadas o ambientes particularmente agresivos.

De acuerdo con un segundo aspecto, la invención también se refiere a un sistema para detectar la presencia de hielo en superficies que comprende al menos un sensor óptico como se ha descrito, y medios para comparar la intensidad de una señal óptica detectada con al menos un valor umbral, y generar una alarma en caso de que la señal óptica sea inferior a un valor umbral.

El sistema puede comprender medios de calibración para determinar al menos un valor umbral, que pueden ser apropiados para determinar al menos un valor umbral una vez que el sistema está instalado en una superficie.

En algunas realizaciones el sistema comprende una pluralidad de dichos sensores ópticos, destinados a ser instalados en una zona predeterminada, a distancia unos de otros, y una unidad de control común conectada a dicha pluralidad de sensores, comprendiendo dicha unidad de control medios para proporcionar información sobre la distribución de hielo en una zona predeterminada, en función de las intensidades de las señales ópticas detectadas en las salidas de la pluralidad de sensores.

De acuerdo con otro aspecto, la invención se refiere a un procedimiento para detectar la presencia de hielo en superficies, caracterizado porque comprende:

- seleccionar una longitud de onda de trabajo λ_T para la cual $n_{agua} < n_{hielo}$
- proporcionar una guía de ondas que comprende un material de revestimiento óptico cuyo índice de refracción $n_{material}$ cumple la relación $n_{agua} \leq n_{material} < n_{hielo}$ a la longitud de onda de trabajo λ_T y una zona de núcleo contenida en el material de revestimiento y apropiada para la propagación de una señal óptica que tiene la longitud de onda de trabajo;
- instalar la guía de ondas en una superficie en la que se debe detectar la presencia de hielo, de tal modo que en un tramo de la guía una cara del material de revestimiento quede expuesta, definiendo un tramo sensor de la guía;
- transmitir una señal óptica con una longitud de onda de trabajo λ_T a lo largo de la guía de ondas, y
- detectar la señal óptica curso abajo del tramo sensor.

Preferiblemente se proporciona una guía de ondas que comprende un material de revestimiento óptico cuyo índice de refracción $n_{material}$ cumple la relación $n_{agua} < n_{material} < n_{hielo}$ a la longitud de onda de trabajo λ_T.

La guía de ondas se puede instalar en la superficie de modo que la cara del material de revestimiento del tramo sensor quede expuesta a través de una abertura en la superficie, y preferiblemente de modo que la cara del material de revestimiento expuesta quede nivelada con la superficie.

En algunas realizaciones, el procedimiento comprende además:

- comparar la intensidad de la señal detectada con al menos un valor umbral, y
- determinar que hay presencia de hielo sobre el tramo sensor de la guía de ondas si la intensidad de la señal detectada es inferior a dicho valor umbral.

El procedimiento puede comprender además determinar al menos un valor umbral; en este caso, la determinación de al menos un valor umbral se puede realizar una vez que la guía de ondas está instalada en una superficie.

En realizaciones útiles para monitorizar una zona de una superficie, el procedimiento puede comprender:

- instalar una pluralidad de guías de ondas en una zona predeterminada, a distancia unas de otras,
- proporcionar una unidad de control común conectada a dicha pluralidad de guías de ondas, y
- proporcionar información mediante la unidad de control sobre la distribución de hielo en la zona predeterminada, en función de las intensidades de las señales ópticas detectadas.

Otros objetos, ventajas y características de realizaciones de la invención se pondrán de manifiesto para el experto en la materia a partir de la descripción, o se pueden aprender con la práctica de la invención.

BREVE DESCRIPCIÓN DE LOS DIBUJOS

A continuación se describirán realizaciones particulares de la presente invención a título de ejemplo no limitativo, con referencia a los dibujos adjuntos, en los cuales:

La figura 1 es una gráfica que muestra los índices de refracción del agua y el hielo en función de la longitud de onda;

la figura 2 muestra esquemáticamente la estructura de un sensor de acuerdo con una primera realización de la invención;

las figuras 3 a 5 muestran esquemáticamente tres realizaciones posibles del sensor; y

la figura 6 es una gráfica que ilustra cualitativamente la atenuación de una señal transmitida a lo largo de la guía de ondas del sensor durante un proceso de formación de hielo.

EXPOSICION DETALLADA DE MODOS DE REALIZACIÓN

De acuerdo con realizaciones de la presente invención, un sensor óptico para detectar la presencia de hielo en una superficie aprovecha el fenómeno de acoplamiento evanescente de modos electromagnéticos guiados para detectar hielo, y en particular para poder discriminar entre la presencia de hielo y la presencia de agua.

Para ello, se transmite una señal óptica a lo largo de una guía de ondas del sensor óptico; el sensor está diseñado de modo que si sobre el sensor hay hielo se produce un acoplamiento evanescente de al menos un modo guiado de la señal con el hielo, y que este acoplamiento no ocurra en presencia de agua: puesto que el acoplamiento evanescente tiene como efecto una atenuación importante de la señal transmitida por la guía de ondas, en presencia de hielo se produce una atenuación significativamente mayor que en presencia de agua, cosa que permite diferenciar las dos situaciones.

A continuación se describen las características concretas de un sensor de acuerdo con algunos ejemplos no limitativos de realización.

Una característica del sensor es que se diseña para trabajar a una longitud de onda de trabajo λ_T para la cual los índices de refracción del agua y del hielo cumplen la relación $n_{agua} < n_{hielo}$.

La figura 1 es una gráfica que muestra la variación del índice de refracción del agua y el hielo en función de la longitud de onda, en una zona del espectro entre 2 μm y 100 μm (escala logarítmica).

Como se puede apreciar en la gráfica, aunque en general los índices de refracción del agua y del hielo son similares, en la zona del espectro entre aproximadamente 3 μm y 90 μm (infrarrojo medio y parte del infrarrojo lejano) hay siete bandas espectrales IR1, IR2, ... IR7, donde el índice del hielo es superior al del agua. Estas bandas se han señalado en la gráfica con un valor medio aproximado, sólo a título ilustrativo y no limitativo, y corresponden a zonas alrededor de aproximadamente 3500 nm (IR1), aproximadamente 4640 nm (IR2), aproximadamente 5860 nm (IR3), aproximadamente 8000 nm (IR4), aproximadamente 14500 nm (IR5), aproximadamente 54000 nm (IR6), y aproximadamente 73500 nm (IR7), teniendo cada banda un ancho de banda espectral característico diferente.

El sensor se diseña por tanto para trabajar con una longitud de onda trabajo $\boldsymbol{\lambda_T}$ que se encuentra en una de estas bandas IR1 a IR7.

La figura 2 muestra parcialmente y de modo muy esquemático la estructura de un sensor de acuerdo con una realización de la invención. El sensor 100 de la figura 2 comprende una guía de ondas 101 que incluye un material de revestimiento óptico (*cladding*) 102 cuyo índice de refracción $n_{material}$ cumple la relación $\boldsymbol{n_{agua} \leq n_{material} < n_{hielo}}$ a la longitud de onda de trabajo $\boldsymbol{\lambda_T}$, y preferiblemente la relación $\boldsymbol{n_{agua} < n_{material} < n_{hielo}}$.

Por ejemplo, si se escoge una longitud de onda de trabajo $\boldsymbol{\lambda_T}$ de 3394 nm, que está dentro del intervalo IR1 de la figura 1, se puede ver que a esta longitud de onda $\boldsymbol{n_{agua}}$ es aproximadamente 1,45 y $\boldsymbol{n_{hielo}}$ es aproximadamente 1,56 por lo que el material elegido para el revestimiento óptico del sensor deberá tener un índice de refracción a 3394 nm que esté entre estos dos valores: por ejemplo, el cuarzo cristalino cumple esta condición, ya que a esta longitud de onda tiene un índice de refracción próximo a 1,5.

Dentro del material de revestimiento óptico 102 existe una zona de núcleo (*core*) 103, apropiada para la propagación de una señal óptica a la longitud de onda de trabajo. La estructura de la guía con un núcleo y un revestimiento óptico se puede formar mediante cualquier técnica conocida: por ejemplo se puede formar la zona de núcleo por escritura

láser en un bloque de material de revestimiento óptico apropiado, de modo que en esta zona el índice de refracción varíe en la medida necesaria para constituir un núcleo apropiado.

Puesto que la diferencia entre el índice de refracción del núcleo y el del revestimiento es en general muy pequeña, en general tanto el núcleo como el revestimiento pueden tener índices de refracción que están entre el del agua y el del hielo, a la longitud de onda de trabajo.

Para que se pueda propagar una señal, el material debe tener un cierto grado de transparencia a la longitud de onda de trabajo (no es necesaria en esta aplicación una transparencia muy elevada, puesto que las distancias son cortas y el objetivo de la guía de ondas no es que la señal se propague con el mínimo de pérdidas), y el núcleo debe tener un índice de refracción ligeramente superior al del material de revestimiento óptico, aunque la diferencia puede ser muy pequeña: por ejemplo, el núcleo puede tener un índice un 0,1% superior al del revestimiento, o incluso sólo un 0,01% superior, como es conocido para un experto en la materia. La figura 2 muestra esquemáticamente y sólo a título ilustrativo un modo electromagnético guiado MG de una señal óptica, que se propaga a lo largo de la guía 101.

La guía de ondas 101 está configurada de modo que tiene un tramo 104, que se denominará a continuación tramo sensor, apropiado para ser instalado en una superficie S, en contacto con un medio exterior M, en la que quiere detectar la presencia de hielo. El sensor se instala de tal modo que una cara del material de revestimiento 102 del tramo sensor 104 quede expuesta a un medio exterior M, que puede ser por ejemplo aire, agua o hielo, del mismo modo que lo está la superficie S.

La forma del sensor puede ser adecuada para que el sensor se instale dentro de la superficie S y el tramo sensor 104 de la guía de ondas 101 quede expuesto al medio exterior M a través de una abertura en la superficie S, y con la cara del material de revestimiento 102 nivelada con la propia superficie S, como se muestra en la figura 2.

En otras alternativas, sobre todo en aplicaciones en que la aerodinámica no es crítica, el sensor se puede colocar sobre la superficie, o sobresaliendo a través de una abertura, con el tramo sensor expuesto.

Si el sensor se debe usar en condiciones ambientales exigentes, puede ser conveniente seleccionar el material del revestimiento óptico también teniendo en cuenta la dureza, para que pueda resistir a rozaduras.

El sensor 100 también comprende en la figura 2 un emisor 105 capaz de inyectar en la guía de ondas 101 una señal óptica con la longitud de onda de trabajo λ_T para la cual $n_{agua} < n_{hielo}$, y un detector 106 capaz de detectar la señal transmitida a lo largo de la guía de ondas 101. El emisor puede ser, por ejemplo, un láser.

Gracias a la condición que se ha elegido para el índice de refracción del material del revestimiento óptico 102, cuando sobre el tramo sensor 104 se forma hielo, en la interfase entre el tramo sensor y el hielo existirá un salto en el índice de refracción, que aumenta en dirección hacia el exterior ($n_{material} < n_{hielo}$), y por consiguiente se producirá un acoplamiento evanescente de al menos un modo guiado con el hielo a lo largo del tramo sensor 104 de la guía de ondas, de manera que la señal óptica quedará confinada preferentemente en el hielo. Como consecuencia de este acoplamiento, la intensidad de la señal transmitida por la guía de ondas y detectada por el detector 106 será significativamente menor que la emitida por el emisor 105.

En cambio, cuando sobre el tramo sensor haya aire ($n_{aire} = 1 < n_{material}$), o bien agua ($n_{agua} \leq n_{material}$), no habrá un aumento del índice de refracción en la interfase entre el tramo sensor y el medio exterior, sino en todo caso una disminución, y por tanto no habrá acoplamiento evanescente con el medio exterior y no se perderá intensidad de señal a lo largo de la guía por este fenómeno.

Factores de diseño del sensor, tales como el material de la guía, el tipo de guía usada, la distancia entre el núcleo 103 y el medio exterior M (es decir, el mínimo espesor e del revestimiento óptico en el tramo sensor 104), la longitud de onda de trabajo concreta elegida, etc., determinan el grado de efectividad del sensor, y pueden ajustarse de acuerdo con los requerimientos concretos de cada caso: por ejemplo, en función del tipo de aplicación y entorno en el que se implemente, el sensor puede ser diseñado para cumplir diferentes requerimientos de tamaño, resistencia ambiental, eficiencia de detección, etc.

Hay que notar que el sensor se puede montar, como en la figura 2, nivelado con la superficie, y que la capa de material de revestimiento óptico 102 presente en el tramo sensor 104 protege el núcleo 103 del ambiente, y de la abrasión, sin perjudicar el acoplo evanescente en el que se basa la detección; todo ello es muy útil por ejemplo en aplicaciones en fuselajes de aviones y similares.

La longitud que debe tener el tramo sensor 104 para que se produzca acoplamiento evanescente en presencia de hielo puede ser muy pequeña, por ejemplo del orden de 1 mm o de unos pocos milímetros, por lo que el sensor apenas afecta la superficie en la cual se instala.

En general, cuanto mayor es la diferencia entre el índice del hielo y el índice del material del revestimiento óptico, menor es la distancia necesaria para que se transfiera una proporción significativa de energía de la guía hacia el medio exterior por acoplamiento evanescente, por lo que la longitud del tramo sensor dependerá también del material elegido.

El espesor e del material de revestimiento óptico 102 en el tramo sensor 104 puede ser de unas pocas micras, pero también puede ser bastante mayor, dependiendo de la longitud de onda concreta de trabajo, la longitud del tramo sensor 104, etc.

El núcleo 103 de la guía de ondas 101 puede tener cualquier sección, por ejemplo redonda o rectangular, y también puede diseñarse como una zona con múltiples núcleos. El material de revestimiento 102 puede tener también cualquier forma que sea apropiada para contener la zona de núcleo 103 y para que el sensor se pueda colocar en la posición de trabajo; aunque también se puede prever que la guía de ondas esté parcialmente rodeada por una funda o que comprenda otro material exterior de protección, que sirva para montar el sensor en la posición de trabajo.

En las figuras 3, 4 y 5 se muestran esquemáticamente tres posibles variantes de realización de un sensor óptico de acuerdo con la invención.

En la figura 3 el sensor comprende un cuerpo de material de revestimiento óptico 102, que contiene la zona de núcleo 103 y que está montado en una abertura A de la superficie S, de manera que una cara del revestimiento 102 del tramo sensor 104 quede expuesta. En las

figuras se ha exagerado la abertura A para facilitar su identificación, pero habitualmente el sensor se montará de modo que no quede holgura entre la superficie S y el sensor.

La zona de núcleo 103 se extiende de una pared a otra del cuerpo de material de revestimiento óptico 102, siguiendo una trayectoria que hace posible que en el tramo sensor 104 quede próxima a la superficie S y al mismo tiempo proporciona suficiente espacio para las conexiones en los extremos de la zona de núcleo. En esta realización, el emisor 105 y el detector 106 pueden estar montados directamente adyacentes al cuerpo de material de revestimiento 102, como muestra la figura.

La figura 4 muestra un sensor similar al de la figura 3, pero en el cual el emisor 105 y el detector 106 están conectados a la guía de ondas 101 a través de unas fibras ópticas auxiliares, 107 y 108, que pueden tener cualquier longitud adecuada para montar el emisor y el detector en posiciones alejadas de la superficie S en la que hay que detectar la presencia de hielo.

Una realización un poco distinta del sensor se muestra en la figura 5: en este caso, la guía de ondas del sensor es una fibra óptica 201. La fibra óptica 201 comprende, como es conocido, una zona de núcleo 203 (*core*), un revestimiento óptico 202 (*cladding*), y un recubrimiento exterior 209 (*coating* o *buffer*). La fibra 201 se selecciona de modo que el revestimiento óptico 202 cumpla la condición que se ha mencionado de $\mathbf{n_{agua} \leq n_{material} < n_{hielo}}$ a la longitud de onda de trabajo $\boldsymbol{\lambda_T}$,
y preferiblemente $\mathbf{n_{agua} < n_{material} < n_{hielo}}$.

La fibra óptica 201 comprende un tramo sensor 204, en el cual se ha retirado el recubrimiento exterior 209, de modo que una cara del revestimiento 202 quede expuesta en la superficie S. En el tramo sensor 204 se puede retirar además una parte del revestimiento óptico 202, dependiendo del espesor e que se quiera dejar entre el núcleo 203 y el medio exterior.

El emisor 105 y el detector 106 están situados en los extremos de la fibra óptica 201, que tendrá la longitud que sea más adecuada para cada aplicación.

En este caso se ha representado la fibra óptica 201 encapsulada en un bloque o cuerpo de soporte 210 de un material cualquiera, como puede ser una resina o un adhesivo, que no interviene en el funcionamiento del sensor y simplemente tiene la función de permitir montar la fibra óptica 201 y en particular el tramo sensor 204 de una manera adecuada en la superficie S.

Los estudios realizados indican que el sensor es capaz de detectar la presencia de hielo desde que se produce la nucleación de los cristales, sin necesidad de que se forme una capa completa o que el hielo se acumule hasta un cierto espesor; por tanto, el sensor permite una detección muy temprana.

En todas las realizaciones del sensor que se han descrito también se puede prever que haya un recubrimiento anti-erosión aplicado al menos sobre el tramo sensor, es decir sobre la cara del revestimiento óptico que queda expuesta: basta diseñar este recubrimiento con el espesor adecuado para no impedir un acoplamiento evanescente significativo en el tramo sensor. Este espesor depende entre otras cosas del material del recubrimiento y de la longitud de onda de trabajo que se escoja, del nivel de efectividad que se requiera, y también de la longitud que tenga el tramo sensor; en algunos casos convendrá que el espesor sea sustancialmente menor que la longitud de onda de trabajo, sobre todo si se quiere que el tramo sensor tenga una longitud reducida.

En una realización, a título de ejemplo concreto y no limitativo, el sensor puede tener las siguientes características:

- material de revestimiento óptico: cuarzo cristalino
- longitud de onda de trabajo: $\boldsymbol{\lambda_T}$ = 3,394 μm
- espesor del revestimiento sobre el núcleo: e = 10 μm
- núcleo de sección circular, de radio r = 10 μm
- longitud del tramo sensor: 10 mm

En un sensor de este tipo, la señal transmitida no sufriría atenuación en presencia de aire en el exterior, mientras que sufriría una importante atenuación de aproximadamente 6 dB (por tanto sólo habría un 25% de transmisión) en presencia de hielo.

Hasta ahora se ha discutido cómo el sensor es capaz de detectar la presencia de hielo, y de discriminarla respecto a la presencia de agua. Sin embargo, realizaciones del sensor de acuerdo con la invención también pueden detectar la presencia de agua (diferenciada de la presencia de aire), para proporcionar una información más completa de la situación en la superficie, en cada instante o a lo largo del tiempo.

En efecto, cuando existe agua sobre el tramo sensor también se produce una cierta atenuación de la señal transmitida por la guía de ondas, pero en este caso la pérdida de intensidad se debe a fenómenos de absorción (no hay acoplo evanescente), y la pérdida es significativamente menor que en presencia de hielo.

En definitiva, el sensor permite identificar tres situaciones distintas, a cada una de las cuales corresponde una cierta atenuación o pérdida de intensidad de la señal:

- cuando el medio exterior M (ver figura 2) es aire, la señal prácticamente no sufrirá atenuación, o en cualquier caso tendrá un nivel (máximo) conocido, que depende de las características del sensor y de la línea entre el emisor 105 y el detector 106;

- si al cabo de un tiempo se deposita agua sobre la superficie S (es decir, el medio exterior M pasa a ser agua), se producirá una cierta pérdida por absorción en la señal; en algunos casos la intensidad de la señal puede quedar reducida por ejemplo a un nivel aproximado del 80% (atenuación de aproximadamente 1 dB);

- si posteriormente en el agua depositada se forman cristales de hielo, de modo que el medio exterior M pasa a ser hielo, se producirá acoplamiento evanescente de al menos un modo electromagnético guiado de la señal con los cristales de hielo, y la pérdida de intensidad en el tramo sensor será muy superior que en el caso del agua; en algunos casos la intensidad detectada en presencia de hielo puede llegar a ser por ejemplo de alrededor del 20% (atenuación de aproximadamente 7 dB).

La figura 6 ilustra cualitativamente la evolución de la intensidad de la señal a lo largo de estas tres etapas en el tiempo, mostrando a la izquierda de la figura un eje con la intensidad de la señal, y a la derecha un eje con la atenuación correspondiente. La gráfica es puramente ilustrativa, ya que los valores concretos pueden variar dependiendo de los

materiales y la geometría del sensor, la longitud de onda de trabajo, las condiciones del medio exterior, etc.

En una aplicación práctica, mediante una calibración del sensor se pueden establecer uno o más niveles de umbral adecuados para proporcionar señales de aviso de la formación o presencia de hielo, e incluso de la presencia de agua. Los umbrales se establecerán para cada aplicación en los niveles más adecuados dependiendo de cómo se quiera monitorizar la situación, de la seguridad exigida, etc.

Además, puesto que el nivel de acoplamiento evanescente dependerá también de las características de la capa de hielo, calibrando adecuadamente el sensor se puede llegar a evaluar el espesor de la capa de hielo.

Utilizando uno o más sensores ópticos de acuerdo con realizaciones de la presente invención se puede construir un sistema capaz de detectar hielo en un punto de una superficie, pero también un sistema capaz de realizar una monitorización y proporcionar información sobre el medio exterior (aire, agua o hielo) que hay en cada momento sobre la superficie, e incluso sobre el espesor del hielo.

En función de la información proporcionada por el sistema, un usuario puede tomar las decisiones que se consideren apropiadas: por ejemplo, si el sistema se instala en el fuselaje de una aeronave, el piloto puede decidir activar medios para eliminar el hielo o para evitar su acumulación. También se puede prever un control automático de sistemas de deshielo o similares, en función de las señales proporcionadas por el sistema de detección.

Con varios sensores instalados a distancia unos de otros y conectados a una unidad de control común es posible también realizar un sensado multipunto, y se pueden utilizar estrategias de inteligencia artificial o lógica difusa para extraer información adicional respecto a la distribución espacial del hielo en la superficie o el tipo de hielo.

En un sistema con varios sensores se puede emplear un emisor y un detector independientes para cada uno de los sensores; en alguna aplicación puede ser útil además que haya sensores con características distintas unos de otros y que trabajen con longitudes

de onda distintas, por ejemplo si algún punto de la superficie a controlar es más crítico, requiere un mayor nivel de precisión, etc.

Alternativamente un sistema con varios sensores puede emplear un emisor común y una única longitud de onda de trabajo.

En todos los casos, la calibración puede ser individual para cada sensor, de modo que cada sensor tenga asociados umbrales distintos; las diferencias entre los umbrales pueden ser debidas a que las características concretas de los sensores son distintas, pero también a la voluntad de realizar una monitorización de unos puntos de la superficie respecto a otros.

La calibración se puede realizar en fábrica o antes de instalar los sensores, pero puede ser más preciso realizarla una vez que los sensores están instalados en una superficie, e incluso re-calibrar el sensor periódicamente. Para ello, la unidad de control del sistema podrá estar dotada de las funcionalidades necesarias.

Se puede realizar una calibración “en seco”, es decir con aire como medio exterior, para fijar el nivel normal o nivel cero de la intensidad de señal, y asignar porcentajes predeterminados de este nivel como umbrales; o bien se pueden realizar calibraciones específicas también en presencia de hielo y/o agua, para fijar umbrales de atenuación apropiados.

Se comprenderá a partir de esta descripción que, en una realización concreta, un procedimiento para detectar la presencia o la formación de hielo puede comprender, por ejemplo:

- seleccionar una longitud de onda de trabajo para la cual el índice de refracción del agua y el índice de refracción del hielo cumplen la condición $\mathbf{n_{agua} < n_{hielo}}$;

- proporcionar una guía de ondas, que puede ser una fibra óptica o una guía de otro tipo, que tiene una zona de núcleo y un revestimiento óptico, de un material cuyo índice de refracción, a la longitud de onda de trabajo, está entre el del hielo y el del agua;

- instalar esta guía de ondas en la superficie de tal manera que en un tramo de la guía, que constituirá el tramo sensor de la guía, el revestimiento óptico quede colocado con una cara expuesta al medio exterior a la superficie;

- transmitir una señal óptica con la longitud de onda de trabajo prevista, a lo largo de la guía de ondas,

- detectar la señal óptica curso abajo del tramo sensor, y

- comparar la intensidad de la señal detectada con uno o varios umbrales, para determinar en función de la atenuación que se ha producido, si sobre el sensor se ha formado hielo.

En todos los casos, la señal óptica transmitida puede ser continua o pulsada, y la detección puede hacerse a intervalos de tiempo apropiados.

El procedimiento puede aplicarse con un sistema de varias guías de onda instaladas a distancia unas de otras, y puede comprender además etapas de calibración, tal como se ha descrito más arriba. También puede utilizarse para emitir no sólo avisos o señales relacionados con la formación o la presencia de hielo, sino también con la presencia de agua sobre la superficie, estableciendo de manera adecuada las características de las guías de ondas, la longitud de onda de trabajo, y los umbrales.

A pesar de que se han descrito aquí sólo algunas realizaciones y ejemplos particulares de la invención, el experto en la materia comprenderá que son posibles otras realizaciones alternativas y/o usos de la invención, así como modificaciones obvias y elementos equivalentes. Además, la presente invención abarca todas las posibles combinaciones de las realizaciones concretas que se han descrito. Los signos numéricos relativos a los dibujos y colocados entre paréntesis en una reivindicación son solamente para intentar aumentar la comprensión de la reivindicación, y no deben ser interpretados como limitantes del alcance de la protección de la reivindicación. El alcance de la presente invención no debe limitarse a realizaciones concretas, sino que debe ser determinado únicamente por una lectura apropiada de las reivindicaciones adjuntas.

Por ejemplo, los usos que se puede dar al sensor son múltiples, aunque sólo se ha hecho referencia explícita a la detección de hielo y/o agua en aeronaves. También en palas de aerogeneradores el sensor puede resultar muy apropiado, ya que estas superficies tienen problemáticas similares a las de las alas de avión por lo que respecta a la aerodinámica.

Otra aplicación puede ser la detección de hielo en superficies que se encuentran sumergidas, ya que el sensor discrimina de modo fiable el hielo del agua; y también puede emplearse para detectar el hielo en frigoríficos o en conducciones de agua, y en general en cualquier circunstancia en que se quiera detectar la formación de hielo de manera rápida y fiable.

REIVINDICACIONES

1. Sensor óptico (100) para detectar la presencia de hielo en superficies, caracterizado porque comprende:

- una guía de ondas (101; 201) con un material de revestimiento óptico (102; 202) cuyo índice de refracción $n_{material}$ cumple la relación $n_{agua} \leq n_{material} < n_{hielo}$ a una longitud de onda de trabajo λ_T para la cual $n_{agua} < n_{hielo}$, y con una zona de núcleo (103; 203) contenida en el material de revestimiento (102; 202) y apropiada para la propagación de una señal óptica que tiene la longitud de onda de trabajo, presentando la guía de ondas (101; 201) un tramo sensor (104; 204) apropiado para ser instalado en una superficie (S) en la que se debe detectar la presencia de hielo de modo que una cara del material de revestimiento (102; 202) del tramo sensor (104; 204) quede expuesta ;

- medios (105) para inyectar en la guía de ondas (101; 201) una señal óptica con una longitud de onda de trabajo λ_T para la cual $n_{agua} < n_{hielo}$; y

- medios (106) para detectar la señal óptica transmitida por la guía de ondas (101; 201) curso abajo de dicho tramo sensor (104; 204).

2. Sensor óptico según la reivindicación 1, caracterizado porque el índice de refracción del material cumple la relación $n_{agua} < n_{material} < n_{hielo}$ a la longitud de onda de trabajo λ_T.

3. Sensor óptico según una cualquiera de las reivindicaciones 1 ó 2, caracterizado porque el tramo sensor(104; 204) es apropiado para ser instalado en la superficie (S) de modo que la cara del material de revestimiento (102; 202) del tramo sensor (104; 204) quede expuesta a través de una abertura (A) en la superficie (S).

4. Sensor óptico según una cualquiera de las reivindicaciones 1 a 3, caracterizado porque la guía de ondas comprende una fibra óptica (201), de la cual se ha retirado el recubrimiento exterior (209) al menos en el área del tramo sensor (204) destinada a quedar expuesta durante el uso.

5. Sensor óptico según la reivindicación 4, caracterizado porque en el tramo sensor (204) de la fibra óptica (201) se ha retirado además una parte del espesor del revestimiento óptico (202).

6. Sensor óptico según una cualquiera de las reivindicaciones 1 a 3, caracterizado porque en al menos el tramo sensor (104) de la guía de ondas (101) la zona de núcleo (103) está fabricada dentro de un cuerpo de material (102) apropiado, de modo que varíe en esta zona el índice de refracción.

7. Sensor óptico según la reivindicación 6, caracterizado porque a un extremo de entrada y a un extremo de salida de dicha guía de ondas (101) que incluye el tramo sensor (104) están acopladas además fibras ópticas (107, 108).

8. Sensor óptico según una cualquiera de las reivindicaciones anteriores, caracterizado porque la longitud de onda de trabajo λ_T es de entre 3000 y 5000 nm, preferiblemente entre 3200 y 4000 nm.

9. Sensor óptico según una cualquiera de las reivindicaciones anteriores, caracterizado porque el material se selecciona entre cuarzo cristalino, cuarzo vítreo, fluoruro de indio, o compuestos de los mismos.

10. Sensor óptico según una cualquiera de las reivindicaciones anteriores, caracterizado porque el espesor (e) entre la zona de núcleo (103; 203) y la cara del material de revestimiento (102; 202) destinada a quedar expuesta es inferior a 250 µm, preferiblemente inferior a 50 µm.

11. Sensor óptico según una cualquiera de las reivindicaciones anteriores, caracterizado porque comprende además un recubrimiento anti-erosión aplicado sobre la cara del material de revestimiento (102; 202) del tramo sensor (104; 204) destinada a quedar expuesta.

12. Sistema para detectar la presencia de hielo en superficies, caracterizado porque comprende al menos un sensor óptico (100) según una cualquiera de las reivindicaciones 1 a 9, y medios para comparar la intensidad de una señal óptica detectada con al menos un

valor umbral, y generar una alarma en caso de que la señal óptica sea inferior a un valor umbral.

13. Sistema según la reivindicación 12, caracterizado porque comprende medios de calibración para determinar al menos un valor umbral.

14. Sistema según la reivindicación 13, caracterizado porque los medios de calibración son apropiados para determinar al menos un valor umbral una vez que el sistema está instalado en una superficie (S).

15. Sistema según una cualquiera de las reivindicaciones 12 a 14, caracterizado porque comprende una pluralidad de dichos sensores ópticos (100), destinados a ser instalados en una zona predeterminada, a distancia unos de otros, y una unidad de control común conectada a dicha pluralidad de sensores (100), comprendiendo dicha unidad de control medios para proporcionar información sobre la distribución de hielo en una zona predeterminada, en función de las intensidades de las señales ópticas detectadas en las salidas de la pluralidad de sensores (100).

16. Procedimiento para detectar la presencia de hielo en superficies, caracterizado porque comprende:

- seleccionar una longitud de onda de trabajo λ_T para la cual $n_{agua} < n_{hielo}$

- proporcionar una guía de ondas (101; 201) que comprende un material de revestimiento óptico (102; 202) cuyo índice de refracción $n_{material}$ cumple la relación $n_{agua} \leq n_{material} < n_{hielo}$ a la longitud de onda de trabajo λ_T y una zona de núcleo (103; 203) contenida en el material de revestimiento y apropiada para la propagación de una señal óptica que tiene la longitud de onda de trabajo;

- instalar la guía de ondas (101; 201) en una superficie (S) en la que se debe detectar la presencia de hielo, de tal modo que en un tramo de la guía una cara del material de revestimiento (102; 202) quede expuesta, definiendo un tramo sensor (104; 204) de la guía;

- transmitir una señal óptica con una longitud de onda de trabajo λ_T a lo largo de la guía de ondas (101; 201), y

- detectar la señal óptica curso abajo del tramo sensor (104; 204).

17. Procedimiento según la reivindicación 16, caracterizado porque se proporciona una guía de ondas (101; 201) que comprende un material de revestimiento óptico (102; 202) cuyo índice de refracción $n_{material}$ cumple la relación $n_{agua} < n_{material} < n_{hielo}$ a la longitud de onda de trabajo λ_T.

18. Procedimiento según una cualquiera de las reivindicaciones 16 ó 17, caracterizado porque se instala la guía de ondas (101; 201) en la superficie (S) de modo que la cara del material de revestimiento (102; 202) del tramo sensor (104; 204) quede expuesta a través de una abertura (A) en la superficie (S).

19. Procedimiento según la reivindicación 18, caracterizado porque el tramo sensor (104; 204) de la guía de ondas (101; 201) se instala en la superficie (S) de modo que la cara del material de revestimiento (102; 202) expuesta quede nivelada con la superficie (S).

20. Procedimiento según una cualquiera de las reivindicaciones 16 a 19, caracterizado porque comprende además:

- comparar la intensidad de la señal detectada con al menos un valor umbral, y

- determinar que hay presencia de hielo sobre el tramo sensor (104; 204) de la guía de ondas (101; 201) si la intensidad de la señal detectada es inferior a dicho valor umbral.

21. Procedimiento según la reivindicación 20, caracterizado porque comprende además determinar al menos un valor umbral.

22. Procedimiento según la reivindicación 21, caracterizado porque la determinación de al menos un valor umbral se realiza una vez que la guía de ondas (101; 201) está instalada en una superficie (S).

23. Procedimiento según una cualquiera de las reivindicaciones 16 a 22, caracterizado porque comprende:

- instalar una pluralidad de guías de ondas (101; 201) en una zona predeterminada, a distancia unas de otras,

- proporcionar una unidad de control común conectada a dicha pluralidad de guías de ondas (101; 201), y

- proporcionar información mediante la unidad de control sobre la distribución de hielo en la zona predeterminada, en función de las intensidades de las señales ópticas detectadas.

RESUMEN

SENSOR ÓPTICO, SISTEMA, Y PROCEDIMIENTO
PARA DETECTAR LA PRESENCIA DE HIELO EN SUPERFICIES

La invención se refiere a un sensor óptico para detectar la presencia de hielo en superficies, caracterizado porque comprende una guía de ondas con un revestimiento óptico cuyo índice de refracción cumple la relación $n_{agua} \leq n_{material} < n_{hielo}$ a una longitud de onda λ_T para la cual $n_{agua} < n_{hielo}$, y un núcleo contenido en el revestimiento y apropiado para la propagación de una señal óptica de λ_T, presentando la guía de ondas un tramo sensor que se instala en una superficie con una cara del revestimiento expuesta; medios para inyectar en la guía de ondas una señal óptica de λ_T; y medios para detectar la señal óptica transmitida por la guía de ondas curso abajo del tramo sensor. Detecta la formación de hielo, diferenciando de la presencia de agua; además es resistente a la erosión, y se puede montar sin que sobresalga de la superficie.

Figura 4

DIBUJOS

FIG. 1

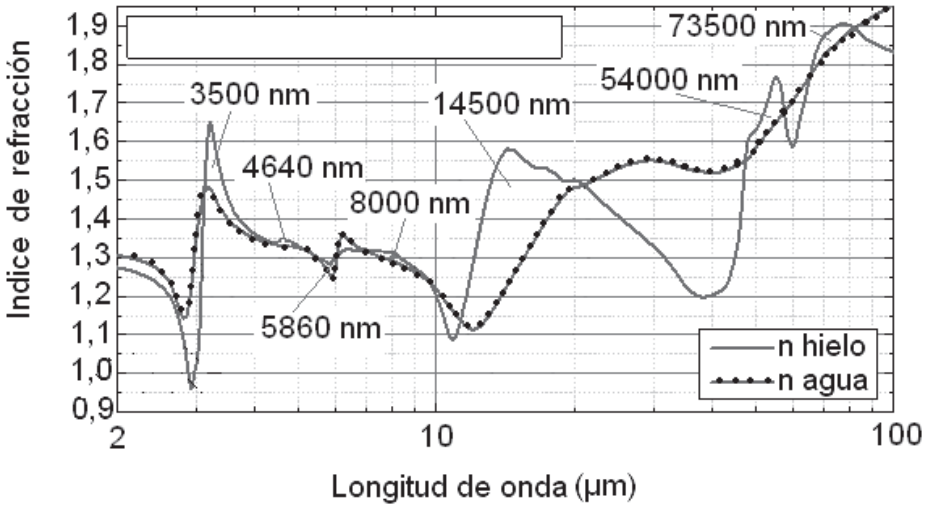

FIG. 2

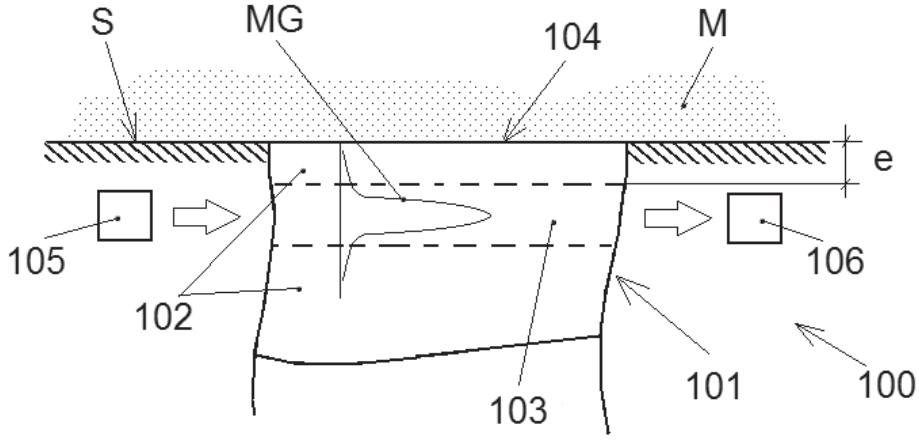

FIG. 3

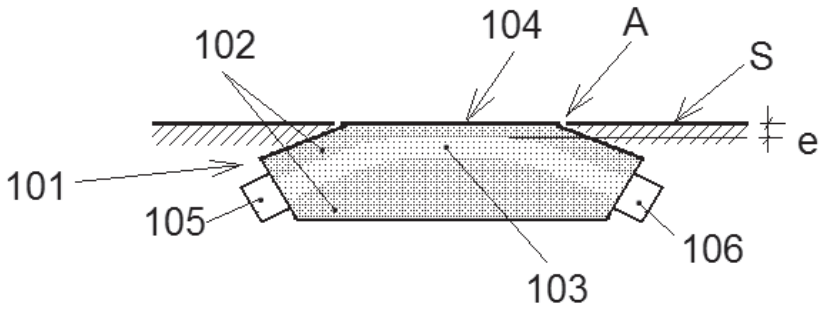

FIG. 4

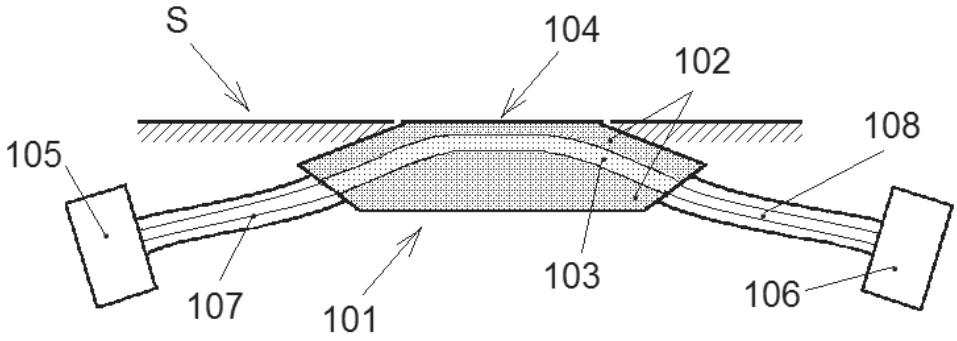

FIG. 5

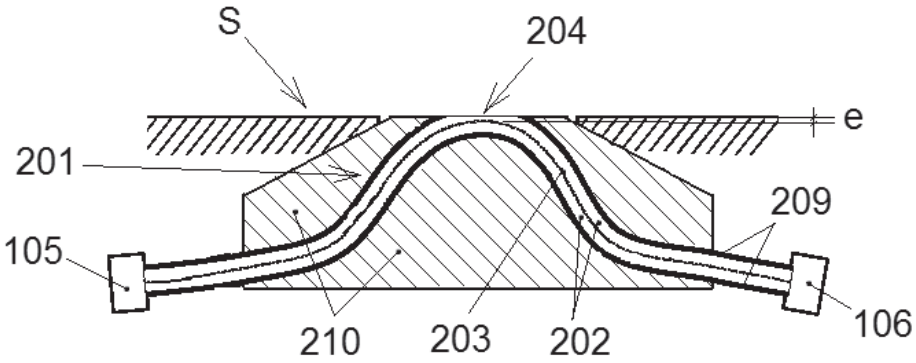
S
204
e
201
209
105
106
210
203
202

FIG. 6

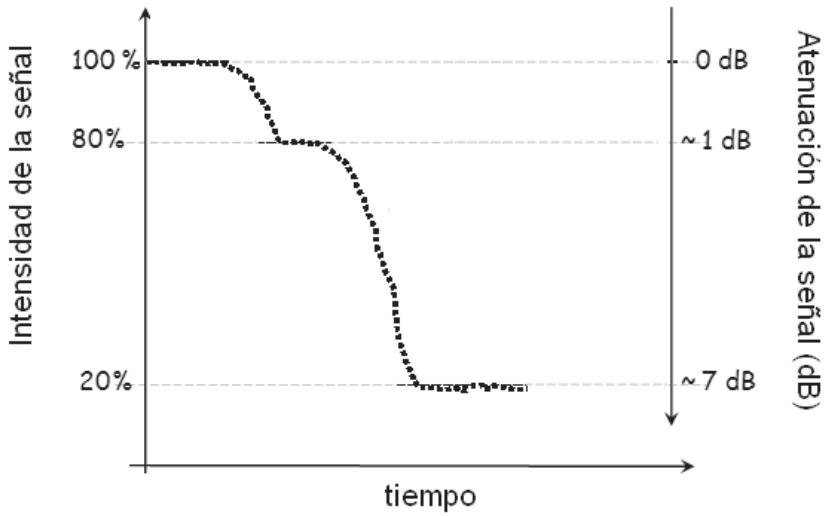
Intensidad de la señal
100 %
80%
20%
0 dB
~ 1 dB
~ 7 dB
Atenuación de la señal (dB)
tiempo

UNIVERSITAT
ROVIRA i VIRGILI